DESIGN AND SYNTHESIS OF CRYPTOPHANE-BASED FUNCTIONALIZED XENON HOSTS FOR MRI APPLICATIONS

Inaugural-dissertation to obtain doctoral degree

Doctor Rerum Naturalium (Dr.rer.Nat.)

Submitted to the Department of Biology, Chemistry and Pharmacy of Freie Universität Berlin by

M.Sc Federica Rossella from Voghera(PV)-IT

This work has been carried out at the Leibniz-Institut für Molekulare Pharmakologie (FMP) Berlin under the supervision of Dr. Leif Schröder.

Reviewer 1:
Prof. Dr. Hartmut Oschkinat
Department NMR-supported Structural Biology
Leibniz-Institut für Molekulare Pharmakologie (FMP)
Robert-Rössle-Str. 10 Berlin

Reviewer 2:
Prof. Dr. Christian Freund
Institute of Chemistry and Biochemistry
Freie Universität Berlin
Thielallee 63 Berlin

Date of defense: 23.10.2015

Table of Contents

Summary

Magnetic resonance imaging (MRI) is an emerging technique for “molecular” diagnostic imaging because of unlimited penetration depth, high spatial resolution and safeness. Currently there is a high demand for developing contrast agents to render the MRI information extremely specific. This has to be combined with efforts to address the well-known poor sensitivity of MRI. Detecting hyperpolarized non-proton nuclei, such as Xe that underwent spin exchange optical pumping is a suitable method that was the method of choice for this thesis because it enables a theoretical 10^7-fold signal enhancement in combination with indirect detection methods such as Chemical Exchange Saturation Transfer (Hyper-CEST). The molecular specificity in this approach is enabled through molecular cages such as Cryptophane-A (Cr-A), that temporarily bind Xe and are conjugate to a targeting unit.

This work aims to advance the design and synthesis of Xe-based biosensors, in particular in the context of Hyper-CEST detection and NMR/MRI performance in cellular environments. In our preliminary studies, CrA-ma was used to label cells and to study the response of labelled cells in Xe-NMR/MRI as a reference for functionalizes sensors. This was complemented by implementing dual sensors through conjugation of CrA-ma with fluorescent dyes. Thi allowed cell tracking and quantification through optical imaging techniques. The two dual sensors (bearing CrA-ma for Xe-MRI and FAM or TAMRA for optical imaging) were tested and used to develop a protocol for Hyper-CEST evaluation with respect to incubation conditions and cell viability in comparison with unfunctionalized cage. This revealed excellent correlation between the response in Xe-MRI and and fluorescence cell analysis.In order to achieve a fast, efficient and flexible synthesis of the dual bisosensors, an optimization of the coupling reaction through microwave-assisted acylation was done. The new mw-assisted synthesis protocol allowed the synthesis of the first targeted biosensors produced in our group, which was an antibody-based anti-CD14 dual sensor. Such a sensor showed a very high specificity in targeting the cell surface receptor CD14 and CrA-ma was detected in Xe-MRI at nanomolar concentration.

In an alternative approach, the possibility of targeting an enzyme was considered because, other than having information about the enzyme activity, a possible further signal amplification through the enzyme can be postulated. Matrix metalloproteinases (MMPs) are largely used in molecular imaging. CrA-ma probes targeting MMP-11 were synthesized first. However, the poor solubility of the probe was a point of concernthough this work could demonstrate a better spectral dispersion after enzyme activation compared to previous studies. We decided therefore to address the new probe to MMP-2/9, a molecular target of considerable interest in cancer diagnostics. Furthermore, the new probe was based on an activatable cell penetrating peptide (ACPP). In such concept, the two read out modules (CrA-ma and FAM) were incorporated in a probe bearing a poly-D-Arg sequence and an inhibitory poly-D-Glu sequence, joined together by a cleavable consensus sequence. Upon proteolysis, our Xe-MRI data showed indeed a Hyper-CEST response of 80% for enzyme-bearing cellular environment and only 20% for the negative control.

Overall, the approaches presented in this work represent key steps to illustrate the potential and robustness of the Hyper-CEST detection technique for molecular imaging throrough the design and synthesis of Xe-based biosensors building blocks and improved MRI performance in cellular environments.

Zusammenfassung

Die Magnetresonanztomographie (MRT) ist wegen ihrer unbegrenzten Eindringtiefe, hohen räumlichen Auflösung und großen Sicherheit innerhalb der sog. "molekularen" diagnostischen Bildgebung eine aufstrebende Methode. Derzeit gibt es einen starken Bedarf für die Entwicklung von Kontrastmitteln, die MRT-Aufnahmen einen spezifischen Kontrast verleihen. Dabei werden gleichzeitig Bemühungen nötig, welche die bekannt schlechte Sensitivität der MRT adressieren. Die Detektion von sog. hyperpolarisierten X-Kernen wie Xe, welche man durch optisches Spinaustausch-Pumpen erhält, ist hierfür eine geeignete Methode. Sie war auch die Methode der Wahl für diese Arbeit, weil sie in Kombination mit indirekten Nachweismethoden wie z.B Sättigungs-Transfer durch chemischen Austausch (Hyper-CEST) theoretisch eine ~10^7-fache Signalverstärkung ermöglicht. Die molekulare Spezifität dieses Ansatzes wird durch molekulare Käfige wie Cryptophan-A (Cr-A) ermöglicht, die temporär Xe binden und mit einer Targeting-Einheit gekoppelt werden.

Ziel dieser Arbeit war das Design und die Synthese neuer Xe-Biosensoren, insbesondere in Zusammenhang mit der Hyper-CEST-Methode und deren Anwendung zur NMR/MRT-Auslese für zelluläre Proben. In diesen Machbarkeitsstudien wurde CrA-monoacid (Cr-ma) verwendet, um Zellen zu markieren und deren Auslese-Antwort in Xe-NMR/MRT-Experimenten als Referenz für spätere funktionalisierte Sensoren zu untersuchen. Dies wurde durch die Implementierung von dualen Sensoren mittels Konjugation von CrA-ma mit Fluoreszenzfarbstoffen ergänzt, was ein Zell-Tracking und eine Quantifizierung durch optische Verfahren ermöglichte. Die beiden dualen Sensoren (welche CrA-ma zur Xe-MRT-Auslese und FAM oder TAMRA zur optischen Detektion tragen) wurden charakterisiert und anschließend verwendet, um ein Protokoll für die Evaluierung von Hyper-CEST-Effekten hinsichtlich der Inkubationsbedingungen und der Zell-Viabilität im Vergleich zur Verwendung nicht-funktionalisierter Käfige zu entwickeln. Dabei ergab sich eine ausgezeichnete Korrelation zwischen dem Verhalten in der Xe-MRT und der Fluoreszenz-Analyse der Zellen. Um eine schnelle, effiziente und flexible Synthese der dualen Bisosensoren zu erreichen, wurde eine Optimierung der Kupplungsreaktion durch die mikrowellenunterstützte Acylierung vorgenommen. Das neue mw-unterstützte Synthese-Protokoll erlaubte in unserer Gruppe die Synthese der ersten Antikörper-basierten Sensoren (anti-CD14) in Form eines zielgerichteten, dualen Sensors. Dieser Sensor zeigte eine sehr hohe Spezifität für den Zelloberflächenrezeptor CD14 und die CrA-ma-Einheit konnte mittels Xe-MRT bei nanomolaren Konzentration nachgewiesen werden.

In einem alternativen Ansatz wurde die Möglichkeit der gezielten Enzym-Detektion untersucht, da hierbei mit der Information über die Enzymaktivität auch eine Möglichkeit zur weiteren Signalverstärkung durch das Enzym selber einhergeht. Matrixmetalloproteinasen (MMPs) werden umfangreich in der molekularen Bildgebung untersucht. CrA-ma-Sonden, welche auf die Detektion von MMP-11 abzielen, wurden hier erstmals synthetisiert. Die schlechte Löslichkeit des Sensors war jedoch ein limitierender Faktor, obwohl in dieser Arbeit eine bessere spektrale Dispersion nach Enzymaktivierung im Vergleich zu früheren Studien gezeigt werden konnte. Wir beschlossen daher, einen neuen Sensor für MMP-2/9 zu entwickeln. Diese MMPs sind von großem Interesse in der Krebsdiagnostik. Der neue Sensor basiert auf einem aktivierbaren, zellpenetrierenden Peptid (ACPP). Bei diesem Konzept sind die zwei Auslesemodule (CrA-ma und FAM) des Sensors mit einer Poly-D-Arg-Sequenz und einer inhibierenden Poly-D-Glu-Sequenz gekoppelt. Letztere sind miteinander durch eine spaltbare Sequenz als Substrat von MMP-2/9 gekoppelt. Nach Proteolyse zeigten unsere Xe-MRT-Daten einen Hyper-CEST-Effekt von 80% für die Enzymtragenden zellulären

Umgebungen und nur 20% für die negative Kontrolle. Insgesamt sind die in dieser Arbeit vorgestellten Ansätze wichtige Schritte, um das Potenzial und die Robustheit des Hyper-CEST-Detektionstechnik für die molekulare Bildgebung durch Design und Synthese von Xe-Biosensor-Bausteinen und die verbesserte MRT-Detektion in zellulärer Umgebung zu illustrieren.

Chapter 1

Introduction

Molecular imaging: visualizing biological processes in a nanomolar regime

Molecular imaging can be defined as the *in vivo* visualization of molecules and molecular targets, achieved through the detection of specific contrast agents or biosensors with imaging techniques such as Magnetic Resonance Imaging (MRI), X-Ray Computed Tomography (CT), Positron Emission Spectroscopy (PET), Single-Photon Emission Computed Tomography (SPECT), Ultrasound, Fluorescence Optical Imaging (FOI), among many others (see Table 1).[1; 2]

In general, an imaging technique should satisfy a least those requirements: obtaining images at high resolution, allowing measurement quantitative and over time (longitudinal), being sensitive to very small perturbation in the system and possibly being standardized.[3] In the beginning, imaging techniques were aimed at the detection of structural abnormalities, possibly linked to diseases, such as with MRI or CT, which rely on energy-tissue interactions. Both MRI and CT allow to obtain morphological information and functional/physiological readouts, although between the two, only MRI gives sufficient contrast for soft tissue imaging. [2] Other techniques like PET/SPECT or FOI need to rely on the presence of imaging agents or reporters in order to detect the signal; such agents can be targeted to cell receptors of interest giving place to a distinctive, specific receptor-mediated response. [2; 4] In general, the use of a reporter is preferable in cancer studies, where the difference between healthy and neoplastic cells it is very narrow. In fact, conventional anatomical techniques can detect cancer in tissue when the size is over 1 cm (corresponding roughly to 10^9 cells), but an early detection of cancer can increase the survival rate to 90%, when measured over a five year time line. To achieve the necessary early diagnosis, key molecular and cellular targets associated with the tumor are identified and selected to be monitored though molecular imaging. [4; 5] Various imaging agents have been developed for this task, such as small ligands, engineered proteins, inorganic or bio nanoparticles, supramolecular structures and environmentally sensitive probes. [5],[6]

Molecular imaging is a versatile diagnostic tool, not only for measuring processes associated with cancer (e.g. angiogenesis, apoptosis, tumor specific cell receptors), but also for detecting processes such as arteriosclerosis, inflammation, and many others. [7] PET is widely used to measure inhibition, biodistribution and pharmacokinetics of ^{11}C and ^{18}F labeled drugs, being that the labeling only minimally affects the physico-chemical properties of the drug. Despite the great sensitivity, the mere use of radiolabeled tracers can cause potential problems and hazards, including handling safety issues and the high cost of equipment.[7] Fluorescence-based techniques such as microscopic and macroscopic fluorescence imaging and fluorescence-mediated tomography (FMT) have the advantage of being sensitive at nanomolar range,[1], versatile and quantitative (in the case of FMT), and don't require expensive equipment, one disadvantage of both MRI and PET.[4] The wide development of near infra-red (NIR) probes also has advantages, over other fluorochromes, of significantly reduce the background signal and the autofluorescence *in vivo*.

Table 1 | Overview of imaging systems

Technique	Resolution*	Depth	Time‡	Quantitative§	Multi-channel	Imaging agents	Target	Cost*¶	Main small-animal use	Clinical use
MRI	10–100 μm	No limit	Minutes to hours	Yes	No	Paramagnetic chelates, magnetic particles	Anatomical, physiological, molecular	$$$	Versatile imaging modality with high soft-tissue contrast	Yes
CT	50 μm	No limit	Minutes	Yes	No	Iodinated molecules	Anatomical, physiological	$$	Imaging lungs and bone	Yes
Ultrasound	50 μm	cm	Seconds to minutes	Yes	No	Microbubbles	Anatomical, physiological	$$	Vascular and interventional imaging‖	Yes
PET	1–2 mm	No limit	Minutes to hours	Yes	No	^{18}F-, ^{64}Cu- or ^{11}C-labelled compounds	Physiological, molecular	$$$	Versatile imaging modality with many tracers	Yes
SPECT	1–2 mm	No limit	Minutes to hours	Yes	No	^{99m}Tc- or ^{111}In-labelled compounds	Physiological, molecular	$$	Imaging labelled antibodies, proteins and peptides	Yes
Fluorescence reflectance imaging	2–3 mm	<1 cm	Seconds to minutes	No	Yes	Photoproteins, fluorochromes	Physiological, molecular	$	Rapid screening of molecular events in surface-based disease	Yes
FMT	1 mm	<10 cm	Minutes to hours	Yes	Yes	Near-infrared fluorochromes	Physiological, molecular	$$	Quantitative imaging of fluorochrome reporters	In development
Bioluminescence imaging	Several mm	cm	Minutes	No	Yes	Luciferins	Molecular	$$	Gene expression, cell and bacterium tracking	No
Intravital microscopy¶	1 μm	<400–800 μm	Seconds to hours	No	Yes	Photoproteins, fluorochromes	Anatomical, physiological, molecular	$$$	All of the above at higher resolutions but limited depths and coverage	In development#

*For high-resolution, small-animal imaging systems. (Clinical imaging systems differ.) ‡Time for image acquisition. §Quantitative here means inherently quantitative. All approaches allow relative quantification. ¶Cost is based on purchase price of imaging systems in the United States: $, <US$100,000; $$, US$100,000–300,000; $$$, >US$300,000. ‖Interventional means used for interventional procedures such as biopsies or injection of cells under ultrasound guidance. ¶Laser-scanning confocal or multiphoton microscopy. #For microendoscopy and skin imaging. (Table adapted, with permission, from ref. 85.)

Tab.1 Overview of imaging techniques, advantages, drawbacks, and sensitivity. From Weissleder R. And Pittet M.J.,(2008) [3]

Despite that, FOI techniques, compared to MRI or PET have a much lower penetration depth and resolution, and this is somewhat limiting when suche techniques are applied *in vivo*. The introduction of contrast agents in MRI represented a crucial step in the tremendous development of imaging techniques.

MRI has a very high spatial resolution (i.e.10-100 μm MRI vs. 50 μm CT and > 1 mm for PET and SPECT) and unlimited penetration depth (for FOI it would be only less than 1 cm), and in combination with contrast agents, it has became an extremely specific technique, thus used extensively for studying specific parameters in living subject, often referred as functional-MRI (fMRI).[2] Despite its intrinsic low sensitivity and expensiveness, MRI remains the technique of choice for diagnostic and drug development, because of the safeness, high penetration depth, and its large spatial resolution. Among the strategies adopted to overcome the low sensitivity, particularly interesting are the detection of protons belonging to non-hydrogen atoms, such as F or Na (so called X-nuclei), or to polarized non-proton atoms, as ^{13}C or polarized noble gas, as ^{3}He or ^{129}Xe. In the case of ^{129}Xe or hyperpolarized-Xe (hp-Xe) based NMR and MRI, a further development of the technique has been achieved through the enhancement of the polarization using Spin-Exchange Optical Pumping (SEOP) instead of the conventional thermal polarization, and through the detection with the Chemical Exchange Saturation Transfer (CEST) method. The use of hp-Xe in combination with CEST has the acronym of Hyper-CEST.

1.1 Xe-based NMR

Xenon is a inert gas, and is present in the Earth atmosphere at a 10^{-6} of a percent. Although chemically non reactive, Xe has biological activity; in fact it has anesthetic properties, although so far the precise mechanism has not been fully elucidated. However, one possible explanation could be its high solubility in lipids (1.17 molar fraction of gas in liquid and gas phase, more than ten times higher than that of Ar) [8] which is a common feature of all known gas anesthetics, or the interaction with the N-methyl-D-aspartate receptor. [9; 10]

Xe has high binding constant for myoglobin, which means that the narcosis occurs promptly, and at low doses. Compared to commonly used anesthetics like fluorane derivatives, it has no negative inotropic effect, and has also shown to be protective for heart and brain.[9] Although there are applications with ^{133}Xe (scintigraphy), the 129 isotope of Xe (26.4% abundance) is the most commonly used in MRI applications: it possesses a simple NMR signal (1/2 spin) and it is less prone to relaxation than ^{133}Xe. (**76**).^{129}Xe can be used for NMR imaging for several reasons:

- Absence of background signal (always present when proton-MRI is performed)
- Lack of toxicity and safety in handling
- Great sensitivity to the chemical environment: chemical shift spanning over 200 ppm.

Hp-Xe has been successfully employed in the imaging of cavities, e.g. lungs, a notable limitation of conventional proton-MRI. Lung Xe-MRI exploits the large hp-Xe chemical shift between hp-Xe dissolved in the alveolar space, the dissolved in the plasma/parenchyma and the one in red blood cells. [11]Pulmonary Hp-Xe MRI has been showed to provide alveolar microstructure information, as well as functional information, such as dynamic ventilation, intrapulmonary partial pressure of oxygen, gas exchange and uptake. **[11-16]** An example of Xe-lung imaging is displaced in Fig.1

Another possible application of hp-Xe as a tracer is for brain imaging, a widely developed field in MRI that, in the case of hp-Xe, can benefit from its solubility in fat, thus crossing hematoencephalic barrier faster. [16-18] Among the applications, brain hp-MRI scans have been used in a C6 glioma rat model [19] in a stoke model, [20] and to study distribution and function in rat brain. [21; 22]

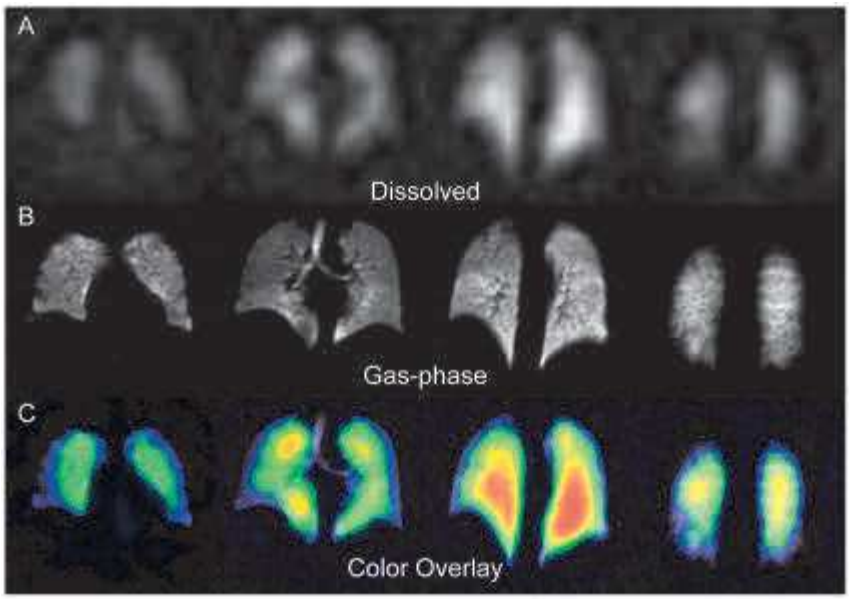

Fig. 1 Lung hp-Xe MRI of a healthy human volunteer. (a) 15-mm-thick sections from a dissolved-phase hp-Xe (12.5 mm×12.5 mm in-plane resolution). (b) Corresponding 15-mm-thick slices from a gas-phase hp-Xe image of the same subject (3.2 mm×3.2 mm in-plane resolution). (c) Dissolved hp-Xe image from (a) (color) overlaid on the gray scale ventilation image from (b).. From Cleveand Z.I. et al, 2010. [14]

1.1.1 Hyperpolarized Xe: Spin Exchange Optical Pumping

Hyperpolarization is defined as the out-of equilibrium nuclear polarization obtained through the magnetization transfer from an ordered system to a less-ordered system.[10] In other words, it is the enhancement of the spin population difference, which, defined by the Boltzmann distribution law, is characterized by a small energy gap at room temperature, even for high magnetic fields, thus a very small difference between the two populations. (Fig. 2A)[23]

Given the cost of high magnetic fields systems and the limitations in decreasing the temperature when biological samples are handled, many efforts have been made to achieve an efficient nuclear polarization.

Hyperpolarized systems can be generated for instance, through ParaHydrogen Induced Polarization (PHIP) or Dynamic Nuclear Polarization (DNP), both used to produce ^{13}C.[24], [10] The incorporation of ^{13}C in probes such as 1-^{13}C-pyruvate has been used successfully in biomedical research given the unchanged pharmacokinetics and biodistribution compared with natural pyruvate. [24; 25]

With the aim of polarizing Xe, a particularly efficient method is Spin-Exchange Optical Pumping (SEOP), whom degree of polarization for Xe is reported to be up to 10^5, considering a magnetic field (B_0) of 1.5 T and a temperature of 300 K. [24] The enhancement in the signal is of 25,000 when compared with Xe thermally polarized (see Fig. 2b)

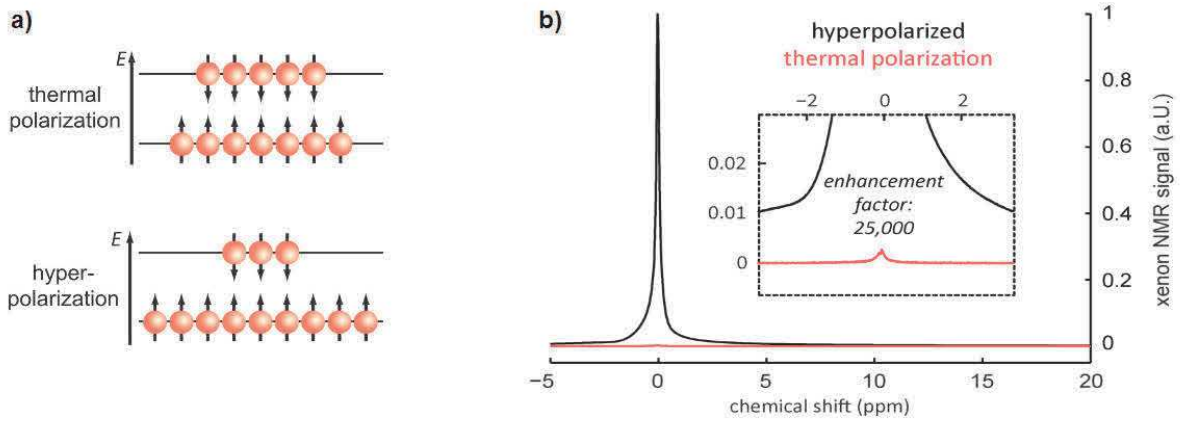

Fig.2a. Difference between spin populations in thermal polarized and hyper-polarized systems. From Schröder L. (2013)[23]
Fig.2b. Comparison of the Xe NMR signal when hp-Xe is produced through thermal polarization (red) and SEOP polarized (black). From Witte C. and Schröder L. (2013)[24]

The production of hp-Xe through SEOP is described in detail in Witte C. et al, (2012) [26] and (2014)[27] .

Briefly, the whole process consists in the hyperpolarization of Xe nuclei though a spin-spin interaction of Xe with an electron of Rubidium (Rb), previously pumped to a specific transition through circularly polarized light. [10] The SEOP process occur in a optical pumping cell, as schematized in Fig.3.The circularly polarized light is produced by a laser with high-power (100 W) diode arrays at 795 nm, which drive the desired D_1 transition in Rb. Rb at low temperature is in vapor state, an important feature for the subsequent collision with the Xe in gas mixture. Such a gas mixture contains a small percentage of ^{129}Xe, the condition necessary for the spin exchange to occur. The yield of Rb polarization is maintained through the exposure of the Rb vapor to a specific magnetic field that enables the selective pumping, enriching one spin state. Finally, the Rb

electron spin polarization is converted into Xe nuclear polarization, through dipolar interaction. [24]

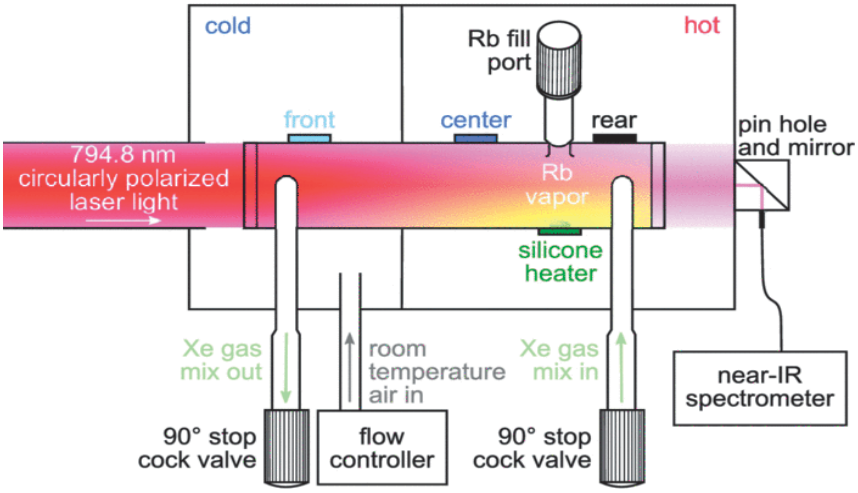

Fig.3 Schematic of the optical pumping cell. Circularly polarized 794.8 nm laser light illuminates the cell from the left. The rubidium droplet is vaporized through the heating produced by a silicone heating strip. The transmitted light passes through a 100 µm diameter pin hole, and the laser transmission is monitored through a near-infrared spectrometer monitor. The cell is placed within an oven divided into two regions, hot and cold. The cold side is in the front of the optical cell. Three thermocouples monitor the temperatures throughout the cell. From Witte et al, (2014) [27]

1.2 Host-guest systems for encapsulation hp-Xe: cryptophanes

1.2.1 Affinity of cryptophanes for Xe

One of the most important features of hp-Xe is its ability to temporarily bind to host-guest systems, like cryptophanes (Fig.4).Hp-Xe, once bubbled or dissolved in an organic or aqueous solution containing cryptophanes, give rise to a unique NMR signal, easily distinguishable both from hp-Xe in solution and Xe in gas (Fig.5). Cryptophanes were developed firstly by Collet and co-workers, with the aim of designing molecular cavities to sense small neutral gas molecules (halomethanes and volatile organic compounds) or charged molecules such as ammonium compounds. [28-30]

Xe has been found to be the ideal guest for cryptophanes for at least two reasons: firstly, its van der Waals volume is 42 Å, therefore it fits perfectly in the cryptophanes' cavities, which are around 0.5-1 times bigger. Secondary, since Xe dissolves easily in apolar mixtures, it has a strong affinity for the hydrophobic cavity.[10]

Chemically, cryptophanes (Fig.4) are supramolecular structures, consisting of two cyclotriveratrylene (CTV) caps with different R_1 and R_2 substituents joined together by aliphatic bonds ($(CH_2)_m$ and $(CH_2)_n$) of different lengths. Examples of cryptophanes are reported in Table 2.

The length of the aliphatic bonds and of the R_1 and R_2 substituents change the size of the cavity and the properties of the cryptophanes, in terms of solubility, exchange rate and affinity for Xe.[31] For instance, NMR studies in 1,1,2,2-tetrachloroethane-d_2 and in D_2O showed that the affinity of Xe for cryptophanes has been found to decrease linearly with size of the cavity [44-45], possibly explained by a decrease of the stability of the interactions between Xe and cryptophanes, assured by London forces.

The shape of the cavity and the type of solvent may play a role as well. [32]

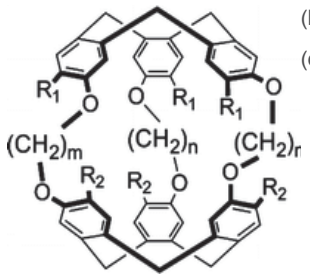

(left) Fig.4 General structure of Cryptophane (from[31])

(down) Tab.2 Name, substitutents and characteristics of cryptophanes.

Name	*m*	*n*	R_1	R_2	Xe K_A (M^{-1})	Cavity size (Å)	Ref.
Cryptophane-A	2	2	OCH_3	OCH_3	3900 [(a)] 2750 [(b)] 3300 [(c)] 40 [(d,1)] 850 [(d,2)]	95	**[32-34, 35]**
Cryptophane-A acid	2	2	OCH_2COOH	OCH_2COOH	6800[(c)]	-	**[33]**
Cryptophane-E	3	3	OCH_3	OCH_3	5-10 [(a)]	121	**[32; 33; 36]**
Cryptophane-C	2	2	H	OCH_3	-	-	**[32]**
Cryptophane 233	3	2	OCH_3	OCH_3	102[(a)]	102	**[10; 32]**
Cryptophane 223	2	3	OCH_3	OCH_3	800[(a)]	117	**[10; 32]**
Cryptophane-E acid	3	3	OCH_2COOH	OCH_2COOH	1000 [(e)]	121	**[10; 37]**
TAAC	2	2	OCH_2COOH	OCH_3	33000 [(f)]	-	**[33; 38]**
TTPC	2	2	triazole propionic acid	OCH_3	17000 [(f)]	-	**[33]**
Cryptophane 111	1	1	H	H	28000[(a)] 30000 [(e)]	81	**[10; 33; 39-41]**
Cryptophane 0-0-0	§	§	OCH_3	OCH_3	-	40	**[42] (§)**
-	2	2	PEG_{11}	PEG_{11}	5800±600[(e)]	-	**[43]**
Tripropargyl-cryptophane	2	2	OCH_3	propargyl	-	95	**[44]**
[G2]-Cryptophane-A	2	2	OCH_3 (‡)	OCH_3(‡)	3200 [(b)]	95	**[34]**

(a) 278 K, in 1,1,2,2-tetrachloroethane d_2
(b) Inversion recovery experiment performed in water with 0.27% DMSO, at 293 K
(c) 293 K, D_2O
(d) a.295 K, in DMSO, measured by qHyperCEST b. 295 K, in water, measured by qHyperCEST
(e) 278 K, in aqueous solution.
(f) 293 K, phosphate buffer, measured with ITC.
(§) instead of O-CH_n-O linkers, Cryptophane 0-0-0 have disulphide linkers, S-S. This cage has been designed to detection of methane.
(‡) One of R1 and one of R2 is bearing a dendrimer [G2] instead of a -OCH_3 group

The affinity for Xe is influenced as well by the nature of R_1 and R_2 substituents: more bulky and hydrophobic substitutents assure a higher affinity. [32; 47-48]Temperature is reported to play an important role: for instance, the affinity of Xe for cryptophane-111 drops almost threefold with a decrease of only 15 K. [23] The difference in chemical shift upon interaction Xe-cage is different for every cryptophane. It increases in smaller cage size, because of the decrease of the Xe intramolecular shielding effect in proximity of neighbour atoms. [23; 49-50] A recently published study has elucidated that this phenomenon is linked to the change in electronic field gradient at the Xe nucleus, due to the changes on electron distribution in the phenolyc rings upon substitution.[41] Among the cryptophanes, the 6-methoxy derivative, cryptophane-A (CrA), is the better

characterized and thus the first used for biosensing. Cr-A has a cavity size of 95 Å, and the reported affinity for Xe is up to 33,000 M^{-1} in aqueous solvents and one order of magnitude lower in organic media. [51] A measurement performed with Isothermic Titration Calorimetry (ITC) in phosphate buffer demonstrated an affinity of 42,000 M^{-1}. [51] Furthermore, the in-and-out Xe exchange rate is bigger than in cryptophane 1-1-1 because of the sterical hindrance provided by its methoxyl groups, but it is still lower than the difference between the resonance frequencies of free Xenon and Xe in the molecular cage, therefore suitable for Xe-MRI experiments. [10; 32; 37]

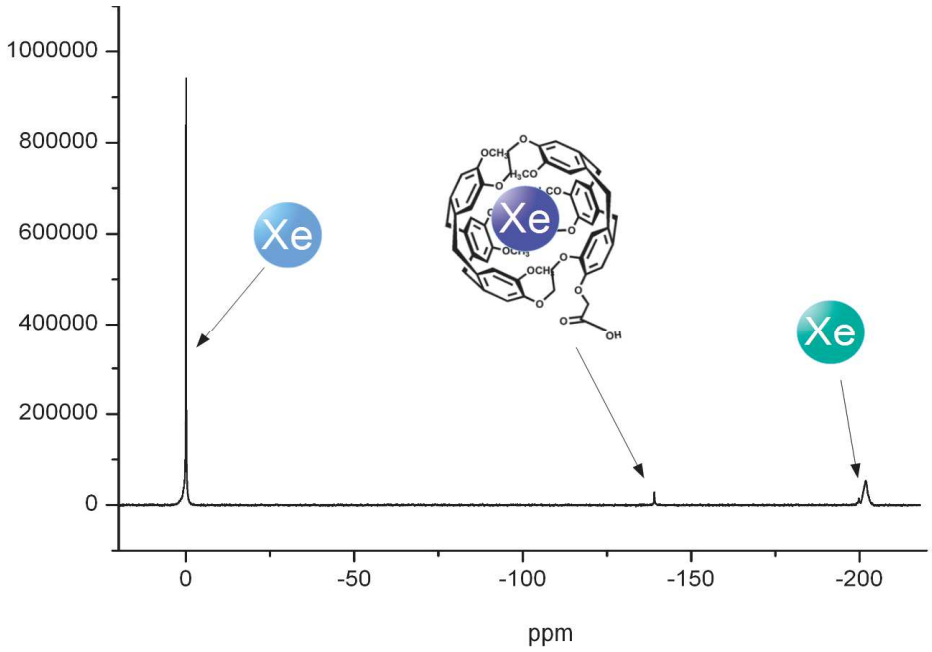

Fig. 5 Example of a Xe-NMR direct spectrum of 70 µM CrA dissolved in a solution of 10% dimethylsulphoxide in water. The peak at 0 ppm is the reference, and it is the signal of hp-Xe in solution. The peak at -201.9 ppm it is the signal arising from Xe in gas and the signal at -136 ppm is the signal from hp-Xe in dynamic exchange with CrA.

1.2.2 "Direct" and "Template" synthesis of Cryptophanes

Cryptophanes, as described so far, present a high symmetry (C_3 symmetry), and therefore have the limitation of not being modifiable once they are synthesized. It is straightforward to imagine, though, that having the possibility of selectively modifying a cryptophane cage according to the use, would be the key step in the development of a targeted biosensors library. The C_3 symmetry limitation arises from the first synthetic route described, the so called "direct (two steps) method" (Scheme 1).

The "direct method" consists in the condensation, gained through treatment with formic acid, of previously prepared bis-vanyllil alcohol derivatives. Although this method is very fast, it has a low yield (2-5% for CrA) and does not allow further modifications. [31] Conversely, the so called "template method" (Scheme 2a-d) is based on the separated synthesis of the two pre-organized CTV caps, starting from different benzyl acid derivatives. Once prepared, the two CTV caps are then joined together in a second step, using acids or catalysts. Although more time consuming, the "template method" offers much greater possibilities and has a better yield. [31; 48; 53- 54]

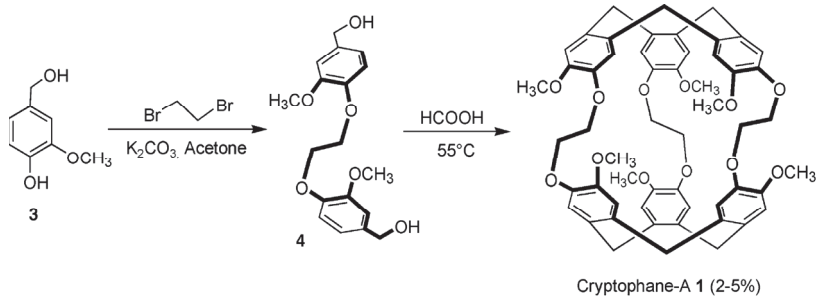

*Scheme 1: the "direct (two-step) method" for the synthesis of CrA. Bis-vanillyl alcohol derivative (**4**) is prepared starting from vanillyl alcohol (**3**), and finally condensed with formic acid (10^{-2} M) to give CrA. From Brotin T. And Dutasta J.P., (2009)*[31]

As shown in scheme 2c, one of the two CTV reacted with two allyl protected benzylic acid derivatives: one has the benzyl moiety tetrahydrohypyranyl (THP)-protected, while the other has a free hydroxyl group. In this way, it is be possible, after the condensation (Scheme 2d) to have one only allyl group subsequently modifiable [31; 55-56] and this will finally lead to the monohydroxyl derivative of CrA (CrA-ma). Such a result was possible through the improvement of protecting groups' strategies and new, efficient CTV caps condensation, both developed by Spence and co-workers and by Dutasta and co-workers. [31; 40; 45; 48; 53-59] CrA-ma presents one only free carboxylic moiety; therefore it can be selectively functionalized once it is converted to an active ester, using activating agents commonly used in peptide synthesis to perform acylation

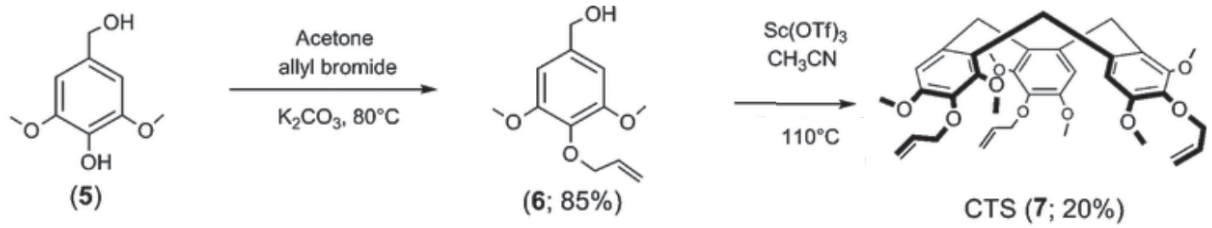

Scheme 2a: formation of one of the two templates. The benzyl alcohol derivative 3,5 dimethoxy-4-hydroxy-benzylalcohol (syringyl alcohol), subsequently allylated and finally condensed with a catalyst, Scandium Trifolate ($Sc(OTf)_3$). In this case, being that the starting material is syringyl alcohol, the template is called CTS (cyclotrisyringyl). The synthesis of CTV occur in a similar fashion, but starting with vanillyl alcohol derivative. In older paper the same condensation reaction has been carried out with acids, as for the "direct method". From Brotin T. et al, 2013 [48]

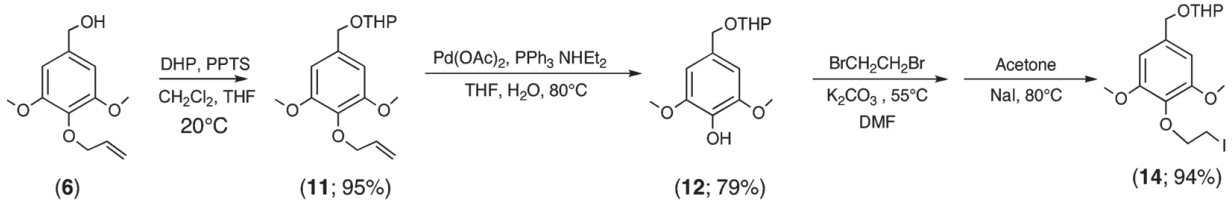

Scheme 2b: synthesis of one of the two building block for the second CTV cap. The benzylic moiety is protected with dihydropyran (DHP), through a reaction cathalized by pyridinium p-toluenesulfonate (PPTS). After reduction of the allylic function to alcohol, the building block is treated with bromoethane and finally with sodium iodide. From Brotin T. et al, 2013 [48]

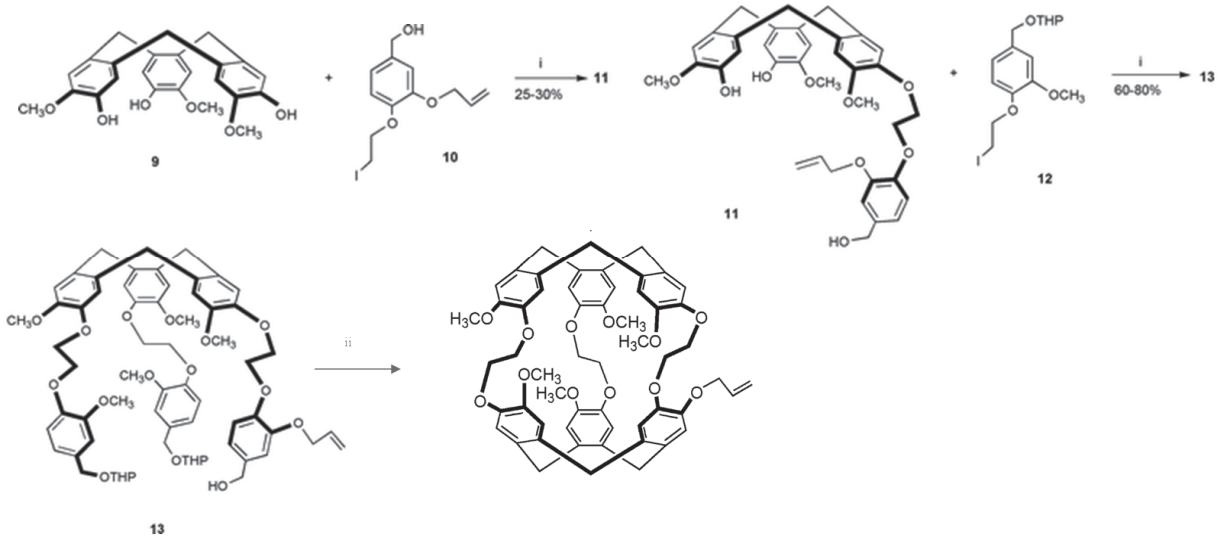

*Scheme 2c: Synthesis of the second CTV caps starting from the building block presented in Scheme 2b. The CTV cap of Scheme 2a reacts with the mono-protected vanillyl acid in presence of $CsCO_3$, in DMF, 80°C, 18 h (i) and compound **11** react with the other vanillyl acid that presents the benzylic function THP-protected, in the same conditions as before.*[52] *In the next step, compound **13** is condensed in presence of formic acid (yield 55-60%).*[31; 53; 55]

Cryptophanes are not the only host-guest systems that interact with Xe. In the literature are reported examples of xeolites, porphyrin cavitands, peptide nanotubes, cyclodextrins, calixarenes, and cucurbit[n]urils. [10; 60-62] The same mechanism of host-guest complexation is also used to detect hp-Xe in gas vesicles [63], in short peptides [64] and in perfluorooctylbromide (PFOB) nanoemulsions.[65-67] Finally, a paper from 2014 showed the detection of bacterial spores through the exchange of hp-Xe with such targets, acting as a molecular cage. [68]

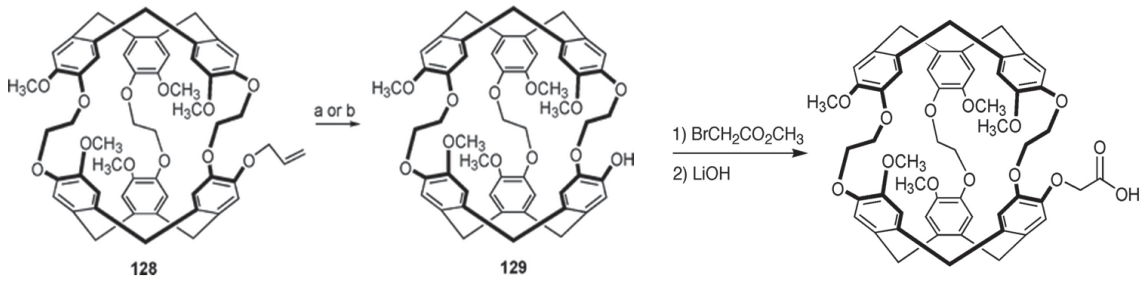

*Scheme 2d: The synthesis of cryptophanol-A **129** by deallylation is carried with reducing agents (a: Bu_3SnH, $Pd[P(C_6H_5)_3]_4$ or b: $Pd(OAc)_2$, $P(C_6H_5)$, $NH_2C_2H_5$, THF, H_2O). The final reaction with methylbromoacetate and in DMF, followed by LiOH in THF:methanoll lead to the desired product cryptophane-A with a yield of 74%* [31; 53; 55]

1.2.3 Cryptophane-based biosensors

The interaction between Xe and biological systems has been used to study specific tissues, cells or interactions such as lipid membranes and suspensions[69; 70], haemoglobin and myoglobin[71], and membrane associated proteins[55]and small peptides.[64] However, the detectable Xe-cryptophanes encapsulation together with the functionalization of the cages with different payloads and ligands, offers the possibility of sensing a specific environment or event, based on the difference in the chemical shift of Xe temporary complexated. [72] The chemical shifts changes upon the molecular targets and the binding event allows multiplexing options.[23; 72]

Targeted Xe-cryptophane biosensors, summarized in Table 3, are designed for detection of receptors, enzymes, metal ions or antibodies. The first proof of principle of a cryptophane-based biosensor [56] was a sensor consisting of a biotin bearing CrA, which, upon interaction with avidin, showed a difference in chemical shift of ≈3 ppm. Such strong contrast is not surprising, being the high association constant between biotin and avidin ($K \approx 10^{14}$-10^{16}). The same concept, though, also works for systems, such as DNA-strand interactions, characterized by much weaker association constant ($K \approx 10^{6}$). [73]

Some of the biosensor systems detect a binding event (being an antibody [74] or a cell-surface detector[75-76]) or a chelating event (in the case of metal ions[77-78]): in such cases, the interaction between the receptor and the Xe in exchange with the cage will give place to a measurable contrast, therefore there would be two signals detectable: Xe@cage free and Xe@cage bound. A binding event can also reveal enzymes: for instance, Human Carbonic Anhydrase II is detected upon coordination of the benzenesulphoamide ligand with the Zn^{2+} of the catalytic site of the enzyme.[79-80] The big chemical shift change (3-7 ppm) is helped by the length of the linker which, by allowing a rapid re-orientation of the cage after the binding, guarantees enough NMR lines' narrowness. [23] Despite a high probe-receptor affinity and a clever design of the linker, a detection based of a binding event may suffer for the limited available quantity of the target present in the cell. Furthermore, the above mentioned examples do not provide information about the enzyme activity: such measurement can be achieved upon detection of cleavage, which also offers the possibility of amplifying the signal.

In a protease study the cage is linked to a peptidic sequence recognized by the targeted enzyme, and, upon cleavage, two different NMR signals are detected, one belonging to the Xe@cage in the uncleaved sensor, and one belonging to the Xe@cage in the fraction produced by enzyme digestion. [81]

In this case, being the small difference between the two probes (cleaved/uncleaved), and the lower affinity involved in the process ($K_M \approx 4 \times 10^{-5}$) the chemical shift change it is also small (< 1 ppm), but the detection is highly informative and specific.

The type of functionalization and of the additional payloads changes not only the quality of the NMR signal, but also the behaviour of the probe in the biological environment. [72; 82] The presence of cell penetration peptides (CPPs) such as as TAT or Poly-r, or the presence of proteins (as transferrine) or peptide sequences (as RGD) recognized by cell-internalization receptors[83-85] lead the probe to be uptaken by the cells, and this may also be a source of an additional modulation of the NMR signal.[23; 72]

In such examples, the presence of the sensor in the cell was verified through with fluorescence detection.[83-85] Although most efforts so far were aimed at designing a biosensor for a biological target, some important works published focused on the behaviour of the non targeted cryptophanes probe in the cell (or in a cell-like, as liposomes) environment.

For instance, a fluorescent dye functionalized cryptophane has been tested on liposomes to determine the membrane incorporation of such probe and the relative signal, which was found to be different according to the hydrophilicity of the dye [86] and to the lipid fractions. [69-70; 87] Such studies open new insights into understanding the influence of the membranes composition in the interaction with Xe@cage and its relative NMR signal. In the same way, the influence of solubility has been studied by comparing the NMR spectra of the apolar cage and the one of cage decorate with different types of dendrimers.[34; 88] Furthermore, attempts to have systems carrying several cages, in order to magnify the signal, have been done both by using viral scaffold [89] and by using liposomes.[90]

These studies help us to understand how to reach desired properties in a sensor, that not only need to have high affinity and specificity for a certain target, but also need to be sensitive, and allow fast and high resolution imaging. Some of those characteristics can be gained through the clever design of a biosensor.

Tab. 3 Examples of Xe-Cryptophanes targeted biosensors.

Ref.	Ligand to CrA	Target	Additional payload	Detection
Spence et al, (2003) [56] Lowery et al, (2006) [82]	biotin	avidin (on proteins)	-$(Arg)_3$ to increase solubility -Aliphatic linker between ligand and reporter to increase flexibility	Xe-NMR spectroscopy
Mynar et al, (2006)[88]	biotin	avidine	PAMAM dedrimer	Xe-NMR spectroscopy
Wei et al, (2006)[81]	RPLA*LWRS	MMP-7	Presence of tryptophan to quantify cleavage through fluorescence spectroscopy	Xe-NMR spectroscopy Fluorescence spectroscopy
Roy et al (2007)[73]	20-mer oligonucleotide	DNA complementary strand		Xe-NMR spectroscopy
Seward et al, (2008)[83] (*)	$(RGD)_4$ or TAT or Poly(r)	$\alpha_v\beta_3$ Integrin receptor	-Cy3	Fluorescence imagin
Aaron et al, (2008) [79] Chambers et al, (2008)[80]	Benzenesulphonamide (coordination with Zn^{2+})	Human Carbonic Anhydrase II		Xe NMR spectroscopy ITC
Schlund et al, (2009) [74]	Hematoglutin peptide	Human leukocyte antigen (HLA) DR1		Xe NMR spectroscopy T-cell assay
Boutin et al, (2011) [84]	Transferrin	Transferrin receptor	-Rhodamine green	Xe NMR spectroscopy Fluorescence imaging
Seward et al,(2011)[85]	$c[(RGDyK]_4$	$\alpha_v\beta_3$ Integrin receptor	-Alexa Fluor 488 -Azidopropionic acid	Xe NMR spectroscopy Fluorescence imaging
Stevens et al,(2012)[75] Palaniappan et al,(2013)[76]	k-fd phage	EGFR receptor		Xe NMR spectroscopy Flow cytometry(a) Confocal microscopy(a)
Zhang et al. (2014) [78]	2-(diphenylphosphino) benzenamine	Zn^{2+}		Xe NMR spectroscopy
Tassali et al, (2014) [77] (**)	carboxy-pentyliminodiacetic acid(NTA)	Zn^{2+}, Cd^{2+}, Pb^{3+}		Xe NMR spectroscopy
Witte C et al (2015) [91]	Byciclononane functionalized peptide	Cell surface glycans (sialic acid)	-FAM	Xe-MRI Flow cytometry Confocal microscopy

(*) In this paper, a tri-propargyl Cryptophane was used.

(**) Cryptophane-E

(a) The fluorescence stain is a anti-fd bacteriophage antibo

1.3 Detection with the Chemical Exchange Saturation Transfer (CEST) method

In the precedent paragraphs we have described how the encapsulation of Xe into a molecular host can give a signal in the NMR spectrum specific for such interaction, separated by a hundred ppm of difference from the Xe in solution. It needs to be pointed out, though, that the signal from Xe in equilibrium with the cage is very small if compared to the one in solution, therefore, a direct detection method would always be restricted to relatively high concentrations of sensors.

This would be a big limitation considering that *in-cellulo* or *in-vivo* molecular targets, even when overexpressed, are most of the time in nanomolar or more often in picomolar concentration [92]: for this reason is important to enhance the MRI signal. In proton MRI, signal enhancement is usually obtained through contrast agents, like paramagnetic complexes (e.g. Gd III chelates) or superparamagnetic particles (ion-oxide nanoparticles), that significantly affect the spin-lattice relaxation time (T_1) and spin-spin relaxation time (T_2) and generate a more marked contrast in the image.[93-95]

Among the techniques to enhance the contrast, there are also detection methods such as Chemical Exchange Saturation Transfer (CEST).

CEST in MRI arises from phenomena described in NMR usually as Saturation Transfer (ST) or Magnetization Transfer (MT). The minimum requirement for MT to happen is to have some sort of chemical exchange in the system (for instance, exchangeable protons, like in a system water/amine). [96]

The CEST mechanism is showed in Fig. 6.

In the example two pools of exchangeable protons, *A* and *B*, are present. When an irradiation pulse corresponding to the resonance frequency of pool *B* is applied, the spin distribution will be altered to the point that the net magnetization will be zero, and no signal will be detected in NMR. At this point, there will be an exchange between the saturated nuclei of pool *B* with the non-saturated on pool *A* until when the system

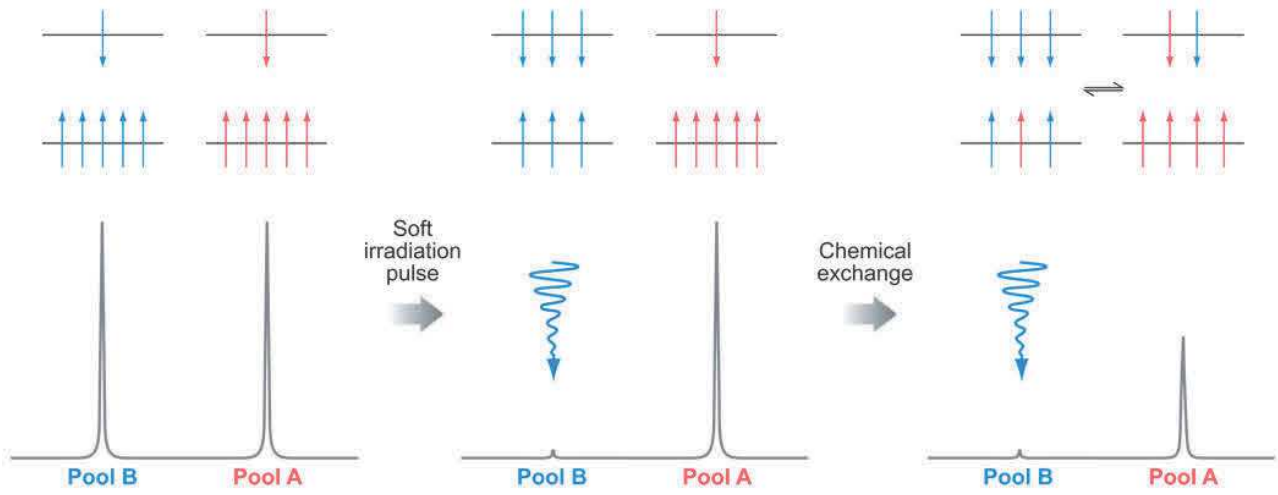

Fig. 6 Mechanism of the saturation transfer from pool A to pool B upon irradiation at a specific saturation frequency. From Scherry AD and Woods M (2008) [96]

would reach an equilibrium. [97]

The CEST effect is graphically represented by the so-called z-spectrum (Fig. 7c), in which the relative intensity of the protons from bigger pool A is plotted in function of the saturation frequency offset (in ppm).

In the example, it is possible to distinguish a peak at 0 ppm corresponding to the direct saturation of spins

from pool A, and, some ppm apart, another dip corresponding to the pool B, the CEST agent.

Through the z-spectrum is possible to evaluate the frequency offset of the mobile CEST protons and the efficiency of the saturation (in %). [93; 98]

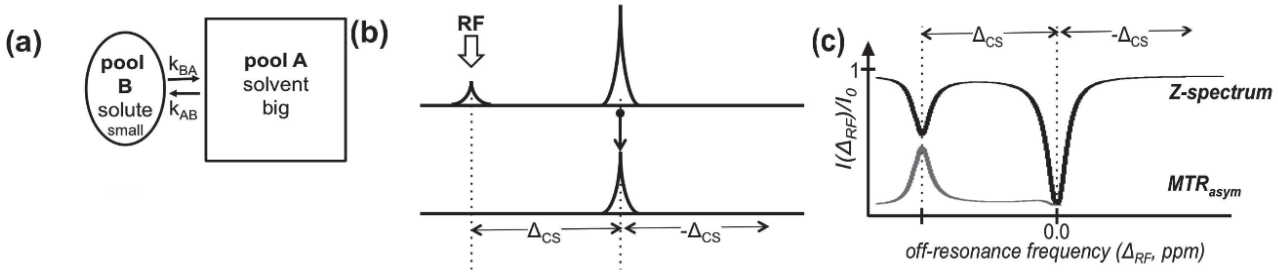

Fig. 7 Graphical representation of the CEST effect a) exchange between pool A and pool B b) Application of the saturation frequency corresponding to the saturation of pool B, separated Δ_{CS} ppm from pool A. c) z-spectrum of the CEST effect. From Vinograd et al, (2012) [98]

When CEST is used in MRI, the saturation scheme previously exemplified is applied before the standard acquisition pulse sequence or some especially developed fast MRI pulse sequences. [99-100] The CEST contrast in imaging (CEST-MRI) reports the effects of the exchanging of the CEST agents and its localization. The localization is obtained by the subtraction of an image acquired after presaturation, at the same frequency but opposite site of the "bulk" dip (no CEST effect), to an image acquired after presaturation (Fig.8).

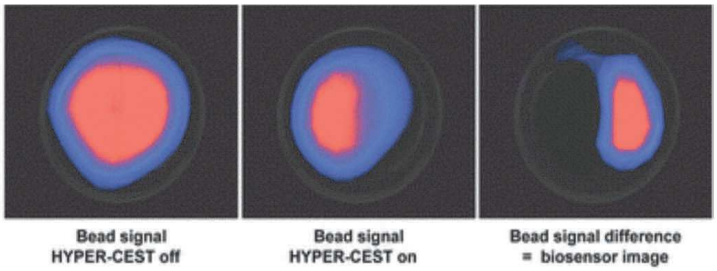

Fig. 8 Example of a Hyper-CEST experiment using a phantom set-up. In this example, the CEST agent is localized in the left (light blue) compartment. The first image arise for the hp-Xe alone, the central one from the caged Xe pre-saturated while the last one is the subtraction of the two that reveal the localization of the CEST agent in the right compartment. From Schröder L. Et al, (2006)[101]

CEST is a sensitive detection method that has the advantage of allowing the detection of a spin pool present in a small quantity (for instance, a solute in exchange in a solution). Therefore, CEST-MRI has been successfully employed as pH, temperature, metabolites, metal ions and gene reporters, cells, liposomes and nanoparticle labeling, protein, DNA and RNA binding detection.

Different groups of CEST agents have been developed to be used as contrast agents in MRI, as paramagnetic (paraCEST) or diamagnetics (diaCEST) species [93; 102-103] , or, named after the proton, glycogen (glycoCEST) [71; 104] or liposomes (lipoCEST) [93] .

Although the sensitivity of the measurement can be greatly improved by CEST detection, still conventional proton-CEST often requires high magnetic fields, both for chemical shift separation and to avoid unwanted fast longitudinal relaxation.

Furthermore, techniques as diaCEST need high concentration of the contrast agent (0.25-250 mM), while

techniques such as lipoCEST, since can rely on a higher number of exchangeable sites, can detect at less than 100 pM. The main concern of all CEST techniques is the so-called “spill over effect”, which is the unwanted saturation of the main spin pool (in general, water) that can occur when the CEST agent is saturated, because of the small chemical shift range of the protons. [23]

This problem is minimized when hp-Xe is used to perform CEST experiments (hyper-CEST). (Fig. 9)

Hp-Xe it is an ideal candidate for CEST experiments because it satisfies the condition *sine-qua-non* for the CEST to be effective: a greater difference in chemical shift ($\Delta\omega$ or Δ_{CS}) between the two polls needs than the exchange rate (k_{ex}). [99]

In the case of hyperCEST, caged Xe will be our “pool B”, while hp-Xe in solution will be our “pool A”.

CrA is an ideal CEST agent, being that in water Xe in exchange with CrA (Xe@CrA) a $k_{ex} \approx 40$ ms; the $\Delta\omega$ is greater than 100 ppm, and this makes Xe an excellent candidate for CEST experiments. [37;105]

Hyper-CEST detection made possible to detect changes in the sensor of 50%, and in nanomolar concentrations. It has been estimated that combining the signal enhancement of SEOP Xe (10^4) with the enhancement deriving from CEST, the total improvement of the detection using Hyper-CEST would be 10^7.

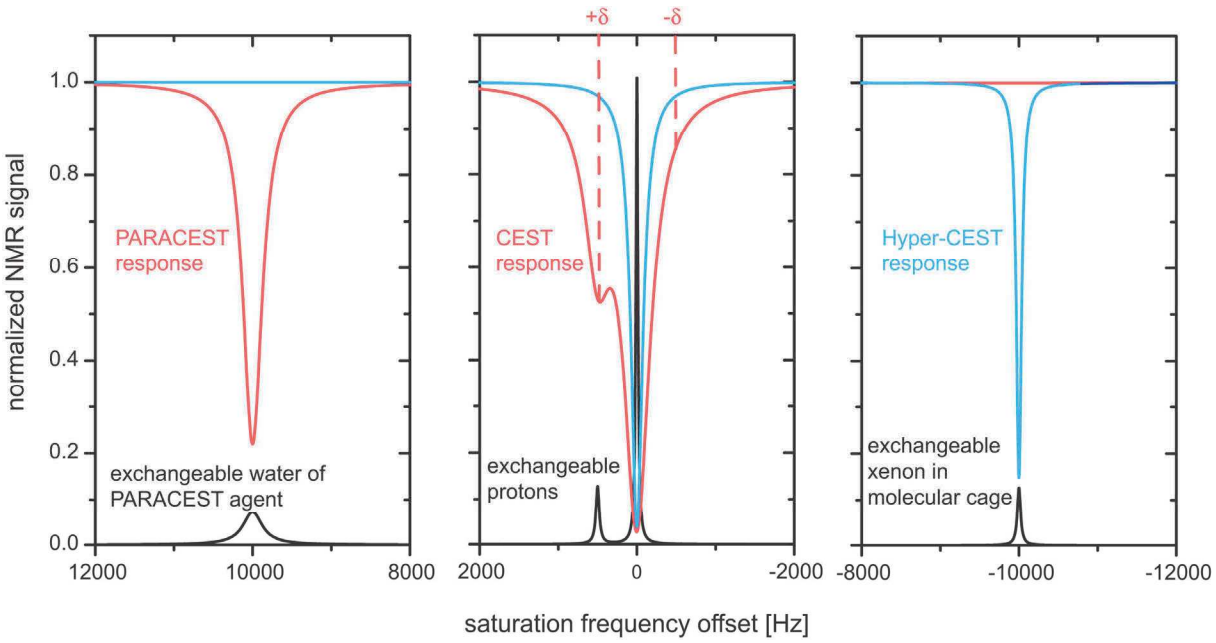

Fig. 9 Improvement of the CEST effect in the case of Hyper-CEST (blue line, third spectrum) compared with conventional CEST. In such experiments (second spectrum) the saturation of the CEST agent +δ is affected both from the direct saturation at 0 Hz, and of the saturation -δ. The problem is overcome by paraCEST (first spectra) by inducing a large chemical shift, but the dips can be broad compared with water. The HyperCEST signal (third spectrum) are characterized by a saturation signal far apart from the solution peak, and by a slow chemical exchange of Xe@cage. HyperCEST detect therefore also small spin pools and give narrower saturation response. From Schröder L. (2013) [23]

Chapter 2

Design and Xe-MRI response of dual-mode cryptophane-based xenon hosts.

2.1 Aim and outline of the work

The functionalized xenon hosts introduced in this project were designed as building blocks for further synthesis of xenon biosensors. When a biosensor for molecular imaging is designed, there are several factors that need to be considered, including specificity, sensitivity, affinity for the target and the ability generate reproducible signals in a fast manner and at high resolution. These criteria are necessary but not sufficient for a probe to generate a detectable and standardizable signal.
In fact, there are some intrinsic reasons why a biosensor might hardly reach its target or generates high quality images. Hence, additional aspects like scarce solubility, low affinity and self-deactivation (as autoquenching in the case of fluorescence) can come into play. The degree of complexity of course increases when a probe is used in vivo. In this case problems such as poor mobility, especially in the presence of biological barriers, or inactivation by metabolic pathways other than the one targeted should be taken into account. [1;99]Those aspects, together with novelty of the Xe-MRI technique, motivated our group to develop dual-mode sensors to be independently detected with Xe-MRI (through CrA) and with optical imaging (through fluorescence) for further validation and elucidation of the fate of these hosts. [106-108]This type of dual probes were then used for multiple purposes:

- localizing and tracking the behaviour of the probe (and the cage) in cellular environments
- studying probe's biocompatibility
- evaluating the occurrence of possible interferences, generated by the dye, in the hyperCEST experiments.

With our experiments we also aim to identify the minimum required cell labelling concentration to detect biosensors with Xe-NMR and in which concentration the contrast agents accumulate into the cells. This information can be deduced from the known ratio of cage and dye in the sensor. For our first studies, CrA-ma (**1**) was linked to a fluorescein (FAM) through a PEG linker as a spacer, to obtain CrA-PEG_3-FAM (**2**) (Fig.1). This simple sensor was then used to track cell uptake and to measure cell toxicity. It was eventually also used to perform the very first live cell MRI experiments with functionalized Xe.
In the subsequent study, we tested two different cell lines and we extended our available dual-mode probes by using an alternative fluorophore, (tetramethylrhodamine, TAMRA). This was motivated by the observation that physicochemical properties of the reporter influence the cell uptake and Xe-NMR response. This second probe, CrA-PEG_3-TAMRA (**3**) (Fig.1) presented a better cell internalization, but also increased toxicity. This work also featured a comprehensive optimization of the probe's synthesis to reduce reaction times and obtain the probe at higher purityThe improved synthesis gave enough flexibility in the design of dye labelled dual probes based on incorporation of a free carboxylic moiety that allows conjugation with free amines (e.g. ε-terminus of lysine). They can therefore serve as building blocks for generating targeted probes.
The last part of this work was dedicated to the synthesis and imaging of a targeted sensor for detecting cell

surface receptors (CD14) via an anti-CD14 antibody. In this study, we compared fluorescence and Xe-MRI response of high-expressing and low-expressing CD14 cell lines varying the read out modalities and type of incubation. For this study, the concept of the double read out was further improved by using a modular design of the probe for quantifying the response in fluorescence flow cytometry, Xe-MRI and in optical imaging.

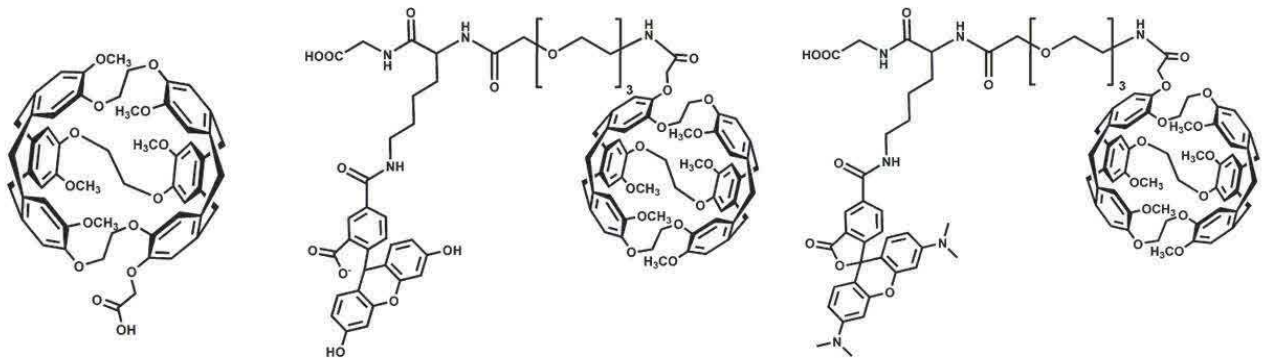

1 **2** **4**

*Fig.1 Chemical structures of CrA-ma (**1**), and of the two fluorescent probes synthesized from it, CrA-PEG$_3$-FAM (**2**) and CrA-PEG$_3$-TAMRA (**4**).*

2.2 Preliminary study of cellular uptake and relative Xe-NMR signals of 1 and 2.

2.2.1 Xe NMR with CrA-ma in cells – the reference case

In this preliminary work the distinctive signature for the Xe-NMR read out module (Cr-A) in cells was investigated (work led by Stefan Klippel) [106]

Mouse fibroblasts (L929) were incubated with CrA-ma (**1**, 90 µM) for three hours. After incubation, cells were washed and resuspended in culture medium, placed in an NMR tube equipped with capillaries (§9.3) and bubbled with hp-Xe in presence of additional 100 µM of **1** to act as extracellular chemical shift reference.

In this way, it is reasonable to assume that in the sample there will be different types of signal arising from hp-Xe (Fig.2a):

1. Xe in gas phase,
2. Xe in solution,
3. Xe in reversibly bound in **1**,
4. Xe reversibly bound to cells, and
5. Xe reversibly bound in the cage being itself associated with cells.

The 64 scans accumulated for the NMR spectrum in Fig. 2b represent the direct detection method and reveal the presence of a peak at 196 ppm related to Xe in cells, another one for Xenon in solution (192 ppm), the extracellular cage reference peak of **1** (59 ppm) and the signal of Xe in gas phase, here set as a reference to zero. Contrary, no signal of Xe associated with **1** in cells was detected.

When the same sample was measured through indirect detection (HyperCEST), two saturation transfer responses were observed in the form of dips (Fig.2c, top), namely one at 200 ppm and another one at ca. 70 ppm. After optimization of the saturation pulse power, each signal was revealed to be the superimposition of two other signals (Fig.c, bottom). The first signal (200 ppm) is the result of the superposition of two signals attributed to Xe in cells and Xe in solution, respectively. The other one at 70 ppm is the result of the superposition of the signal attributed to Xe in **1** (Xe@CrA-ma) and to Xe in **1** bound to the cells (Xe@CrA-ma@cells) based on the comparison with the reference signal of Xe in **1** (59 ppm).

The peak for Xe@CrA-ma@cells appears ca. 10 ppm shifted downfield from Xe@CrA-ma. We speculated that the signal appears smaller because of a lower concentration of the Xe in the sensor associated with cells than the one of the free sensor, as the lack of the signal in the direct spectrum would suggest.

However, the CEST signal appears to be equal for one reason which is linked to better CEST conditions in the cell, namely a more favourable exchange rate when the cage is associated with the cells (most likely hydrophobic membrane cores).

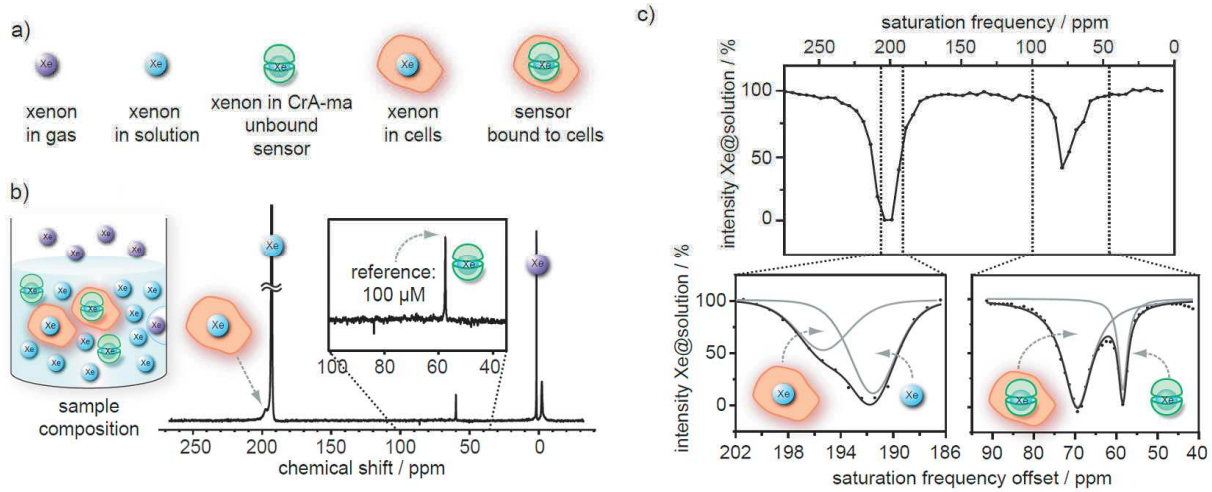

Fig.2 Direct Xe-NMR spectra of CrA-ma labelled cells. (a) schematic of the different Xe pools. (b) samples' composition and related direct Xe NMR scan. (c) Upper part: HyperCEST experiment performed on the same sample of 2b. The bottom part is the separation of the peaks by changing the saturation power. It is possible to discriminate between the different Xe pools in solution and in cells (left) and Xe in CrA-ma and in CrA-ma associated with cells (right). From Klippan S. et al, (2013) [106]

Interestingly, the indirect detection method was not only able to detect the sensor at very low concentration, but was also able to resolve the signal from the sensor *in cellulo*.

In this context it becomes crucial to have the possibility of detecting cellular uptake with an alternative method. Fluorescence imaging is the method of choice to visualize the localization of **1** in cells (e.g. in cytosol, lysosomes or other cell compartments), since our results revealed a high sensitivity of Hyper-CEST detection for the cellular environment. It is noteworthy to mention that previous to this study, the only example of cellular uptake of a CrA-based biosensor was performed by incorporating CPPs in the sequence [83], or by targeting a cell-internalization receptor, as in the case of integrin [85] or transferrin receptor [84]. Hence, this work is the first one investigating cellular uptake which is mainly driven by the hydrophobicity of the cage.

2.2.2 Synthesis of CrA-PEG$_3$-FAM (2)

The sensor CrA-PEG$_3$-FAM (**2**, Fig.1) was synthesized to perform cell labelling. In particular, it enables dual-mode cell labelling as it presents carboxy fluorescein (FAM) as fluorophore and CrA for Xe-NMR detection. The probe was designed to have the following characteristics:

- contain a functional group which can be selectively derivatized;
- have sufficient water solubility to be biologically compatible;
- preserve both the photophysical properties of the dyes and the xenon NMR/MRI characteristics of the Cr-A moiety

The derivatizability is possible though the presence of a free carboxyl-terminus (see Fig.1), which can be easily activated with coupling agents and being coupled with amino groups for further functionalization. Such a compound can then be used as a building block to add targeting peptides or proteins for further xenon-MRI biosensor development.

The free carboxylic terminus was obtained through Fmoc-SPPS by using the acid-sensitive resin linker 2-Cl-Trytil. The use of such a linker and the relative mild cleavage modality is a practical and easy approach to produce peptide fragments and to generate a library of peptides.[109] The initial Gly as spacer was introduced to stabilize the ester linkage, other than to avoid epimerization. [110] In order to assure water solubility and biocompatibility, **2** features also three PEG groups as spacer. [111-112] PEGylation is commonly used in sensor design because PEG groups are soluble in both organic and aqueous media and are stable under many conditions used during chemical reactions, including treatment with acids and at high temperature.[43; 111-112] PEG spacers also offer enough distance in between the two read out modalities to successfully perform Xe-NMR experiments and to avoid line broadening.[72]

Fluorescein, one of the most widely utilized fluorophores in biochemical research, has been chosen because of its convenient properties: high molecular absorptivity (extinction coefficient $\varepsilon = 9.3\times10^4$ $M^{-1}cm^{-1}$) brightness (quantum yield $\Phi=0.95$), good water solubility. FAM is particularly suitable for fluorescent labelling of peptides, as it is stable under synthesis conditions required for solid phase peptide synthesis (SPPS), such as treatment with trifluoroacetic acid (TFA). [110,113-115] Furthermore, fluorescein maximum excitation (494 nm), falls conveniently close to the bandwidth of Argon laser (488 nm), therefore FAM is successfully used for flow cytometry and confocal microscopy. [115] One of the possible disadvantages of fluorescein, other than a certain degree of photo-bleaching, is its pH-sensitivity (**671**). However, the pKa tunability has been exploited, upon modification on the aromatics rings of the xantene core or on the appended groups to create pH sensors. [114] The labelling of a peptide with the amine-reactive fluorescein derivative such as fluorescein isothiocyanate (FITC) on a solid support is reported to be challenging because of the cyclisation of the N-FAM labelled peptide to thiohydantoine in the case of and its subsequent removal, occurring during the cleavage from the resin in acid environment. [116] For this reason, the more convenient and stable FAM has been used.

In particular, the use of the fluorescent building block Fmoc-Lys(5,6,FAM)-OH in the peptide sequence is beneficial since it offers enough flexibility in the design and avoids additional coupling steps [117] or removal procedure necessary when FAM is coupled to in situ activated side chain of the peptidic backbone. [118]

Probe ***2*** was synthesised in two steps; the initial FAM PEGylated building block (PEG-FAM) was synthesized via standard Fmoc-SPPS, while the coupling with CrA-ma was carried in solution in order to avoid the high excess of the acylating group normally required for SPPS.

The synthesis of **2** (Scheme 1) is described in details in Material and Methods (§7.2).

Briefly, 2-Cl-Trytil resin, functionalized with Gly, was coupled overnight with Fmoc-Lys(FAM)-OH, after activation with 1-Cyano-2-ethoxy-2-oxoethylidenaminooxy)dimethylamino-morpholino-carbenium hexafluorophosphate (COMU), in presence of N,N-Diisopropylethylamine (DIPEA).

The Fmoc group was removed from the resin using 25% piperidine in DMF, and then the peptide was PEGylated though coupling with Fmoc-NH-PEG_3-COOH, using the already mentioned procedure. After the last Fmoc-deprotection, cleavage from the resin, and RP-HPLC purification, the peptide was coupled in solution with **1** in presence of COMU/DIPEA. [74, 106] The reaction mixture was separated with HPLC-UV and the fractions were analysed through a MALDI-TOF spectrometer (Fig.3a and b). The calculated mass was m/z = 1670 for $C_{92}H_{94}N_4O_{26}$, but the predominantly found mass on MALDI-TOF analysis was m/z = 1674, corresponding to m+1 of the quinoid form, 1673 (Fig. 3a).

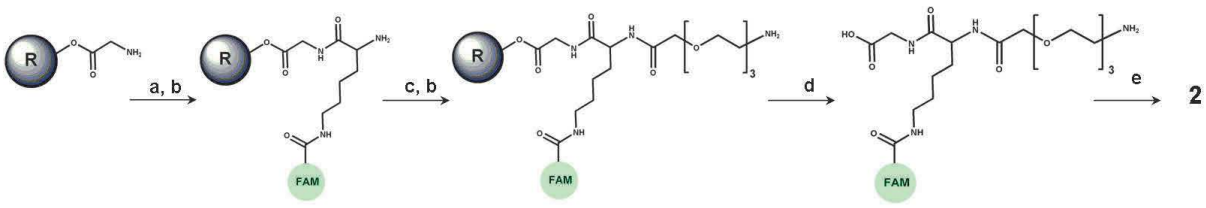

Figure 1Scheme1. Synthesis of 2. Reagents and conditions: (a) Fmoc-Lys(5,6 FAM)-OH (2 eq.), COMU (2 eq.), DIPEA (4 eq.), RT, overnight. (b) 25% piperidine in DMF, RT 15 min, twice. (c) Fmoc-AEAAA (2 eq.), COMU (2 eq.), DIPEA (4 eq), RT, overnight (d) TFA/TIS/H_2O (95/2.5/2.5) RT, 2 hours, followed by azeotropic evaporation and precipitation in cold ether. (e) CrA-ma (1 eq), COMU (1 eq), DIPEA (2 eq) in DMF, 45°C for 2 hours, followed by RP-HPLC purification. Overall yield: 50%. From Rossella F. et al, (2014)[107]

.

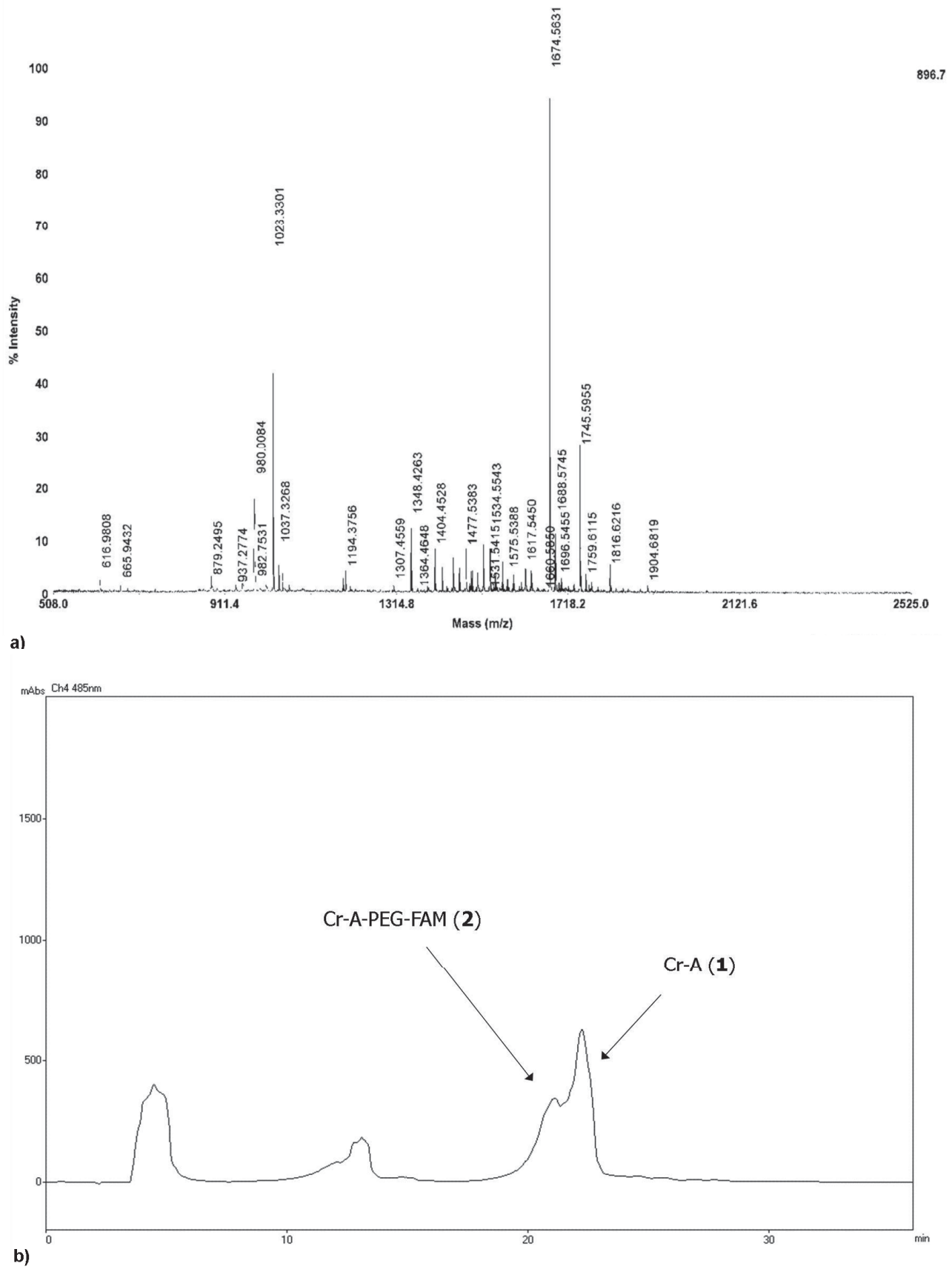

*Fig.3 (a) MALDI-TOF trace of **2**. The detected mass was 1674, corresponding to the m+1 of the quinoid form. (b) HPLC-UV trace, at 485 nm of 2, highlighting presence of unreacted **1** (second peak) and **2**, at an earlier retention time. From Rossella F. et al,*

2.2.3 Fluorescence and Xe-NMR response of a dual (FAM/Cr-A) sensor in cells

For measuring the cell uptake, L292 cells were incubated with 75 µM of **2** for a time ranging from 10 minutes to 20 hours, at 37°C. (§8.3) Confocal microscopy data showed a time dependent uptake (Fig.4) and a detectable presence of the fluorescent sensor in the cytosol.

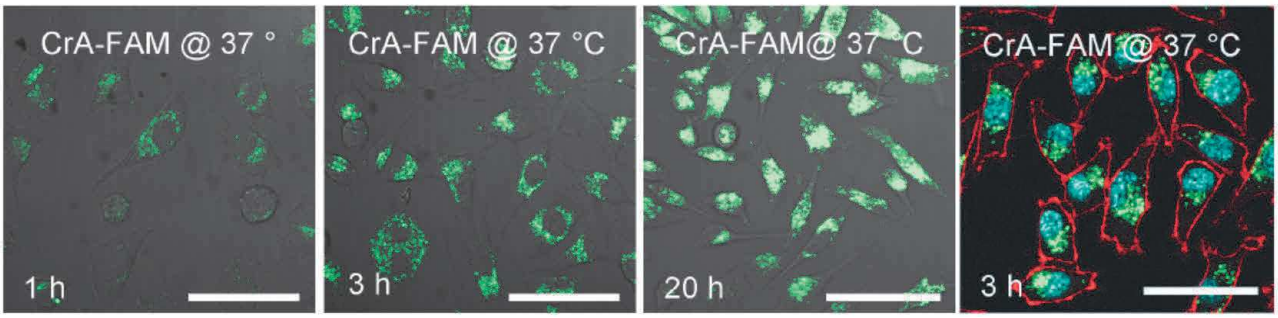

*Fig.4 Time-dependent uptake of **2** in fibroblasts (first three panels). In the forth panel, cells incubated with **2** for 3 hours have been stained with a nuclear stain (Hoechst 3342, in blue) and with a membrane stain (Trypan blue, in red) to localize the compound and measure cell toxicity. from Klippel S. et al, (2013)* [106]

In the above mentioned previous studies [83-85] it was speculated that the presence of payloads like CPP or targeting units was the main determinant of the cellular uptake. In a previous paper [86], the uptake of two constructs based on a lipophilic or a hydrophilic dye conjugated with CrA was studied using liposome as model of cell membrane. The relative fluorescent data showed that the compound was present in the phospholipidic membrane, but was not able to cross it.

In our experiment, conversely, **2** crosses the membrane. This is compatible with an active mechanism of uptake such as pinocytosis [106; 119-120] Localization of the compound and cell toxicity were studied using Trypan blue to stain the membrane (Fig.4, fourth panel, in red) and Hoechst 3342 as nucleus stain (Fig.4, fourth panel, in blue): it is then possible to highlight the presence of this Xe host (in green) in vesicles. Cell toxicity (§8.5, Fig. 5c) turned out to be lower for **2** than for **1**, probably due to a higher hydrophobicity-driven uptake associated with the latter one. Although it is not possible to measure the cellular concentration of **1** by fluorescence, the comparison of the *in cellulo* Hyper-CEST response (Fig 5a) of the two compounds would

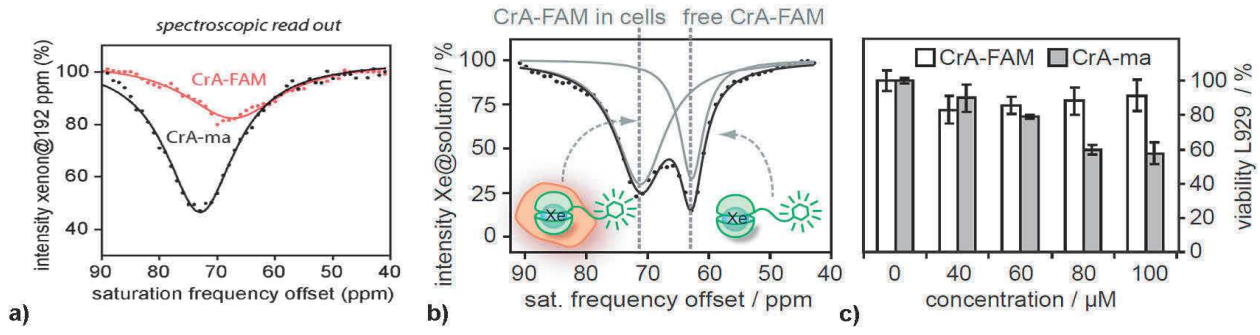

*Fig.5 (a) Comparison of Hyper-CEST response in cells of **1** and **2**. (b) The Hyper-CEST response of **2** shows two dips, one assigned to the compound associated with cells (left) and one assigned to the free compound (right). (c) cell toxicity associated with **1** and **2** after incubation with different concentrations for 6 hours at 37 °C. From Klippel S. et al, (2013)* [106]

suggest a bigger intracellular concentration of **1** than of **2**.
As shown in Fig.5b, the Hyper-CEST response of **2** in cells, analogously to **1**, reveals two dips, one at 71 ppm attributed to Xe@CrA-PEG$_3$-FAM@cells and one at 63 ppm attributed to Xe@CrA-PEG$_3$-FAM. (§2.2.3)
The 10 ppm difference in chemical shift between the two dips of **2** is comparable with the one measured for 1 in cell suspensions, although the intensity of the signal of **2** is ca. 2.5 times lower.
Our findings together show that **1** has higher cell affinity and an increased Hyper-CEST response. We hypothesize the bigger lipophilicity of **1** to be the main reason for these observations.

2.3 Comparison of dual-mode probes, optimization of their synthesis and systematic studies of the Xe-NMR response on cells.

2.3.1 Mw-assisted coupling optimization: synthesis of Fmoc-Lys (CrA)-OH as a model.

The synthesis of **2**, carried on a non-automatized system, turned out to be more time-consuming than expected and gave products for which purification was challenging.
Microwave-assisted organic and peptide synthesis has been shown be to extremely beneficial in decreasing reaction time, reducing side reactions and in increasing the purity of the product. [122-123] In particular, many studies show how this technique is suitable also for peptide chemistry, both for the production of building blocks [117], or for entire peptidic sequences [124], being particularly recommended for challenging peptide sequences. [125] As such, this technique could be used to reduce reaction times, racemization, and aspartamide formation [126] and also simplifies separations. The mw irradiation is compatible, with few exceptions, with most of the reaction's condition required in SPPS, and with most of coupling agents [121, 125; 127] and solvents. [123] Furthermore, the recent development of new resins supports such as ChemMatrix® [128-129] allow to synthesis very long sequence of peptides at high purity and in short time, which turns also into a reduction of the use of solvents. [124] One other advantage of mw-assisted organic synthesis is that it improves significantly reactions' reproducibility therefore it is particularly suitable for optimization. [122, 124]
Therefore, we decided to optimize CrA coupling to amino terminus, using as a reaction model the synthesis of Fmoc-Lys-OH bearing Cr-A at its ε-amino terminus (Fmoc-Lys(Cr-A)-OH, **3**) (Scheme 2, §7.3). The obtained **3** could then be used as a Fmoc-protected ε-substituted amino-acid for extended peptide sequences or for protein modification (as it has been shown for fullerene). [130] The results of the optimization are summarized in Table 1.
The mw coupling optimization was based on the previously tested conditions for performing the synthesis without the mw-assisted synthesizer: The stoichiometry of Cr-A: Fmoc-Lys(OH) was 1:1, while the stoichiometry of coupling agent COMU and DIPEA was 1: 2.5. Time and temperature of reaction was 2 hrs, 45°C, therefore, the equivalent used in mw-assisted synthesis is 75°C, 10 min.
In our optimization, we first varied the coupling agent (Tab.1a).
After identifying the most effective of the four tested conditions, we varied the stoichiometric ratio of **1** and the amine, here represented by Fmoc-Lys-OH (Tab.1b). Finally we tested four different temperatures and reaction times (Tab.1c) based on the Arrhenius table.[123-124]

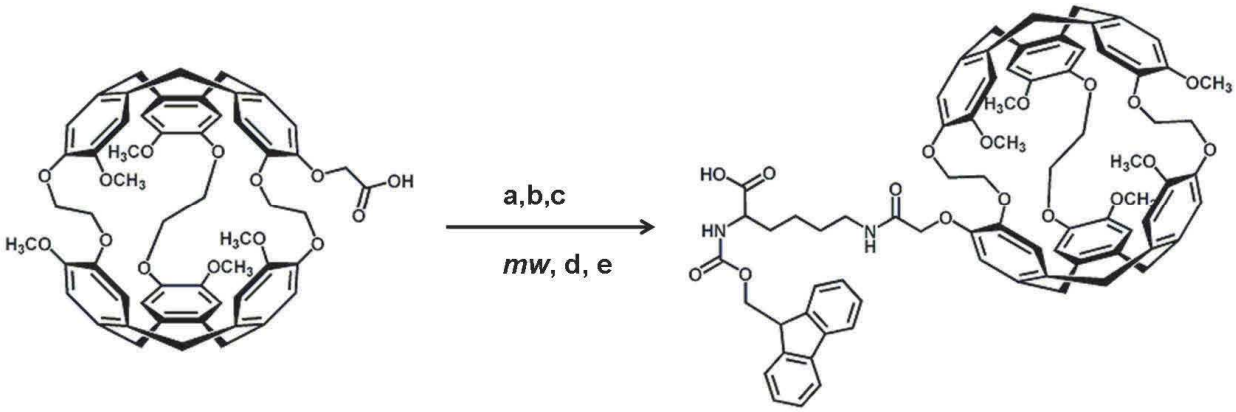

*Scheme 2. Model reaction for the coupling of CrA-ma (**1**) to an amino group. (a) Fmoc-Lys OH, variable equivalents. (b) Coupling agent (HATU, COMU, PyOxim, PyBOP) variable equivalents (c) DIPEA, 2.5 eq. (d) Variable temperature (75, 50, 100 °C) (e) Variable times (5-10-20-30 min).*

Each single reaction has been carried out the same way: after 2 minutes of preactivation with the desired coupling agent, **1** (0.1 M) was placed in a special 1 mL mw vial containing the Fmoc-Lys-OH. The same concentration was used for synthesizing **2** in solution. [106]

The reaction was carried out under mw irradiation for the predetermined time and temperature (see Table 1c for the used conditions). Finally, the 700 µL reaction solution was quenched with 4 mL of mobile phase (30% CH_3CN in water, 0.1% TFA) and purified with RP-HPLC (Fig.6a). Each collected fraction separated through specific Fmoc-UV absorption (290, 301, 267 nm) has been analysed with MALDI-TOF (Fig. 6b).

The calculated mass for **3** was m/z 1288.5, and the predominantly found mass was m/z 1311,6 corresponding to m+23 (mass added Na^+).

Tab.1 Yield percentage of Fmoc-Lys(Cr-A)OH obtained though microwave-assisted solution coupling in different conditions.

a) **Coupling agents** (*)

	COMU	HATU	PyBOP	PyOxim
Fmoc-Lys(Cr-A)OH (%)	34.6	41.0	16.5	46.6

(*) all reactions were carried out for 10 min at 75 °C, using 1 eq. of Fmoc-Lys(OH) (*amine*), 1 eq. of Cr-A (*acid*), 1 eq. of coupling agent and 2.5 eq. of DIPEA as base.

b) **Stoichiometry** amine:carboxylic acid:coupling agent (**)

	1:1:1	1:2:2	2:1:1
Fmoc-Lys(Cr-A)OH (%)	44.8	25.2	35.3

(**) all reactions were carried out for 10 min at 75 C°, using different equivalents of amine, but the same equivalent of coupling agent and carboxylic acid, and 2.5 eq. of DIPEA relative to each equivalent of coupling agent.

c) **Microwave irradiation temp./time of reaction.**(***)

	75°/10'	75°/30'	50°/20'	100°/5'
Fmoc-Lys(Cr-A)OH (%)	45.8	14.5	29.1	-

(***) all reactions were carried out with 1 eq. of Fmoc-Lys(OH) (*amine*), 1 eq. of Cr-A (*acid*), 1 eq. of coupling agent and 2.5 eq. of DIPEA as base. Temperature/time combinations were chosen based on Arrhenius table provided by the instrument manufacturer.[1]

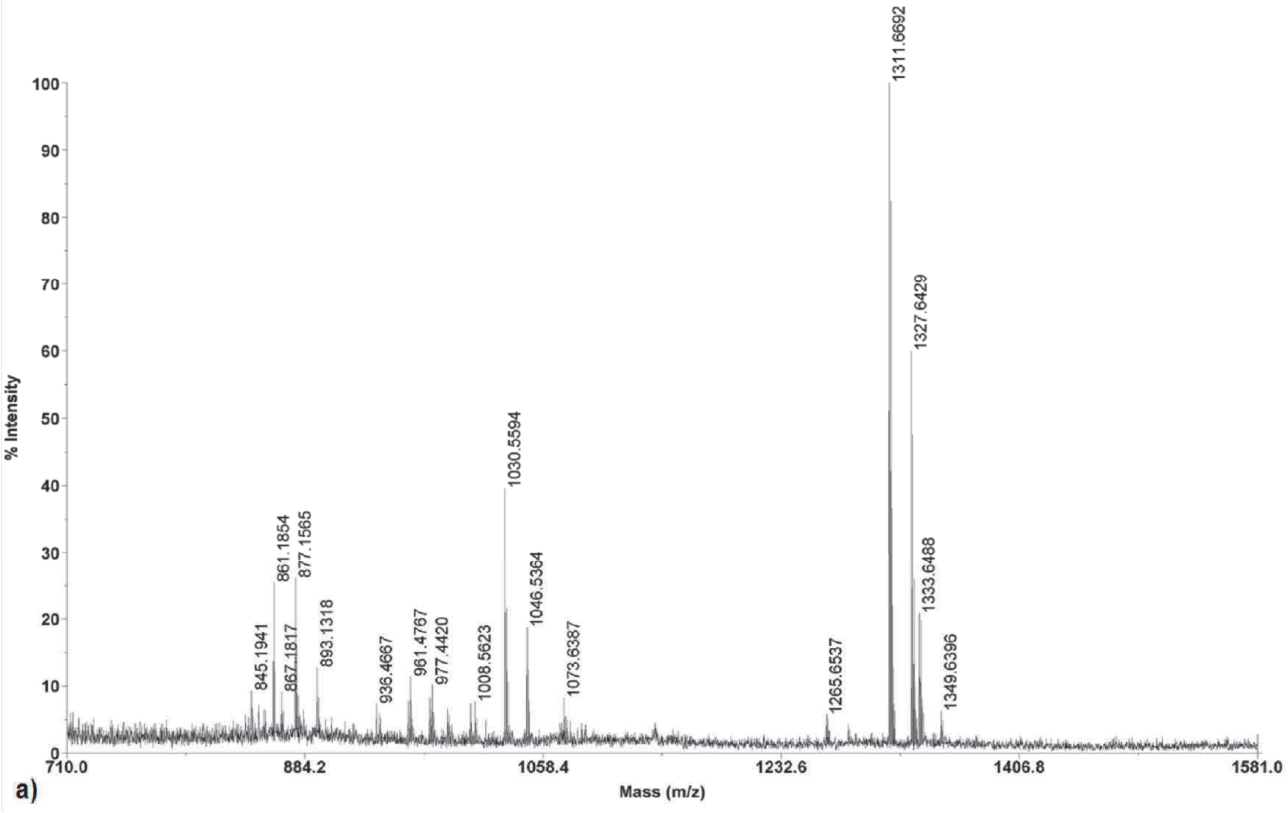

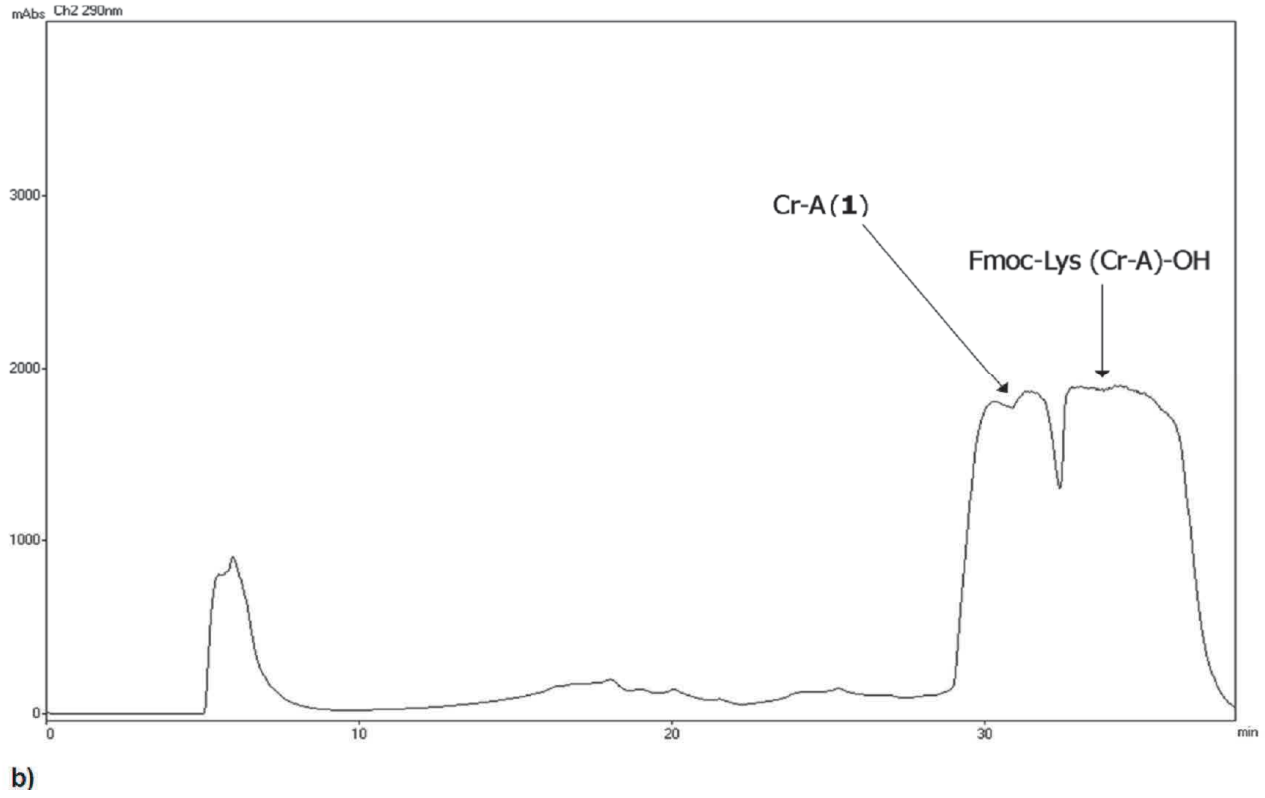

*Fig.6 (a) MALDI-TOF trace of **3**. The detected mass was 1311, corresponding to the m+23. (b) HPLC-UV trace, at 290 nm of **3**, highlighting presence of unreacted **1** (first peak) and **3,** which, being more lipophilic, elute with a bigger percentage of acetonitile. From Rossella F. et al, (2014)[107]*

Four coupling agents have been tested (Fig.7), the already mentioned *COMU*, [Ethylcyano(hydroxyimino)acetato-O_2]tri-1-pyrrolidinylphosphonium hexafluorophosphate (*PyOxim*), 1-[Bis(dimethylamino)methylene]-1H-1,2,3-triazolo[4,5-b]pyridinium 3-oxid hexafluorophosphate (*HATU*) and benzotriazol-1-yloxytri(pyrrolidino)-phosphonium hexafluorophosphate (*PyBOP*).

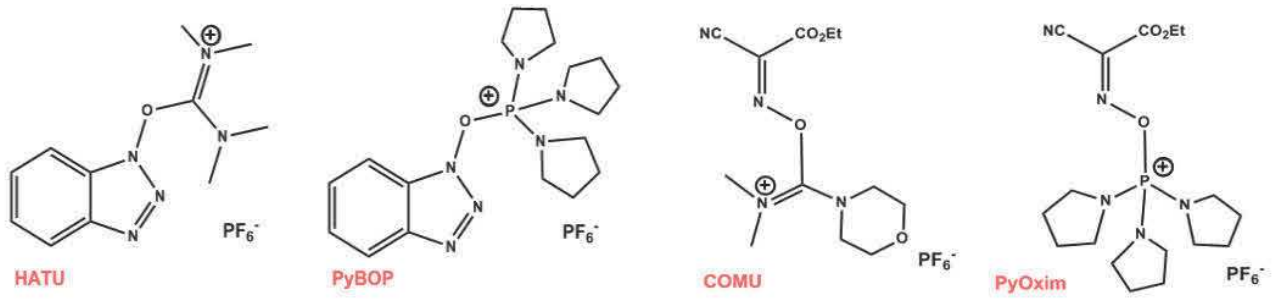

Fig.7. Chemical structures of the coupling agents used for the synthesis optimization. Left to right: the two uronium salt derivatives HATU and PyBOP. COMU (third) is the morpholino derivative of Oxyma, and shares with PyOxim (fourth) the ethylhydroxyiminocyanoacetate leaving group, although this latter one is a phosphonium salt as PyBOP.

HATU and PyBOP are based on the 1-hydroxy-7-azabenzotriazole (HOAt) group.

HOAt and 1-hydroxy-1H-benzotriazole (HOBt) are used in peptide chemistry as additives to the carboimidic coupling agents (as diisopropylcarboimide, DIC and dicylclohexylcarboiimide, DCC). Carboiimides activate promptly the carboxylic acid through the *O*-acylurea intermediate that, in turn, can lead to undesired side product due to the formation of *N*-acylurea or formation of carboxyl acid anhydride. The use of HOAt and HOBt as additives helps in preventing epimerization and leads to a better yield. [131] However, the explosive properties of HOBt [132] represent a safety problem, especially when are used in a closed or pressurized environment such as the microwave synthesizer. Therefore, HOBt/DIC has not been considered in our optimization, although such procedure has been reported by others.[125]

HATU is a uronium salt of HOAt and is a very fast and efficient coupling agent, that forms the very reactive OAt ester upon reaction with carboxylic acid. However, the nature of the activation of the carboxylic acid by *HATU* (Scheme 3a) can lead to an unwanted guanidinylation. [131,133] (Scheme 3b)

PyBOP is based on the same HOAt group, but it is a phosphonium salt. It is the safer pirrolidino-derivative of BOP, whom use has been limited due to his toxicity. [131]

In the case of *PyBOP* the coupling occurs through a phosphinic-carboxylic intermediate (Scheme 3c); the presence of such leaving group is reported to reduce guanidinylation. [134]

COMU is an Oxyma-derived [132] coupling agent that presents a morpholin-imine derivative as proton acceptor and the ethylhydroxyiminocyanoacetate leaving group. [135-136] *COMU* has been reported to be a safer and more efficient coupling agent than HATU and particularly suitable for mw-SPPS. [137]

PyOxim, as *PyBOP*, is a phosphonium salt, but it presents same leaving group as *COMU* (Scheme 3d). Therefore it incorporates features from both *COMU* and *PyBOP*, namely high efficiency and safety, low side reactions, and it is particularly soluble in DMF and in DCM, hence allowing a highly concentrated solution. Furthermore, it is reported to be more stable to hydrolysis than PyBOP, and reduce significantly the recemization and aspartimide formation. [138-139]

Among the tested coupling agents (Tab 1a), PyOxim gave the best results. This is probably because of its

better stability and solubility which allowed us to utilize higher concentrated solutions. The yield obtained with *PyOxim* is similar to the one obtained with *HATU*, but with less risk of an undesired side reaction.

The lower *COMU*-induced activation in mw-assisted synthesis (34.6% vs. 46.6% PyOxim) was somehow surprising since it has been reported to be very suitable for such applications. [137]

However, a similar result has been recently reported and has been related with its low stability in organic solvents at high temperatures. [140]

Stoichiometric evaluation (Tab 1b) showed that the reaction is more efficient when amine, carboxylic acid and coupling agent are used with the same equivalence.

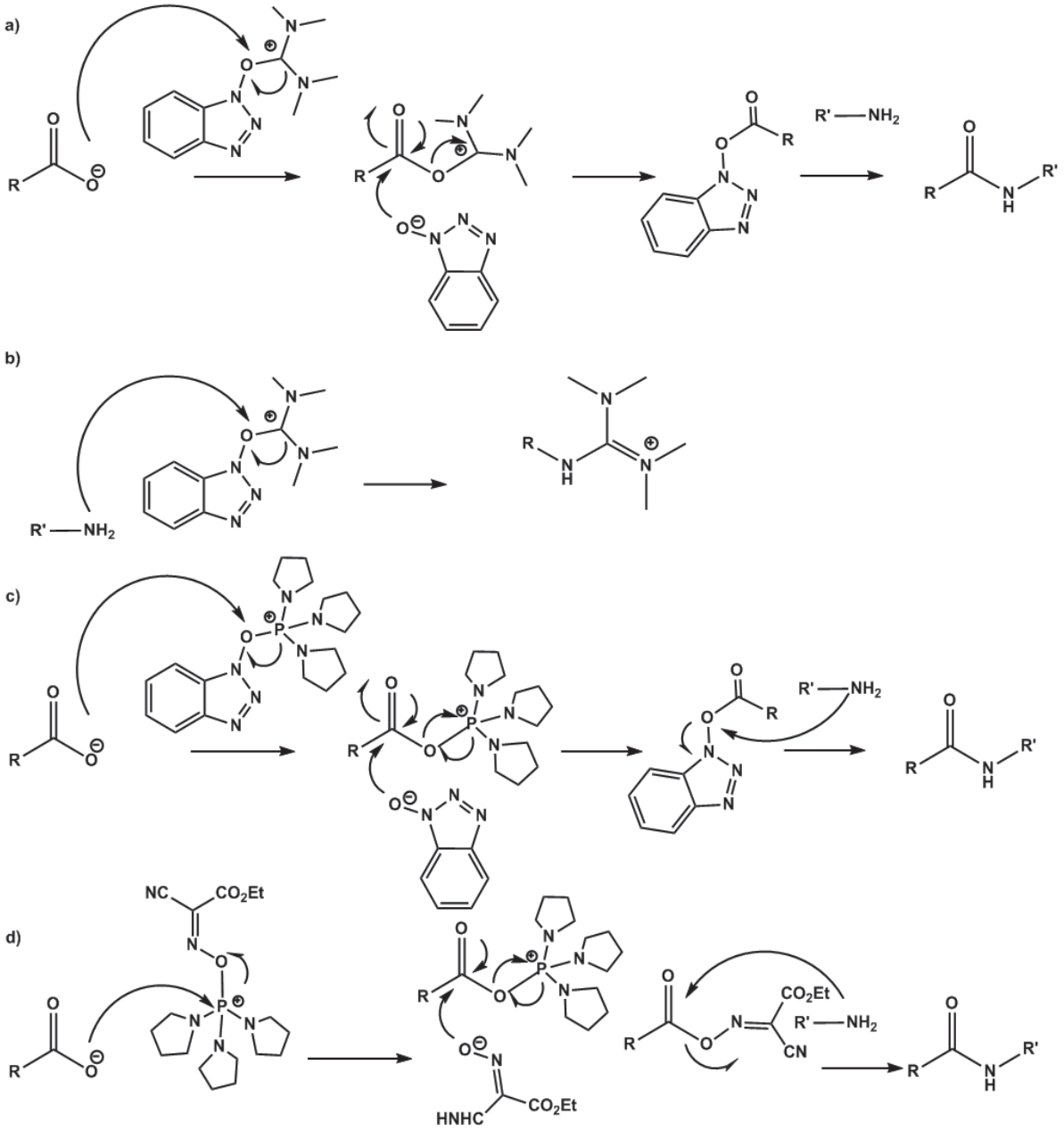

Scheme 3 (a) Mechanism of activation of uronium salts and its subsequent (b) guanidinylation side effect reaction.(c) Mechanism of activation of a phosphonium salt, here PyBOP. From Valeur E. And Bradley M. (2009) [131] (d) mechanism of activation of an Oxyma derivative salt, in this case PyOxim. The activation of COMU it is totally similar. From Subiros-Furnosas et al, (2013) [137]

This is consistent with the procedure previously reported for Oxyma pure® and COMU®, which share with PyOxim the same ethylhydroxyiminocyanoacetate leaving group and a similar mechanism of activation. [136]
Prolonged mw irradiation or increased temperature (Tab. 1c) negatively affected the peptide stability, as previously reported by others. [124, 126, 141]
According to our optimization, we developed a satisfying protocol for the synthesis, which was used for the coupling of our next biosensors.

2.3.2. Microwave-assisted synthesis of CrA-PEG$_3$TAMRA

The better cellular uptake of the hydrophobic cage **1** prompted us to develop a compound with a more lipophilic dye such as tetramethylrhodamine (TAMRA).
Rhodamine dyes have a good signal-to-background ratio, photostability are relative insensitive to pH: this lead the rhodamine-conjugated probes to be particularly stable in cellular environments (i.e. upon internalization in acid compartment in the cell such as endolysosomes [142]), therefore are suitable for multiple applications, such as DNA sequencing, production of enzyme responsive probes, ion detection. [114-115; 142-145]
Moreover, rhodamine dyes have tunable spectral properties, upon modification on the xanthene core or on the benzene unit, therefore are used to produce caged probes. [114, 144]
The methyl derivative TAMRA is characterized by a high molar absorptivity ($\varepsilon = 7.4\times10^4$ $M^{-1}cm^{-1}$), brightness (Φ=0.92) [114, 142; 144] and stability in the in the conditions needed for Fmoc-SPPS therefore is an attractive dye for peptide and protein labelling. [110; 115] In order to increase the solubility of the constructs compared to bare Cr-A, as in **2**, three PEG units were introduced to the conjugate as a cross linker between the optical dye and the Cr-A.
In the previous paragraph we have shown how the use of an optimized coupling protocol in tandem with mw-assisted synthesis leads to a product with better purity and in much shorter time, as illustrated by the fact that the acylation was carried out for a maximum time of 10 min and only the final purification step was required. For these reasons, we decided to synthesize the TAMRA derivative CrA-PEG$_3$-TAMRA **4** using a microwave (mw)-assisted solid phase peptide synthesizer, as summarized in Scheme 4. (§7.4)
Briefly, a Gly-preloaded resin was coupled with Fmoc-Lys (OH), using mw irradiation for 10 min at 50º C, following a standard mw-assisted peptide coupling procedure. [124]
PyOxim was used as a coupling agent due to its high coupling yield, high solubility in dimethylformamide (DMF) and inability to guanidinylate the amino terminus, a crucial feature when fragment peptides are synthesized. [138; 146]
The free ε-amino terminus of the Lys was then coupled with 5,6-TAMRA (mw, 10 min at 50ºC) in order to obtain the desired fluorescent payload. We believe this on-resin approach has a better cost-benefit than the use of commercially available Fmoc-Lys (TAMRA)-OH building blocks and it is compatible with the rest of the synthesis. After Fmoc deprotection and coupling with three PEG units building block (Fmoc-AEAAA), the resin was cleaved for 30 min in mild conditions, and finally coupled with 1, using a mw-assisted protocol derived from our previous solution-phase protocol.[106]
Contrary to what has been observed for **2**, the intermediate product TAMRA-Lys-PEG$_3$-NH$_2$ (see scheme 3, fourth chemical structure) was pure enough to be coupled with **1** without further purification, while in the case of FAM-Lys-PEG$_3$-NH$_2$ (scheme 1, fourth chemical structure) this extra purification step, based on mass

analysis, was needed. Although necessary, an extra purification step means often a loss of material, which was not the case for the precursor of **4**.

As for **2**, after the coupling with **1**, the reaction mixture was separated with RP-HPLC and the fractions were analyzed through a MALDI-TOF spectrometer (See Materials and Methods).

The calculated mass was m/z = 1724 for $C_{96}H_{104}N_6O_{24}$ (**4**), referred to the lactone form, and the mass found in MALDI/TOF analysis was m/z 1725, corresponding to the m+1 of the lactone form (Fig. 6a).

As showed both in the mass spectrum trace and in the HPLC-UV traces at 560 nm (Fig. 6b), the purity of such compound was considerably better than the previous one.

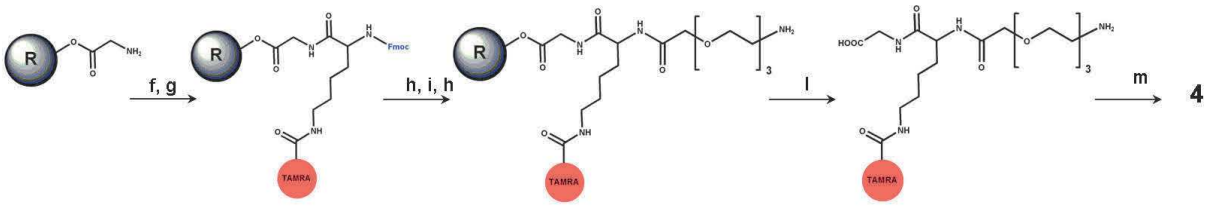

*Scheme 4. Synthesis of **4**. Reagents and conditions: (f) Fmoc-Lys(5,6 FAM)-OH (3 eq.), PyOxim (3 eq.), DIPEA (6 eq.), mw, 50°C, 10 min. (g) 5,6 TAMRA (3 eq.), PyOxim (3 eq) , DIPEA (6 eq.) mw, 50 °C, 10 min (h) 25% piperidine in DMF, RT 15 min, twice. (i) Fmoc-AEAAA (3 eq.), PyOxim (3 eq.), DIPEA (6 eq), mw, 50°C, 10 min (l) TFA/TFE/CH_3COOH (8/8/1) RT, 30 min, followed by azeotropic evaporation and precipitation in cold ether. (m) CrA-ma (1 eq), PyOxim (1 eq), DIPEA (2.5 eq) in DMF, mw, 75°C for 10 min, followed by RP-HPLC purification. Overall yield 45% From Rossella F. et al, (2014)*[107]

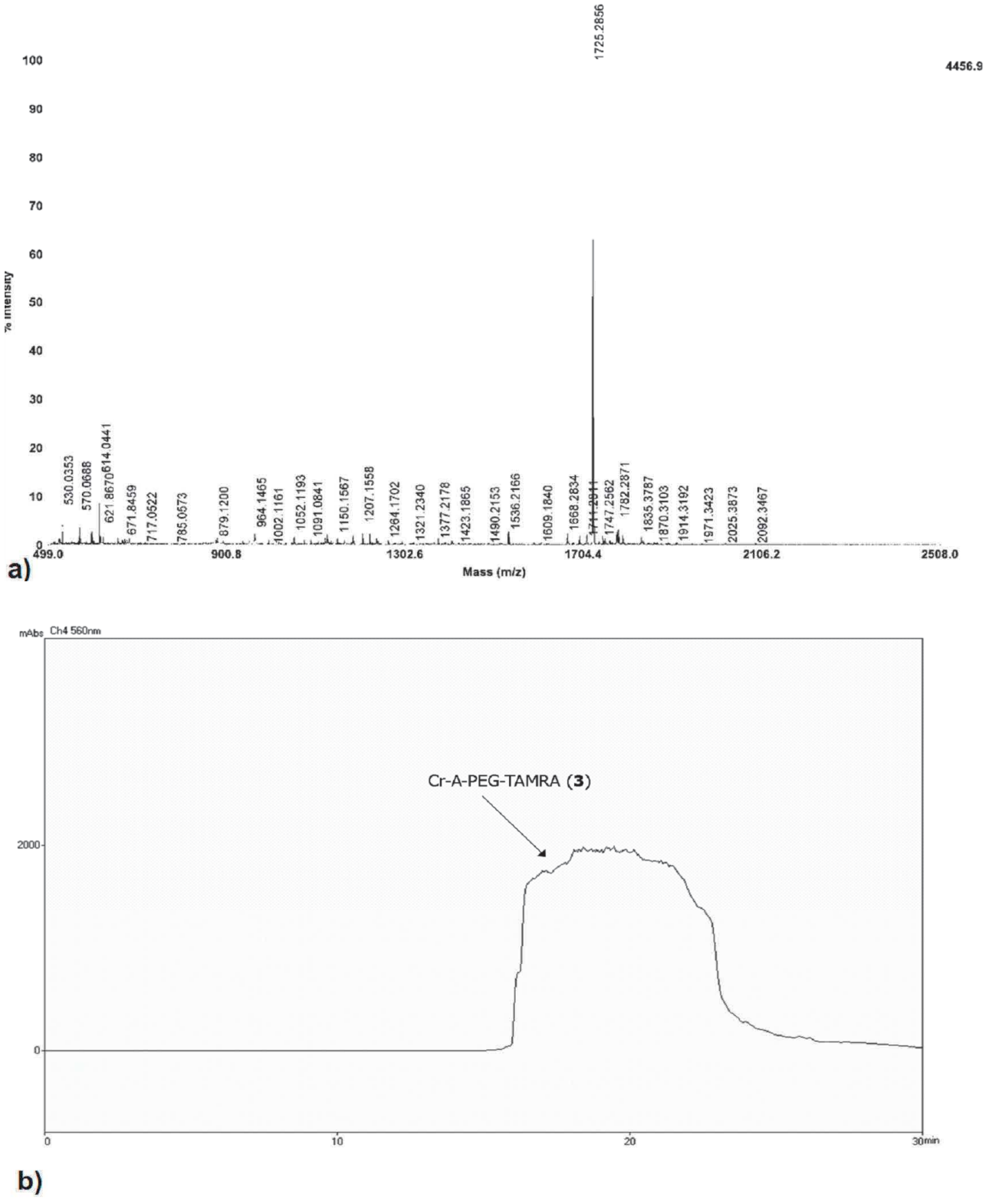

*Fig.7 (a) MALDI-TOF trace of **3**. The mass found was 1725 corresponding to the m+1 of the lactone form. (b) HPLC-UV trace, at 560 nm of **3**, highlighting the predominant presence of **4**. From Rossella F. et al, (2014)*[107]

2.3.3 Evaluation of the fluorogenic properties of 2 and 4

Our initial experiments showed that, aside of difference in cells uptake due to an increased hydrophilicity, the conjugation of the cage with different payloads does not hamper or decrease the efficiency of the hyper-CEST experiments.

In the same way, it is important to verify if the fluorescence proprieties are unchanged when a dye such as FAM or TAMRA is conjugated with different molecules. [147-148]

The measure of the relative quantum yield (Φ) is an important parameter that allows comparing the brightness of the conjugated dye with the non conjugated version in order to quantify how much the fluorogenic properties are retained.

The quantum yield *Φ* has been calculated as follows:

$$\Phi = \Phi_R \frac{I}{I_R} \frac{OD_R}{OD} \frac{n^2}{n_R^2}$$

Where, *I* is the integrated fluorescence intensity, *n* the refractive index of the solvent, and *OD* is the optical density. The subscript "R" refers to the reference fluorophore of known quantum yield, in our case 5,6-FAM (Φ=0.95 in ethanol) for **2** and 5,6-TAMRA (Φ=0.68 in ethanol) for **4** as reference. [149-150]

In order to not take into account the refractive index as a contributing factor, the two constructs and their relative reference have been measured in the same solution (0.1% DMSO in ethanol). (§7.12)

The low contribution of DMSO was considered to be negligible; therefore the measured Φ has been directly compared with the reference quantum yield in pure ethanol.

Examples of the measurement of Φ upon conjugation of the dye has been reported not only when modifications are carried out on the aromatic rings [144; 151-153], but also when the modifications are simply on the linker, as in our case. [142; 147-148]

Our findings shows that in general the photophysical properties of the two fluorophores are maintained, having the Φ_R of **4** almost unchanged in comparison with 5,6 TAMRA (0.67 vs. 0.68) and obtaining a value of Φ_R for **2** that is only ≈ 18% less compared to its reference (0.68 vs. 0.95).

A major sensitivity in the spectral response of conjugated FAM has been reported in several papers. [147]

For instance, conjugation of FAM with oligonucleotides leads to a decrease in quantum yield between 23% and 87%, depending on oligonucleotide, [154] while a decrease of up to 42% has been measured when FAM was conjugated with a bigger payload such as BSA. [155]

Rhodamine, similar also to our findings, seems more robust in retaining fluorescent properties.

Almost unchanged quantum yield has been measured when rhodamine was conjugated with riboflavin [156] or with DNA aptamers. [147; 157]

The quantum efficiency of a dye has been related with the photoinduced electron transfer from the electron donor part of the fluorescein (benzene unit) to the acceptor (xanthene unit). The presence of a non-conjugated substitutents in position 5' of the benzene ring was showed to be essential for maintain the electron donor and acceptor orthogonal to each other and therefore the quantum efficiency. [158]

We could therefore speculate that the presence, in our case of a free carboxylic unit in 5' both in 2 and 4 lead to the retaining of the initial photophysical properties.

2.3.4 Cell uptake and cell viability studies using 2 and 4 as cell marker

Cellular uptake and impact on cell viability was quantified for both **2** and **4** and to compare their performance as cell markers for NMR detection. Furthermore, we extended the panel of our study to two different cell lines, the already mentioned L929 fibroblasts and RAW 264.7 macrophages. Fibroblasts and macrophages present different physiological function and location, the first ones being used as model of stromal cells and the other as model of inflammatory cells. A difference in cell uptake and cytotoxicity is therefore expected and has been previously reported. [159]

The cell uptake, toxicity, and fluorescent imaging of cells treated with **2** are presented in the left column of Fig. 8, while the relative results for **4** are in the right column. L929 and RAW cells were incubated with for 18 hrs with either **2** or **4** at concentrations of 0-100 μM. (§8.3)The cellular uptake of each construct (in fmole per cell) was quantified in cellular lysates by fluorescence (§8.6). As shown in Fig.8 A and B, there is a linear increase in the total cellular uptake of both constructs with increasing incubation concentration. We observed a consistently higher uptake in RAW 264.7 macrophages than in L929 fibroblasts. The higher uptake of macromolecules from RAW cells has been similarly reported elsewhere. [159]

At each incubation concentration, **4** displays approximately a three-fold higher cellular uptake than **2**, and, similarly, a higher degree of cell toxicity, as shown by comparing Fig.9 C and D. Both the degree of cellular toxicity and amount of non-specific uptake is consistent with that of un-targeted cryptophane-based constructs reported by other groups. [83-85] We speculate that the lipophilicity of TAMRA, compared to FAM, could explain the increased cell uptake of **4.** This would be in line with our previous study in which we showed that **1** has a higher degree of cellular uptake and higher cell toxicity compared to the more hydrophilic **2**. [106]

As shown also in our preliminary experiments for both dyes, the absence of any cell-penetrating peptides or specific cell-targeting units on either **2** or **4** did not represent a problem to get sufficient cellular uptake for xenon-MRI studies as demonstrated in the following section. Although a high degree of biosensor cellular uptake is desirable for MRI studies, high cell viability is equally critical for future *in vivo* applications. Cell toxicity tests were performed with alamarBlue® for **2** (Fig. 9D), while for **4** (Fig. 9E) Cell Meter™ has been used, since alamarBlue® absorbs in the same spectral region as TAMRA. (§8.5)

The cell viability of **2** is around 70% for a 100 μM incubation concentration. This is consistent with what has been previously reported [83-85]. Unsurprisingly, incubation of cells with **4** results in a more pronounced decrease in cell viability, most likely a direct cause of the higher cellular uptake of this construct. Although in our preliminary test a concentration of 100 μM of **1** results in comparable loss of cell viability [106] it is reasonable to hypothesize a contribution of TAMRA to cytotoxicity. Cell toxicity associated with rhodamine derivatives has been reported [160], although the contribution of TAMRA alone to the overall cellular toxicity of the construct could be not ruled out. We decided to use a threshold of >75% viability as an internal quality standard, therefore solutions of 50 μM for **2** and of 20 μM for **4** were used both for optical imaging and for NMR/MRI experiments, as indicated by the grey bars in Figure9 A-D. Hence, the incubation concentrations are tailored to result in comparable intracellular uptake of Cr-A for both constructs.

From the fluorescent quantification analysis we can estimate that to the cells incubated with 50 μM of **2** for 18 hrs, contained the compound corresponding to an intracellular concentration of 55 μM ± 8 μM in the case of RAW 264.7 macrophages and of 21 μM ± 9 μM in the case of L929 fibroblasts.

Similar degrees of uptake are achieved with 20 μM of **4**, for which we measured intracellular concentrations of 63 μM ± 10 μM for RAW 264.7 macrophages and 18 μM ± 5 μM for L929 fibroblasts.

Microscopy data (Fig. 8.E. for **2** and Fig. 8.F for **3**) show similar intracellular distributions of both constructs in vesicular structures, in both macrophage and fibroblast cell lines. (§8.9) This intracellular distribution, along with the linear dependence of cellular uptake with incubation concentration and the higher uptake of the constructs by the macrophage cell line is consistent with a macropinocytosis-dependent uptake mechanism**.** [107, 119-120] In comparison, earlier crytophane biosensors that bear CPPs show a distinctly different localization, along with a higher degree of cellular uptake and cytotoxicity over our smaller non-specific

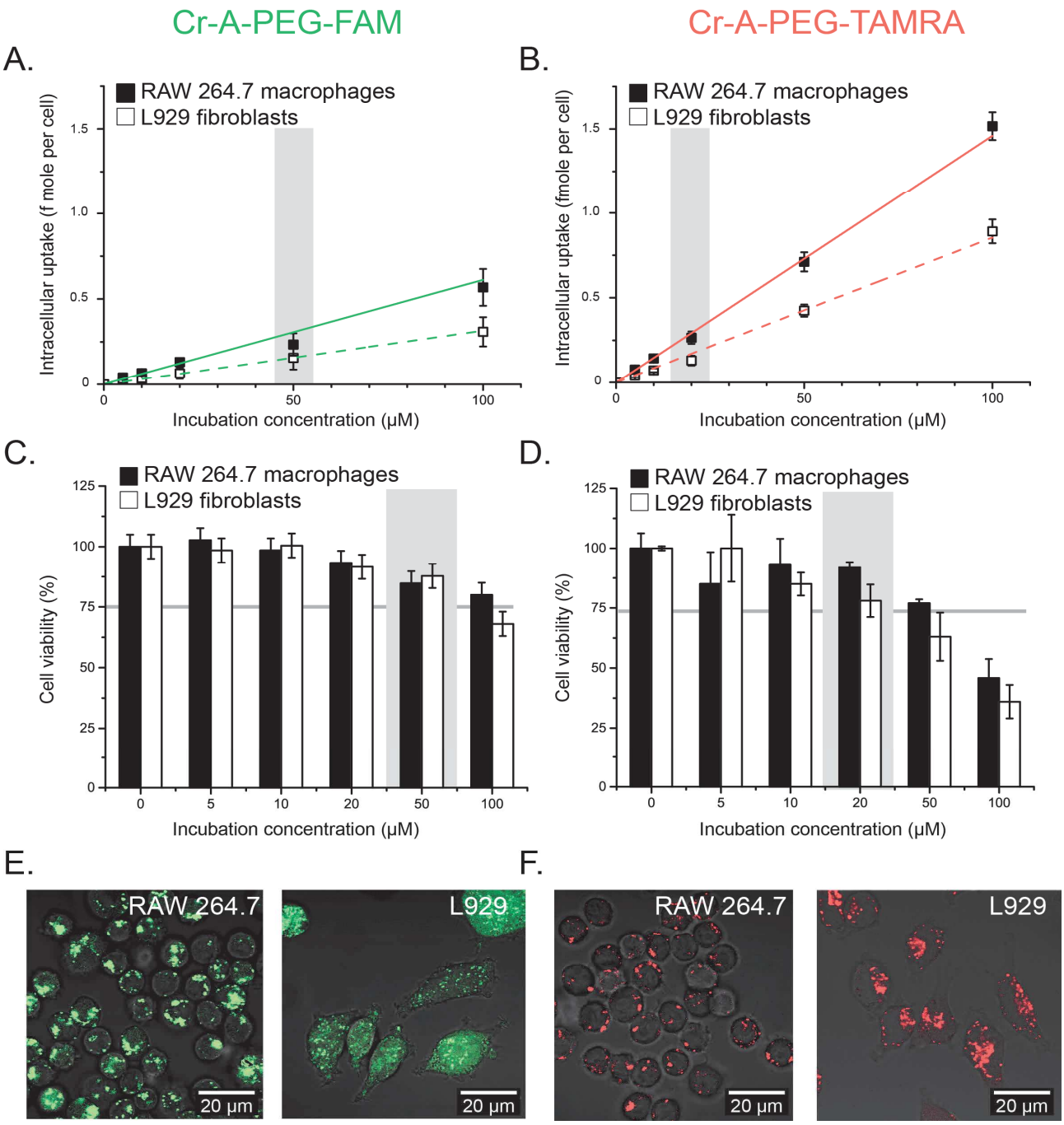

*Figure 8. A. and B. Intracellular uptake after 18 hrs incubation of cells with 0-100 μM **2** (A) or **4** (B). Grey bar indicates working concentrations used for NMR and microscopy experiments. C. and D. Cell viability after 18 hrs incubation of cells with 0-100 μM **2** (C) or **4** (D.). Grey bar indicates working concentrations used for NMR and microscopy experiments, where cell viability was >75% for both cell lines. E. and F. Fluorescence microscopy after incubation of cells with 50 μM **2** (E.) or 20 μM **4** (F.) showing similar intracellular distribution of both constructs. From Rossella F. et al, (2014)[107]*

constructs. [83; 85] Having a fluorophore within the construct allows for a fast and simple quality control of samples, using live cell flow cytometry, prior to time consuming MRI experiments.

Flow cytometry (§ 7.8) provides valuable supporting data on the relative uptake of a single construct in different cell lines (for example by confirming quantitative data in Figure 10 B, by showing a relative 3-fold higher uptake in RAW 264.7 cells than in L929 cells with 20 µM of **4,** Figure 9). As flow cytometry analysis requires less than 20,000 cells per sample, it can easily be incorporated into the MRI sample preparation routine.

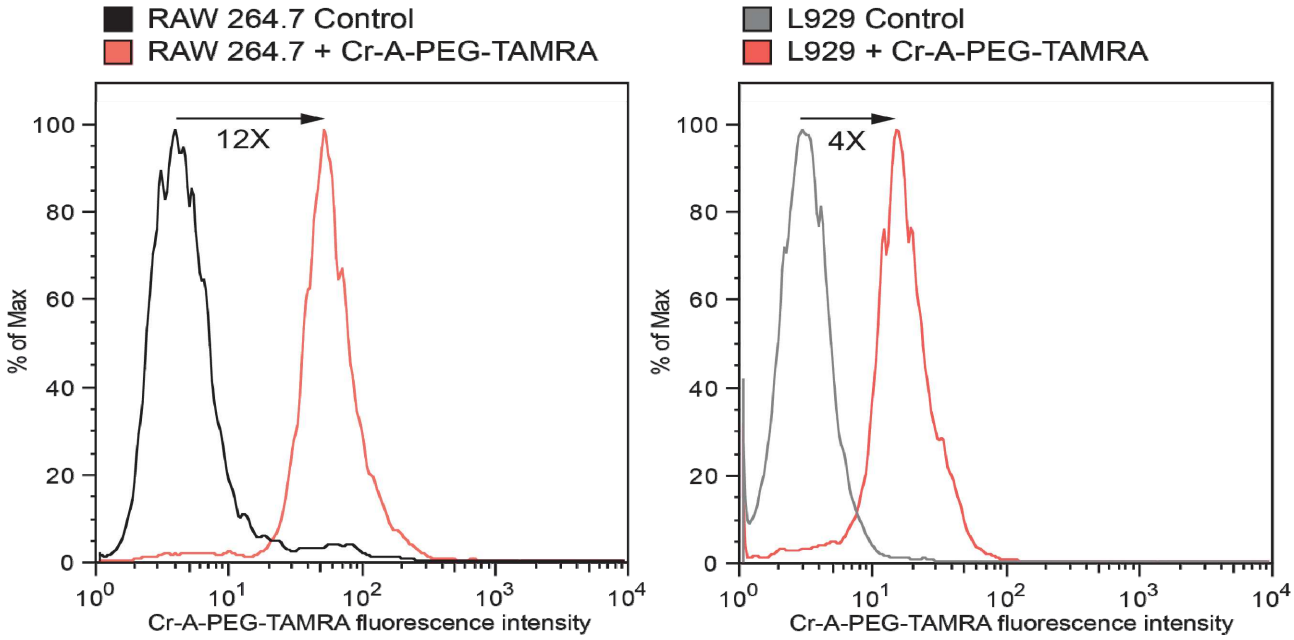

*Fig. 9 Flow cytometry data on cells incubated with 20 µM of **4** for 18hrs. Results show the histograms of fluorescence intensity for RAW 264.7 cells (left panel) and L929 fibroblasts (right panel). The arrows indicate the shift in median fluorescence intensity between the control and the experimental samples. This data shows that RAW 264.7 cells take up on average 3-fold higher Cr-A-PEG-TAMRA construct than L929 cells. From Rossella F. et al. (2014)*[107]

.

2.3.5 In cellulo Hyper-CEST response of 2 and 4

The work flow of our xenon-MRI based experiments with a double phantom is summarized in Scheme 5 and demonstrates how after uptake of the bi-functional contrast agent into cultured cells, the cells can conveniently be analysed by either fluorescence read-out or xenon-MRI/NMR read-out. (§ 9.4)

Following our toxicity test, cells were incubated with a 50 µM solution of **2** or 20 µM of **4** for 18 hours at 37°C in a 5% CO_2 cell culture After incubation, the construct-containing solution was removed, the cells washed with PBS and harvested from the culture plate (Scheme 5, 2). The cell pellets were then re-suspended in PBS for MRI measurement. The experiment involved two NMR tubes (the so called “MRI double phantom”), one nested inside the other. The inner tube contains cells incubator (Scheme 5, 1) (at a density of 10 millions/mL) that were labelled with the bifunctional construct, while in the outer tube contains unlabelled cells at the same density (Scheme 5,3). Hp-Xe was delivered into both compartments simultaneously through capillaries and images were acquired with on-resonant (-124 Hp Xe ppm relative to the xenon in free solution at 0 ppm) and off-resonant (+124 ppm) saturation and used to calculate the CEST images (Fig.10).

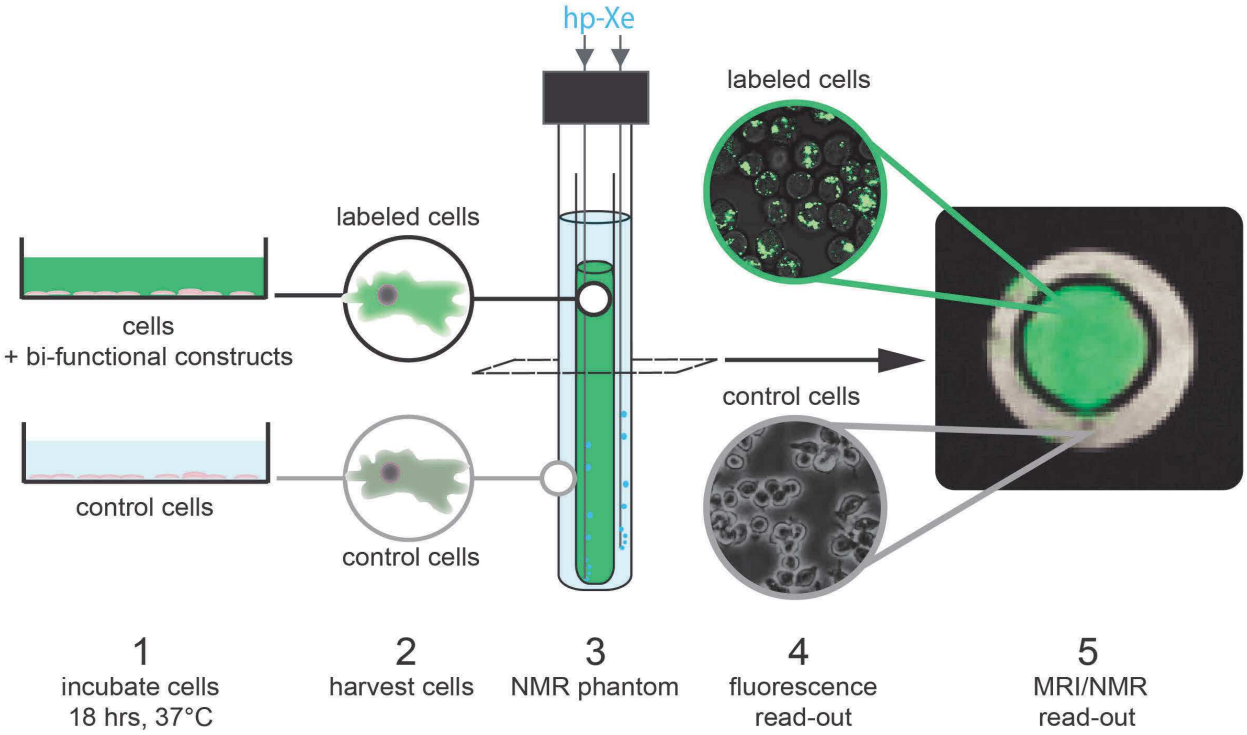

Scheme 5. Diagram of work-flow with bi-functional fluorescence/xenon-MRI constructs. Step 4 and 5 show examples of the fluorescent read out (microscopy images) from labelled and control cells, and of Xe-MRI (transverse section of the double phantom with color-encoded CEST effect). From Rossella F. et al, (2014) [107]

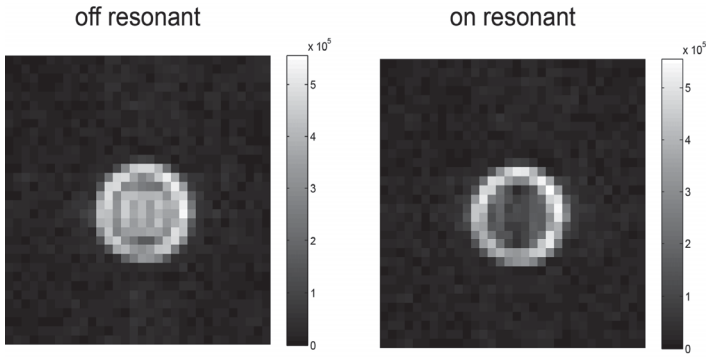

Fig. 10 Example of Xe off-resonant (left, at -124 ppm relative to Xe in solution) and on-resonant images (right, at +124 ppm). Each image is the result of 10 averages. From Rossella F. et al, (2014)[107]

A signal mask was created from the off resonant xenon image (threshold set to 25 % of the maximum pixel intensity).

The Hyper-CEST images (Fig. 11) were calculated pixel wise from the masked off-resonant and on-resonant images using the following formula:

$$CEST\ image = \frac{(off\ res) - (on\ res)}{(off\ res)}$$

Negative values were set to zero.

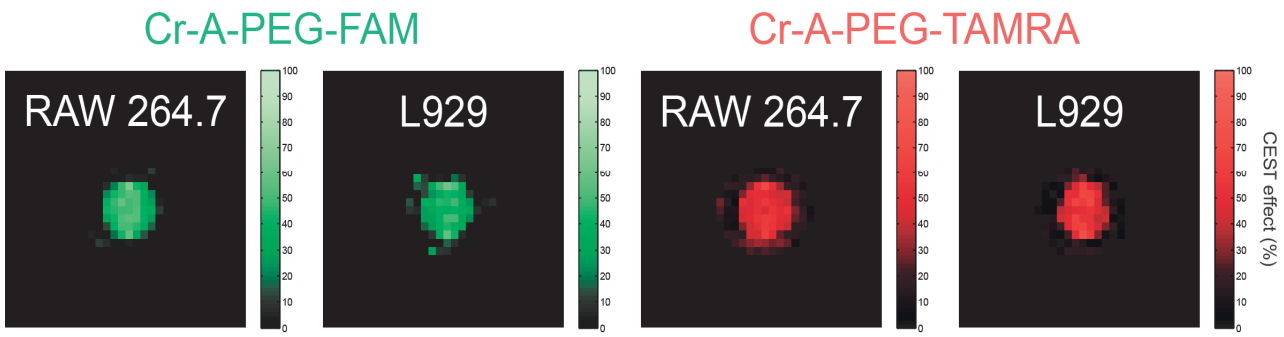

*Fig. 11 Hyper-CEST images of RAW 264.7 and L929 cell lines incubated with **2** and **4**, without proton overlay. From Rossella F. et al, (2014)*[107]

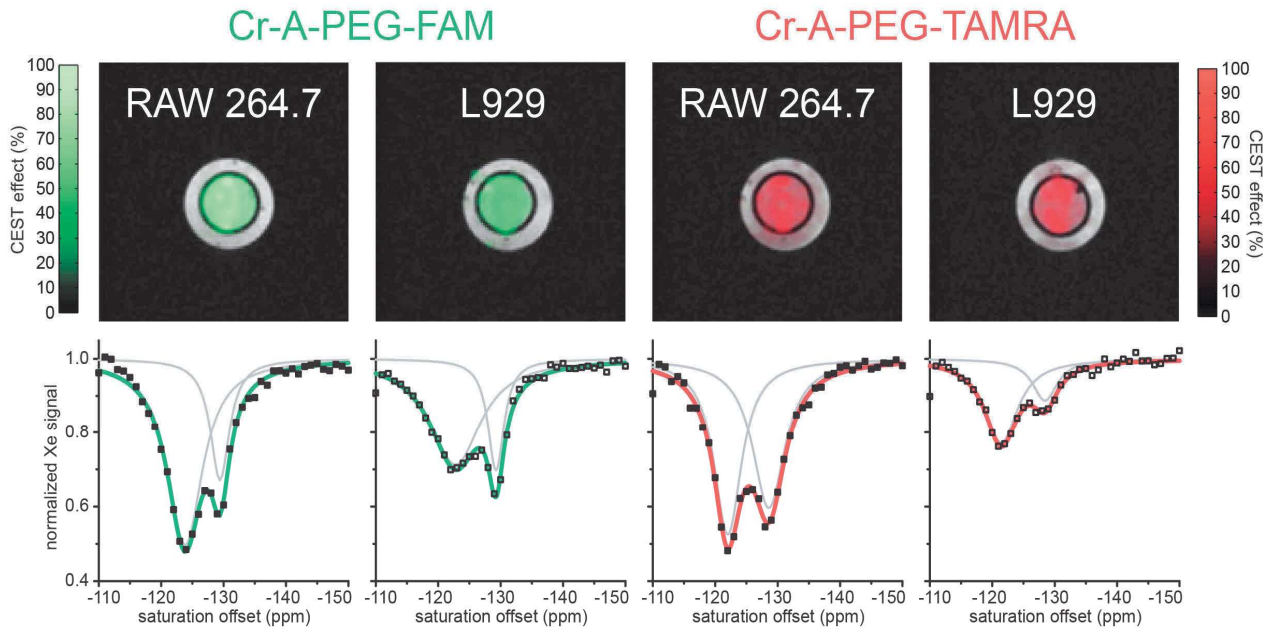

*Fig. 12 Xenon magnetic resonance experiments for cells incubated with 50 µM **2** (green) and 20 µM **4** (red). Top row: Magnetic resonance imaging (20 x 20 mm² FOV) where the inner compartment contains labelled cells and the outer compartment contains unlabelled cells. Xenon Hyper-CEST imaging is overlaid in false color on high resolution b/w proton images.*
Bottom row: CEST-spectroscopy of labeled cells. The filled squares indicate data for RAW 264.7 cells and the open squares indicate data for L929 cells. The complete fit is indicated with the solid coloured lines and the two individual components of the fit are indicated in grey. In each case two resonances can be clearly resolved, one associated with the bi-functional constructs in a lipidic environment (left peak) and the other in an aqueous environment (right peak). In both spectroscopy and imaging we observe a higher uptake of both constructs in RAW cells. From Rossella F. et al, (2014)[107]

The high sensitivity of xenon to its local environment together with the chemical shift selectivity of the saturation pulse allow us to perform MRI based on the unique signal for xenon bound to the construct that is associated with cells.

In the upper row of Figure 12 the CEST images (interpolated from 32×32 pixels to 128×128 pixels) have been overlaid in false colour over high resolution proton images of the phantom.

For all samples we can clearly localize the labelled cells in the inner compartment demonstrating the utility of these constructs for xenon Hyper-CEST cell labelling experiments.

In addition, CEST-spectra were acquired from the labelled cells, see Fig 12 lower part.

It is possible to distinguish two signatures, both belonging to the xenon in exchange with CrA associated in

cell suspensions: the dip at the left corresponding to CrA associated with lipidic cellular environments, and the one at the right side corresponding to CrA associated with aqueous environments.

These results show the unique ability of xenon NMR in detecting differences in the micro-environment by separating the spectral population into two spin pools.[69; 84; 86]

We hypothesize that the larger contribution from Cr-A in lipidic cellular environments is a result of the faster Xe exchange in this environment [69; 86] and also of the efficient partitioning of cryptophane into membrane material. [70; 84]

This partitioning of the construct into these two micro environments and a selective detection of the two pools would be difficult to observe using only fluorescence techniques.

Despite the differences in the details of the CEST-spectrum, RAW 264.7 and L292 cell lines shows a similar pattern with each of the constructs: consistent with the fluorescence and microscopy data (previous section) RAW 264.7 cells shows a larger uptake of the constructs when compared with L292 and thus a more pronounced CEST response.

For further analysis, the data was fit to the exponential of the sum of two Lorentzians (fit shown as a solid coloured line):

$$f(x) = e^{-(lor(A_1,\omega_1,x_1,x)+lor(A_2,\omega_2,x_2,x))}$$

where $lor(A_2,\omega_2,x_2,x)$ is a Lorentzian with maximum A, full width at half maximum ω, and centre x_0, and x is the saturation frequency offset in ppm. The contribution to the fit from CrA in each of these environments is indicated by the grey lines. The high quality of these z-spectra allows for accurate analysis of the line shape parameters. The corresponding results of this analysis of the z-spectra are summarized in Fig.13.

Chemical shifts of the CEST responses could be determined with an SD of 0.1 – 0.4 ppm although the line widths are as high as 9 ppm (with an SD of 0.3 – 1.1 ppm). Extra-cellular peaks show the typical clear upfield shift compared to intracellular signals (Fig 13a). The signals from **2** appear systematically at larger saturation offsets than those from **4** and L929 cells seem to induce a systematic shift towards lower saturation offsets. Upon internalization, xenon in **4** seems to experience larger changes than for **2** with a more clearly

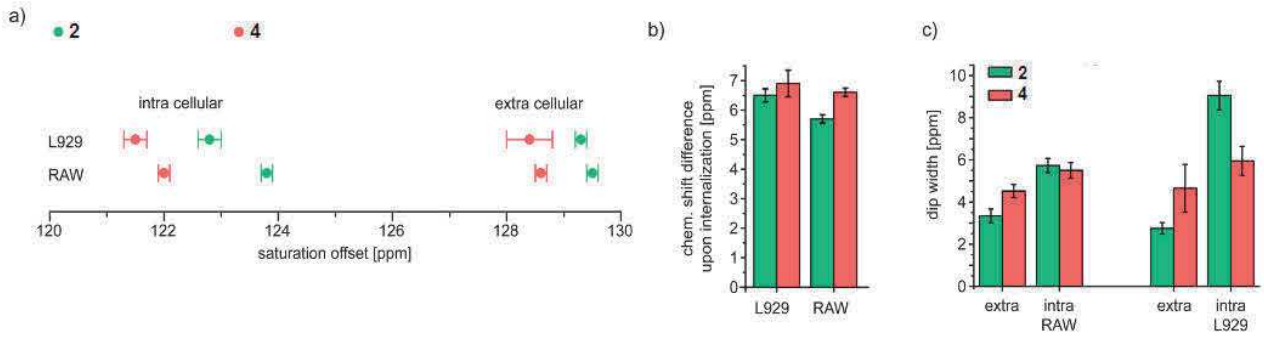

Fig. 13 Detailed analysis of the z-spectra from Fig.12 after fitting exponential Lorentzian line shapes to the CEST responses. (a) Saturation offsets relative to the solution pool of free Xe for maximum CEST response; the error bars represent the SD of the center position of the individual Lorentzian components. (b) Changes in chemical shift upon internalization of the compounds. (c) Comparison of widths of the individual Lorentzian components.

pronounced effect for the RAW cells (Fig.13b). Cellular internalization causes an expected line broadening (Fig.14c), though the extracellular resonances are broader for **3** when compared to **2**.
In summary, CEST responses from compound **2** appear systematically at larger saturation offsets that those for **4**. With respect to the impact of the cells, L929 cells seem to induce a systematic shift towards lower saturation offsets. Compound **4** shows slightly larger shifts upon internalization, however we can conclude that **2** and **4** have a comparable performance and can be consider largely equivalent. This suggests that the dye moiety can be freely chosen to best meet the needs of the desired biological application.
With respect to this Xe-MRI data and the cell toxicity test, FAM has been considered a good candidate for our next screenings and to synthesize targeted sensors, therefore, we concentrate our effort toward this latter one.

2.4 Preparation for live cell studies: Comparison of the direct-bubbling method and the indirect delivery through the bioreactor

In the previous experiments, hp-Xe has been delivered to the cell suspension through a direct delivery system (Scheme 6). In this system, hp-Xe was bubbled into the MRI sample phantom (SP) through fused silica capillaries. The flow of hp-Xe was controlled by two spectrometer-triggered gas flow regulators (GR). The tubes into the GRs are connected through a switchable valve, therefore the gas can be either bubbled into the SP or be deviated through a bypass during the data acquisition. This allows keeping the flow through the polarizer cell constant and reduces the noise in the CEST data.
For each scan, Xe was typically bubbled for 10-15 s and then a 2 s delay was added to let the Xe bubbles collapse prior the acquisition. The presence of bubbles and foam would disturb the detection process; therefore, 0.1% of cell-compatible antifoam agent (Pluronic L-81) was added to the sample solution.
The direct gas delivery might affect cell viability and integrity. Such effect was firstly investigated [106] by comparing the NMR results of a suspension of L292 fibroblasts incubated with **1** (Fig.14 a) with the Hyper-CEST response of the supernatant from the same cell suspension, using the same parameters.

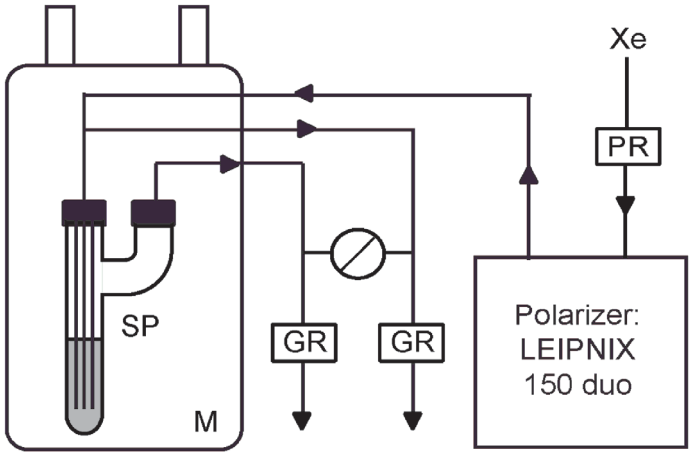

Scheme 6: Set up for direct delivery of hp-Xe to the sample. Xe from the gas bottle was delivered into the polarizer (see Introduction) via a pressure regulator (PR). Once polarized, hp-Xe can be delivered to the sample phantom (SP) through the silica capillaries. During acquisition to the gas flows through a bypass to keep the flow conditions in the polarizer constant. Those processes are regulated by spectrometer-triggered gas flows regulators (GR). From Klippel S et al, (2013)[106]

The spectrum from the supernatant (Fig. 15b) showed again the typical second, broader peak at 71 ppm that was assigned to Xe in cell/membrane-associated CrA (see Fig.2c). However, the CEST response is weaker when compared to the result from the full cell suspension (Fig.15 a).

The peak at 61 ppm, attributed to the unbound sensor, was at a comparable intensity in the two measurements. We attributed therefore the peak at 71 ppm to compound **1** bound to cell fragments that are generated from the bubbling process.

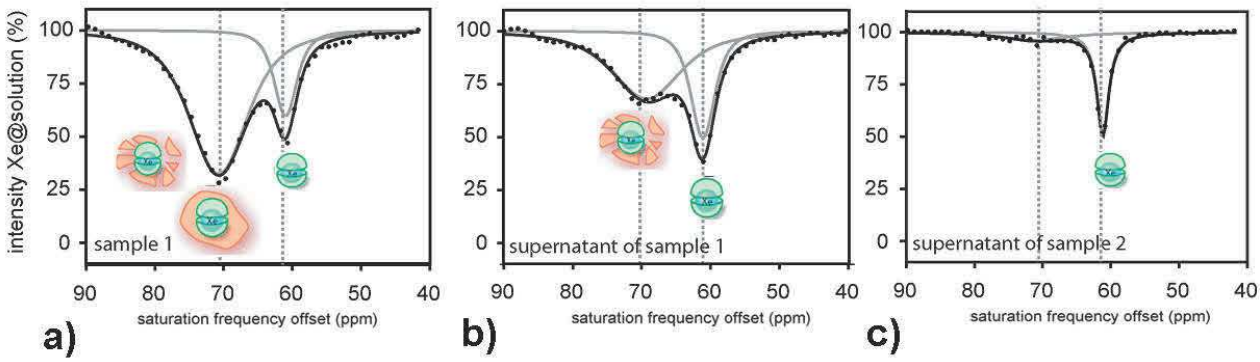

*Fig. 15 Hyper-CEST response of (a) cell suspension after incubation with **1** (b) the supernatant of the same cells centrifuged after the Xe-NMR determination with direct bubbling on cells (c) supernatant of cells incubated with **1**, but not previously measured with direct bubbling. From Klippel S et al, (2013)*[106]

To confirm this hypothesis, a third sample was prepared (Fig.15c), in which cells were incubated with **1** in the same condition of the previous experiments, but instead of being measured in the NMR phantom, were directly centrifuged, and only the collected supernatant was measured. In this case, only one peak was measured, namely at 61 ppm, corresponding to the unbound sensor.

Therefore, we concluded that in the experiment a) and b) the peak at 71 ppm is the result of the sensor bound to the cells and the sensor bound to an increasing amount of fragments that are generated during direct gas delivery.

We expect bursting gas bubbles with corresponding shear forces to cause the cells to break. An independent experiment using FACS was then carried out (Fig. 16). Cell suspension of RAW 264.7 and L929 fibroblast at the same concentration used in the Xe-NMR experiments (10 millions cells in PBS with 0.1% Pluronic-L81) were prepared. The two samples were then undergoing the previously described Hyper-CEST measurement by direct bubbling on Xe into the NMR phantom. Before and after the measurement, samples of 1 million cells were collected and stained with 7-aminoactionmycin-D (7-AAD), a fluorescent marker of DNA (λ_{ex}=488, λ_{em}=647) that can penetrate the cellular membrane only when it is compromised, therefore can be used in flow cytometry as viability dye, by measuring fluorescence on the FL-3 channel. In Fig.16 (upper part) histograms and scatter plots of the control cells (before Xe direct bubbling) showed a low percentage of the total cell population (6.02% and 6.52% for RAW 249.7 and L929 respectively) over the threshold of detection of the viability dye (FL3-H intensity 15; orange line on Fig.16).Conversely, data acquired after Xe direct bubbling (15 seconds time, see Material and Methods section), presented in Fig. 16 bottom part, showed a substantially drop in cell viability (17.4% and 22.2% of cells alive for RAW 249.7 and L929 respectively). Similarly to the previous experiment, also in this case it is possible to notice that the direct-bubbling of Xe compromises cell viability. However, the direct-bubbling method of xenon delivery can be still considered a useful method for preliminary study of a sensor on a cell line because this enables the quick screening of

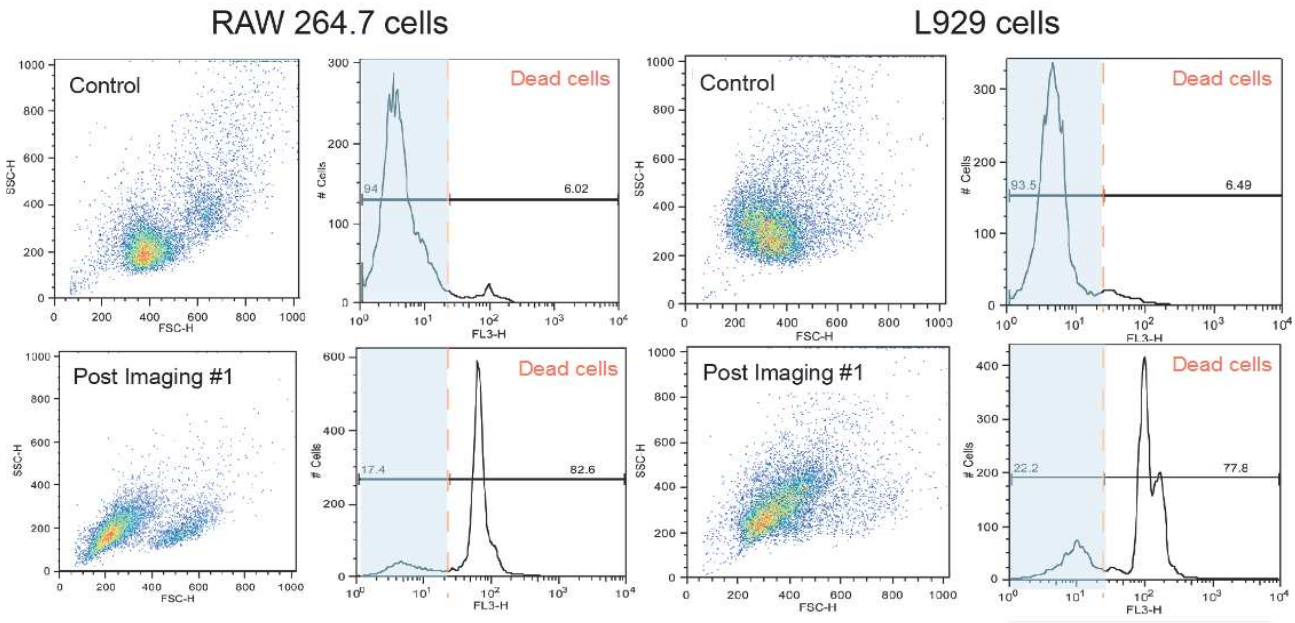

Fig. 16 Flow cytometry analysis of RAW 264.7 cells (left column) and L929 cells (right column) after XE imaging protocols in double phantom NMR bubbling chamber. Scatter plots show the cell populations at each sample time. Histograms of FL-3 fluorescence (measuring the incorporation of the DNA-binding viability dye 7-AAD) show that there is substantial cell death after running the Xe imaging protocol. From Rossella F et al, (2014) [107]

new cryptophane constructs.

A valid and safer alternative for *in cellulo* Xe-MRI is performing the indirect delivery of hp-Xe with a so called "bioreactor" (Scheme 7 details described in Klippel S et al, 2013[106]) In this system, Xe is not bubbled directly into the sample, but it is rather delivered first into a bubbling chamber sitting upstream to the sample (BC in the Scheme 7) into which flows the culture media for the cells from a medium reservoir (MR). The medium enriched with hp-Xe then finally flows into the sample phantom (SP) that contains cells encapsulated in alginate beads (for immobilization against the flow).

Similarly to the previous system, pressure, flow, temperature and oxygen content of the system were monitored by several controllers located before and after the two containers, and the flow from BC to SP was triggered by the spectrometer. For each scan the sample is perfused with Xe-saturated medium for 30-60 s at a flow rate of 7.5 mL/min.

As in the previous system, the flow to the sample was stopped before acquisition. The sample phantom was split into two compartments along the direction of the flow (Scheme 7, left part): in one part there were unlabelled cells, while the other part contains cells labelled with **2** for fluorescence and NMR detection.

Both types of cells were first encapsulated in alginate beads. The embedded cells (10^5cells/mL) were incubated with 50 μM of **2** for 20 hours. An intracellular concentration of 15 μM was estimated by measuring the fluorescence intensity in cell lysate. Figure 17 represents the Xe-MRI hyper-CEST effect in the double phantom bearing labelled and unlabelled cells. Also shown is the fluorescence imaging, acquired with a confocal microscope of the same cells.

The CEST effect has been calculated as the results of 20 on-resonant and 20 off-resonant images, even though it is possible to measure a distinguishable effect also after one single CEST acquisition. The compartment containing labelled cells could be distinguished from the other by a CEST effect of over 70%, whereas the control volume showed no significant CEST effect.

To ensure advancements compared to direct gas delivery, the cell viability has been measured using

Ethidium homodimer III (EtD-III). We estimated that over 90% of cells were alive after the measurement. The setup presented here as a “bioreactor” is a very valid system to approximate the in-vivo condition and to somewhat simulate Xe-perfusion experiments in organs.

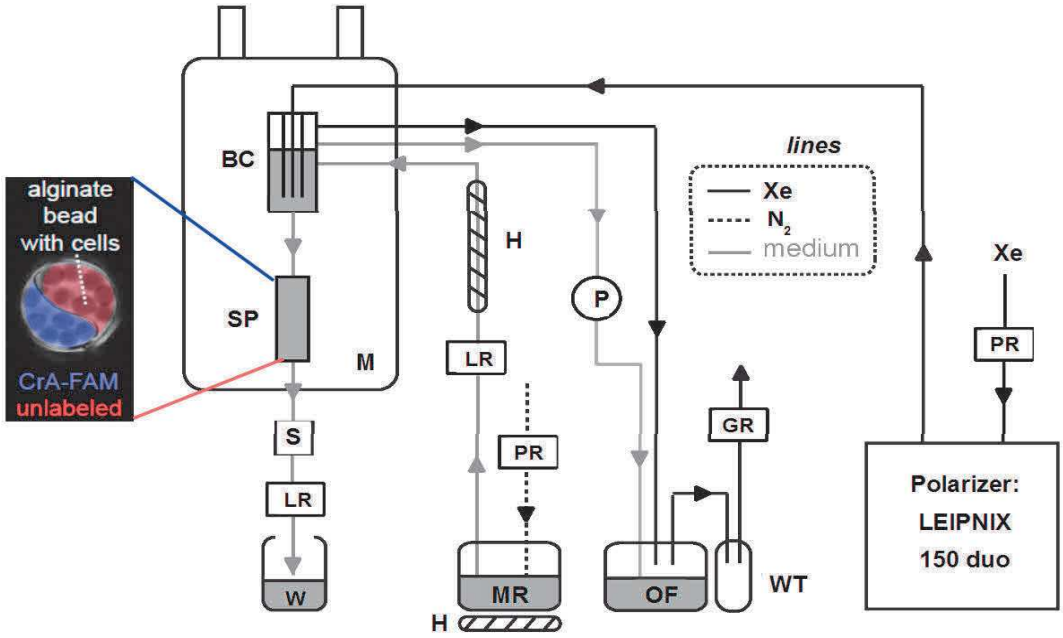

Scheme 7. Continuous flow bioreactor setup for indirect delivery of hp-Xe. Xe flows into the polarizer through a pressure regulator (PR), and leaves then to the bubbling chamber (BC). The BC receives fresh media from the media reservoir (MR), heated up by a silicon heating device (H). A liquid flow regulator is installed prior the BC. The system is equipped also with an exchange system consisted in an overflow tank (OF) and a water trap (WT), monitored by gas flow (GR) and pressure (P) regulator. The Xe-saturated medium from BC flows into the sample phantom (SP). This is divided in two parts, as shown in the picture in colour. Cells are encapsulated in alginate beads. The medium flows eventually to a waste collector (W) via sensors (S) that measure temperature, pH and oxygen pressure. From Klippel S et al, (2013)[106]

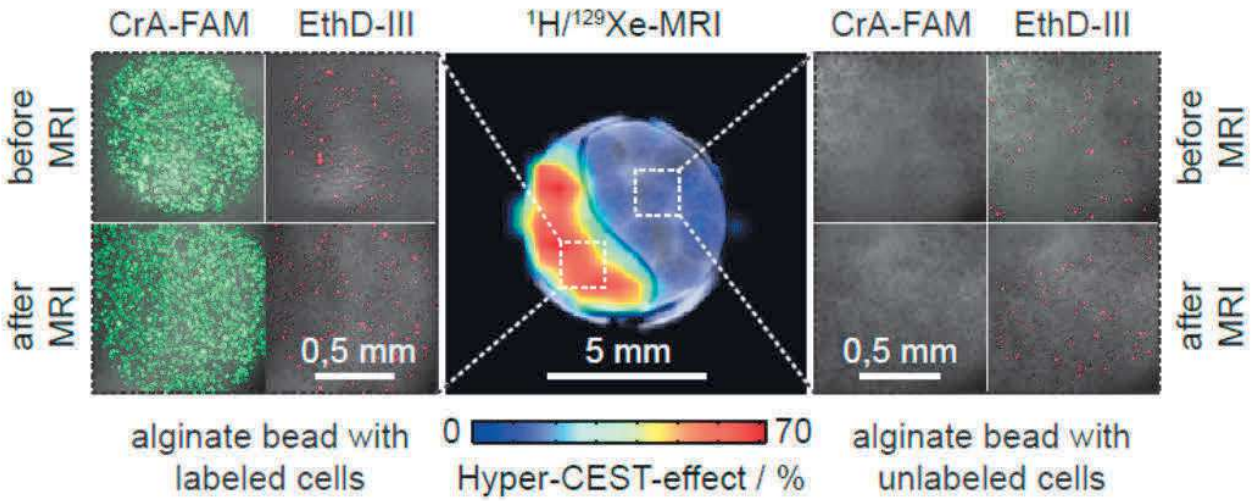

*Fig.16 Hyper-CEST effect of cells encapsulated in alginate beads (left part of centre MRI) and labelled with **2**. Confocal microscopic images of the two conditions showed that **2** was uniformly distributed in the beads (far left image). The images taken before and after MRI showed a substantially unchanged labelling and distribution. The cells were treated with EthD-III to measure the amount of dead cells. Dead cells should be coloured in red. We estimated that the amount of dead cells were around 10% in both cases. From Klippel S et al, (2013)* [106]

.

With respect to available Xe NMR signal intensity, Fig. 18 shows a comparison of the Xe-signal in solution obtained with direct-bubbling and with indirect delivery through the bioreactor. Due to comparable signal intensities we can consider both methods appropriate for study the behaviour of our sensors in cells.

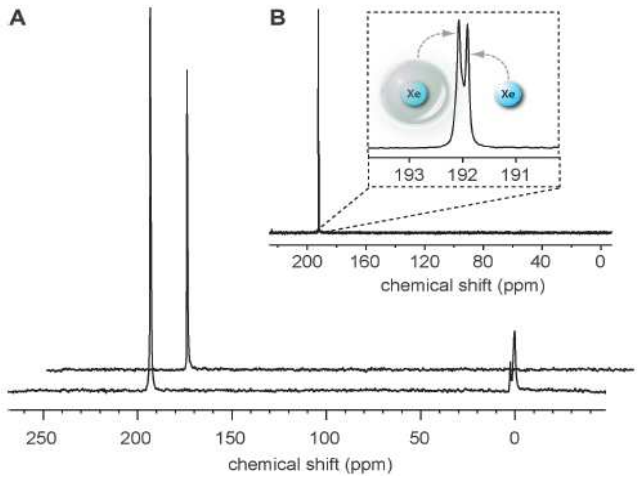

Fig.18 A. Comparison of the Xe signal achieved with direct and indirect delivery (4 scans each, 37°C).
B. In the spectrum obtained with the bioreactor, an additional peak downfield to the resonance frequency of the dissolved Xe has been detected and attributed to Xe dissolved in the hydrogel of the alginate beads. From Klippel S et al, (2013)[106]

2.5 Dual-mode cryptophane-based biosensor for the targeting of cell surface receptors (CD14)

The work done on the dual sensors and the good cell uptake and viability opens the possibility to design and test a sensor aimed for a specific cellular target. Having a dual imaging scheme is beneficial for pilot studies not only as a confirmation of the uptake or the targeting, but, more importantly, it allows to quantify the effective concentration of our sensor in the desired target prior the Xe-NMR analysis.

With regard to the MRI readout, the Cr-A read-out offers, in combination with Hyper-CEST, the great advantage of the multiplexing detection. In fact, contrary to relaxivity agents, the presence of Cr-A based sensors can unambiguously be detected thanks to their unique resonance frequency. As mentioned above, this technique is also superior to fluorescence in as much as the Xe NMR signal allows one to distinguish between cell-associated and free compounds. Thanks to the free selection of the saturation frequency during the Hyper-CEST detection, the contrast agent can also be switched on and off through the pulse sequence. This is an important feature for minimizing the possible background signal.

A suitable cellular target for an initial study should ideally be abundant and be easily reachable. For this reason, the choice of a cell membrane target was considered optimal, especially since our previous results on cells provide the possibility of discriminating the presence of free and bound sensor via the interaction with membrane material. Therefore we decided to target CD14, a glycosylphosphatidylinosil-anchored protein, which is present on the cell surface of myeloid cells.

CD14 has been reported to be overexpressed in macrophage activation, a mechanism common in many

pathologies such as atherosclerosis and in tumours.[161-162] It is therefore considered as an interesting target for diagnostics, as already shown in the case of atherosclerosis studies with proton MRI [163] and tumour-associated macrophages.[164]

Previous experiences taught us that one of the main pitfalls is the unspecific cellular uptake of the cryptophane biosensors, mainly due to the lipophilicity of the cage. This was reported both in our studies and by other groups.[84; 106] A pronounced unspecific uptake, even when the cryptophane is linked to other groups, could lead to false positives, especially if the target is in low abundance, as it is often the case. In order to minimize this problem it is ideal to have a targeting unit that is as specific as possible.We therefore decided to use an antibody as a targeting unit as the best answer to this challenge.

Commercially available monoclonal antibodies have been widely used in immunohistochemistry, enzyme-linked immunosorbent assay,[165] and molecular biology and in general in diagnostics because of their straightforward and easy labelling and their great specificity.

In the next section, the design, synthesis, fluorescence and in cells Xe-MRI response of a anti-CD14-based sensor (work lead by Dr. H.M.Rose)[108]is presented and discussed.

2.5.1 Anti-CD14 antibody based biosensors: experimental design.

The design of our dual-mode CD14 biosensor is illustrated in Scheme 8.

The sensor is composed of two parts (Scheme 8, upper part), namely an anti-CD14 antibody (“targeting module”) conjugated with avidin and three types of reporters (“read out modules”) that can be Cr-A, FAM or a branched cage construct that contains both in a fixed 1:1 ratio (see next paragraph). All of these read out modules are conjugated with biotin in order to “click” them to the reporter module via the avidin-biotin interaction. (§8.4)

Avidin is a 66-kDa glycoprotein formed by four identical subunits, each of them having a single binding site for biotin. The affinity of avidin for biotin is extremely high with a dissociation constant of 10^{-15} M.

The anti-CD14 IgG2b monoclonal antibody and the negative control, IgG2b, that does not target CD14, are conjugated with avidin through their lysine side chains. The read out modules (Fig. 19) are conjugated with biotin though acylation.

The biosensor can be applied to cells by sequential incubation (Scheme 8, *A and B*), in which cells are first incubated with the targeting module, followed by the readout modules. In the first case, the biotinylated Cr-A and FAM read outs are added to the avidin-conjugated antibody at a variable ratio, while, in the case of the “branched construct” the presence of the two read-outs is in a fixed ratio of 1:1. Alternatively the incubation can be done with the preconnected complete construct (Scheme 8, *C*).

Once the units are connected, they are incubated with high CD14 expressing cells (RAW 264.7 macrophages) or with low CD14 expressing cells (3T3 mouse fibroblasts), as control. As in the previous experiments, cells were washed and harvested after the incubation, analysed through flow cytometry and microscopy, and finally placed in the dedicated NMR double phantom to perform Xe-MRI experiments.

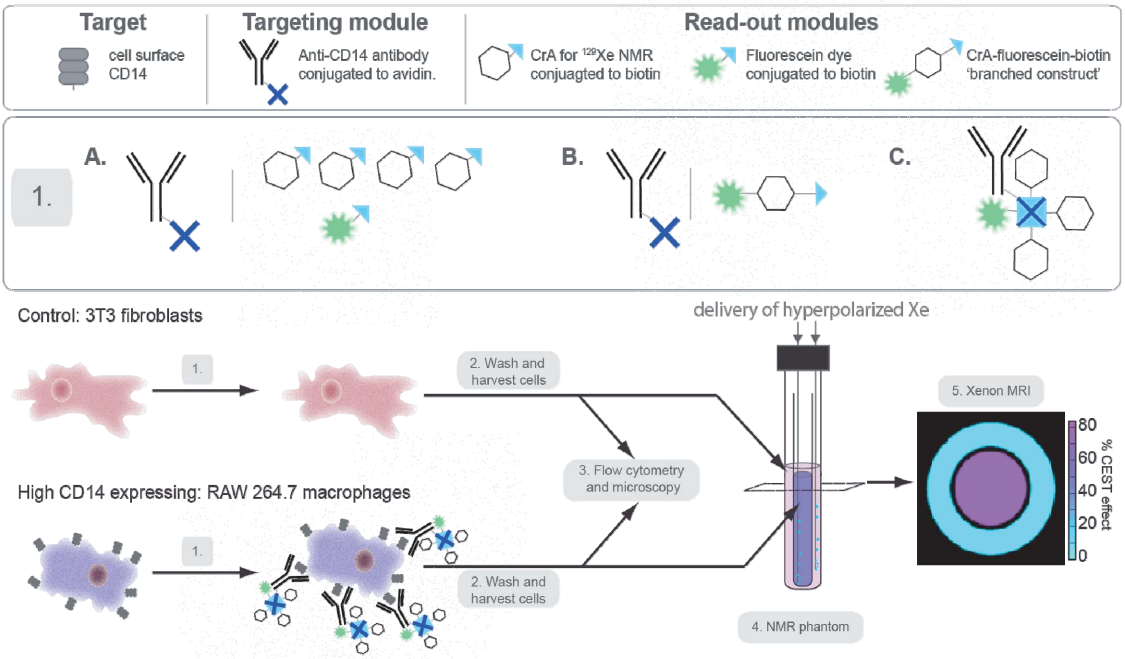

Scheme 8. Experimental design. The CD14 biosensor consists of an avidin-conjugated antibody targeting module and a set of biotin-conjugated readout modules for NMR/fluorescence. (1) The biosensor can be applied to cells by sequential incubation (A), in which cells are first incubated with the targeting module, followed by the readout modules. Alternatively the incubation can be done with the preconnected complete construct (C). The type of incubation of (B) works as well a sequential incubation, but with a construct that has both read outs in a fixed 1:1 ratio. Step 2: Cells are washed and harvested and cellular uptake, biosensor specificity and cellular localization are evaluated with fluorescence measurements (Step 3). The cell suspensions are placed into separate compartments into the NMR double phantom that ensures Xe delivery (Step 4). Step 5 Xe-MRI is represented by an illustrative cross section of the NMR double phantom containing the cells in the two conditions. From Rose HM et al, (2014)[108]

2.5.2 Synthesis of the read out modules

As mentioned in the previous paragraph, the synthesis of the CD14 sensor had to incorporate both the FAM and the Cr-A as reporter on the same sensor. The modular design allowed us to test two types of incubation: the "sequential incubation" and the "complete incubation". Scope and outcome of the two are discussed in the following paragraph.

In order to try the two scenarios, three read out modules were used as summarized in Fig. 19. The commercially available Fluorescein-Biotin (**5**) contains a FAM unit connected to biotin through a two-unit PEG spacer. Cryptophane-A-Biotin (**6**) is an in-house prepared construct, that differs from **5** just by the reporter (Cr-A) and by an additional unit of PEG, which was consider necessary to increase the solubility of the probe.

6 has been prepared with mw-assisted acylation, following the same protocol developed for **3** (§7.3).

Briefly, 0.1 M of Cr-A-ma (1 eq.) were activated with 1 eq of PyOxim and 2.5 eq of DIPEA and then coupled with the commercially available building block Biotin-PEG_3-amine (1 eq.). The acylation was carried out using microwave irradiation for 10 min at 50 °C. The reaction mixture has then been separated with RP-HPLC and quantified with MALDI-TOF. The calculated mass was m/z = 1338 for $C_{73}H_{86}N_{18}O_{18}S$.

The analysis showed m/z = 1339 (corresponding to m+1) and m/z = 1361 (corresponding to m+23, mass + Na^+) (Fig.20 A). The final yield was 48%.

The “branched construct” (**7**) was produced by connecting three parts: (i) biotin-$(PEG)_3$-amine, (ii) Cr-A diacid, and (iii) (Scheme 9),(§ 7.6).

PEG_3-FAM-amide has been synthesized in the same way as **2**, but adapting the protocol for mw-assisted SPPS. In this case, we needed to avoid having another free carboxylic group, therefore we used a resin bearing a rink amide linker instead of 2-Cl trytil, Furthermore, instead of the polystyrol support, we used the ChemMatrix® one which is reported to outperform other supports in mw-assisted synthesis. [128-129]

The yield of the initial coupling of 5 eq. of Fmoc-Gly(OH) on the resin, activated with PyOxim/DIPEA, measured through Fmoc-UV evaluation [166], was 92%, hence higher than the one reported for the mw-assisted synthesis of **4.** [107] After Fmoc deprotection, the resin was then coupled with Fmoc-Lys(5/6 FAM)-OH and finally coupled with Fmoc-AEAAA, using the same protocol used for Fmoc-Gly-OH. Prior to the cleavage for 2 hours with a mixture of TFA/TIS/H_2O (95:2.5:2.5), the last Fmoc group on the Fmoc-AEAAA was removed to have a free amino group. The cleavage mixture was precipitated in cold ether, separated with RP-HPLC and quantified with MALDI-TOF. (iii) was obtained with a final yield was 53%.

7 has been synthesized connecting (iii), the cryptophane diacid (ii), which presents two free equivalent carboxylic groups, and the commercially available (i).

We used a “one pot” protocol [167] for mw-assisted synthesis modified for the acylation, assuming that the amino groups of (iii) and (i) have the same reactivity. 1 eq. of Cr-A diacid has been activated for 2 min with 2 eq of PyOxim and 5 eq of DIPEA in order to activate both carboxyl groups. Then, the mixture was placed in a mw vial and 1 eq. of (i) and 1 eq of (iii) were added.

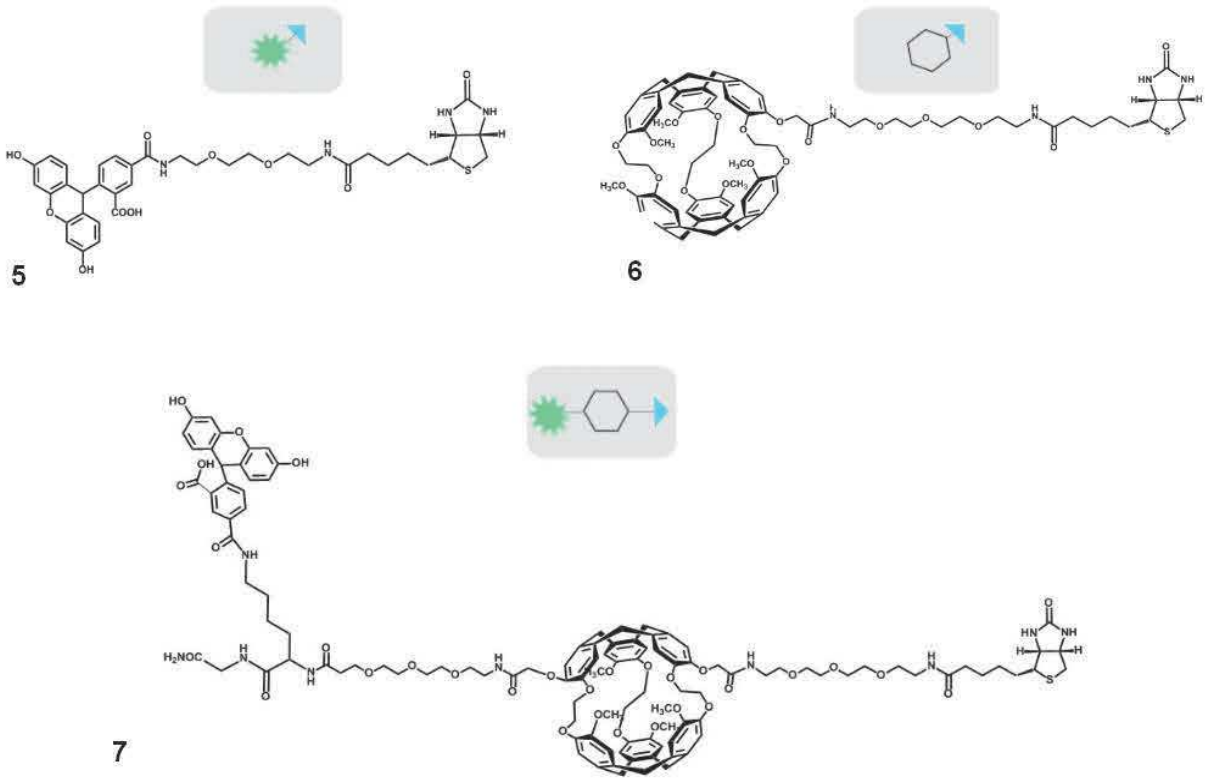

*Fig. 19 Chemical structures of the readout modules: **5** fluorescein-biotin (commercially available), **6** Cr-A-biotin (in-house produced) and **7** Cr-A (diacid)-fluorescein-biotin (in house produced). **7** have a fixed 1:1:1 ratio of Cr-A:fluorescein:biotin. This was called “branched” construct as it is based on the presence of the two carboxylic moieties of the cryptophane diacid.*

The reaction was carried out for 10 minutes, irradiating with mw at 50°C. After that, the reaction was quenched with mobile phase (30% CH_3CN in water, with 0.1% of TFA) and purified. The calculated mass was m/z = 2141 for $C_{114}H_{135}N_9O_{30}S$. MALDI-TOF analysis showed a m/z = 2164 (corresponding to m+23, mass + Na^+) (Fig.20 B).

During the analysis, traces relative to the Cr-A diacid connected with two (iii) units or of the Cr-A diacid connected with two (i) units were found, as well as some unreacted (i) or (iii). The fractions corresponding to those ones were discarded, while the fractions corresponding to CrA−fluorescein−biotin were lyophilized, and the final yield was 10%. Although the yield is low, we consider this type of reaction as a good compromise, being that subsequent steps of protection of the carboxyl/amino units and purification would lead to a similar or bigger loss of yield.

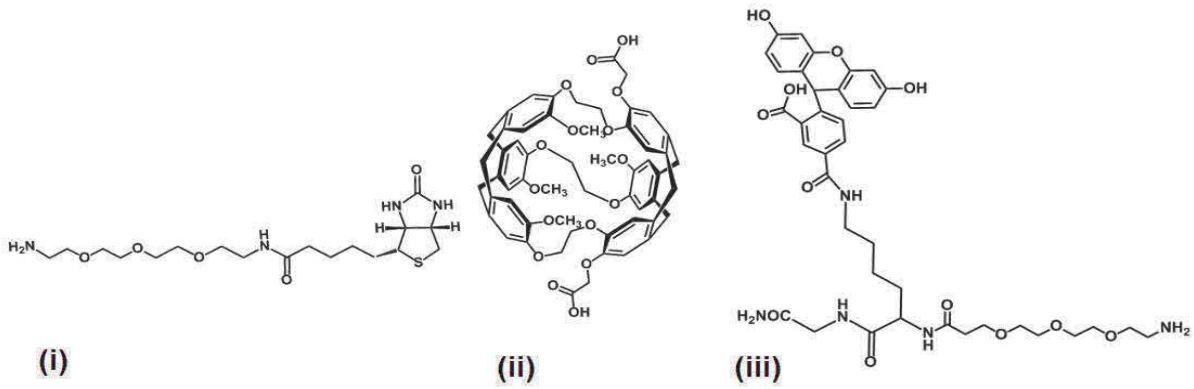

*Scheme 9: Chemical structure of the three parts that compose the "branched construct" **7**. (i) PEG3-Biotin (ii) Cr-A diacid (iii) PEG3-Lys (5,6 FAM)-amide.*

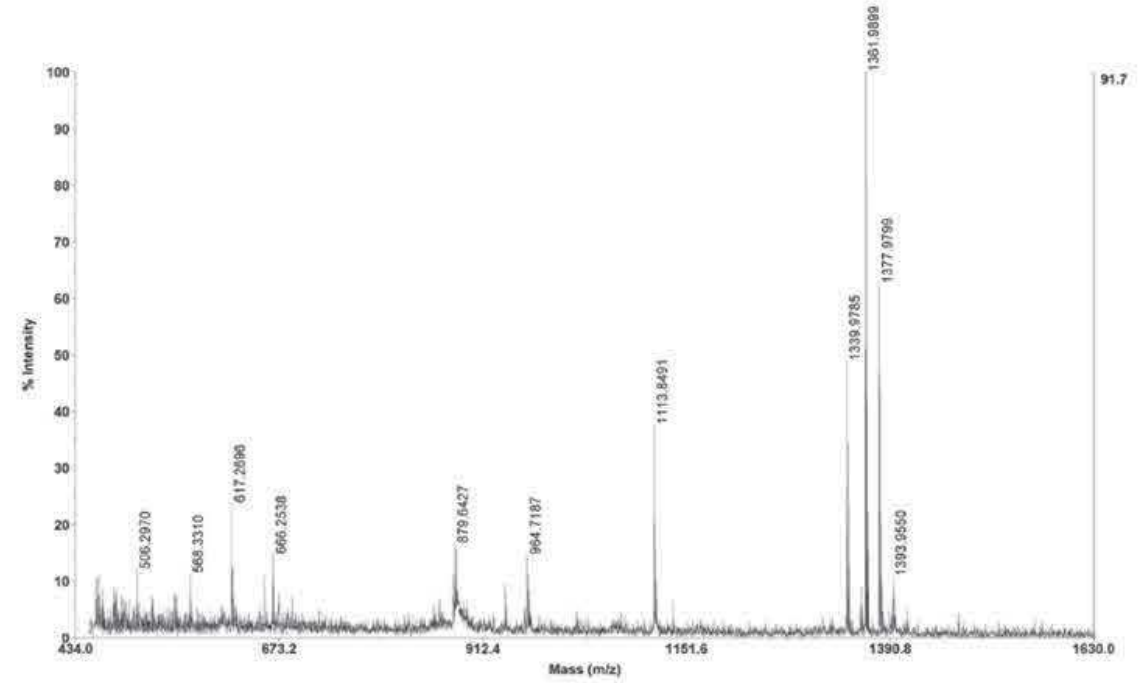

a)

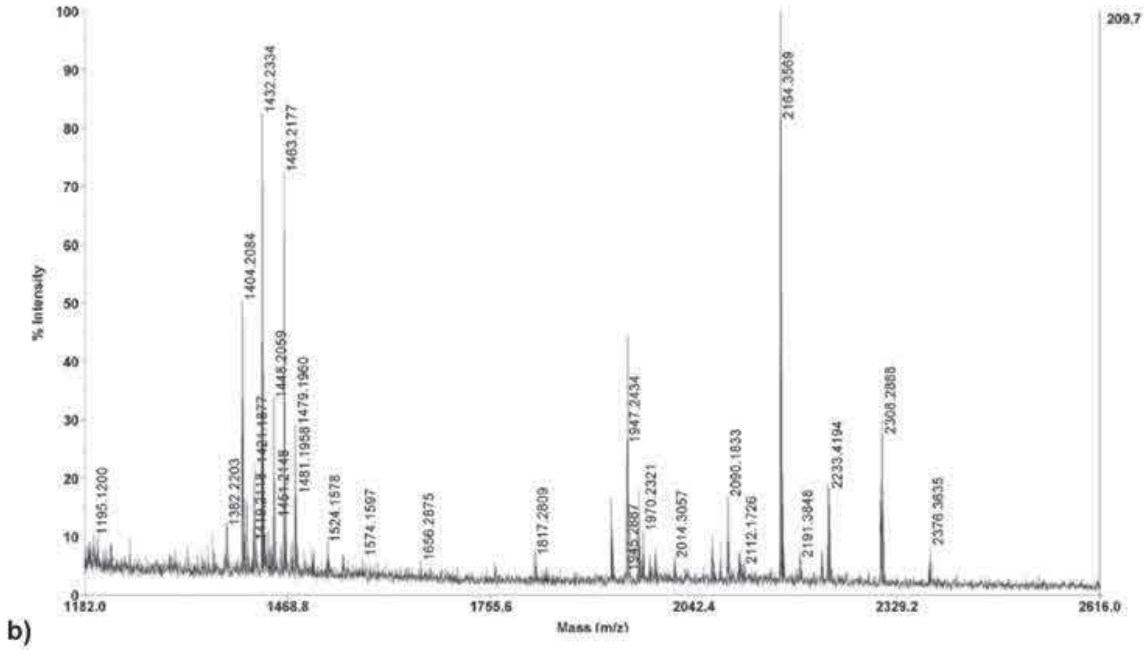

b)

*Fig. 20 MALDI-TOF mass spectrometry analysis of the two custom synthesized cryptophane-A read-out modules: a) Cr-A biotin 6 and b) Cr-A-diacid-fluorescein-biotin **7**. From Rose HR et al, (2014) [107]*

2.5.3. Comparison of the incubation mode and quantification of the sensor in the cells

The versatile and modular design of the CD14 sensor allowed three different cells incubation modalities: the sequential incubation (Fig. 21a), the incubation with the "branched construct" **7** (Fig. 21b) and the incubation with the complete, preconnected construct (Fig. 21c),

Figure 21 illustrates for each incubation modality the relative proton overlay Hyper-CEST effect (see Fig.21d for one raw data example) of the double phantom which contains cells that overexpress CD14 (RAW 264.7 cells, inner compartment) and cells that have a low expression of CD14 (3T3 fibroblast, outer compartment).

In all the three cases, the measurement revealed an expected CEST effect significantly higher (up to 80% vs. <20%) in the inner compartment due to the targeting of CD14 in cells. The fluorescence response for the different incubation modalities were measure with FACS and compared to each other (Fig. 21a-c, third column).

In the case of the complete construct (Fig. 21c) the read-out modules **5** and **6** were incubated first with the antibody to yield the complete sensor. In the first case (Fig.21a) the cells were initially incubated with the anti-CD14 antibody (or the control antibody) and in a second step with the read out modules **5** and **6**.

As each avidin linked to the antibody can bind a maximum of four biotins from read out modules, the increase of the signal, upon interaction with the read out modules can be from one to three-fold for either fluorescence or NMR read out.

The advantage of the sequential incubation is the customizability: since the read out modules are added after the incubation, it is possible to change their ratio, for instance to increase the signal of one reporter over the other. This of course would rely on the equal binding affinity of the two type of read out modules assured by the avidin-biotin binding. In order to investigate the linearity of the response upon changing the ratio of **5** and **6**, a FACS experiment has been set up, in which RAW 264.7 cells, after incubation with the antibody, were incubated with known ratios of **5** and **6** and the fluorescence of FAM has been measured.

As shown in Fig. 22, the response increases linearly with the fraction of **5.** This linear behaviour means that

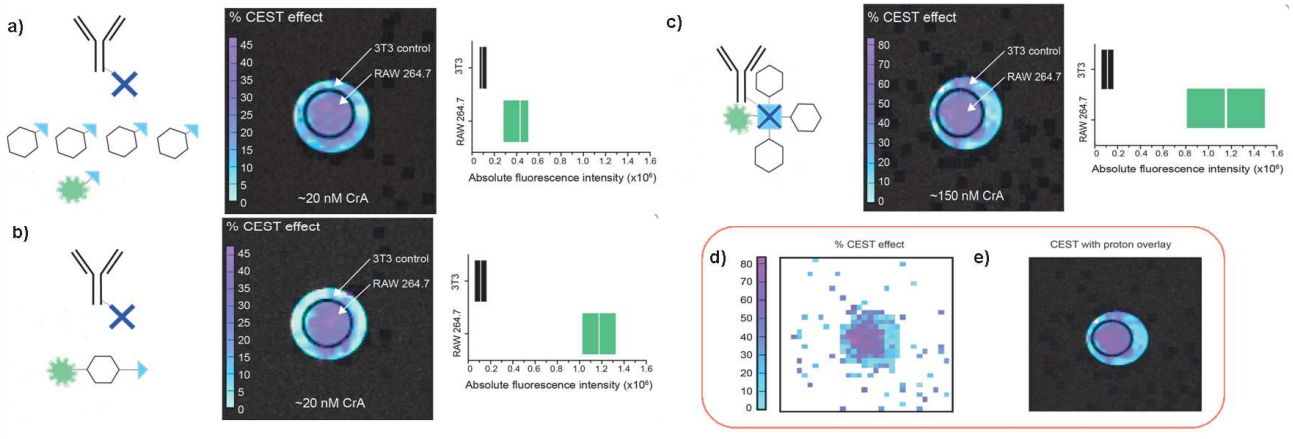

*Fig. 21 left: FACS and Hyper-CEST response of the CD14 expressing cells and controls incubated with (a) sequential incubation (b) "branched construct" **7** (c) preconnected construct.*

Fig.21 bottom: (d) Percentage of the CEST effect calculated for the double phantom which contains the high CD14 expressing cells in the inner compartment (RAW 264.7) and low expressing cells in the outer compartment (3T3). (e) representation of the CEST effect with proton overlay. From Rose HR et al, (2014) [108]

6 does not quench fluorescence of **5**. The curve presented in Fig.22 also enables to extrapolate the concentration of Cr-A present in the cells from the relative quantification of FAM once the mixing ratio of **5** and **6** is known.

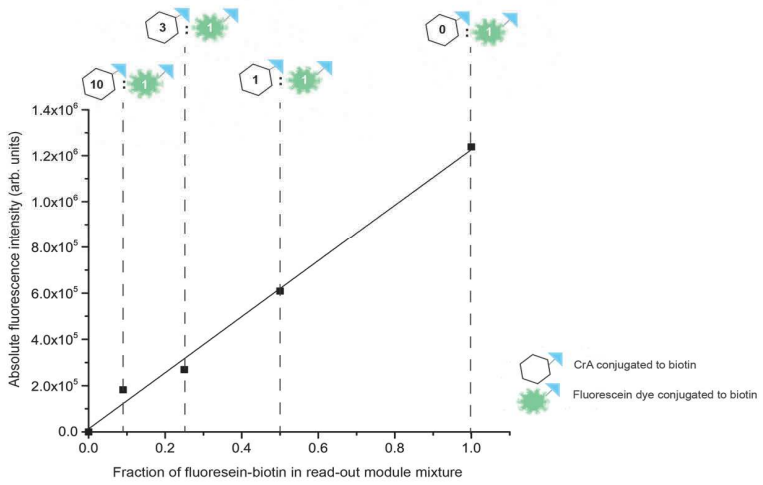

*Fig. 22 Flow cytometry analysis of sequential incubation method. RAW 264.7 cells were incubated with the antibody and in a second moment incubated with **5** and **6** in a defined ratio. Analysis of the absolute fluorescence intensity by FACS shows a linearity of the response. From Rose HM et al, (2014)* [108]

Although the fluorescence response after incubation with the complete construct was higher (compare Fig. 21c and 21a), the modular approach of the sequential method is very useful not only because it allows to change read out module composition (e.g. different fluorophores), but it would also allow to easily set up panels of avidin-conjugated antibodies for screening other potential targets without having to re-design *de novo* a biosensor.

Our alternative incubation moiety (Fig. 21b) is the "branched construct" **7** in which the two read out modules FAM and Cr-A are contained in a fixed 1:1 ratio in the same molecule. Testing the idea behind such a design

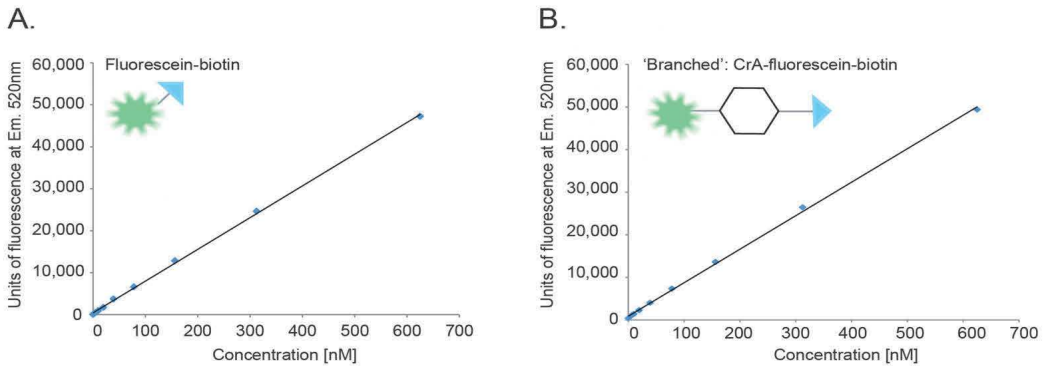

C.

RAW 264.7 cells	Fluorescence	total fluorescein concentration/well [nM]	Well volume (l)	# cells/well	fluorescein per cell (nmol)	Effective NMR (Fluorescein) concentration [nM]		Effective NMR (Cryptophane A) concentration [nM]
Sequential	1558	15	$0.15x10^{-6}$	$2 x10^{6}$	$9.9x10^{-10}$	5	x4	20
Branched	6300	69	$0.15x10^{-6}$	$2 x10^{6}$	$4.3x10^{-9}$	22	x1	22
Complete	8955	112	$0.15x10^{-6}$	$2 x10^{6}$	$7.7x10^{-9}$	38	x4	153

*Fig. 23 Quantification of Cr-A bound to target cells. (A and B) Standard curves of the fluorescence of **5** and **7**: the response practically equivalent. (C) Estimate of Cr-A concentration based on the calibration curves. In samples where the CrA:fluorescein ratio was 4:1, the calculation was adjusted accordingly from the fluorescein concentration determination. This was not necessary for the sample using the branched construct where a 1:1 ratio of CrA:fluorescein is present. From Rose HM et al, (2014)* [108]

with a straightforward quantification of Cr-A is illustrated in Fig. 23. Two calibration curves measuring the fluorescence signal of FAM has been determined for **5** and **7**. Unsurprisingly, the two read out modules (Fig. 23 A and B) have the same response. This calibration data has then being used to estimate the concentration of Cr-A in cells before the NMR experiment while taking the volume of each well and the number of cells into account. (Fig. 23 C).

Such quantification it is important to understand if the concentration of Cr-A is enough to yield sufficient Hyper-CEST contrast in the MRI experiments or if, as in the case of the sequential incubation, the ratio needs to be adjusted. The higher Cr-A concentration after "complete" incubation with respect with the other two incubation protocols (~150 nM vs. ~20 nM, see Fig. 23c) has been attributed to a more efficient incubation modality.

2.5.4 Xe-MRI double phantom experiment with the CD14 sensor

The concentration estimation of Cr-A in cells yielded values of ~20 nM for the sequential incubation.

Despite being low, this concentration was considered to be sufficient for performing the NMR experiments since it resembles realistic target concentrations in future applications (§9.5)

RAW 264.7 and 3T3 cells were incubated with the anti-CD14 antibody or with the negative control (IgG).

In a second step, the two read out modules have been added in a ratio 4:1 Cr-A: fluorescein.

The absolute fluorescence measured in the two cell population with FACS (Fig. 24 A) indicated that discrimination between the two populations should be possible with our construct(s). The 3T3 cells and/or the RAW 264.7 cells treated with the control IgG do not show any fluorescence, as expected. When treated with the anti-CD14 antibody, our completed sensor can be easily localized on the cell surface (in green; in red the Hoechst nucleus stain, Fig. 24 B).

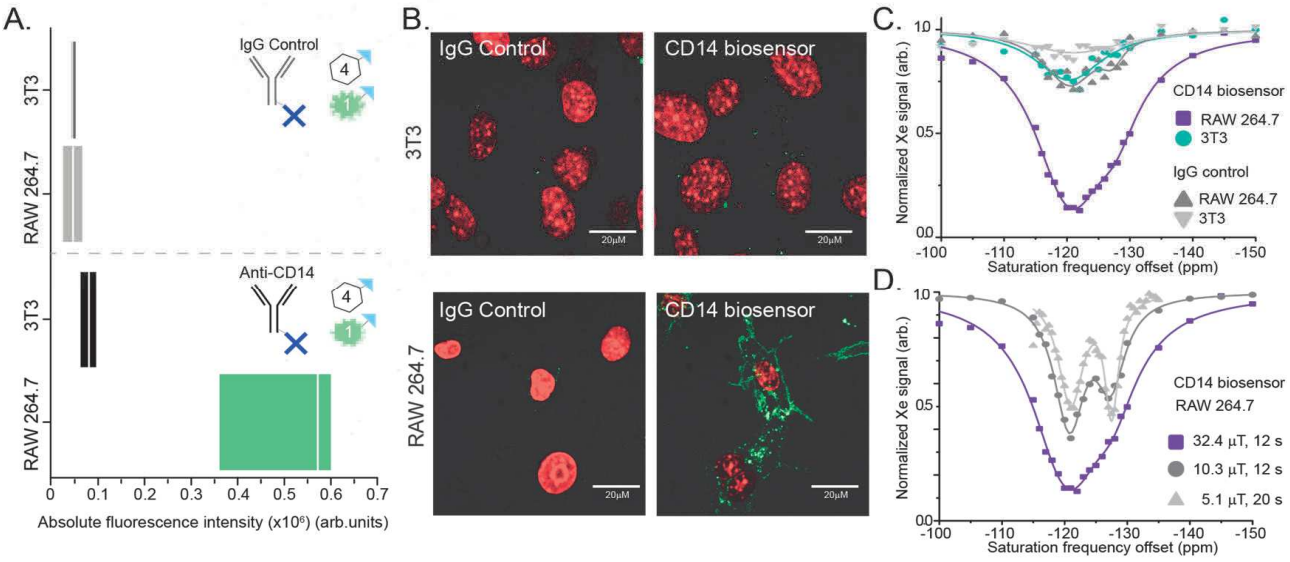

Fig 24 (A) The absolute fluorescence evaluated by flow cytometry shows the specificity of the CD14 sensor in targeting RAW 264.7 vs. 3T3 (B) Fluorescence microscopy of the two cells lines. In green FAM,in red the nuclei stained Hoechst (C) Xenon CEST spectroscopy (using a saturation pulse of 32.4 μT for 12 s) of cells shows a specific response at the resonance frequency for CrA, confirming the specific binding to the target RAW 264.7 cell line. (D) Using low-power saturation pulses (of 32.4 μT for 12 s, 10.3 μT for 12 s, and 5.1 μT for 20 s, respectively) we can reveal two peaks of Xe in exchange with Cr-A in the lipid environment of the cells (left dip) and of Xe in exchange with Cr-A in the aqueous environment of the cells. From Rose HM et al, (2014)[108]

Similarly to the FACS data, also the Hyper-CEST detection (Fig. 24C) showed no response from both cells when treated with the control IgG. As expected, it also yielded a non-significant response from 3T3 cells treated with anti-CD14 and a clearly responsive dip in the case of RAW 264.7 treated with the anti-CD14 antibody.
When the saturation power was carefully reduced (Fig. 24D), the signal from RAW 264.7 cells was further identified as the superimposition of two peaks. This result is similar to what has been shown in Fig. 2 and in Fig. 13, and was attributed respectively to the Xe in exchange with Cr-A in the lipid environment of the cells (left dip) and to the Xe in exchange with Cr-A in the aqueous environment of the cells. Both peaks were attributed to the cellular uptake at the end of the incubation, as cells were washed carefully before the measurement and therefore all the unbound read out module **6** has been cleared.

2.6 Conclusion and outlook

The results presented in this section are a very important preliminary work for the design of Xe-based biosensors. Through this work, we learned that Cr-A can label cells and is sufficiently internalized in the nanomolar range. An unwanted signal from unspecific uptake is still detectable but significantly lower than for sensor incubation on target cells.
We learned that having a fluorescent and quantifiable read-out module is a useful prerequisite to plan efficiently the NMR experiment. In fact the results from fluorescence analysis allow for mock-up experiments with single Cr-A moiety **1** to adjust for optimum MRI parameters after its concentration has been determined for a specific protocol with respect to time and concentration for the incubation and satisfying cell viability.
Our work on the sensor design and synthesis from certain building blocks give enough experience in handling Cr-A in a modular platform to design further constructs that present the desired characteristics, such as solubility, biocompatibility, and so on. The mw-assisted peptide synthesis reveals to be a very efficient technique to test and optimize synthesis and make it more economical in terms of saving time and reaction solvents.
The work done on direct and indirect delivery of Xe in the cells was a very important step to advance towards new types of experiments under more physiological conditions. Using this setup, a careful optimization of the Hyper-CEST parameters could successfully be implemented to reveal the presence of Cr-A in different chemical environment of the cells. This can be exploited to study in a very sensitive way the performance of sensors in cell experiments.
Our work with the antibody-based sensor showed all the anticipated potential of specificity and sensitivity of the NMR technique. Furthermore, the modular design makes this approach ideal to study new cellular targets. The contrast was provided by the interaction of the sensor with the target, which is obviously extremely specific in the case of an antibody. With the idea to work on an in vivo system, antibodies often represent a problem in clearance and, more importantly, can provide only information concerning the localisation and quantity, but not on the activity of a receptor or an enzyme. In order to incorporate this aspect of functional imaging, we also started working on targeting enzyme activity with smaller, cleavable molecules that can be more easily functionalized (for instance with CPPs if the target is intracellular) and can provide information on the activity of a certain molecular target. This approach will be discussed in the following chapter.

Chapter 3

Matrix metalloproteinases-an overview

Matrix metalloproteinases (MMPs) are a large family of Zn-containing, Ca-dependent, proteolytic enzymes. MMPs are able to degrade extracellular matrix (ECM) proteins, such as collagen, proteoglycan, laminin, and fibronectin, and thus are involved in connective tissue remodeling both in physiological and pathological processes. [168-170] However, recent substrate identification studies show that MMPs are also involved in the release of chemokines, cytokines, growth factors and antibiotic peptides. This suggests a participation of MMPs in several key processes such as adaptive and innate immunity, inflammation, angiogenesis, bone remodeling and tissue growth. [171-173]

At the current state of the art, twenty-three different types of MMPs have been described in humans, both membrane-anchored and membrane secreted. Although they have been identified mainly in the extracellular environment, at least three of them (MMP-1, MMP-2 and MMP-11) have been localized also in the intracellular environment. [174]

MMPs are divided into subfamilies (Fig.1a) according to their presented domains, modules and motifs.

As shown in Fig.1 (top), a typical MMP consists of:

- a propeptide or prodomain containing the “cystein switch”;
- a catalytic domain containing Zn^{2+};
- a linker of variable length (called also “hinge region”);
- a hemopexin (Hpx) domain.

MMP-7 and MMP-26 are the only two that lack both the linker and the Hpx domain. All the other MMPs (see Fig.1B) have Hpx domain and a hinge region. Furthermore, some MMPs present additional features, such as a furin cleavage site (MMP-11, -21, -28), or type II fibronectin repeats (MMP-2 and -9). The hinge region in MMP-9 is different than the other MMPs because it is highly O-glycosylated.

Two groups of MMPs are membrane-anchored and present a transmembrane domain and a cytoplasmic tail: a type-I transmembrane domain in the case of the membrane-type (MT) MMPs (MMP-14, -15, -16 and -24) and a glycosylphosphatidylinositol (GPI) moiety for the GPI-anchored ones (MMP-17, -25).

The transmembrane MMP-23 has a unique structure as it presents a cysteine-rich domain and an immunoglobulin-like domain. [174-175]

Table I shows the classification, natural substrates and the associated biological activity of MMPs. Based on the substrate preference and the domain organization, MMPs are grouped into:

- collagenases;
- gelatinases;
- stromelysin;
- matrilysins;
- membrane-type MMPs;
- and others.

In general, the presence or lack of a specific motif determines the specificity for a substrate, however there are a few exceptions. [175]

For instance, in addition to gelatin, the gelatinase MMP-2 also cleaves collagen efficiently, but is not classified as collagenase (as MMP-1,-8 and -13) because it presents a fibronectine type II motif like the other gelatinase MMP-9. [174] Another example is MMP-11: despite its structural classification as stromelysin, MMP-11 presents a furin-cleavage site and does not have the same substrates as MMP-3 and -10.

Several studies have shown that MMP-11 has a very weak proteolytic activity towards most of the ECM proteins, and its natural substrates have not yet been fully identified. [174-176]

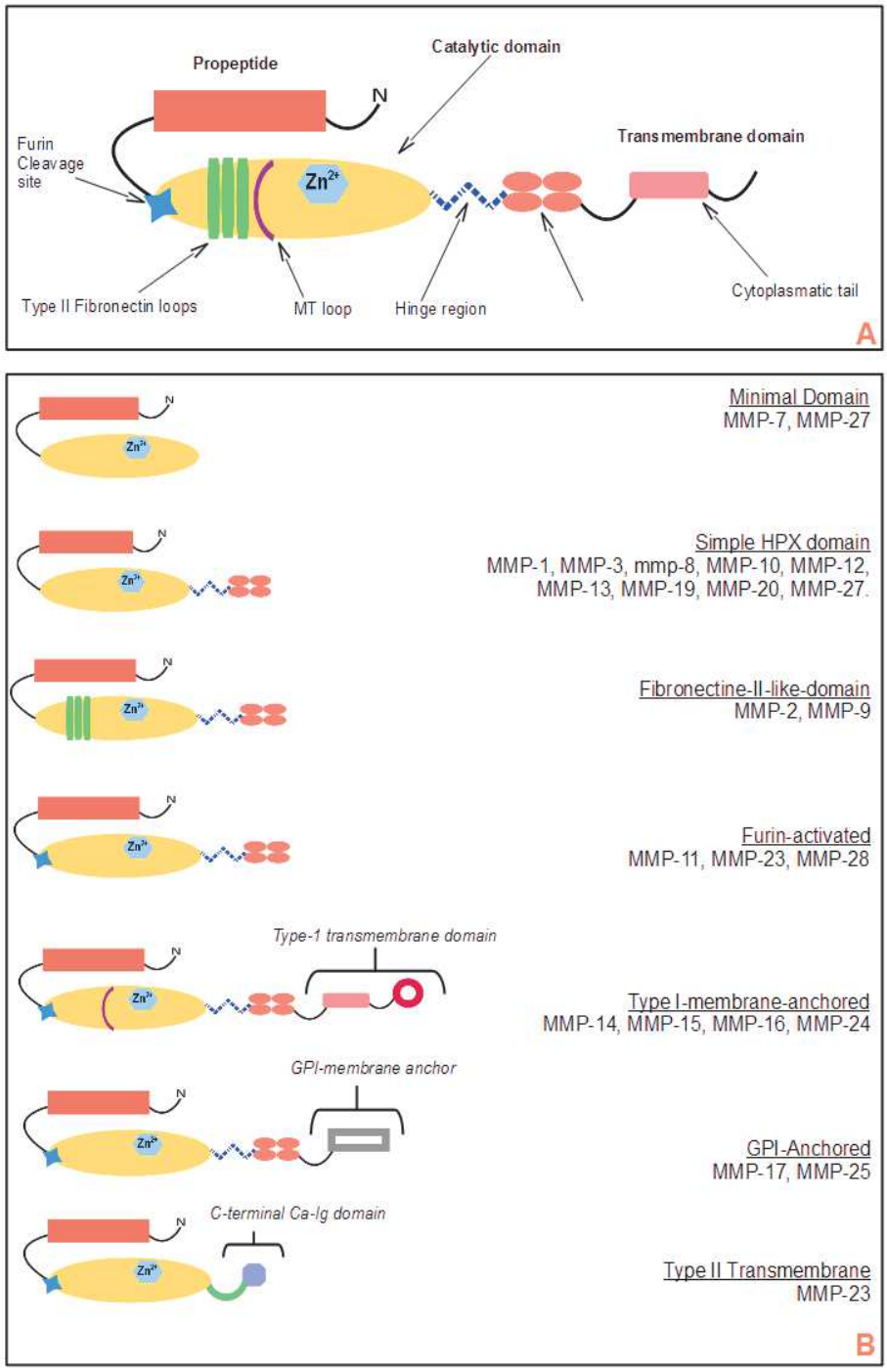

Fig.1 A Schematic of the different structure domains of the MMPs. B, subgrouping of MMPs based on their

Table I: Names and substrates of matrix metalloproteinases

MMP subfamily	Enzyme (trivial name)	MMP	Matrix substrates	Bioactive substrates
Collagenases	Collagenase 1	**MMP-1**	-Native collagen (III>I>II, VII, X) -gelatin -aggrecan -entactin -tenascin -link protein -myelin basic protein -versican	-MCP-1,3,4. -IGFBP-1, -2 -IL-1β -SDF -perlecan -Pro-TNF-α -α1-proteinase inhibitor -α1-antichymotrypsin -α2-macroglobulin -Pro-MMP-1, -2 -casein -serum amyloid A -C1q
	Collagenase 2	**MMP-8**	-Native collagen (I>II>III, VII, X) -gelatin -entactin -aggrecan -tenascin	-IGF-BP -α-1-proteinase inhibitor -MCP-1 -Pro-TNF- α -α2-macroglobulin -Pro-MMP-8 -C1q -Plasmin C1-inhibitor -angiotensin I and II -bradykinin -Substance P
	Collagenase 3	**MMP-13**	-Native collagen (II>III>I, VII, X) -gelatin -entactin -aggrecan	-MCP-3 -SDF -Pro-TNF- α -α1-antichymotrypsin -α2-macroglobulin -Pro-MMP-9,-13 -casein Factor XII
	Collagenase 4 (*Xenopus*)	**MMP-18**	-Native collagen type I, II, III -Collagen type I (rat)	
Gelatinases	Gelatinase A	**MMP-2**	-Gelatine -Native collagen I, IV, V, VII, X, XI -elastin -fibronectin -laminin-V -aggrecan -brevican -neurocan -BM-40 -decorin -vitronectin -SPARC -myelin basic protein -galectin-3	-MCP-3 -IGFBP-3.5 -Pro-IL-1β -Pro-SDF -substance P -Pro-TNF-α -α1-proteinase inhibitor -FGF-R1 -α2-macroglobulin -galectin-3 -mannose-binding lectin -big endothelin-1 -Pro-MMP-2, -1, -13 -serum amyloid A -α1-antichymotrypsin -latent TGFβ -substance P
	Gelatinase B	**MMP-9**	-Gelatine -elastin -fibronectin -laminin -SPARC -galectin-3	-PF-4 -Pro-IL-1β -SDF -Pro-TNF-α -pro-TGF-β1 -α1-proteinase inhibitor

			-aggrecan -link protection -vitronectin -myelic basic protein	-FGF-R1 -α2-macroglobulin -galectin-3 -plasminogen -pro-IL-8 -CTAP-III/NAP-2 -GRO-α -cell surface IL-2Rα -Pro-MMP-2,-9, -13 -angiotensin I and II -substance P -casein -carboxymethylated-transferrin
Stromelysins	Stromelysin 1	**MMP-3**	-Fibronectin -Perlecan -Aggrecan -Laminin -Gelatin -Vitronectin -Elastin -Non tryple helical regions of native collagen types II, III, IV, V, IX, X, XI. -Link protein -SPARC -myelic basic protein	-E-cadherin -Plasminogen -MCP-1,-2,-3,-4 -SDF -Pro-TNF-α -L-selection -Pro-HB-EGF -Pro-IL-1β -IGFBP-3 -Pro-MMP-1, -3, -7, -8, -13 -α1-proteinase inhibitor -α1-antichymotrypsin -α2-macroglobulin -carboxymethylated-transferrin -ovostatin -substance P -antithrombin III -serum amyloid A -osteopontin
	Stromelysin 2	**MMP-10**	-Gelatin types I, III, IV, V -Fibronectin -Proteoglycan -Collagens type III, IV and V -Link protein	-Transin-2 -Pro-MMP-1, -8, -10 -Casein
	Stromelysin 3	**MMP-11**	-Fibronectin(*) -Laminin(*) -Gelatine(*) (*) weak cleavage activity	-IGFBP-1 -α1-proteinase inhibitor -α2-macroglobulin
Matrilysins	Matrilysin 1	**MMP-7**	-Fibronectin -Laminin -Gelatin -Aggrecan -Entascin -Tenascin -Non helical segment of nat. collagen IV, V, IX, X, XI -Fibrin -Vitronectin -SPARC -myelin basic protein	-Pro-α-defensin -Cell surface bound FAS-L -Pro-TNF-α -E-cadherin -Syndecan-1 -Plasminogen -Decorin -Pro-MMP-1, -2, -7, -9 -α1-proteinase inhibitor -α2-macroglobulin -β4 integrin -carboxymethylated-transferrin -Casein
	Matrilysin 2	**MMP-26**	-Native type IV collagen -Gelatin -Fibronectin -Fibrin -Fibrinogen	-IGFBP-1 -Pro-MMP-9 -α1-proteinase inhibitor

			-Vitronectin	
Membrane-type (MT)- MMPs Transmembrane	MT1-MMP	**MMP-14**	-Collagen (I, II, III) -Fibronectin -γ2-subunit of laminin-5 -Syndecan-1 -Aggrecan -Vitronectin	-MP-3 -SDF -Cell surface CD44 -Cell-surface tissue transglutaminase (tTG) -Pro-TNF-α -Pro-MMP-2 -ProMMP-13 -Pro α_v integrin chain -α1-proteinase inhibitor -α2-macroglobulin -ovostatin -factor XII
	MT2-MMP	**MMP-15**	-Proteoglycan -Fibronectin -Tenascin -Entactin -Aggrecan -Perlecan	-Pro-MMP-2 -Cell surface bound tTG -Pro-TNF-α -Tissue transglutaminase
	MT3-MMP	**MMP-16**	-Native collagen type III -Fibronectin -Syndecan -Vitronectin	-Pro-MMP-2 -Cell surface bound tTG -Pro-TNF-α -Tissue transglutaminase
Membrane-type (MT)- MMPs Transmembrane	MT5-MMP	**MMP-24**	-Fibronectin -Proteoglycans -Gelatin	-Pro-MMP-2 -Tissue transglutaminase
Membrane-type MMPs GPI anchored	MT4-MMP	**MMP-17**	-Gelatin -Fibrin -Fibrinogen	-Pro-MMP-2 -Pro-TNF-α
	MT6-MMP	**MMP-25**	-Native collagen type IV -Gelatin -Fibronectin -Proteoglycans (DSPG, CSPG) -Laminin-I -Fibrin -Fibrinogen	-Pro-MMP-2 -Pro-MMP-9 -α1-proteinase inhibitor
Others	Macrophage elastase	**MMP-12**	-Elastin -Fibronectin -Laminin -Proteoglycan -Fibrin -Fibrinogen -Osteonectin -Myelin basic protein	-Pro-TNF-α -α1-proteinase inhibitor -Plasminogen -Factor XII -casein
		MMP-19	-Entacyn -Tenascin -COMP -Aggrecan -Gelatin -Fibronectin -Laminin -Fibrin -Fibrinogen	-Pro-MMP-19
	Enamelysin	**MMP-20**	-Amelogenin -COMP -Aggrecan	-Pro-MMP-20
	XMMP (Xenopus)	**MMP-21**	-Gelatin	-casein
	CA-MMP	**MMP-23**	-Gelatin	

	CMMP (Gallus)	**MMP-27**	-	-casein -pro-MMP-27
	Epilysin	**MMP-28**		-casein

From: Overall CM (2002)[177], Visse R and Nagase H (2003)[171]; Klein T and Bischoff R, (2010) [178]; Nagase H et al, (2006)[174]

3.1 Structures, substrate interaction, activation, and inhibition of MMPs.

The structure of the different domains of the MMPs has been revealed through NMR spectroscopy and X-ray crystallography. [168;170; 179]

The catalytic domain consists of five stranded β-sheets, three α-helices and connective loops. It contains two zinc atoms (one catalytic and one structural), and up to three calcium ions, which stabilize the structure. [170;174] The catalytic Zn^{2+} is additionally linked to a water molecule.[171; 180]

When a substrate interacts with the catalytic site (Fig.2), the carbonyl group of the substrate interacts with the Zn^{2+}, displacing the water molecule. The hydrolysis is performed through a nucleophilic attack of the water molecule on the carbonyl carbon of the peptide bond, using the Gln as base. [170-171]

The pocket to the right of the Zn^{2+} active-site is called "specificity pocket" or S_1'. It is usually a deep, hydrophobic pocket; in fact most of MMPs' substrates contain a hydrophobic amino acid (usually Leu) in the correspondent P_1' position. The S_1' subsite is also the docking point of most of MMPs' inhibitors. [181-182]

Despite the similarities, the size of this hydrophobic pocket is different for each MMP and it is one of the major determinants of the substrates' specificity. [177]

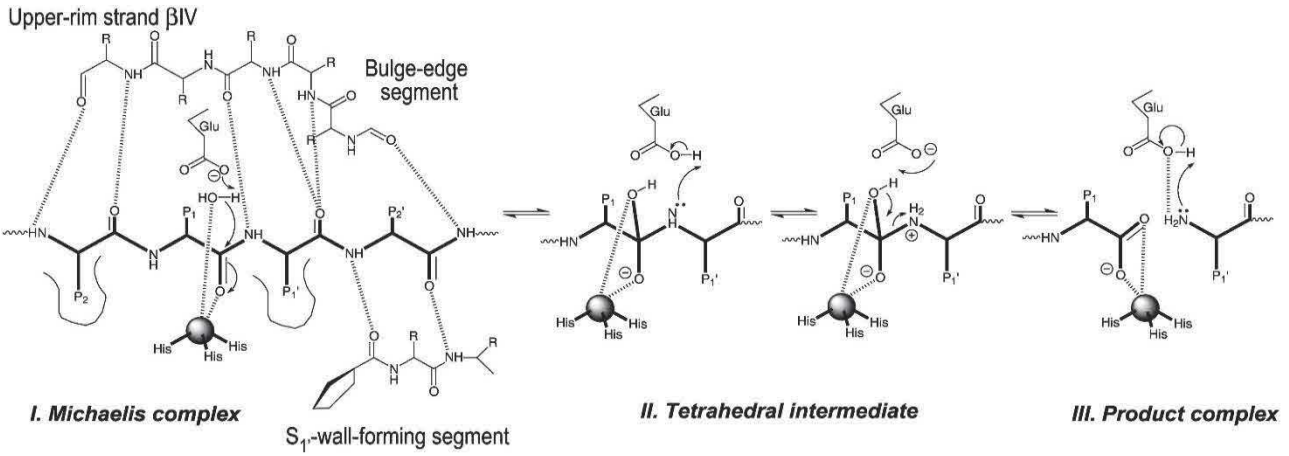

Fig. 2 Catalytic mechanism of MMPs. In the figure, the catalytic Zn2+ (grey sphere) coordinates with three imidazole groups (His).The upper rim of the catalytic site includes the bulge-edge segment, while the lower rim, other than Zn^{2+}, includes the S_1-wall forming segment. from: Tallant C et al, (2010) [180]

Most MMPs are secreted as pro-enzymes: the catalytic domain is kept inactive through a "cysteine switch", a ligand formed by the thiol group of the Cys and the active Zn^{2+}. [171; 174; 179]

As shown in Fig.3a, MMPs are activated by proteinases or by chemical agents, such as $HgCl_2$, oxidized glutathione, sodium dodecyl sulphate (SDS), chaotropic and oxydating reagents, which essentially disrupt the thiol-Zn^{2+} interaction of the "cysteine switch". Other pathways of activation have also been described: through plasmin (pro-MMP-1, -3, -7, -9, -10), serine-proteases (pro-MMP-2, -9), through already activated MMPs and MT-MMPs. [171; 180; 183]

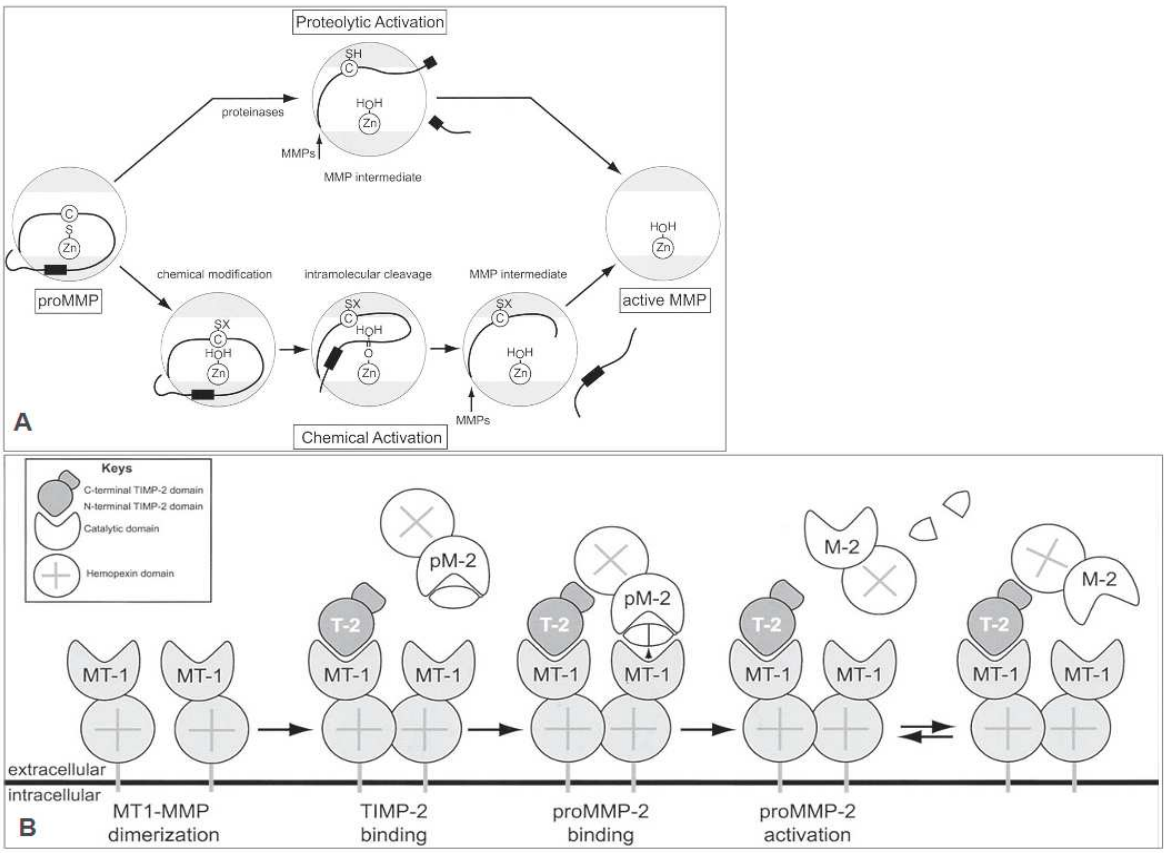

Fig.3A, left: stepwise activation mechanism of pro-MMPs. B) MT-MMP and TMP mediated activation of MMP-2. (From: Visse R and Nagase H (2003)[171]

One example of MT-MMPs-mediated activation is MMP-2 (Fig.3b).

The stepwise activation of Pro-MMP-2 consists in the binding of the tissue inhibitor of the MMP-2 (TIMP-2), to the active (dimerized) MT-MMP-1, inhibiting TIMP-2 activity. Then, pro-MMP-2 binds to the C-terminal domain of the TIMP-2 and such complex interacts with the MT-MMP-1 unit free from TIMP-2. Then, the cell surface MT-MMP-1 activates the pro-MMP-2, and the active enzyme is released. [171]

The function of MMPs is regulated genetically (through growth factors and cytokines), by cell interaction, by the activation of pro-enzymes and by endogenous inhibitors of MMPs. [178; 183]

Two types of endogenous inhibitors have been described: α_2-macroglobulin and TIMPs. The first one is a plasma glycoprotein that inhibits the proteases' activity by entrapping them into the macroglobulin, facilitating the clearing of the complex by endocytosis. TIMPs are specific inhibitors of MMPs that interact with the MMPs by bidental chelation of the catalytic Zn^{2+} at the N-terminal amino group while their C-terminus causes the expulsion of the water molecule through interaction with the Cys. [168; 174; 179]

3.2 Function and localization of MMPs: role in health and disease

For a long time, the role of MMPs was considered the degradation and remodeling of ECM molecules, [168; 171; 180] therefore they have been related to many biological processes such as embryonic development, bone growth and modeling, morphogenesis, cell migration, differentiation, apoptosis, tissue remodeling, inflammation and wound healing. [169; 184]

In more recent years, degradomics studies [173] as well as studies on gene knockout mice [169] have shown a more complex scenario, as MMPs do not only act on ECM proteins, but also modulate cytokines, growth

factors [185], and membrane-spanning proteins. [169]

Fig.4a exemplifies the old concept of MMPs as purely cytosolic ECM proteins degrading enzymes, while Fig. 4b exemplifies the new findings about MMPs' substrates and their localization, which is far more complex than what has been described before.

The great overlap of the specificity among the MMPs' endogenous substrates (see Table 1) is controlled by exosite recognition mechanisms, such as MT-MMPs and other surface receptors (integrins, CD44, membrane proteoglycans or low density lipoprotein receptor) that specifically bind certain MMPs conditioning their localization and their activities. [169; 186-187]

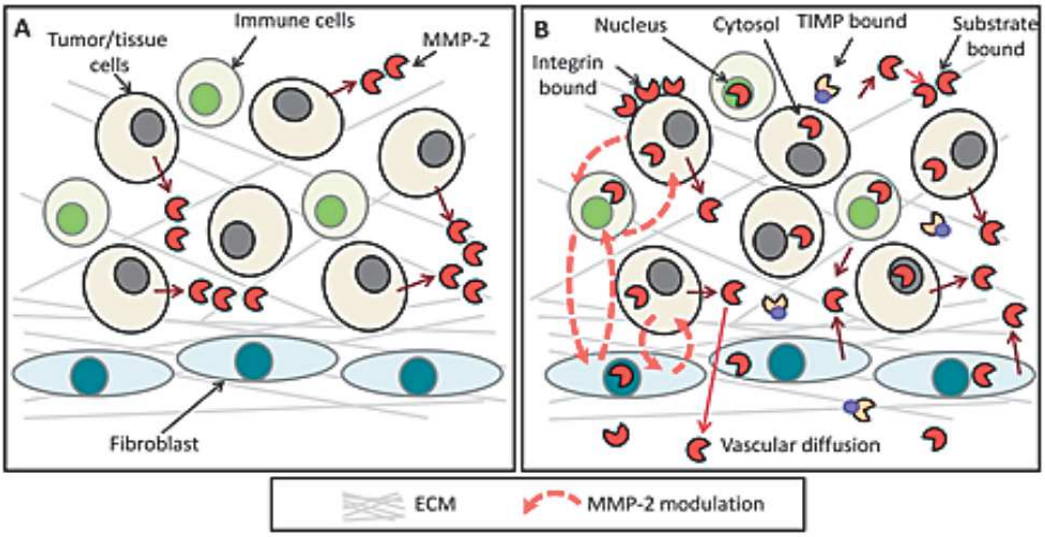

Fig. 4A and B. Schematic of localization and function of MMP-2. On the left (A) the early finding presenting MMP-2 as pericellular enzyme which degrade only ECM, on the right (B) the most modern model which reports MMP-2 as present in several compartments and regulated by different factors, such as Integrin. From Lebel L and Lepage M, (2014) [92]

In fact, although specificity profiling based on oligopeptides was showing a redundancy, degradomics studies on gelatinases, using the whole, folded protein, showed a limited overlapping, and this could be explained by their interaction with different, specific exosites which, in turn, also influences their localization and compartmentalization. [169; 173; 175; 177]

In fact, more advanced models of MMPs localization include their presence in nucleus, vesicles, and the cell surface other than in the pericellular environment. [175]

The main interest in studying MMPs as suitable biomarkers of disease or as therapeutic targets is due to the evidence that MMPs contribute to cancer progression. [188-190]

Their role was initially explained by the cleavage of key ECM proteins such as laminin V, perlecan or collagen type IV, which favors cell migration. [188] In recent years, however, animal studies have shown that MMPs' contribution to carcinogenesis is beyond the mere ECM degradation, as they affect multiple signaling pathways, as shown in Fig. 5. [189; 191]

MMPs affect growth signal pathways by modulating tumor growth factors such as TNF-α, TNF-β (MMP-2, -9), or by interacting directly or indirectly (through the cleavage of e-cadherin) with the epidermal growth factor receptor (EGDR), a pathway described in breast cancer (MMP-3). [189-191]

MMP-7 is reported to interfere with the induction of apoptosis in tumor cells through the cleavage of the Fas ligand, a key protein in the regulation of the apoptosis' cascade. [189-191]

Moreover, angiogenesis, an essential mechanism for tumor growth, is directly regulated by MMP-2, MMP-9

and MMP-14. As an example, MMP-9 promotes vasculogenesis and angiogenesis by regulating the bioavailability of the vascular endothelial growth factor (VEGF), or through cleavage of plasminogen (Plg).[192] Experimental evidence of the role of MMPs in metastasis relies on *in vitro* invasion assays and *in vivo* xenografts. The steps in which MMPs are involved are migration (cleavage of laminin V by MMP-2 and MMP-14 and of CD44 by MMP-9), disruption of cell-cell adhesion (e-cadherin cleavage by MMP-3 and -7), formation of invadopodia, and intravasation. [177]

MMP-1 and -3 are involved in the processes of inflammation and the production of cytokines which are linked to cancer progression: as an example, the monocyte chemoattractant proteins (MCP) interact with MMP-1 and MMP-3. [188; 189]

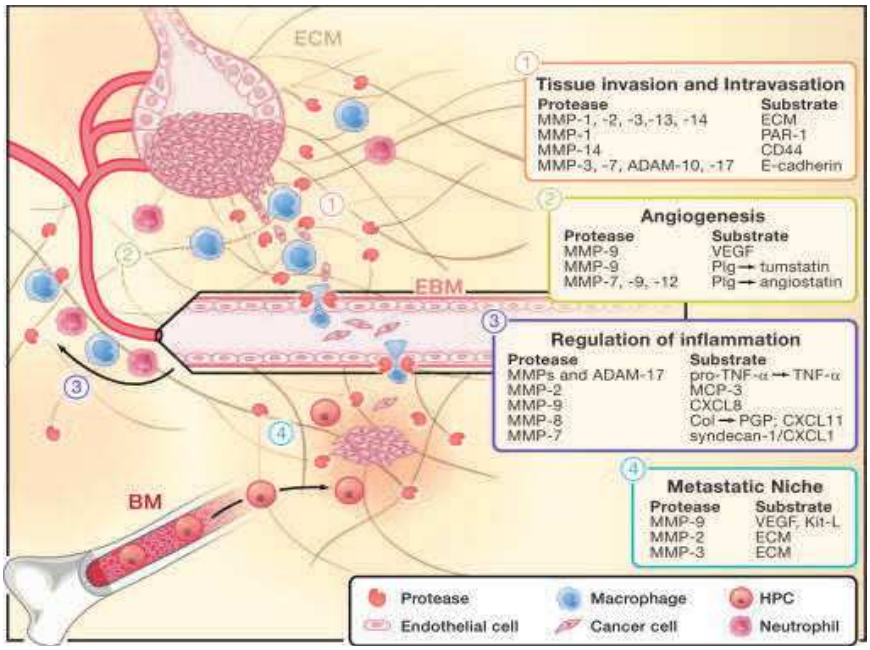

Fig.5 Schematic of the principle mechanism of cancer progression and invasion mediated by MMPs. From Kasselbrok et al, (2010)

A special mechanism in carcinogenesis has been described for MMP-11, which mediates the cross-talking between invading cancer cells and de-differentiated adipocytes, which, in turn, favor tumor survival through the recruitment of non-malignant peritumoral fibroblasts. [176]

3.3 Imaging matrix metalloproteinases in cancer and in disease

In the past 30 years, because of their previously described role in several diseases such as cancer [188; 190], as well as circulatory [171; 193-194], immunological [192] and pulmonary disease, [195] a great number of *in cellulo* and *in vivo* MMPs responsive probes have been developed. MMP-targeted probes are used for the detection of cancer cells at low concentrations, and are also utilized as tools for monitoring the therapeutic response to anticancer therapy. [196-198]

The advantages of using MMPs as molecular targets are multiple. Firstly, they are abundantly expressed in the above mentioned pathological diseases [199-201] and are predominantly secreted in the extracellular environment. They therefore do not require the probe to be internalized on cells and are active at physiological pH. Most importantly, they are catalytic enzymes, which means that they produce a signal amplification. [198]

Antibodies, inhibitors and specific synthetic peptide sequences have been used as targeting modalities. Techniques such as qPCR, zymography and immunoblotting provide information about the state of activation or quantity of a specific MMP in a tissue. [202-203] Although essential in understanding pathology and in designing an animal experiment, they do not provide information about the enzyme activity *in vivo*. For such information, imaging modalities such as optical imaging (OI), single-photon emission computed tomography (SPECT), positron emission tomography (PET) and magnetic resonance imaging (MRI) are preferred because they can combine spatial and quantitative information with an activity measurement.[92]

Some probes for SPECT and PET are based on inhibitors; although such techniques are very sensitive, the binding response requires a sufficiently high concentration of the probe at the desired target, which is not always feasible. Furthermore, some of the inhibitors are not specific enough to detect only one MMP type. [92]

Labelled monoclonal antibodies are instead very specific, but, as inhibitors, do not lead to any information about activity and, unless they are low molecular weight fragments (nanobodies), their clearance is usually problematic. [92; 198]

Synthetic peptide sequences specific for a certain MMP or a determined group of MMPs are widely used because they are very specific and easily modifiable with different payloads and read outs, which, for instance, could cause the probe to be activated or deactivated upon cleavage by the enzyme. [92]

Contrary to SPECT and PET, for which radiotracers cannot be “tuned off”, MRI and OI offer the interesting features of being modulated upon cleavage. For instance, probes carrying a fluorophore and a quencher have been used for Förster Resonance Energy Transfer (FRET) measurement: the probe would light up only upon cleavage [204-206]. Probes for OI have the advantage of being quantitative and very sensitive, but in many examples suffer from poor photo stability and the inherent limitation of the technique, i.e., the lack of penetration depth. [198; 207]

In contrast to OI, MRI, although being less sensitive than PET and SPECT, comes with great penetration depth, and, because it does not use radiotracers, is a very safe technique. Once conveniently functionalized, MRI probes allow a modulation of the signal; for instance, a whole group of MMP-2 sensors are based on a solubility switch [205; 208-209] or on self-assembling [210; 211] or on the chemical shift change of hyperpolarized Xe, like in the case of the MMP-7 biosensor developed by Wei and co-workers [81]

A very interesting group of probes are based on the intracellular accumulation of the reporter occurring after the release of a cell penetrating carrier upon cleavage like in the case of activatable cell penetrating peptides (ACPPs). [212-222] ACPPs have been used also for PET/SPECT [214; 216-217; 220] for OI [212; 215; 218-219; 221-222] and for MRI. [213]In the next section, examples of probes for the detection of particularly interesting MMPs will be described.

3.4. MMP-11 as possible early diagnostic marker

MMP-11 was isolated for the first time in the c-DNA library of breast cancer, and has been found to be overexpressed in gastric, pancreatic, ovarian, colon, prostate and skin cancer. [223-226] MMP-11 seems to be involved in cancer invasion: it is expressed not by tumor cells themselves, but in tumor stroma by fibroblast surrounding the tumor cells.

Although MMP-11 cleaves poorly the ECM proteins, it is known that it has some activity against α1-protease inhibitor, α_2-macroglobulin and the insulin-like growth factor binding protein, leading to an inhibition of apoptosis and increased tumorgenesis. [62]

The particularity of such an enzyme is also in its activation which occurs intracellularly by the Golgi-associated protease furin. [206] Those findings, and the difference from the others MMPs in the aminoacid of the S1' subsite of the catalytic unit (Glu215 instead of a conserved Leu)[228] motivated the idea that MMP-11 plays a key role in cancer progression and thus it is considered a suitable biomarker for early cancer diagnostic.
In the past years, an antibody based assay [229] and a FRET probe [206] have been developed.
This latter one was able to discriminate the MMP-11 presence in a pancreatic cancer cell line (MIA PaCa-2) from control cells.

3.5 MMP-2/9 as molecular targets

Gelatinases have been widely studied because of their overexpression in a variety of malignant tumors such as breast, brain, ovarian, colorectal, prostate, and bladder cancer as well as in haematological malignancies such as acute lymphoblastic leukemia and chronic B leukemia. [230-231] Their expression is also often associated with tumor aggressiveness and poor prognosis.
MMP-2 and MMP-9 are both secreted as inactive zymogen, and are activated by serine proteinases and through a mechanism that involves MT-MMP-1 and TIMP (see Fig.3b), or by thrombin the case of MMP-2, whereas MMP-9 is activated by plasmin, trypsin-2, MMP-2 and MMP-13. [178] Once activated, MMP-2 and MMP-9 degrade various components of ECM and non-matrix proteins (see Table I), and thus play a role in cell migration, invasion and angiogenesis through modulation of the bioavailability and bioactivity of proteinases, chemokines and adhesion receptors. [231]
MMP-2 is a 72-kDa protease, ubiquitously expressed and subject to extensive glycosylation. MMP-2 degrades collagen in the vascular basal membrane, modulating neovascularization. Furthermore, it triggers migration of cells both by direct degradation of the membrane or by allowing infiltration of cytokines and chemoattractants, in a process known as “ectodomain shedding”. [230-231]
MMP-9 is a 92-KDa protease first discovered in neutrophils. Similarly to MMP-2, it cleaves gelatin, elastin, and type IV collagen, but, unlike MMP-2, it is not able to degrade type I collagen. MMP-9 also plays a role in angiogenesis through the cleavage of the VEGF. Furthermore, it processes cytokines and chemokines (IL-1β and transforming growth factor β) in a similar manner than MMP-2. It is reported to play a role in the development of acute asthma and chronic obstructive pulmonary disease. [178]
Both MMP-2 and MMP-9 possess three fibronectin type-II-like repeats inserted in tandem just before the catalytic zinc, which confers the ability to cleave gelatin and type IV collagen. [232-233] Although the two gelatinases show very similar catalytic activity, the hinge region in MMP-9 is highly O-glycosylated [175] and this finding, together with studies on MMP-9 knock out mice, suggest that the two enzymes have different biological activities, for instance, in the process of inflammation [234] as well as in angiogenesis. [181]
However, in most synthetic peptide library screenings, MMP-2 and MMP-9 are reported to cleave, with equal efficiency, the same consensus sequences, derived by gelatine. [186; 232; 235-237]
Given their importance in pathology, several probes have been developed for the detection of MMP-2/9. Selected examples of those probes are summarized in Table II.

Table II Selected studies featuring MMP-2/9 responsive probes.

Imaging technique (reporter)	**Probe type**	**Cells lines or animal models**	**Reference**
FOI (FITC)	Poly-Lys peptide sequence:GPL*GVNGL	In cellulo: HT1080 In vivo: athymic mice HT1080 xenografts	Bremer C (2001)[238]
MRI (NPs) FOI (Cy5.5)	Inhibitor Chlorotoxin	In cellulo: 9L	Veiseh O (2005)[239]
FOI (QD)	ACPP seq: GPL*GVRG	In cellulo: HT1080	Zhang Y (2006)[204]
MRI (NPs)	Self-assembly probe GPL*GRVG	In cellulo: HT1080	Harris TJ (2006)[210]
MRI (Gd-DOTA)	Solubility switch probe Seq.: SPAYYTAA	In vivo: MC7-L1-WT tumour bearing mice	Lebel R (2008)[208] Jastrzebska B (2009)**[209]**
FOI (Cy5.5)	Inhibitor CGS27023A CGS25966	In cellulo: HT1080, BT-20, A-673	Faust A (2009) [240]
FOI (Cy5)	ACPP seq.: GAL*GLP	In cellulo: HT1080 3D cell lines in vivo: athymic mice HT1080 and PyMT mice (spontaneous tumour) xenografts	Jiang T (2004) [221] Aguilera TA (2009)[212] Olson ES (2009) [222]
PET (^{18}F) FOI (FITC)	Inhibitor Marimastat boronate	In cellulo: MDA-MB-231 In vivo: 6725 tumor bearing mice	Auf dem Keller U (2010) [241]
MRI (Gd-DOTA) and FOI (Cy5)	ACPP seq. GAL*GLP	In vivo: athymic nude mice HT1080 and PyMT mice xenografts	Olson ES (2010)[213]
MRI (Gd-DOTA) FOI (FITC)	ACPP seq.: GAL*GLP	In cellulo: SKOV-3	Zhai X (2011) [242]
MRI (Ferritin) FOI (FAM)	Self-assembly probe seq. GAL*GLP	In cellulo: HT1080	Matsumura S (2011) [243]
SPECT (^{177}Lu and ^{125}I)	ACPP seq: GAL*GLP	In cellulo: HT1080 in vivo: athymic mice HT1080 xenografts	Van Duijnhoven SM (2011) [214] Van Duijnhoven SM (2014) [217]
FOI (Cy5/Cy7)	Ratiometric ACPP seq.: GACm*GLP	In vivo: nude mice HT1080 and PyMT mice xenografts	Savarian EM (2012)[215]
FOI (Cy5.5)	Inhibitor AF485	In cellulo: HT1080, BT-20, A-673 In vivo: athymic mice HT1080 xenografts	Waschkau B (2013)[244]
NIR FOI (LS276)	Triple helical probe	In cellulo: HT1080 In vivo: athymic mice HT1080 xenografts	Akers WJ (2012)[211]
FOI (DOX)	ACPP seq.: GAL*GLP	In cellulo: HT1080 (antiproliferative assay)	Shi NQ (2012) [248]
PET/SPECT (^{64}Cu ^{123}I)	RGD-dual peptide seq.: PLG*VR	In cellulo: M21 cells	Mebrathu E (2013)[246]
PET (^{18}F)	Inhibitor arylsulphone derivative	In vivo: nude mice xenografted with U-87 MG glioblastoma	Casalini F (2013)[247]
SPECT (^{177}Lu and ^{125}I)	ACPP seq.: GAL*GLP	In vivo: Myocardiac infarction mice model xenograft	Van Duijnhoven SM (2014)[216]
FOI (Cy5)	ACPP seq.: GACm*GLP dual probe(RGD/integrin)	In vivo: PyMT mice and MDA-MB-231 tumor model mice xenografts	Crisp JL (2014)[218]

SPECT (^{111I}n)	MDAP probes sequence: GPL*GVRG	In cellulo: HT1080 In vivo: athymic mice HT1080 xenografts	Temma T (2014)[248]
MRI (NPs)	ACCP w/Angiopep-2 sequence: GAL*GLP	In cellulo: C6 and BMEC In vivo: nude mice xenografted with C6 glioma	Gao H (2014)[249]
MRI (^{19}F)	Activable ^{19}F probe sequence: GPL*GVRG	In cellulo: SCC7 cancer cells	Yue X (2014) [250]
MRI (SPION) FOI (Cy5.5)	Fluorescence quencing probe sequence: GPL*GVRG	In vivo: SCC7 xenografted mice	Jang ES (2014)[251]
FOI (DY676)	ACCP seq. GPL*GLP	In cellulo: HT1080	Tansi F (2014)[252]

Glossary

ACPP: activable cell penetration peptide

Cy5: Cyanine 5

Cy5.5: Cyanine 5.5

DOX: doxorubicin

FAM: fluorescein

FITC: fluoresceinisotiocyanate

FOI: fluorescence optical imaging

Gd-DOTA: Gd-1,4,7,10-tetraazacyclododecane-1,4,7,10-tetraacetic acid

MDAP: matrix metalloproteinase activity dependent probe

MRI: magnetic resonance imaging

NPs: Iron oxide nanoparticles

PET: positron emission tomography

QD: quantum dots

RGD: integrin binding domain

SPECT:single-photon emission computed tomography

SPION: superparamagnetic iron oxide nanoparticles

Chapter 4

Design and Xe-NMR response of a cleavable Xe-NMR biosensor

4.1 Aim of the work

In parallel with the previously mentioned work with fluorescent Xe-NMR sensors for cell labelling, we devoted our efforts to the design of a MMP-11 responsive biosensor. As already discussed MMP-11 activity could provide an important target for diagnostics based on the role of those enzymes in carcinogenesis. [176; 253-257] We were particularly interested in developing a cleavable MMP-11 Xe-NMR biosensor for which the imaging mechanism is selectively triggered through enzyme activity and for which the NMR signal is amplified by the enzyme. In fact, although successful targeting of MMPs is done through inhibitors or antibodies, such systems cannot give information about the activity and are limited to the presence of the enzyme in the cells, which is likely to be in the picomolar concentration range. [92] The proposed enzymatic cleavage/Xe-NMR response system is schematized in Fig.1. The MMP-11 sensor was designed by coupling a cryptophane unit (for Xe-NMR read-out) with a peptide which contains an MMP-11 consensus sequence (I), also called "full" or "uncleaved substrate". This uncleaved substrate is characterized by a specific signature in the Xe-NMR spectra. Upon cleavage with the enzyme (II), a new population of truncated sensors would be generated (III), also called the "cleaved substrate", which ideally is associated with a second Xe-NMR signal that is distinguishable from (I) through a chemical shift. In a first step towards demonstrating this proof of principle, the two sensors (I and III in Figure 1) were individually synthesised and the chemical shift difference between the two compounds evaluated. This same approach has been adopted by Wei et al., who synthesized a cryptophane-based MMP-7-responsive sensor. [81] The chemical shift of the cleaved and uncleaved sensor,

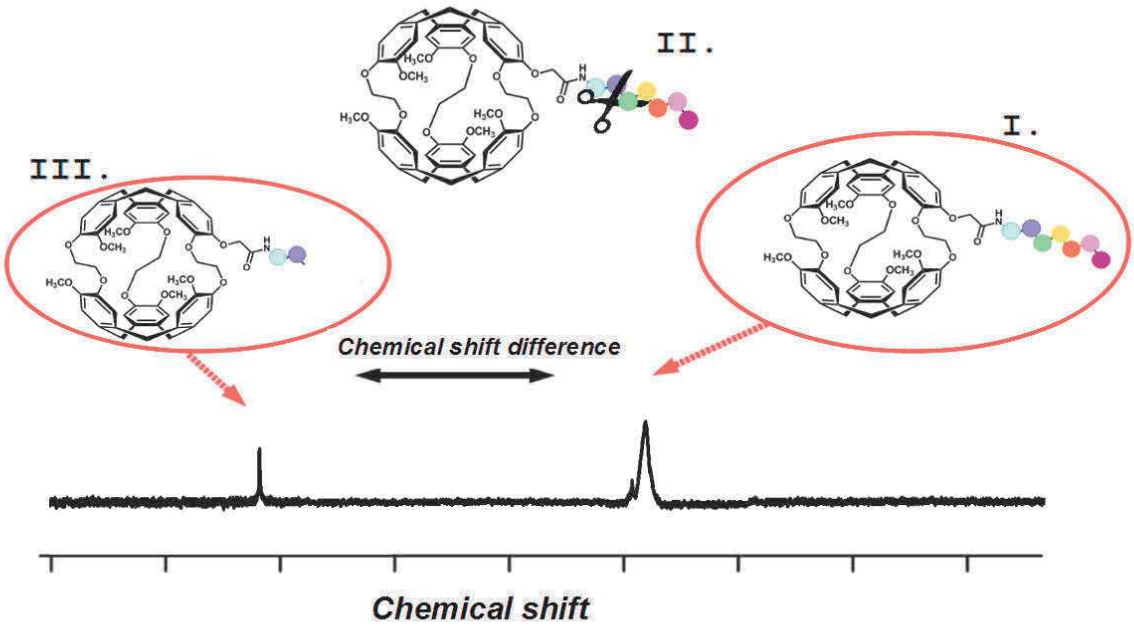

Fig 1. Schematics of the detection of the cleavage with Xe-NMR. I. Cr-A is functionalized with a peptidic sequence recognized by an enzyme: such a sensor would give a specific Xe-NMR signature. II. The sensor is cleaved by an enzyme. III. The cleaved part is characterized by a specific Xe-NMR signature which is now shifted due to the different chemical environment experienced by the Cr-A cage.

synthesized separately, was then measured with Xe-NMR and a chemical shift difference of 0.3 ppm was observed. [81]

Data in that previous study was acquired through direct detection, which is limited by sensitivity. Part of this work here is to identify whether the cleaved and uncleaved sensors can be identified and distinguished by the Hyper-CEST method, which would potentially provide far greater sensitivity of detection. Therefore, a component of the work presented here is the identification of the suitable conditions for revealing enzymatic activity through the Hyper-CEST method, especially in the case of a very small shift (such as the one demonstrated by Wei et al).

In this section, the design of the cleaved and uncleaved MMP-11 sensors, based on published MMP-11 responsive consensus sequences [227] as well as the characterisation of the Xe-NMR signature from each sensor will be described. Subsequently, a sensor presenting an alternative consensus sequence, which was made in collaboration with the group of Prof. Rademann at the FMP will be presented. For the latter sensor, a more complex design including a custom-designed PEG for improving water-solubility was made.

4.2 Synthesis and Xe-NMR response of MMP-11 responsive Cr-A biosensors

Two pairs of sensors (compounds **8**/**9** and **10**/**11**) containing consensus sequences for MMP-11 have been synthesized (Scheme 1) using standard Fmoc-SPPS followed by coupling of **1** in solution.

The consensus sequences for the pair **8**/**9** is RVL*NAA, while for **10**/**11** is MRL*EAY, both of them were individuated by a phage display study. [227] The asterisk sign (*) here marks the cleavage point of the enzyme.

The reported affinity of MMP-11 for those two sequences, was in the millimolar range (K_m of 0.705 mM and K_m of 0.207 mM for the same sequences used in,**8**/**9** and **10**/**11** respectively), while enzyme efficiency was

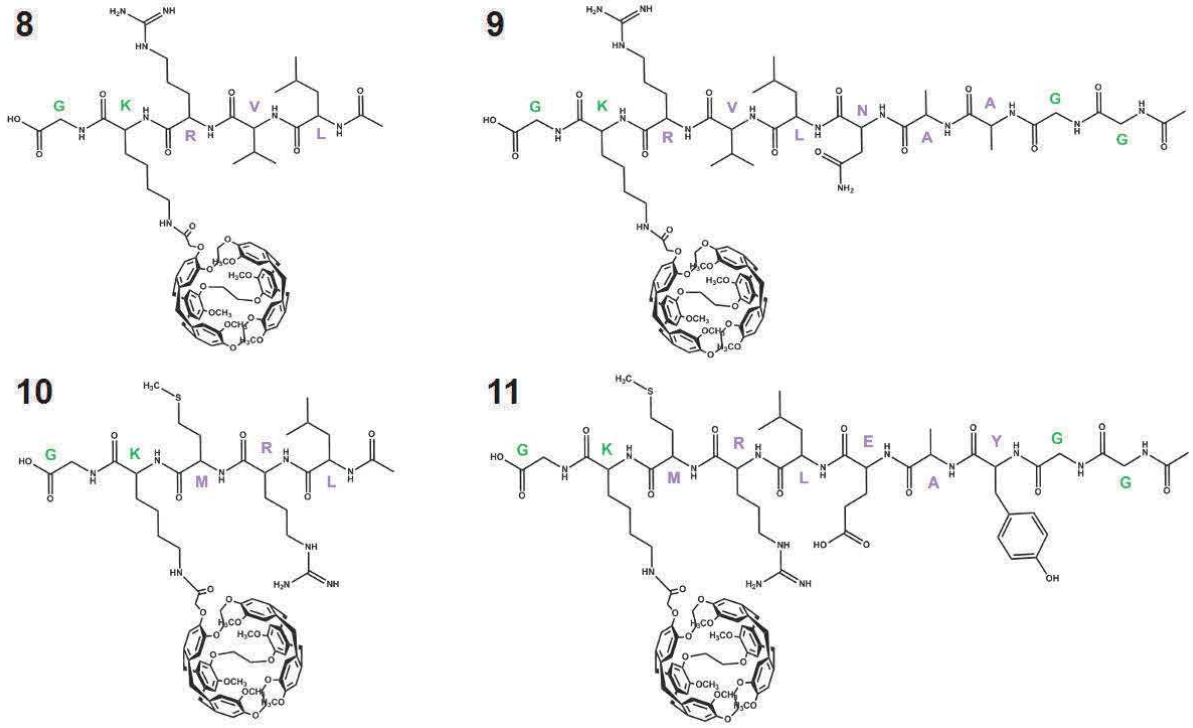

*Scheme 1. Chemical structure of the two pairs of sensors (cleaved/uncleaved) for Xe-NMR detection. 8 and 9 refer to the consensus sequence RVL*NAA, while 10 and 11 to the sequence MRL*NAA. Both sequences were taken from a phage display study. [227] Details of the synthesis are given in the Materials and Methods chapter, §7.7 and §7.8.*

as high as K_{cat}/K_m 978 $M^{-1}s^{-1}$ for the sequence used for **8/9**, while K_{cat}/K_m 2700 $M^{-1}s^{-1}$ for the sequence used for **10/11**.

The Cr-A unit was carefully incorporated to not be directly present on the cleavage sites, L*N (**9**) and L*E (**11**), to reduce the risk that it affects the selectivity of the enzyme of the peptide. [82]

The two pairs of sensors were synthesized with standard Fmoc-SPPS with a starting Gly, a triphenylmethyl (Trt)-protected Lys followed by the consensus sequence and two final Gly as spacers. Details of the synthesis are reported in §7.7 and §7.8 of the Materials and Methods section.

We used a carboxyl terminus resin in order to have one last active group for further functionalization.

Upon cleavage from the resin, the Trt group is removed from the ε-amino terminus of the Lys and it is prompted for acylation. The peptides, once purified with RP-HPLC, were finally coupled in solution with Cr-A-ma. The two MMP-11 responsive sensors were dissolved in a solution of water:DMSO 9:1 at the concentration of 70 μM for the Xe-NMR determination.

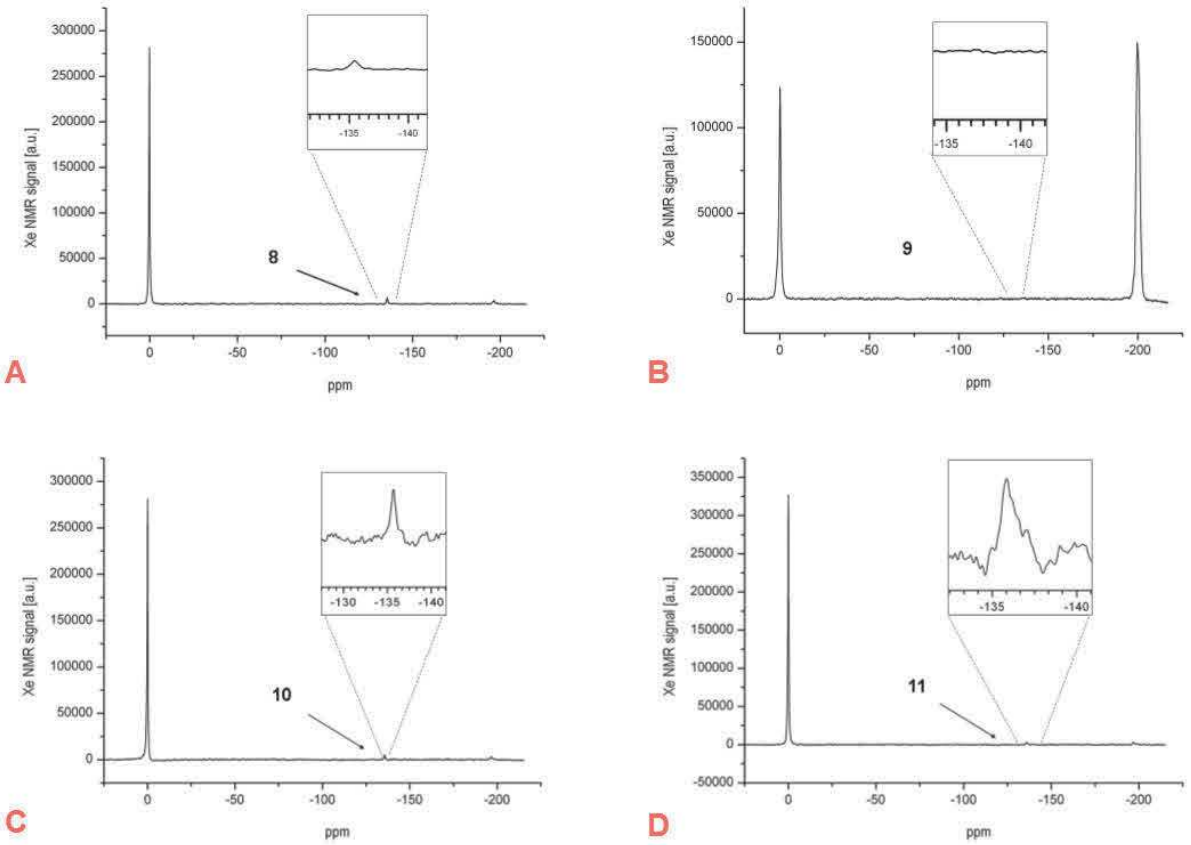

*Fig.2A-D Xe-NMR spectra of the MMP-11 responsive probes. A-B are related to the cleaved (8, -135.41 ppm) and the uncleaved (9, not identifiable due to excessive foaming as illustrated by the intense gas peak, at -200ppm) version of RVL*NAA, while C-D to the cleaved (**10**, -135.71 ppm) and uncleaved (**11**, -135.87 ppm) version of MRL*EAY. In all spectra, the peak at 0 ppm is assigned to Xe in solution.*

The results of the two pairs are presented in Fig.2 A-D. All the signals were detected around -135 ppm (with reference to Xe in solution peak, set to 0ppm). The two "uncleaved substrates" (Fig. 2A and 2C) have in general a detectable but small Xe-NMR signal by direct spectroscopy. The signal from **9** was impossible to detect due to excessive foaming of the sample during xenon bubbling. The foaming of the sample is illustrated by a high gas peak (-200pm) seen in this sample by direct spectroscopy (Fig. 2B). **10** and the paired uncleaved sensor **11** were both detectable at -135.71 ppm and -135.87 ppm, respectively.

The chemical shift difference between **10** and **11** is ~ 0.2 ppm, which is similar to what was shown by Wei and coworkers for MMP-7. [81] They gave as reasons for the difference in the chemical shift the different electrostatic environment produced by the different charge of the peptide. This would, of course, be maximized by having the Cr-A in close proximity to the cleavage site, which in return might impair the enzyme activity. We therefore decided to test another compound for larger differences in chemical shift.

4.3 Design of a "Y-shape" PEGylated MMP-11 responsive biosensor

Although we were able to reproduce a result similar to the one published, we decided to improve our sensor in terms of maximizing the chemical shift difference and improve the probe's solubility. This second approach is based on a study from 2013 in which a FRET probe for MMP-11 has been synthesized and validated by the group of Prof. Rademann. [206] Such a probe (Fig. 3) presents different features from the previous one.
Firstly, its consensus sequence is MRC(Mob)*NAA, where C(Mob) is a p-hydroxybenzil-protected cysteine. The choice of this unusual aminoacid was the result of a study by Mucha et al. (1998)[258] in which the C(Mob) residue in correspondence to the P_1' position showed better affinity for the MMP-11 catalytic site than Leu, a residue usually reported in most of MMPs' responsive sequences. Such a finding is also compatible with the known unique cleavage properties of MMP-11 which does not have usual ECM proteins as substrates. [228; 258-259] The enzyme activity for the new consensus sequence, measured with FRET through the FAM/Dabcyl pair, was higher than the ones that previously discussed (K_m of 8 μM, K_{cat} 0.073 s^{-1} K_{cat}/K_m 9160 $M^{-1}s^{-1}$).

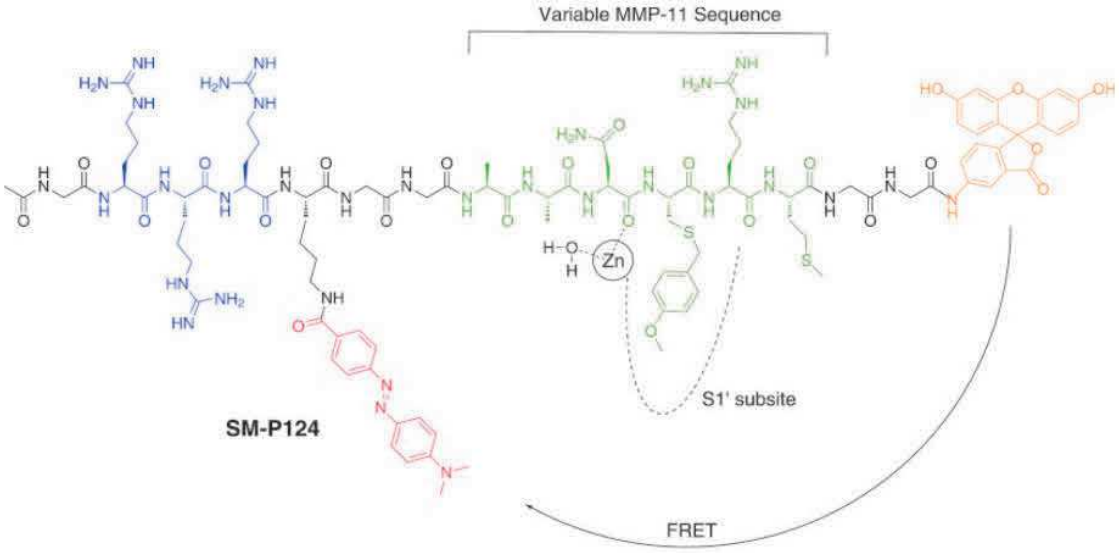

Fig.3 Chemical structure of the sensor SM-P124. The FRET pair FAM/Dabcyl is illustrated in red, the consensus sequence MC(Mob)NAA n green. The presence of the C(Mob) assures better affinity for the S1' subsite which is responsible for enzyme selectivity. In blue, the 3-Arg units for solubility. (from Meyer SB and Rademann J, 2013)[206]

The probe presents, aside from the FRET pair whose fluoresceine has already been directly incorporated on the resin [260], a $(Arg)_3$ unit as solubility enhancement unit/CPPs.
We decide therefore to change the design of our biosensors by selecting payloads that could help water solubility. Although FAM is moderately hydrophilic, its presence on the carboxyl-terminus was not beneficial since it was capping one possible charged unit. The three Arg units present were not consider sufficient to

assure water solubility; instead polyethylene glycol (PEG) units were employed to improve the solubility of this construct.

The synthesis of **12** (cleaved peptide) and **13** (uncleaved peptide), are reported in detail in the Materials and Methods (§7.9). Both **12** and **13** (Scheme 2) comprise, after the first Gly, three PEG groups to assure water solubility. Since most of the amino-acids of the consensus sequence are hydrophobic, as is the Cr-A itself, we decided to put at the end of **13** a custom-made "Y-shape" PEG group. The advantages of using such a branched PEG in comparison with a linear spacer include the fact that a branched unit will act to protect the peptide sequence from carboxy-peptidase driven proteolysis as well as reduced immunogenicity [111-112]

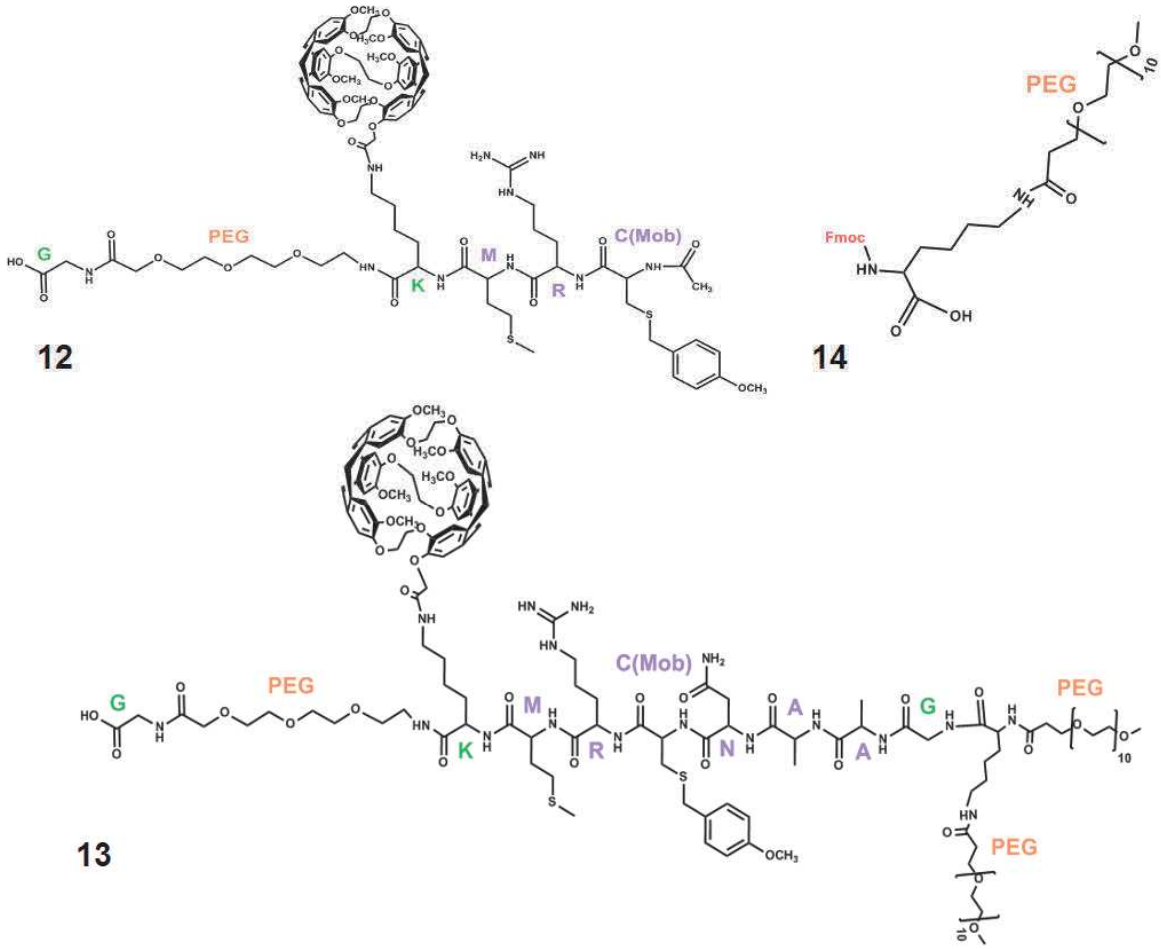

Scheme 2: Chemical structure of the PEGylated MMP-11 responsive biosensor couple (cleaved/uncleaved) ***12*** *and* ***13****.* ***13*** *presents the custom made "Y shape" PEG terminus, produced from the building block Fmoc-Lys(PEG_{10})-OH* ***14****.*

Because of the unavailability of commercially produced branched PEG modules of a defined molecular weight, we synthesized our own PEG building block (details in the Materials and Methods section). The "Y shape" construct was obtained by coupling the custom-made **14**, consisted of a Gly-Lys building block (§7.10). The Lys in **14** is Fmoc-protected on the α-terminus while a $PEG_{10}OCH_3$ was present on the ε-terminus (Scheme 2).

After coupling with another m-PEG_{10} chain to the trifunctional spacer, the desired "Y shape" construct was obtained.

Briefly, 2-Cl trityl resin was coupled with Fmoc-Gly-OH and with Fmoc-AEAAA, which carries three units of PEG. After Fmoc deprotection, a building block Fmoc-Lys(Cr-A)-OH carrying Cr-A (§2.3.1), which was previously synthesized for testing the coupling, was coupled to the resin. Using such a building block can be useful when long peptide sequences are developed as in this case. After coupling with Met, Arg and Cys(Mob), the resin has been split in two parts. One part, after Fmoc deprotection and capping by acetylation, was cleaved from the resin, resulting in probe **12**. The other part has been coupled with Asn and two Ala previous to coupling with **14**. A second m-PEG_{10} was coupled on the α-terminus once this was deprotected, and in this way the peptide was capped, and the "Y-shape" with 10-PEG units on each side was synthesized directly on resin.

After cleavage, we obtained the probe **13**, with a yield of ca. 30%. All the protecting groups on the amino-acids were removed during treatment with TFA, with the exception of the Mob group on the Cys, which, in our case, is needed to be anchored to the thiol group after cleavage. The Mob group is reported to be partially removed from Cys when percentages over 90% of TFA are used [261], therefore we decided to use an acid-sensitive resin for the synthesis (2-Cl Trytil) and a mild cleavage, using 75 % TFA. In the MALDI-TOF evaluation (reported in Materials and Methods, §6.9) no mass corresponding to the unprotected Cys residue has been found.

4.4 Hyper-CEST spectroscopy of sensors 12/13

For Xe-NMR tests (§9.6), **12** and **13** were dissolved in water:DMSO (99:1) containing 0.1% anti-foam agent (Pluronic L81) at a concentration of 100 μM. The samples were then placed individually in a tube equipped for Xe bubbling, and the Xe-NMR signature of the two was measured. The results are showed in Fig. 4 A-D.

The Xe-NMR signal of **12** was measured at -131.2 ppm (Fig. 4a), while the one of **13** at -130.1 ppm (Fig. 4b): the signal of **13** appears bigger than the one recorded for **12**. We attribute that do the fact that **12**, which has only 3-PEG units, has a limited solubility in the water/DMSO mixture, therefore the given concentration in solution might be overestimated, and the compound might be partially precipitated. Because of the presence of the branched PEG, **13** has better water solubility compared to **12**, therefore a bigger concentration is present. Fig. 4c shows a close-up of the chemical shift difference between the two probes.

With our new probes we measured a chemical shift difference of 1 ppm in the direct spectra, which is more than the double of our previous probe. The chemical shift difference between the two probes in this approach appears to be much improved with respect of the previous ones. The difference in molecular weight of **12** and **13** is 1.7 fold, while the one of **10** and **11** is 1.3 fold, which should yield comparable conditions in terms of molecular mobility reflected by the NMR line width. We can hypothesize that the presence of a sterically bulky group in one of the probes, as described for the biotin-avidin sensor by Spence et al [55-56], helps in maximizing the effect of induced changes in chemical shifts.

In order to mimic the situation of enzymatic cleavage, during which both compounds would be present in variable concentrations in the same solution, we mixed the two compounds (1:1) into the same tube performed Hyper-CEST. As showed in Fig. 4d, Using Hyper-CEST we can still accurately resolve the two compounds and the difference between the two peaks is again ca. 1 ppm. This demonstrates that with these two sensors we have the potential to measure the production of the cleaved product by the enzyme in the presence of the substrate sensor in an unambiguous way. So to further recapitulate conditions suitable for

enzymatic cleavage, the probes were again mixed in a 1:1 ratio, but dissolved in MMP-11 enzymatic reaction buffer (see Materials and Methods, §6.1.13), which contains salts, including $CaCl_2$.

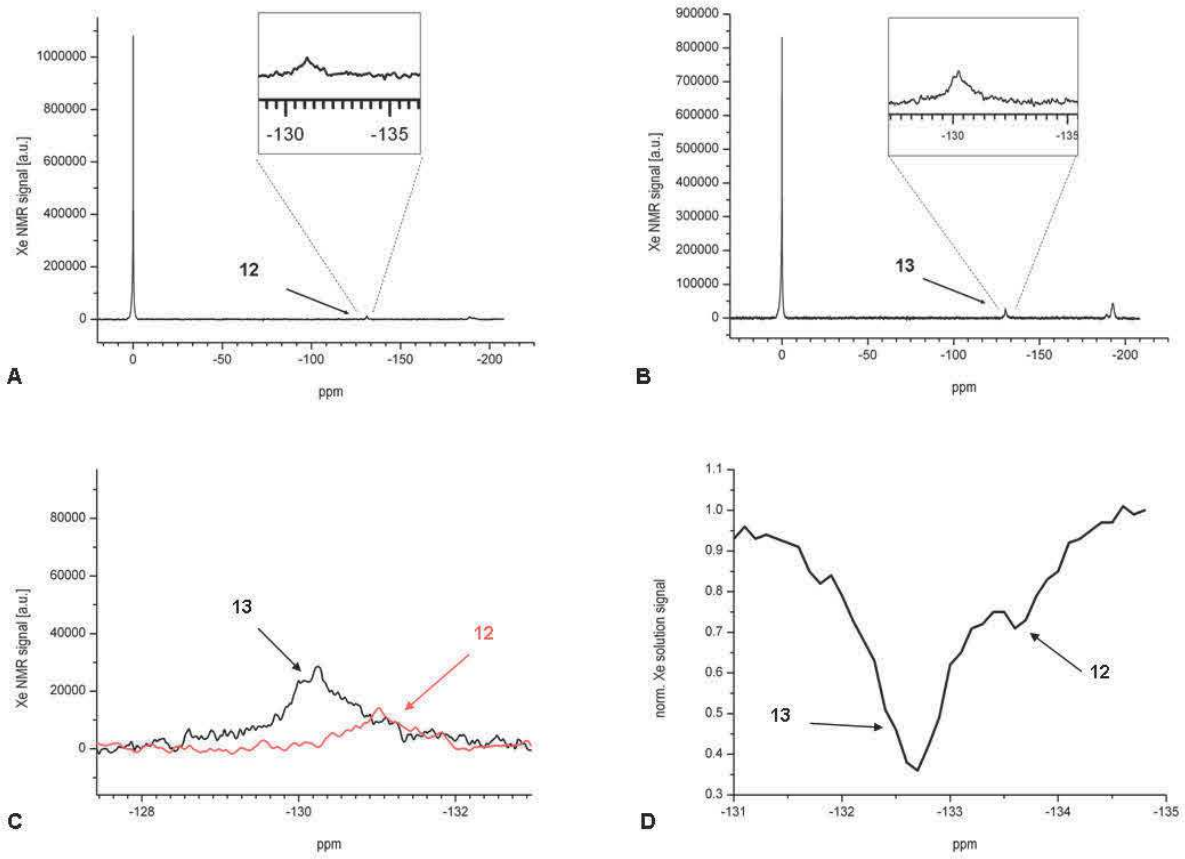

*Fig. 4 Xe-NMR spectra of the MMP-11 responsive probes. (a-b) are related to the cleaved (**12**, -131.2 ppm) and the uncleaved (**13**, -130.2 ppm). In all spectra, the peak at 0 ppm is assigned to Xe in solution. (c) close up of the difference in chemical shift of **12** and **13**, superimposing the two spectra putting at 0 ppm the Xe solution peak. A difference in chemical shift of ~ 1 ppm was measured. (d) Hyper-CEST effect of a solution of 50 µM of 12 and 13 in the same tube. Signal intensity is scaled to the height of the observed solution peak while saturating the sensor peaks. The two peaks show again a chemical shift separation of ca. 1 ppm.*

Although the two signals could be resolved in the spectra, the signal-to-noise ratio for both constructs appeared to be worse, probably due to a weaker binding of Xe to CrA in buffer, which has a bigger ion strength than water.

To test this, we systematically tested the contribution of each component of the enzymatic buffer solution on the direct spectrum of Xe in CrA. In order to do this we dissolved 100 µM of **1** in solutions water:DMSO (90:10) containing additionally only one of the buffer components, and we measured with Xe-NMR direct spectroscopy as described before. The signal of Xe@Cr-A in water:DMSO (90:10) was used as reference. Our results (Fig. 5) shows that the presence of salts lead to a signal depletion, especially in the case of $CaCl_2$ (almost 90% decrease).In fact, it has already been reported that the presence of ions such as Ca^{2+} affects the Xe-cage exchange and cage occupancy.[263] Ca^{2+} is however a fundamental co-factor of the MMPs enzyme [262], therefore, it is a necessary component of the buffer. However, Hyper-CEST has been proven to be very efficient not only in increasing the sensitivity of our detection, but also in minimize potential negative factor such as the presence of ions.

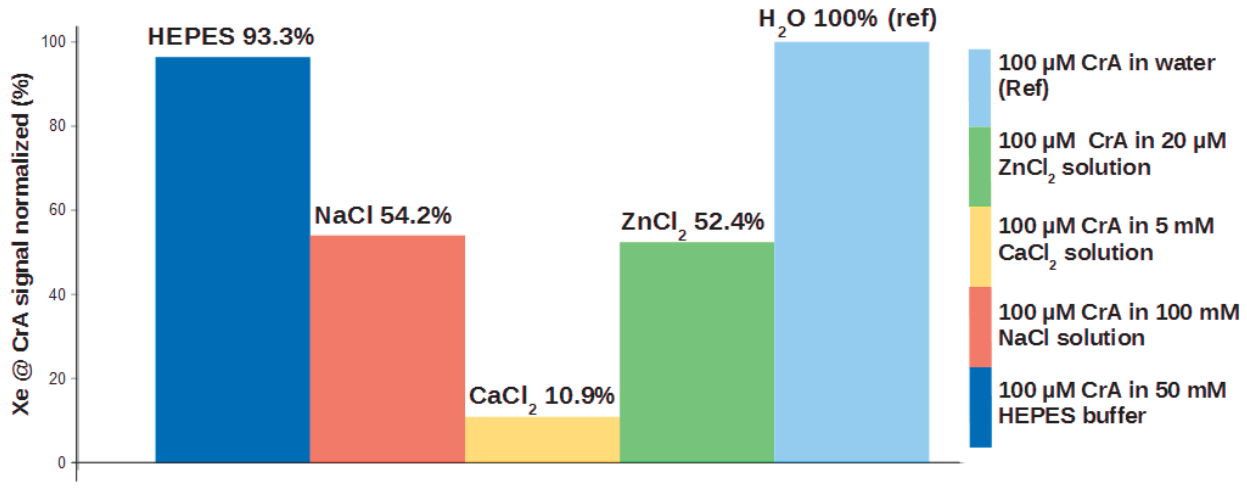

Fig. 5 Signal depletion of Xe@CrA in solution containing different salts in MMP-11 reaction buffer. The signal of Cr-A in aqueous solution (with 10% DMSO) was used as a reference.

4.5. Time course response of 13 by Xe-NMR

As our NMR reporter Cr-A is situated apart from the MMP-11 consensus sequence; we expected our probe to have the same activity as the one investigated by Meyer S and Rademann J, (2013) which used an identical consensus sequence. [206] In order to evaluate the enzymatic activity on our probe we performed a series of cleavage tests in vitro and measured the resulting products by LC/MS. The signal relative to **13** in LC/MS was revealed by a peak at the retention time 5.29 min. In the relative mass spectrum it is possible to distinguish m/z 1107 (corresponding to m+3) and 831 (corresponding to m+4). 100 µM of **13** was dissolved in the reaction buffer (see Materials and Methods) and incubated with 5 nM of the catalytic site of MMP-11. The reaction was carried out overnight, at 37°C. After that, the sample was injected in an LC-MS/MS. A second peak, corresponding to the non-acetylated version of **12** was detected at r.t. of 4.96 min, with a mass corresponding to m+3 (m/z 914). Attempts to measure the kinetic on a 3-hours scale both with Isothermal Titration Calorimetry (ITC) and with HPLC-UV failed due to the too slow enzyme kinetics.

To test the enzymatic activity on Xe-NMR, a sample containing **13** dissolved in the previous mentioned reaction buffer, in the presence of MMP-11 was prepared. The cleavage reaction was carried out over a time course ranging from 0 minutes until 48 hours, and aliquotes of the sample were collected at different data points and detected with Hyper-CEST. A plot of the different z-spectra over time is reported in Fig.7.

In the z-spectra, a second peak corresponding to the cleaved version, was detected for prolonged cleavage times (>20 hrs) and was more convincingly detectable after 48 hours of detection.

These results were confirmed by the HPLC-MS/MS measurement: we could distinguish a second peak corresponding to a cleaved product just after prolonged (>20 hrs) reaction times. However, such slow cleavage does not allow to make a dynamic measurement in Xe-NMR, which was our main interest.

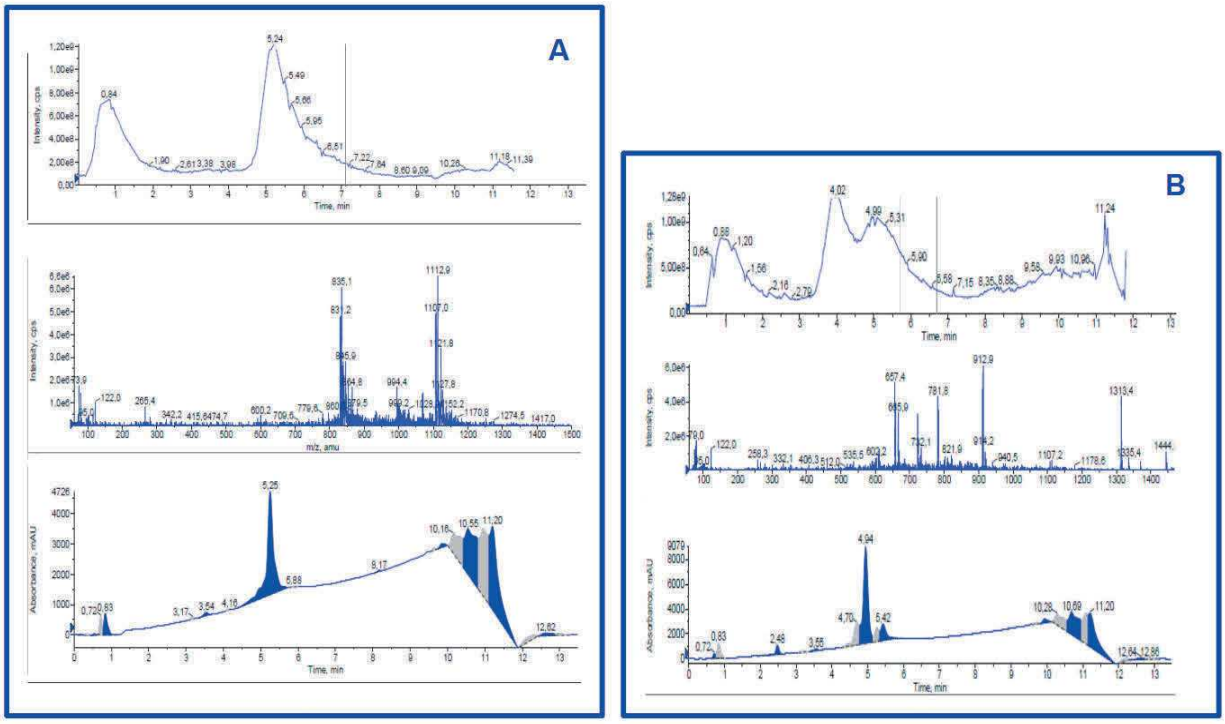

Fig.6 LC-MS/MS chromatography of 18 (A) before cleavage (B) after cleavage. In every panel, the Total Ion Count (TIC), the MS/MS spectra and the UV trace at 290 nm is reported.

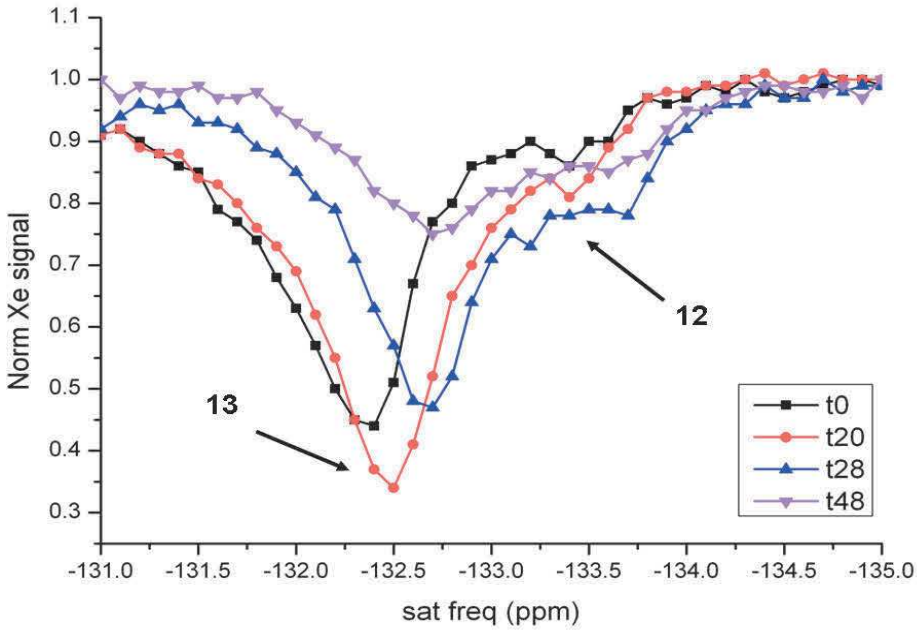

Fig.7 Time-dependent Hyper-CEST response of the cleavage of 13. Qualitatively the signal from 13 decreases, the one for the „cleaved" increases, However, such signal seems to suffer from low solubility of the compound which not allow for a more quantitative analysis.

4.6. Conclusions and outlook

Designing an efficient biosensor for MMP-11 turned out to be very challenging, because of several factors. Firstly, the signal from the “cleaved” version **12**, both in the preliminary test in solution and then in the time-course experiment, was always very low. This was probably due to the poor water solubility of the probe, since the presence of only three PEG units was not enough to counterbalance the hydrophobicity of the cage. Furthermore, the scarcity of other molecular probes, or of validated cellular and animal models to compare to the MMP-11 response, was another limiting factor.

We decided therefore, to change the design of the activatable probe in order to obtain a better water solubility and a reliable traceability. We also decided to slightly change our target by addressing MMP-2/9 instead which is a relevant molecular diagnostic target for which an extensive literature and many cellular/animal models are available. Finally, we aimed to modify the design of our new sensor, such that it could be better translated to tests *in cellulo*, as we will discuss in the following chapter.

Chapter 5

Design of an activatable cell penetrating peptide-based dual probe for fluorescence and Xe-MRI

5.1 Aim and outline of the work

Molecular imaging modalities are increasingly focused on probes that dynamically change their physico-chemical properties upon interaction with the target. These type of probes are also called “activatable probes” (APs) or “smart probes”. Such an approach is very attractive as it is theoretically very specific since the probe is only activated in the presence of the desired target while it appears “silent” in the other cases. This allows imaging with a high signal to background ratio. [95; 264-265] Of particular interest are APs that target an enzyme, since probe activation could then be used to determine enzyme activity and in addition the enzyme activity brings with it an inherent amplification factor (in which multiple probes can be processed by a single enzymatic unit).

Techniques such as zymography or western blotting measure in a given tissue the enzyme quantity, including also the inactive secreted enzyme (pro-enzyme) which is scarcely relevant when a pathological process is studied.[92; 203; 252] By contrast, APs enable direct measurement of the enzyme activity, which in turn can be correlated with a pathological status or with the progression of a disease or of a treatment. [92; 95; 252]

Proteolytic enzymes such as MMPs are among the main targets of APs in molecular diagnostics, in therapeutic assistance and, also in surgery.[266-267] Several examples of protease-responsive APs are reviewed in Elias DR (2008)[264] and include auto-quenched and self- quenched fluorescent probes [204; 238] dual quencher/fluorophore probes for FRET imaging,[268] activatable bio-luminescent probes, [269] T_1 and T_2 activatable contrast agents,[95;210;243] ^{19}F activatable probes for magnetic resonance spectroscopy [250] and protease-activated cell penetrating probes. [212-222]

The term activatable cell penetrating peptides (ACPPs) defines a probe in which a cationic cell penetrating peptide (CPP) chain, usually an Arg-rich peptide, is linked to an anionic peptide chain through a protease-sensitive linker. The anionic part counterbalances the cationic part and makes it inactive through electrostatic interactions. ACPPs have therefore a total net charge of zero and the entire molecule will not have strong affinity for the cell membrane (Fig.1). Upon recognition and cleavage of the peptide sequence linker by the enzyme, the probe is cleaved in two parts; one with negative charge, therefore not internalized, and one with the unmasked CPP that will easily cross the cellular membrane. This latter part is the one that bears the reporters and facilitates imaging. Through this modality, the imaging process is amplified not only by the enzymatic cleavage, but also by the cellular uptake, which yields a local accumulation and can generate a strong contrast.[92;264] In fact, in this case, the cell internalization, contrary to the one driven by to commonly used CPPs such as the Trans-Activator Transcription Protein (TAT), is specific to the enzyme activity, therefore to a specific tissue or cell line. In fact, the first studies on animal models of pathologies correlated with overexpression of MMP-2 (see Chap. 2) in tumors, asthma and myocardic infarct, showed that ACPPs probes were indeed activated and accumulated in the target tissue, producing a measurable contrast distinguishable from healthy tissue. [212-222]

Furthermore, another crucial aspect of using small molecules such as ACPPs *in vivo*, aside from the possibility to measure the enzymatic activity is the more favorable clearance and biodistribution.[92,212] One

other relevant aspect of the ACPPs probes is their versatility, as the same concept has been proposed for several imaging techniques, including near infrared (NIR) optical imaging, PET, SPECT and MRI. A model probe similar to the one shown in Fig.1 was firstly developed by Jiang T and coworkers [221] for living cells and mouse fluorescence and NIR optical imaging, [212; 222] then used for FRET imaging [215] and further for a Gd-DOTA-based MRI contrast agent.[213] Dual Gd-DOTA (MRI)/FITC (microscopy) probes were also proposed by the group of Zhai XH,[242] while Zhang and colleagues[204] developed a shorter ACPPs quantum dots for NIR spectrometry. In a recent paper Tansi F. and coworkers compared the cellular uptake measured with NIR spectrometry of an ACPP based probe and other CPP types.[252] The response of a ratiometric dual radiolabeled ACPP probe for MMP-2 was measured using PET/SPECT by van Duijnhoven S.M.J. and colleagues[214]and the same group developed also a dual probe for PET/SPECT and FRET.[217] Following the same approach, a radiolabelled probe for imaging cardiac infarct was proposed.[216] ACPPs were also the base for a simultaneous diagnostic/drug delivery system, for the delivery of doxorubicin in fibrosarcoma cell lines [245] or doxatocel in glioma xenografted mice. [249] Overall, these studies show that ACCPs are versatile and compatible for in vivo experiments, making them ideal design candidates for a Xe-NMR based MMP-2/9 sensor.

In the previous chapters the feasibility and validation of dual (CrA/fluorescent) sensors was described and similar examples of targeted sensors were shown. The use of a peptidic sequence was preferred because it has an amplification modality through the enzyme activity. Nevertheless, the MMP-11 responsive probe, despite showing a detectable spectral dispersion and a specific response, did not produce enough contrast to be measurable on cells. Furthermore, the lack of reliable cell and animal models and the not optimal enzymatic activity brought us to address to MMP-2 instead. This is a diagnostic and therapeutic target of significant interest for the imaging community for which several cells and animal models have been

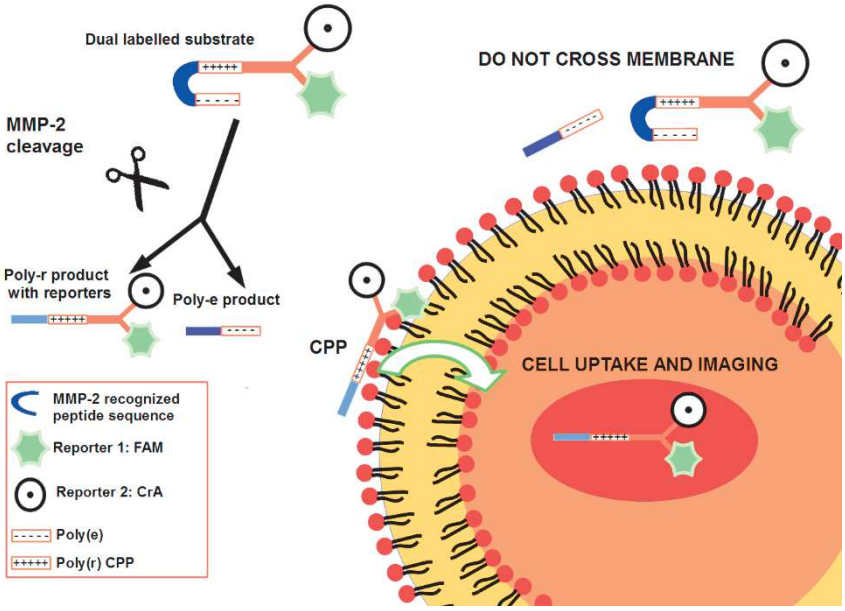

Fig.1 General Schematic of the ACPP-dual sensor for detecting MMP-2 activity. The sensor features five essential parts (see box at bottom left): a synthetic peptidic sequence recognized by the enzyme, an anionic part, consisting of a chain of nine D-Glu that is counterbalanced by a cationic part, consisting of a chain of nine D-Arg. Linked to this latter one through a spacer are two reporters, one for fluorescence (FAM) and the other for Xe-NMR (Cr-A). Upon cleavage, the positively charged part bearing the two reporters will be internalized on the cells because of the presence of nine Arg. Both the anionic part and the complete substrate that does not bear net charges will be not taken up by the cells. The complete substrate presents the same reporters as the cleaved one and can therefore be detected as a negative control.

described. Furthermore, our work with in cellulo-MRI showed that though Hyper-CEST it is possible to visualize a precise signature of the Cr-A sensor in the cell, in particular discriminating when the probe is in the hydrophobic or in the hydrophilic cellular environment. [106]

We decided therefore to design an ACPP-based probe that can generate a specific hyper-CEST signal, not by chemical shift upon cleavage, but rather one whose signal accumulates and is concentrated by the sequential events of enzymatic activation and then cellular uptake. In our previous studies [106-108] we showed the detection of Cr-A sensors associated with cells in a nanomolar range. This was obtained by incubated concentrations over 20 μM of contrast agent.[106-107]. By using a ACPPs, and exploiting the favorable accumulation of the probe in the target, we expect to measure a similarly efficient *in cellulo* Hyper-CEST effect by using a lower concentration of biosensor. As perfomed in our previous works [106-108], the incorporation of a fluorescence moiety in a known ratio with Cr-A was included to quantify the cell labeling with optical imaging. In the following paragraphs the design, synthesis, cell uptake and MRI response of a dual-ACPP sensor responsive to MMP-2 will be demonstrated.

5.2 Design and synthesis of an MMP-2 ACPP probe for Xe-MRI

5.2.1 Probe design: general considerations.

The MMP-2 responsive probe **15** is presented in Fig. 2A, while the product bearing Cr-A after cleavage in Fig. 2B. The probe has been designed to be measured by Xe-MRI and through optical imaging and to be internalized upon cleavage by MMP-2 similarly to the examples discussed in the previous paragraph.

As illustrated in Fig.1, **15** presents the following features:

- a “functional linker”: MMP-2-recognized peptide sequence, *PLG*LAG* (* labels the cleavage site);
- anionic CPP-inhibitory peptidic sequence (e_9);
- cationic CPP peptidic sequence (r_9);
- inert spacer (aminohexanoic acid, Ahx) in between r_9, e_9, reporters and peptidic sequence;
- Cr-A as the Xe-NMR reporter;
- FAM as the fluorescence reporter.

The MMP-2 responsive sequence *PLG*LAG* [212-214; 221.221; 248-249; 252] was firstly reported by Selzer JL et al., starting from the sequence of MMP-2's natural substrate, gelatine. Fluorimetric measurements were showing a K_m of 270 μM and K_{cat} of 3.54 s^{-1}.[232] As for most MMPs, Pro in P_3 appears to be essential for the hydrolysis, as also the presence of a large hydrophobic residue, here Leu, at the cleavage site. [181; 252]

The anionic CPP-inhibitory chain (e_9) consists of 9-D-Glu units and the cationic one (r_9) of 9-D-Arg units. To avoid unwanted cleavage of the chains, it is essential to use D-amino acids as they are not recognized by the enzymes.

The strength of the intramolecular association between e_9 and r_9 needs to be big enough to assure the inhibition of the CPP activity, but weak enough to restore it upon cleavage. In other words, it has to be smaller than the Effective Molarity (EM) of the linker. [270] Such an hypothesis has been tested by the group of Jiang T. using two independent methods, namely isothermal titration calorimetry [212] and homonuclear two-

dimensional NMR.[221] Both measurements showed that there is an electrostatic interaction between the two charged chains, which suggest a “hairpin-like” structure, with the two chains facing each other (Fig.1), and that this interaction appears to be around 100 times smaller in magnitude than the EM. Hence, cleavage of the linker by the enzyme causes the two parts to be separated. Once the enzyme cleaves off the polyanionic-attenuating part, the probe presents a 9-unit linear poly-D-Arg which then acts as a CPP.

Such CPPs, comprised of oligo arginines (also termed arginine-rich peptides (Poly-R)) are peptides consisting of L- or D-Arg which are able to translocate into the cytoplasm of cells, both alone or with a cargo. They are therefore used in drug delivery and in diagnostic applications. The mechanism underling the translocation was in the beginning identified as a direct, non-receptor and energy dependent mechanism explained by the interaction of the bidentate hydrogen bonds between the basic Arg guanidinic group and the negatively charged phosphate, sulphate and carboxylate groups that constitute the cell membrane. Conversely, more recent studies showed that the translocation is more accurately explained by endocytotic pathways, such as macropinocytosis, clathrin-mediated and caveloin-dependent endocytosis. [271-274] The translation efficiency depends on many factors, such as cell types, temperature, types of cargos, labelling, CPP concentration, and number of Arg units. Peptides bearing between 6 and 9 Arg showed efficient and fast uptake (70%-90% [275-277]), while longer or shorter Arg chains lead to scarce or slower uptake. One study [275], compared Arg L- and D- conformations and concluded that they were equal in their translocation properties.

Poly-R peptides are also associated with a certain degree of cell toxicity due to the possible interaction of the guanidinic group of Arg with DNA.[278] Poly-R mediated cell toxicity is concentration-dependent and also depends on the number of Arg units: the use of 9-Arg has been reported to be the best match as regarding transduction efficiency and limited cell toxicity (<80% for 50 μM).[279] We had two important considerations for cell toxicity when developing this MMP-2 biosensor. Firstly, the complete uncleaved substrate must have low toxicity and (in terms of future *in vivo* applications) be suitable for distribution to the tissues of interest with minimal non-specific uptake. Secondly, once cleaved by MMP-2, the sensor must achieve a balance between suitable cellular uptake for efficient MRI signal detection and the intracellular toxicity of the active probe. Both of these considerations are addressed by our probe. The presence of the anionic counterpart in the ACPP increases the biocompatibility before activation, and is reported to be from 4-15 times less toxic in cells and in animal models [212; 279] and the 9-Arg CCP should provide suitably efficient uptake whilst retaining cell viability.

The use of a hydrocarbon spacer such as aminohexanoic acid (Ahx) in between the charged group and the cleavable peptide sequence has a double role of a) improving the interaction between the enzyme and the consensus sequence [252] and b) to offer enough space and flexibility between the reporters and the r9 sequence. This minimizes possible inhibitory hydrophobic interactions reported for fluorophores. [280-281]

FAM was chosen once more as the optical reporter, as our previous experiences showed negligible cell toxicity, low auto-quenching and, even more important, no interference with the Hyper-CEST experiments (see Chap. 3).

Similarly to the biotin-CrA and the MMP-11 sensors, CrA is conjugated to the probe through the amino terminus of the Lys which allows for both the performance of the Xe-MRI experiment and to choose easy acylation after the synthesis of the peptidic backbone.

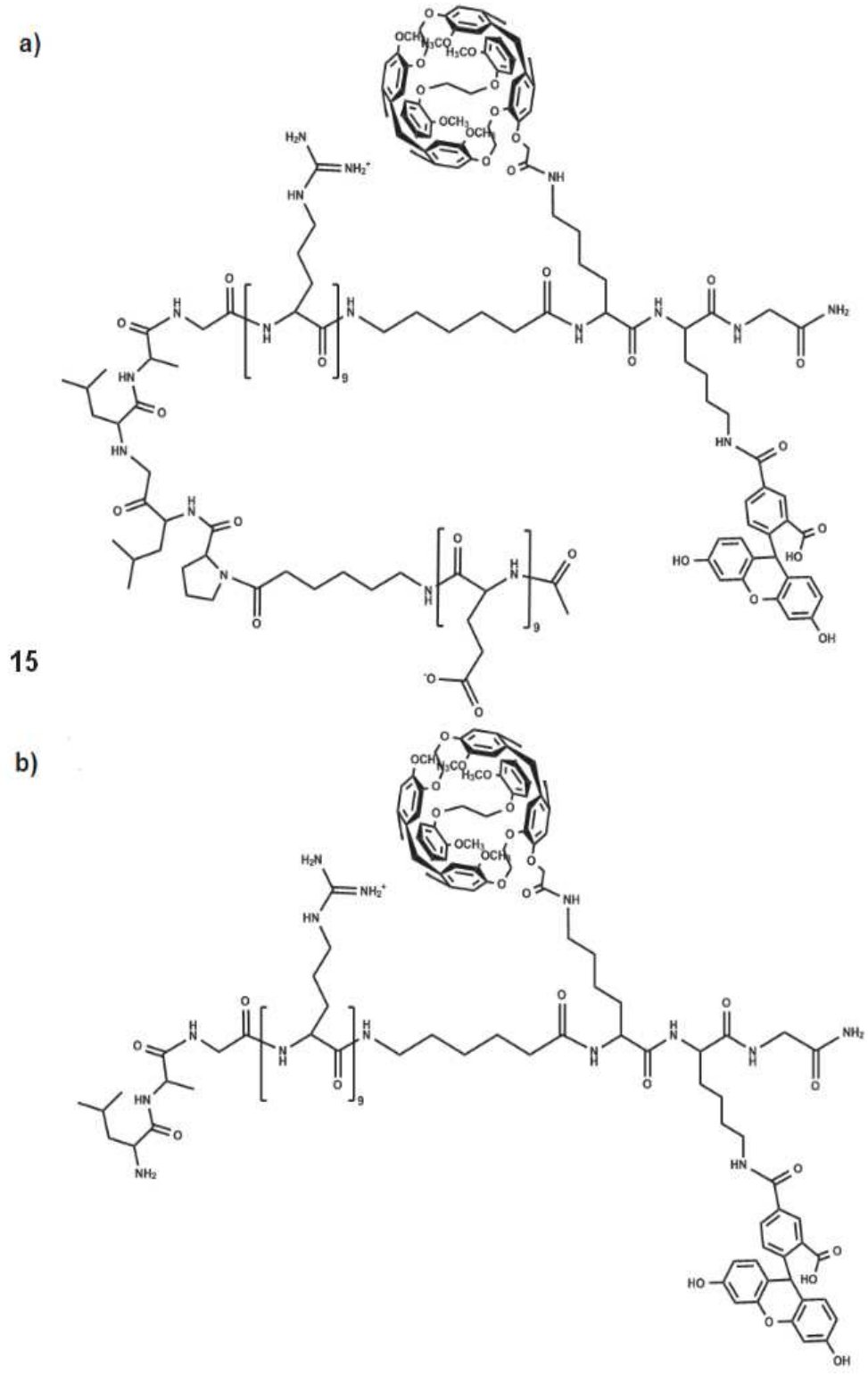

*Fig.2. Chemical structure of the ACPP-based probe **15** (a) and chemical structure, the probe after cleavage from MMP-2 (b).*

5.2.2. Synthesis of 15

The carefully designed ACPP-based probe **15** has been synthesized by Biosytan GmbH through Fmoc-tert-Butyl (tBu) simultaneous multiple peptide synthesis using an automatized SPPS synthesizer. [282] Briefly, coupling wer performed using 3-6 equiv. of Fmoc-amino acid activated with same equivalents of TBTU and 6-12 equiv. N-Methylmorpholine, using Tentagel S RAM resin (loading: 0,28 mmol/g resin). At every step, the Fmoc group has been removed with 20% piperidine in DMF and finally the peptide has been cleaved from the resin using TFA/thioanisole/thiocresol (95:2,5:2,5) for 3h and finally assing triethylsilane (5%) for 1 hr. [283-284] The crude peptide was finally coupled in solution with Cr-A-ma (2 eq.) previous activation with TSTU/DIPEA. The peptide was purified through RP-HPLC (Fig3 a) and the mass was confirmed through MALDI-TOF (Fig3 b). The calculated mass for $C_{227}H_{327}N_{59}O_{67}$ was m/z 4954.6, and the founded mass was m/z 4955.7, corresponding to m+1. Details of the synthesis, HPLC trace and MALDI-TOF spectrum are reported in the Materials and Methods section (§7.11).

5.2.3 Cleavage test of 15 and retaining of fluorescence properties.

The affinity of MMP-2/9 for the sequence *PLG*LAG* when being included in a charged peptide such as the ACPP used here has in principle already been tested. Jiang T. et al. [221] measured that the cleavage of 500 µM of peptide by 0.8 µM of enzyme was complete within 30 minutes. The same group tested the probe (3 µM) with MMP-2, MMP-9 and other proteases at the concentration of 50 nM with gel electrophoresis. [212] Also in this case, after 30 minutes of time, around 90% of the probe was cleaved by MMP-2, while 80% was achieved by MMP-9 for which an overlap of specificity with the other gelatinase MMP-2 is expected. The affinity for other proteases was low, with the exception of MMP-14.

Obviously, the quantity of enzyme used in the test played a role. Von Duijnhoven et al tested the cleavage of 100 µM of probe with 5 nM of enzyme for 1 hour and the percentage of cleavage was lower (around 80% for MMP-2, and only 30% for MMP-9). [214] Also, Shi N-Q. et al. tested the enzymatic cleavage in a 4-hours range, using different ratios of MMP-2:probe. The ratio 0.1:1 resulted in a complete cleavage within 1 hour, while for lower percentage of enzyme, a predominant presence of the product (>80%) was measured only for times over 2 hours. [245] A dual radiolabeled/FRET probe (0.64-3.6 µM) was digested by MMP-2 (5 nM) with an efficiency characterized by K_{cat}/K_m of 4.0 ± 0.7 M^{-1} s^{-1}. [217] FRET is an accurate and precise method for enzyme kinetics tests because the quencher keeps the probe non fluorescent as long as it is not cleaved. For using our compound **15** in cellular environment, however, the fluorescence measurement of the uncleaved probe is crucial, as we expect a certain degree of unspecific uptake by the cells due to the hydrophobicity of the cage. Such preliminary fluorescence studies are also important to identify the best incubation condition for *in cellulo* Xe-MRI.

To test the cleavage, **15** was dissolved, at the concentration of 100 µM, in an MMP-2 reaction buffer, containing 50 mM of Tris base, 300 mM of NaCl, 5 mM of $CaCl_2$, 20 µM of $ZnCl_2$ (pH=7.5). Then, the activated MMP-2 was spiked in the reaction mixture to a final concentration of 5 nM and the sample was placed in a dark vial at 37°C for 2 hours. The samples were analyzed with an HPLC-UV equipped with a fluorescence detector to monitor the FAM signal (ex.485 nm/em.510 nm). For each data point (0, 30, 60, 120 minutes), 1 µL of the sample was taken from the mixture and analyzed with MALDI-TOF. Fig.3 shows the MALDI-TOF spectra of each data point. At 30 minutes, the spectrum shows a new mass (m/z 3368) which

corresponds to the cleaved product ($C_{161}H_{230}N_{46}O_{35}$ m/z=3367.7). This signal gains in intensity with the increase of time. The latest data point shows a only small peak corresponding to **15** and, at the far left, a visible peak of m/z 1624, which correspond at m+Na^+ of the other anionic cleaved part ($C_{66}H_{99}H_{13}O_{33}$ m/z=1601.65). We estimated that around 80% of **15** was cleaved after 120 minutes.

Both for fluorescence and Xe-MRI studies, it is important to test the "precelaved product" as a "positive control" as it is the part of the molecule that carries the CPP and therefore it can be used to verify the Hyper-CEST response. Furthermore, preliminary tests of uptake efficiency and of CPP-mediated cytotoxicity need to be incorporated in the panel of studies. Having the "positive control" produced by enzymatic cleavage and not through synthesis has the advantage of being closer to the real situation in cells.

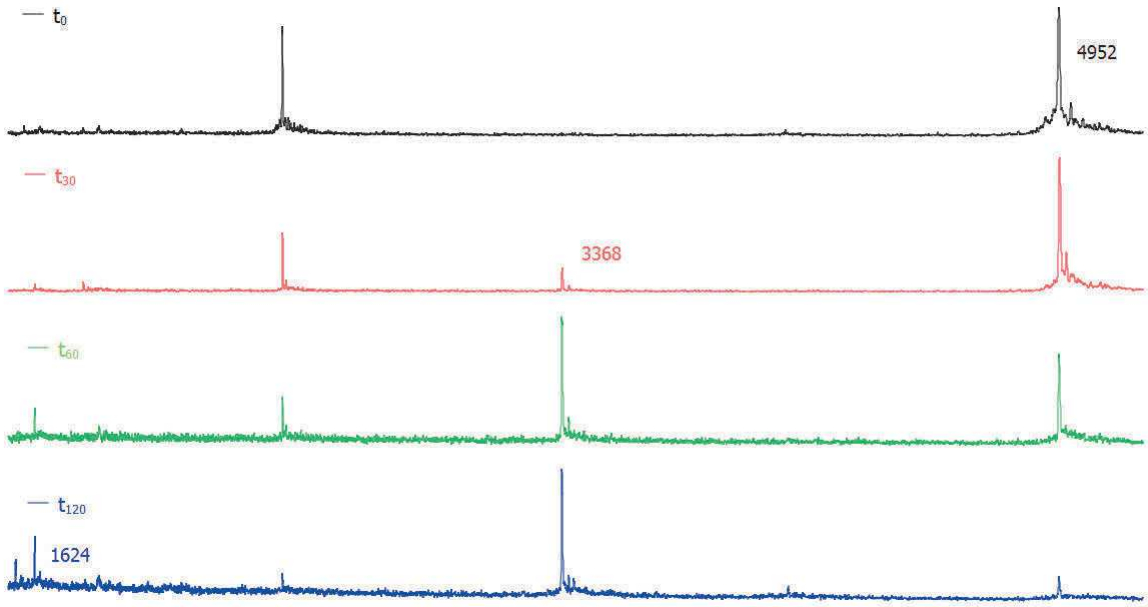

*Fig.3 MALDI-TOF spectra of 100 µM of **15** cleaved for time 0-2 hours. From t_{30} it is possible to spot a new peak corresponding to the product. The anionic inhibitory part (as m+23, m/z=1624) is also visible. The starting compound is depleting over time.*

To test whether we could obtain the fully cleaved product at the highest percentage possible, we incubated 200 µM of **15** with 50 nM of enzyme, based on the fact that a ratio 100 µM/30 nM had been reported to cleave the same sequence at 100% .[214]

After 24 hours the reaction mixture was measured with MALDI-TOF, and, as it is illustrated in Fig. 4, we can assume to have 100% cleavage.

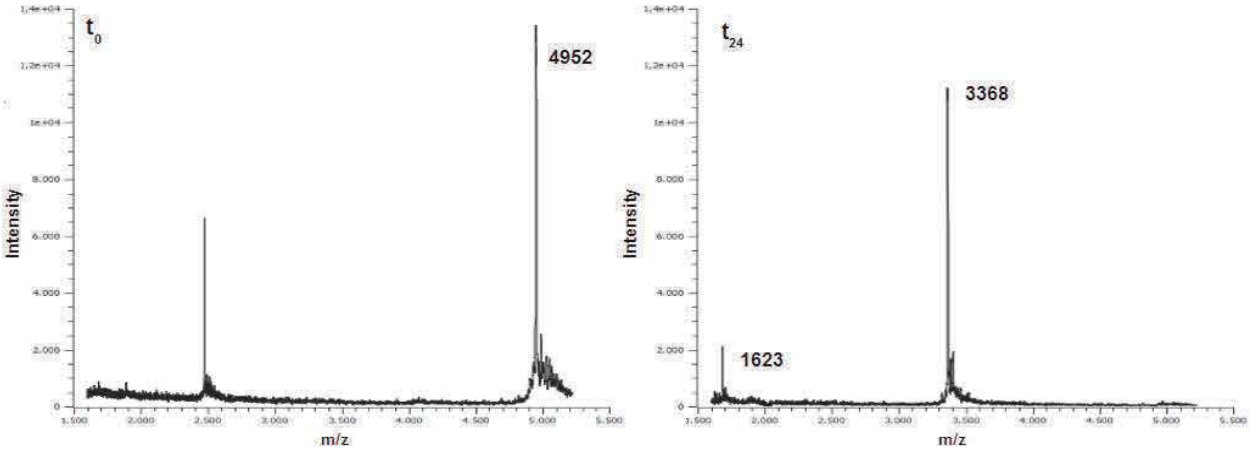

*Fig.4 MALDI-TOF spectra of 200 µM of **15** cleaved for time 24 hours. In the left, at time zero, only the complete substrate **15** is visible. After 24 hours, the cleaved construct 15 is present at 100%.*

MALDI-TOF measurement was chosen to verify the complete cleavage as only a very limited amount of sample (1 µL) is needed for the determination and the analysis is very fast and reproducible.

In the cell environment, a large number of MMPs are present, and previous studies have shown that the sequence *PLG*LAG* is partially cleaved also by MMP-14. [212; 214]

Therefore to generate a true negative control for *in cellulo* tests, and avoid false positives from cross-reactivity with other MMPs, we used a broad-spectrum MMP inhibitor, GM6001, which is a Zn^{2+} chelator. [212; 214] We tested the efficiency of the inhibitor in our *in vitro* cleavage test after 2 hrs, which was previously used to obtain a large amount of product. Briefly, 100 µM of **15** was incubated with 5 nM of enzyme, and then divided in two samples: in one, GM6001 was added to a final concentration of 100 mM, and then both samples were kept at 37°C for 2 hours. After that, 1 µL of each sample was collected and analyzed with MALDI-TOF. The results, are shown superimposed in Fig. 5, and show that after 2 hours there is no cleavage of **15**, validating the use of GM6001 with **15** for providing the "negative control" of our study.

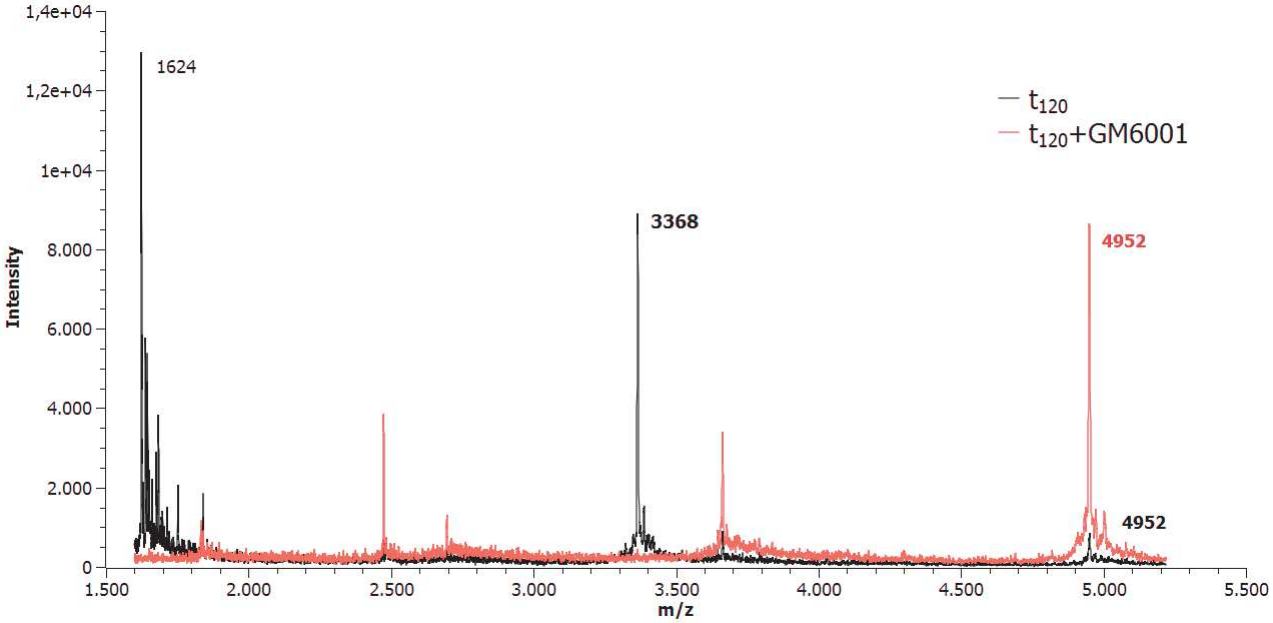

*Fig.5 Superposition of the two MALDI-TOF spectra of 100 µM of **15** cleaved for 2 hours in presence (red) and absence (black) of GM6001. The spectrum shows that GM6001 clearly inhibits the cleavage, as no peak corresponding to the cleaved substrate has been found*

As a final test, we calculate the Φ of **15**, as already discussed for the probes 2 and 4 (Cap.3). Also in this case, FAM was used as reference and the analytes were dissolved in ethanol. The calculated Φ is 0.52, lower than what we had for **2**; such decrease is probably due to the high presence of sterically hindred groups that affect the response of FAM, as already reported.[147; 154-155]

5.3 Cell tests for the dual-ACPP sensor

The endogenous expression levels of individual MMPs in different cell lines have been reported using RT-PCR [199] and zymography [201] techniques. Among various cell lines, the fibroblasts cell line, HT-1080, has shown to highly express MMP-2 (along with MMP-1,-7,-14 and -9). This type is therefore the cell line of choice as a positive control line to study MMP-2/9 responsive probes. Bremer and coworkers [285] measured MMP-2 expression in HT1080 cell lines and in tumor tissue homogenate through zymography and found a

high expression of the activated form of MMP-2 (64 kDa) along with the inactive pro-MMP-2 (74 KDa) (Fig. 6A and 6b). In the case of tumor tissue, the quantity of MMP-2 measured was 435 U/g tumor. More recently, the activity level of MMP-2 in different cell lines, including HT-1080, was measured by cleavage of a fluorescence reporter. Both in whole cells and in supernatant, HT-1080 showed a higher MMP-2 activity than other cell lines (Fig.6c). [252]

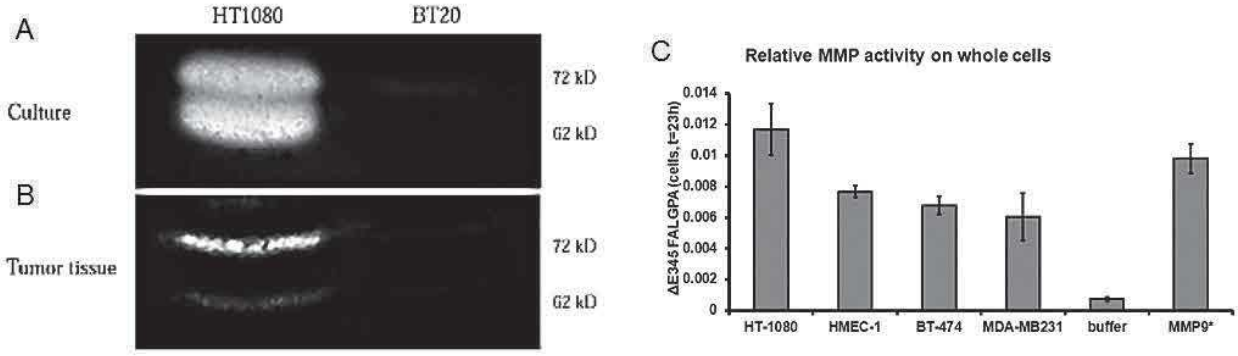

Fig.6 Left, A) and B) zymography of high expressing MMP-2 cell line (HT-1080) and low expressing (BT-20), in cell culture and in tumor homogenate from Bremer C (2003)[285] C) shows the MMP-2 level, measured through a fluorescence reporter, of different cell lines, including HT-1080. MMP-9 is used as reference; from Tansi F (2014). [252]

However, the expression has been reported to be extremely low in 2-D cell culture; even if overexpressed, MMP-2 would be too dilute in 2-D culture and would lead to a slow cleavage and inefficient uptake. [212]
For this reason, the use of exogenous proteases or pre-cleaved probes is common in many protocols of ACPPs proof of principle studies. [212; 214; 216-217]
For *in cellulo* tests, HT-1080 fibroblasts were grown in VLE/Dulbecco's modified eagle medium supplied with fetal calf serum (FCS) as described in details in Materials and Methods. To test cell toxicity, HT-1080 cell lines were incubated with 1 and 10 μM of **15** for incubation times ranging from 30 minutes to 24 hours. The percentage of live cells, as evaluated by Trypan Blue staining, was over 95% for every time point for 1 μM concentration, while it was decreasing for 10 μM (90% cells alive). This result confirms overall the suitability of our uncleaved probe, 15, to be used in cellulo. Cells were also incubated with the same concentration of probe with the addition of 100 μM of GM6001, and no difference in cell toxicity was measured.
The possible toxicity of CPPs has been discussed in *§5.1.* Despite the fact that different toxic thresholds for the CPP concentration were reported, the lowest one reported for Arg-rich peptides which are similar to our pre-cleaved probe was 10 μM [278]. Therefore, as a precaution, we decided to use a concentration of 2 μM of the full probe, **15**.
The fully cleaved substrate (Fig.2b) was produced by 24 hours cleavage of **15** and the mass was confirmed through MALDI-TOF. HT-1080 cells were then incubated with the pre-cleaved substrate at the concentration of 2 μM for incubation times ranging from 30 minutes to 24 hours. Cell viability, as determined by Trypan blue staining, was always over 95% for all conditions tested.
The cellular uptake of 2 μM of **15** and "pre-cleaved" was tested for 30, 60 and 120 minutes at 37°C, and the relative fluorescent signal was measured by flow cytometry (Fig. 7 upper part). Unsurprisingly, the "pre-cleaved" probe consistently shows higher cellular uptake than **15** (shown by the histogram plots and median FL-1 signal). In particular, such uptake was from 2 times higher (for 30 minutes) until 5 times higher (1 hour).

However, the difference between the two compounds was lower for longer incubation times, suggesting an increase of the unspecific uptake over time, as already reported for much higher concentrations of fluorogenic probes in Chap. 3. The unspecific uptake was investigated further by incubating HT-1080 cells for the same time points and at the same concentrations at 4 °C (Fig. 7 lower part) in order to reduce the cells' metabolism and in turn reduce non-specific uptake. Indeed, the results show a reduced uptake (as evaluated by the median FL1 fluorescence) for both compounds at 4 °C, and that this was more pronounced for **15**. The unspecific cell uptake for the longest incubation time was in fact 20 times lower compared to

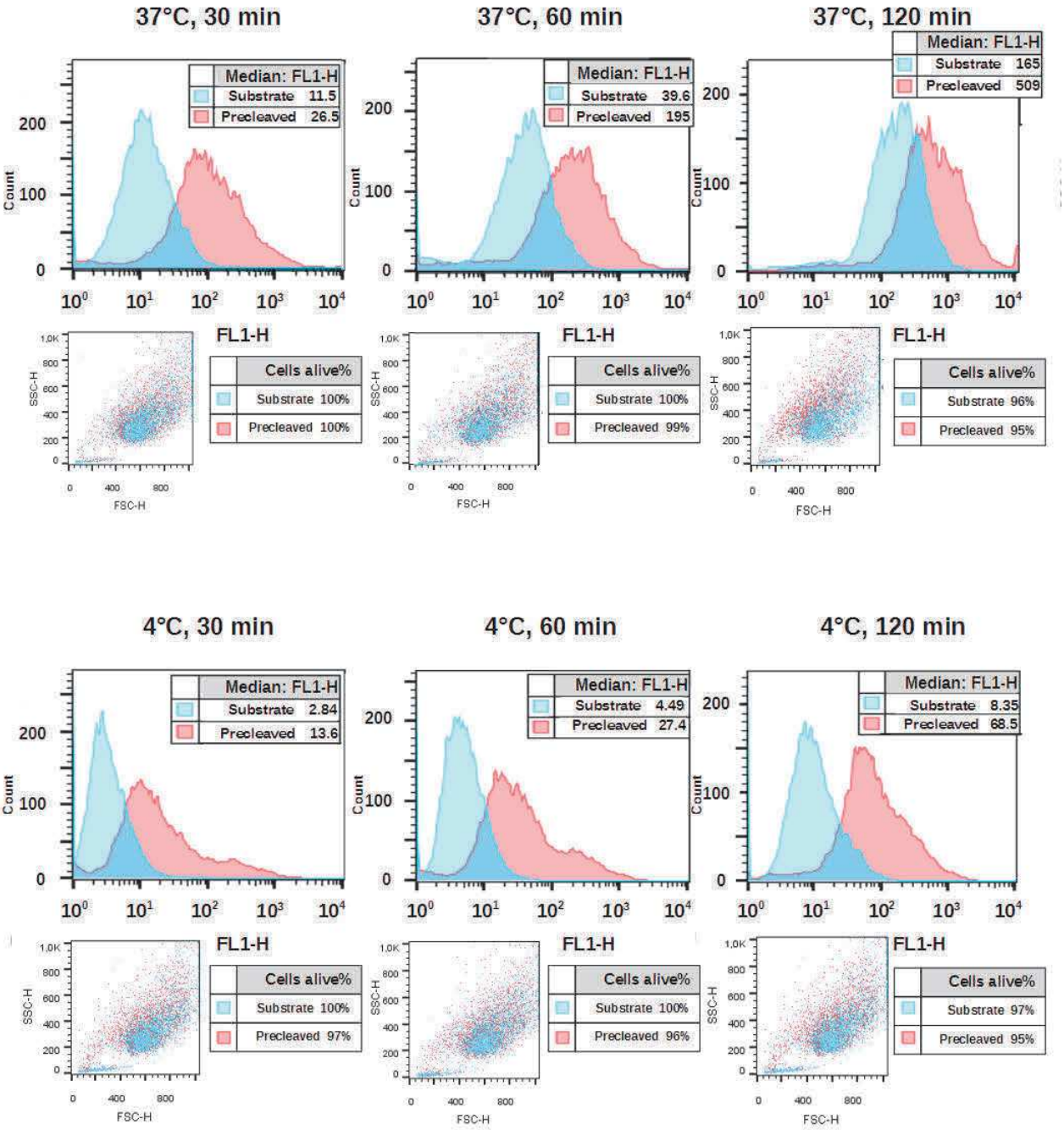

*Fig.7 Flow cytometry data of the uptake of 2 µM of **15** and its pre-cleaved substrate for HT-1080 cells incubated for 30, 60 and 120 minutes at 37°C (upper part) and at 4°C (lower part). Scatter plots show the cell populations at each sample time and the percentage of cells alive. At each time point the uptake of the "pre-cleaved" is higher than **15**. The uptake of both species is significantly lower at 4°C.*

conditions at 37°C. In comparison, the uptake of the “pre-cleaved”, even though it was also significantly lower, was only 8-fold reduced.

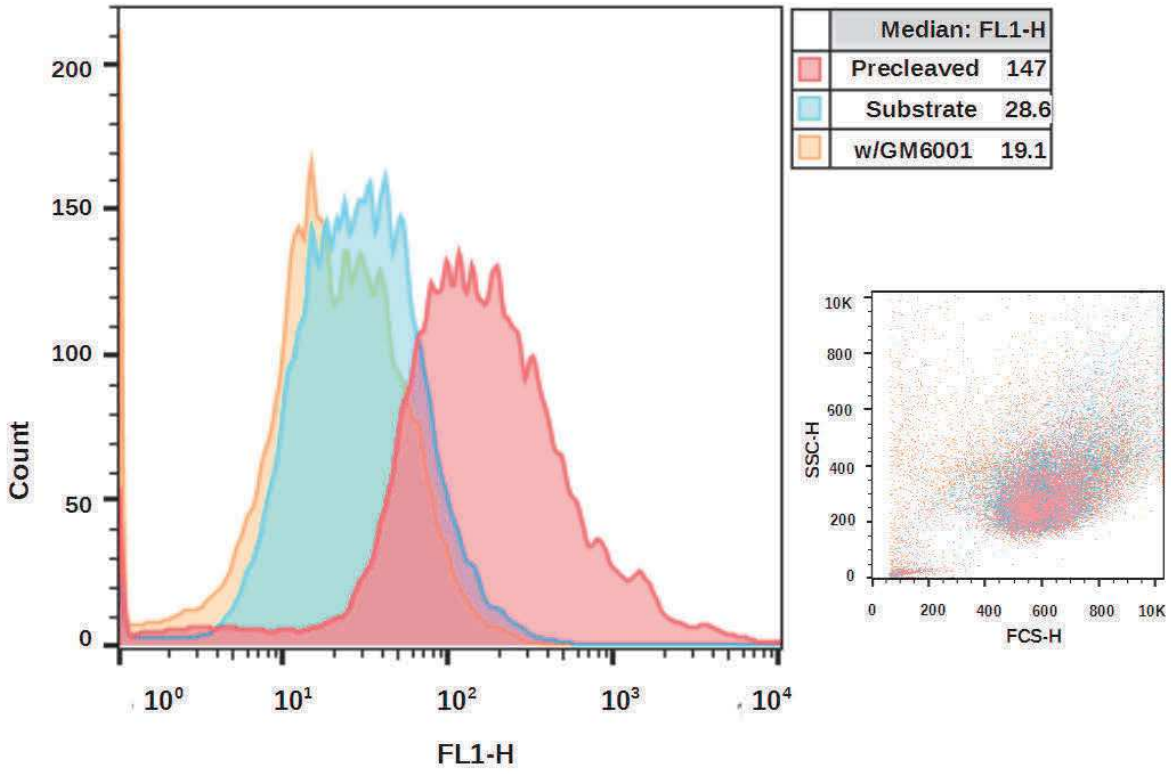

*Fig.8 Flow cytometry data of the uptake of 2 µM of **15** (blue), **15** with inhibitor (orange) and pre-cleaved (pink), incubated for 1 hour at 37°C. There is only a small difference between **15** and **15**+GM6001, while the uptake of 15 is 3 times higher.*

It can be assumed that at 4°C the endocytosis mechanism that regulates the CPPs uptake is inhibited, but others mechanisms, such as direct translocation, come into place. [272; 275; 286] We decided therefore to continue our tests at 37°C in order to have reproducible physiological conditions and to have a better cell labeling for Xe-MRI experiments.

The influence of GM6001 on cellular uptake of the compounds was also tested. In Fig. 8, flow cytometry data of the three conditions (completely cleaved, substrate **15** and substrate **15** + GM6001) showed a substantial overlapping of the substrate and the substrate + GM6001, while the cleaved substrate shows a 3-fold higher uptake. This verifies that the presence of the inhibitor GM6001 does not substantially affect the non-specific uptake of **15**.

Whilst flow cytometry is a useful method for relative comparison of fluorescence, it was important to have a more quantitative evaluation of the cellular uptake of the compounds. For this, we examined the total fluorescence from known numbers of cells after incubation with the “pre-cleaved” probe and **15**, as analyzed by a Tecan plate reader. The amount of cellular uptake was then quantified by comparing the values to a reference fluorescence curve generated by dissolving **15** in PBS. For the three probes in the considered time scale the cell-associated fluorescence for the “pre-cleaved” was measured to be ca. 6 times higher than the one measured for **15**. (Fig. 9d) The probe concentration, based on the fluorescence measurement and normalized by the number of cells, was performed for incubation times ranging from 30 minutes-24 hours.

Although the uptake of **15** appears higher than **15**+GM6001, the profile of uptake is similar for both conditions (Fig.9a and b) suggesting a similar mechanism of uptake, which we expect to be mainly driven by the hydrophobic interactions of the compound with the cell membrane.

Not surprisingly, the pre-cleaved probe showed a more linear uptake profile, compatible with a different mechanism. (Fig. 9c).

It is necessary to point out that the scale of the measurement for **15**w/GM6001 is close to the detection limit, therefore a direct quantitative comparison with the pre-cleaved is difficult.

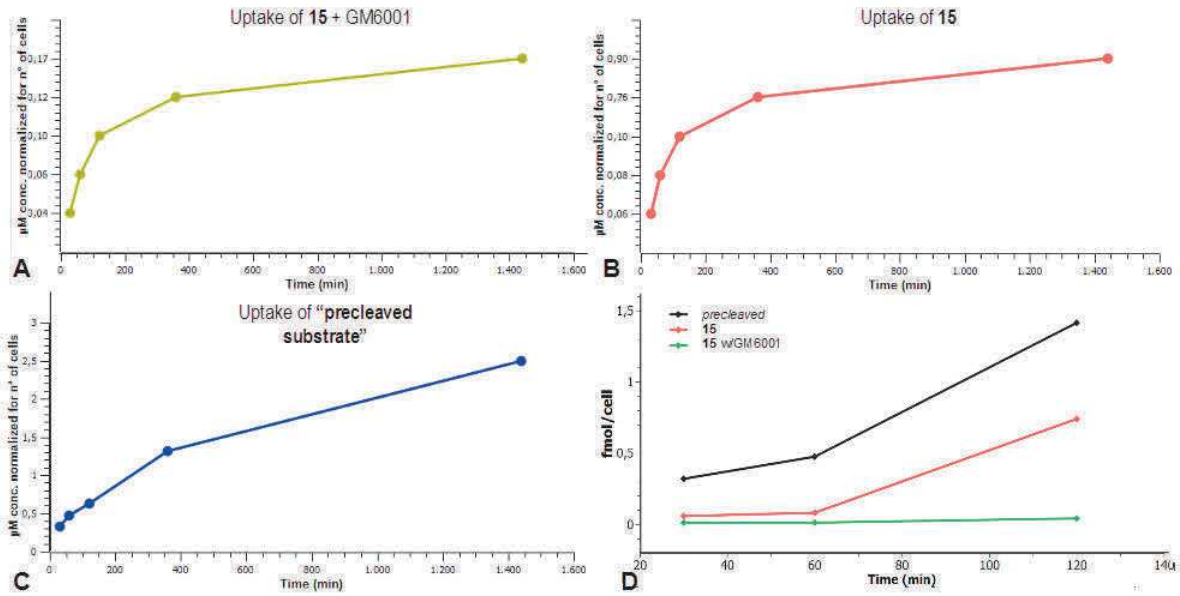

*Fig 9a-c Fluorescence quantification of 2 µM of **15**, **15** w/GM6001 and the "pre-cleaved substrate" over 24 hours time. Fig. 9d represents the fmol/cell concentration of the three tested conditions (30, 60, 120 min incubation/37°C).*

Both flow cytometry and fluorescence quantification via the plate reader experiment are not able to discriminate between internalized probe and any probe associated with the extracellular cell membrane, therefore additional microscopy analysis was performed. Confocal microscopy facilitates the detection of both the presence and the localization of the probe in different cell compartments and can provide additional supporting information as to the uptake mechanisms and cellular distribution of the probes.

In Fig. 10 confocal microscopy imaging of HT-1080 cells that were 1.) untreated 2.) treated with 2 µM of **15** 3.) treated with 2 µM of **15** w/GM6001 (100 µM) and 4.) treated with 2 µM of "pre-cleaved" are presented. The cells were co-stained with Hoechst 3342, as a nuclear stain and with Trypan blue, as a cell membrane stain..

High cell viability was observed during the measurement. Comparing the images of 1.), 2.), and 3.), it is possible to see no difference between these three conditions. In other words, there is no appreciable uptake of the fluorescent probe in those cases. Conversely, image 4.) indicates significant uptake of the fluorescent sensor which appears to be concentrated in the cytosol, most likely inside vesicles (as suggested by the punctuated staining pattern).

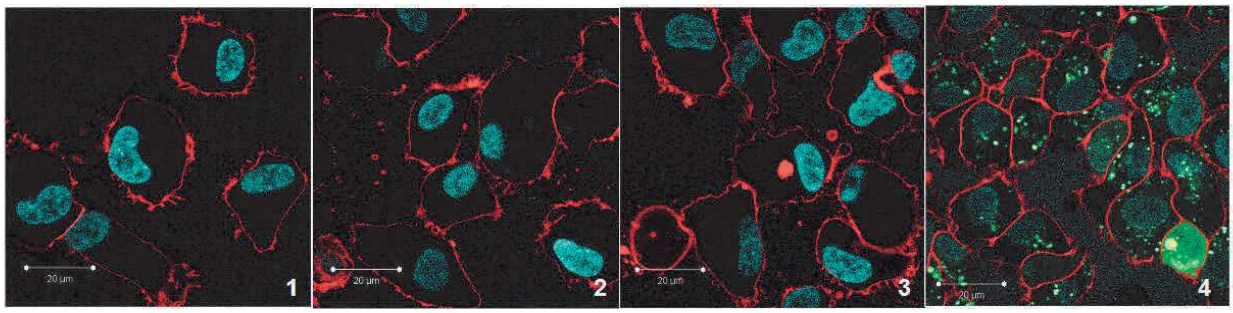

*Fig.10. confocal microscopy imaging of HT-1080 cells. All cells were stained with Hoechst 3342 (blue) to detect the nucleus and with Trypan blue to detect cell membrane. The GFP channel was used to detect the probe through FAM. 1. control cells, untreated 2. cells treated with 2 µM of **15** for 2 hours. 3. cells treated with 2 µM of **15** w/GM6001 4. cells treated with 2 µM of "pre-cleaved". Only in this case it is possible to see the probe (in green) present in the cytoplasm.*

As expected, there is no presence of the sensor in the nucleus, which supports the lack of toxicity at this concentration. To further evaluate the intracellular distribution of the "pre-cleaved" in the cytosol, z-stack images of the positive control (4. in Fig. 10) and negative control (3. in Fig. 10) were acquired. Such an image series moves through the cell and can be used to verify the localization of the probe.

The comparison of the z-stack of the negative (Fig.11, upper part) and positive (Fig.11, lower part) control shows that the compound the pre-cleaved probe is present in the cytosol, confirming its ability to cross the cellular membrane. In comparison, the z-stack images of Fig.11B does not show any internalization. In the image at 8.0µm (far right, Fig. 11 top and bottom), some green fluorescent spots with a shape completely different than the one present into the cytosol are pointed out in the orange circle. These have been attributed to a small fraction of the compound that precipitated into the cell culture plate coating material.

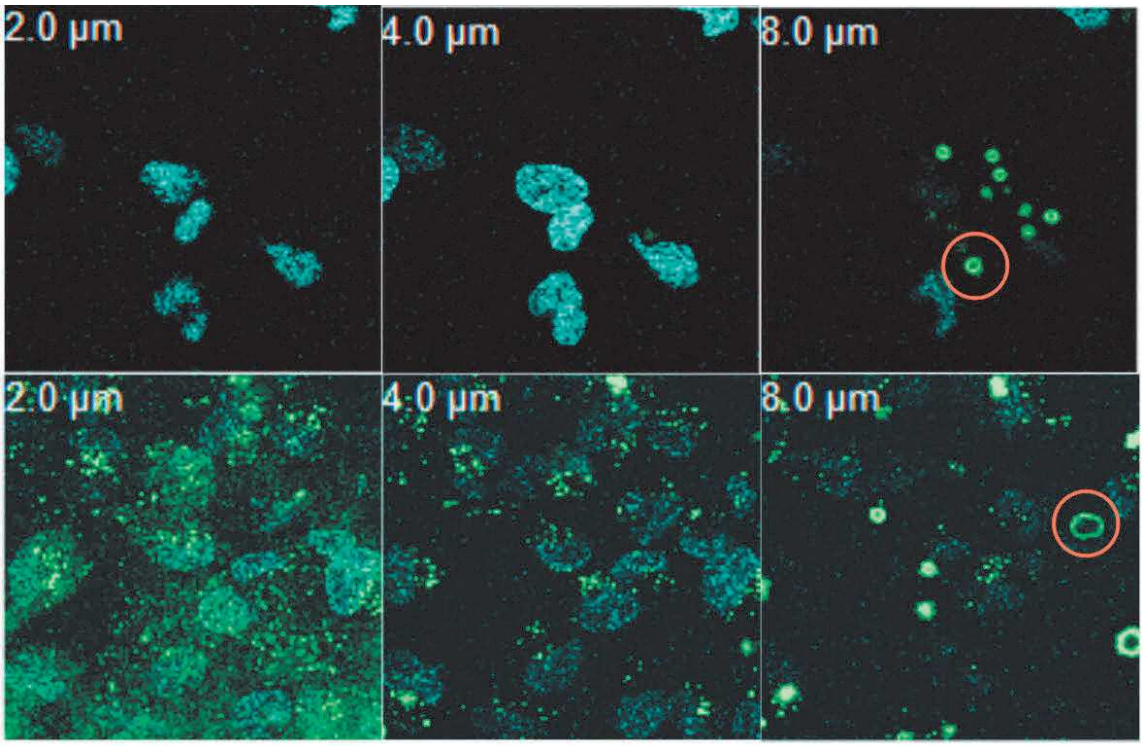

*Fig.11. Z-stack microscopy experiment of HT-1080 cells treated with 2 µM of **15**w/GM6001 (upper part) or 2 µM of the "pre-cleaved" (lower part). Cell nuclei were stained with Hoechst 3342 (blue). In green the fluorescent probe (containing FAM).The sensor is present in cytosol only for the incubation with the "pre-cleaved". The spots present in the last images (in the orange circle) are due to the precipitation of unbound compound.*

This was not entirely surprising, as for microscopy experiments the extensive wash steps with PBS after incubation (which were previously performed for flow cytometry measurements) were not possible as this could reduce the adherence of the cells to the cell culture plate. We can therefore assume that some of the unbound compound has not been entirely washed away. Comparing the performance of our previously synthesised fluorescent sensors, it is possible that with the "pre-cleaved" probe we can achieve a much higher degree of cellular uptake with around 20 times less compound and in a short amount of time. In fact, we could achieve around 1 fmol/cell for 1 hour incubation with only 2 µM, vs. less than 0.25 fmol/cell for 18 hrs incubation with 50 µM of CrA-PEG_3-FAM (**2**). (see §2.3.4)

5.4 In-cell Xe-MRI experiments.

The previously described panel of fluorescence tests on cells allowed us to determine the optimal conditions to perform in cell Xe-MRI. The corresponding work flow with the double phantom for Xe-MRI experiment is summarized in Scheme 1.

Similarly to the anti-CD14 antibody construct and the two fluorescent cell labelling probes **2** and **4**, the cells can be analysed either by fluorescence read-out or xenon-MRI/NMR read-out in within the same experiment.

Firstly, the positive control was produced from 200 µM of **15** by an extended (24 hrs) cleavage with 50 nM of enzyme (Scheme 1.1). This reaction was carried out in the MMP-2 reaction buffer (§4.1) in a controlled temperature heating unit, set at 37°C, in dark vials to preserve the fluorescence. The total reaction volume (20 µL) was sufficient to reach the desired 100-fold dilute concentration (2 µM) on cells with a typical volume for 6-well plates of 2 mL. Such a dilution is also important because previous experiences taught us that there is an influence of cations such as Ca^{2+} (which is present in the MMP-2 reaction buffer) in the Hyper-CEST experiment (§4.3).

After 24 hours, 1 µL of the cleavage mixture was sampled and placed in a MALDI plate for mass confirmation. Then (Scheme 1.2) HT-1080 cells were incubated with a final concentration of either 2 µM of "pre-cleaved" substrate, 2 µM of **15** supplied with 100 µM of GM6001, or 2 µM of **15 alone**. As mentioned

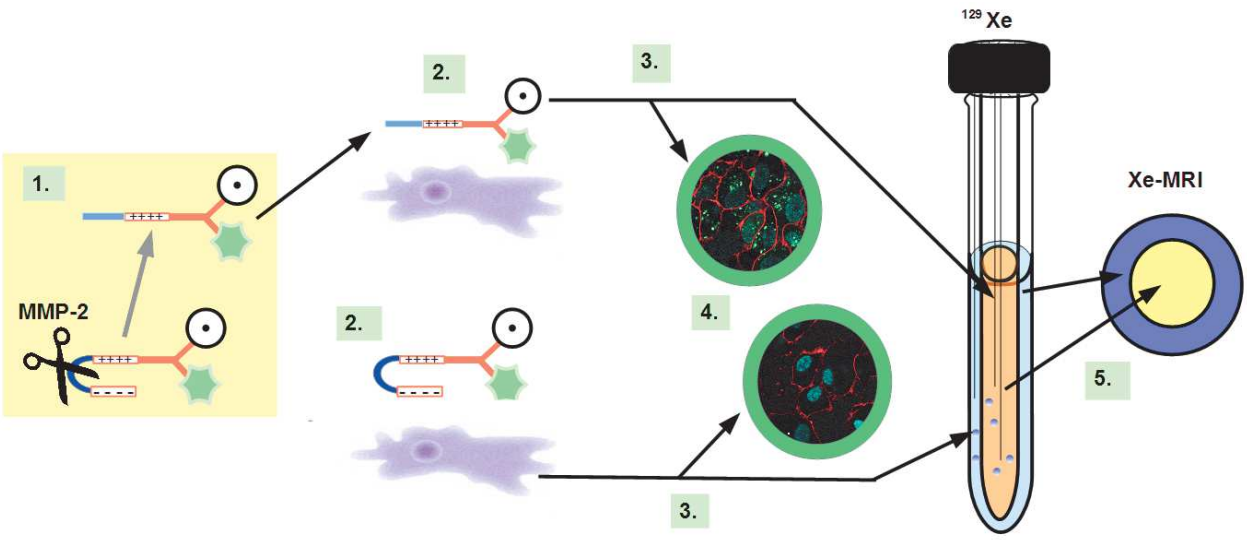

Scheme 1 Work-flow with dual ACPPs fluorescence/xenon-MRI constructs. 1. Production of "pre-cleaved" through cleavage with MMP-2. 2. Incubation with the positive (upper part) and negative (lower part) control construct on cells (37°C, 1 hrs, 2 µM final concentration for each). 3. washing and harvesting of cells. 4. FACS and cell plate measurements. 5. Double-phantom Xe-MRI.

before, the “pre-cleaved” substrate was produced from 200 µM of **15** in 20 µL of buffer; therefore, for having the samples at the same conditions, we used individual stocks of 200 µM of **15** in 20 µL of buffer, then diluted this to 2µM in a final 2 mL of cell culture media.

For the negative control sample, 0.8 µL of a 1000 mM stock of GM6001 in DMSO was added. All other samples therefore also contained the same final concentration of DMSO (0.1%) than the one of **15** w/GM6001. The cells were incubated in the dark for 1 hour at 37°C in a 5% CO_2 cell culture incubator.

After incubation, the media was removed and the cells were washed 5 times with PBS in order to efficiently remove all unbound sensor before cells were harvested from the culture plate (Scheme 1.3) and the cell pellets resuspended in PBS. From the same sample, a small fraction (ca. 20000 cells/mL) was collected (Scheme 1.4) and measured with flow cytometry, to confirm the degree of cell labelling.

The other fraction of each sample, usually consisting in ca. 10 millions of cells/mL, was placed in a dedicated double-phantom for MRI equipped with capillaries for Xe bubbling (Scheme 1.5).

In this set-up, the inner tube contains cells labelled with the positive control (“pre-cleaved”), while in the outer tube contains cells labelled with **15** or with **15** w/GM6001. Prior to performing the experiment on cells, the Hyper-CEST effect of **15** and its pre-cleaved derivative at 9.8 µM in PBS were tested separately for different saturation conditions (Fig12a and b).

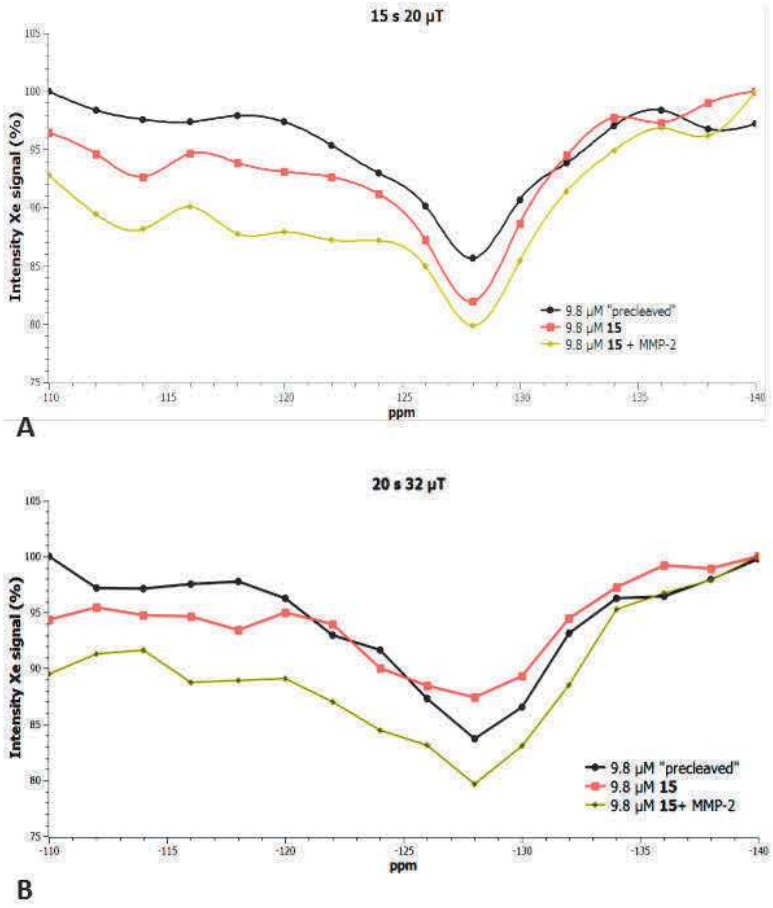

*Fig.12 Hyper-CEST response of 9.8 µM of **15**, **15** w/MMP-2 and “pre-cleaved” in PBS. A. 15 s, 20µT sat. B 20 s, 32 µT sat.*

As mentioned previously, the “pre-cleaved” substrate was produced by enzymatic cleavage, but has not been separated from the enzyme. We considered this unnecessary given the low final concentration after dilution (2.5 nM of enzyme vs. 9.8 μM probe).

However, MMP-2 is a 62 kDa protein, therefore we needed to test whether it had a negative influence on acquisition, being that proteins can cause an increase of foaming once xenon is bubbled into the sample. We prepared therefore two controls, one consisting of **15** at 9.8 μM, and the other of **15** at the same concentration, but with 2.5 nM of enzyme. MMP-2 was spiked into the solution and the sample was immediately measured, therefore we can assume that no cleavage was happening during the measurement.

Fig.12a shows the Hyper-CEST response at 20 s, 32 dB (36 μT) saturation pulse, while Fig.12 b shows the Hyper-CEST response at 12 s, 40 dB saturation pulse (20 μT).

In general, the Hyper-CEST response of **15** and “pre-cleaved” is modest (only 20%) if compared with other constructs we discussed. However, even if low, the two constructs respond in a very comparable way. No influence of the presence of MMP-2 was noticed: there was not a pronounced foaming during Xe bubbling.

We expect anyway that the main contribution of the Hyper-CEST effect would come directly from the very efficient cell uptake in the case of the pre-cleaved sensor that would provide a sufficient contrast from the uncleaved sensor **15**.

In cell Xe-MRI experiments in fact fully confirmed our idea. In Fig.13 results from the Xe-MRI double phantom containing cells labelled either with the “pre-cleaved” (inner compartment) or **15** w/GM6001 (outer compartment).

The Hyper-CEST effect (Fig. 13c and d) of the positive control is ca. 80% higher compared to the response from **15**. In comparison, the Hyper-CEST response of ca. 20% from the negative control is significantly lower. This correlates with our flow cytometry data that showed for one hour incubation a ca. 5-fold increased uptake of “pre-cleaved” with respect to **15**. Based on the fluorescence quantification, knowing the number of cells and the volume of the well plate and of the NMR phantom, a presumable concentration of around 2 μM of CrA could be calculated for the inner compartment and around 0.16 μM for the outer compartment. This result confirms the possibility to predict the Hyper-CEST response of a sensor also based on the fluorescent measurement, as we had already shown in previous work.

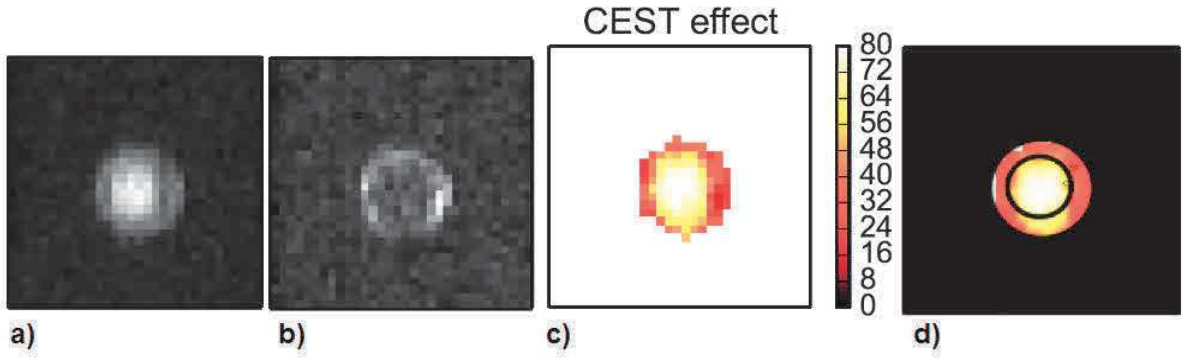

Fig.13 Double-phantom Xe-MRI response of 15/GM6001 (outer compartment) and “pre-cleaved” in the inner compartment. a) and b) on- and off-resonant images acquired at 124 ppm and -124 ppm saturation offset. c) Hyper-CEST images of cells incubated without proton MRI.

Furthermore, comparing the fluorescent labelling, the incubation of 50 μM of our probe **2** in cells would produce an intracellular uptake of 1.6 μM; while the incubation of 25 times less of the pre-cleaved sensor for only 1 hour time was already resulting in ~ 2 μM concentration (Tab 1). This reinforces the benefits of having

Tab1: Example of calculatation of estimated concentration of Cr-A in the two phantom compartment based on the measurement of fluorescence associated with cells in a plate reader.

Compound (*)	"pre-cleaved"	**15**	**15**+GM6001
Fluorescence (Abs)	1225	127	118
Tot. FAM conc. [µM]	2.49	0.26	0.26
# cells/well (**)	433000	471000	628000
conc. sensor[fmol/cell]	0,534	0,0548	0,0341
# cells/MRI phantom (***)	4700000	4700000	4700000
Conc. CrA sensor in MRI experiment [µM]	2.5	0,26	0,16

(*) incubation conc. 2 µM
(**) volume x well, 100 µL
(***) volume MRI phantom, 1 mL

a cell penetrating peptide sequence as a component of the biosensor. Indeed, as for similar experiments with ACPPs, the very good imaging performances are mainly explained by a very efficient accumulation of the sensor in the desired target, which is, in this case, cells overexpressing MMP-2/9.
The Xe-MRI response was also measured with the same parameters using **15** without the inhibitor as control in the outer compartment. (Fig. 14) Also in this case, a bigger Hyper-CEST response associated with the cell internalization of the "pre-cleaved" was measured. The response of **15** was, however, not as uniform and as low as the one of the previous examples. In fact a Hyper-CEST effect ranging from 25-50% was measured.

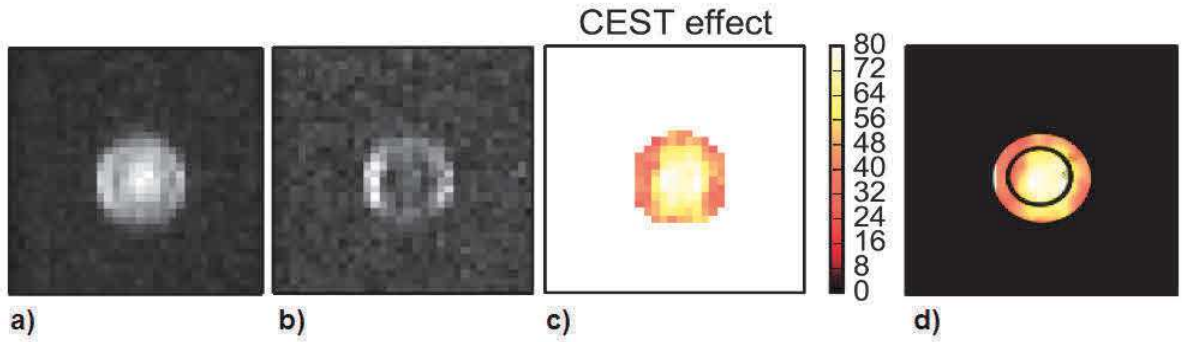

Fig.14 Double-phantom Xe-MRI response of 15 (outer compartment) and "pre-cleaved" a) and b) on- and off-resonant images acquired at 124 ppm and -124 ppm saturation offset. c) Hyper-CEST images of cells incubated without proton overlay d) overlay of CEST MRI and proton MRI for geometrical reference.

The corresponding fluorescence quantification in this case yielded 30 nM for **15**, i.e., more than ten times lower than that for "pre-cleaved" but higher than that for **15**+GM6001 The relative florescence from flow cytometry data in general showed a similar response for the cells in the presence or absence of the inhibitor (Fig.8). Moreover, the previous fluorescence quantification of **15** and **15** w/GM6001 were also comparable (0.1 fmol/cell) at such short incubation time. However, although the cellular uptake, which is significantly facilitated for the CPP construct, is the main reason to explain a better contrast in Hyper-CEST a partial cleavage of **15** in a 1-hour time scale cannot be fully ruled out. To further validate this method as a tool to discriminate between cells with different MMP-2/9 activity, we would ideally expand these experiments to

include additional control cell lines with low MMP-2/9 activity, cell lines in which the MMP-2/9 is fully activated [242] or with 3D-cultures. [212]

5.5 Conclusions and outlook

Probes based on ACPPs are a very attractive platform for designing imaging agents as they combine ability for efficient amplification with high specificity. Furthermore, the presence of a CPP can be used to deliver the reporter to the cytosol at a low, non-toxic concentration. This is very important as it is otherwise hard to reach a sufficient concentration to produce a contrast in imaging when the target of interest is inside the cells.

The versatility of the design, offered by the functionalisation of the peptidic backbone, has been proven to enable efficient response and signal contrast upon MMP-2/9 cleavage with many imaging techniques, from PET/SPECT, to MRI and to NIR fluorescence. Our MMP-2/9-responsive-ACPP probe produces a strong, specific contrast upon activation both in Xe-MRI and in fluorescence.

Once again, our flow cytometry and fluorescence quantification data agreed with the measurement on Xe-NMR and represent valid methods to pre-determine the optimal conditions for NMR experiments.

Furthermore, the flexibility of the peptide-based probe is a key point, as it allows several modifications on the backbone, specially bearing in mind to optimize such probe for *in vivo* detection in future. Indeed, ACPPs have been tested in vivo, and in some studies a non-specific activation of the probe has been reported. [217] The presence of Tissue Inhibitors of MMPs (TIMPs) in cell stroma could lead to a physiological inactivation of the enzyme, and also, a short half-time of the probe and the increased perfusion in tumour tissue could easily lead the probe to be insufficiently activated by the target enzyme.[92] For this reason, the probe's functionalization with albumin has been used to increase the probe circulation in blood stream: this strategy is however not specific.[216] A very elegant solution is, for instance, using a double signalling modality for the same cells, such as the MMP-2/9 cleavable sequence in tandem with a cyclid RGD, recognized by the integrin receptor. Both targets are reported to be present on tumour cells, and the integrin, which is a cell membrane receptor, would provide an extra anchoring point to the cell for the same probe, increasing specificity.[218]

Improvement in specificity can also be achieved by the use of ratiometric read outs.[215] In our case, using such a strategy both for fluorescence and for Xe-MRI, seems a good way to obtain a more reliable quantification.

To conclude, compound **15** represents a probe that could satisfy some of the most important features such as biocompatibility, sensitivity and specificity. The results warrant future studies under more complex physiological conditions

6.General conclusions

The Hyper-CEST Xe-NMR/MRI technique offers great possibilities for performing molecular imaging by combining good penetration depth, high sensitivity, high specificity and convenient safeness. The use of hyperpolarized Xe provides the sensitivity component whereas the incorporation of specific functionalized Xe hosts such as Cr-A yield specificity by determining the selective saturation frequency to also allow multiplexed imaging. Furthermore, the additional signal enhancement obtained through the indirect detection with Hyper-CEST allows improving significantly the sensitivity which is usually a well-known drawback of proton MRI. This means also that a much lower (nM instead of µM) concentration of contrast agent is needed for detection, therefore there is also less risk with regard to possible toxic side effects. However, Cr-A-based sensors available prior to this work suffered from narrow synthesis design and even more advanced versions potentially reporting on enzyme activity had only been demonstrated with direct detection, thereby neglecting the amplification potential of Hyper-CEST. The aim of this thesis was therefore to a) develop flexible building blocks for various sensors and b) demonstrate the concept of enzymatic amplification in the context of Hyper-CEST MRI, preferably under live cell conditions and with complementing readout techniques for independent verification.

The feasibility of the previously mentioned theoretical concepts including in situ retention of enzyme-specific reporters through activatable cell penetrating peptides was fully proved by our *in cellulo* studies. Design of these compounds started with characterization of uptake of unfunctionalized Cr-A into cells as a reference point. This first step illustrated sufficient internalization in the micromolar range, though requiring still comparable extracellular incubation concentrations. The uptake driven by the hydrophobicity of the cage and its measurable partition in the lipid environment was studied through Hyper-CEST spectroscopy.

These preliminary studies focused on unspecific labelling of cells to identify the contribution of the hydrophobic cage where this aspect would be an unwanted behaviour that could mask targeted uptake. The experiments also correlated for the first time Hyper-CEST performance with quantitative uptake analysis through dual labelling (fluorescence/Xe-MRI). The synthesized probes allowed developing protocols for subsequent functionalized cage compounds to track and quantify the biosensor in the cells through optical methods. A set of experiments with different cell lines and dyes (hydrophilic or hydrophobic) gave useful information about the sensor impact on cells, in particular the link between facilitated cellular uptake and decreased cell viability, Hence, they were a useful prerequisite to plan efficiently the NMR experiment. This includes a rational probe design concerning choice of the fluorescent dye, linker length, and their impact on optimum MRI parameters. These can be pre-determined for a specific protocol with respect to time and concentration for the incubation and satisfying cell viability by performing NMR test scans with unfunctionalized cage at concentrations corresponding to the ones determined by the fluorescence analysis of the synthesized dual probes. The development and testing of novel Xe biosensor was efficiently streamlined through this approach.

In our probe design, we decided to start from with a peptidic backbone, synthesized through Fmoc-SPPS, that then was conjugated to Cr-A-ma through acylation. This simple design offers the advantage of being easily modifiable not only according to the desired targets or but also to the desired payloads. The mw-assisted peptide synthesis reveals to be a very efficient technique to test and optimize synthesis and make it more economical in terms of saving time and reaction solvents. By coupling the Xe host unit with

commercially available or custom-made building blocks we could set up a modular platform which allowed us to improve solubility and biocompatibility of the sensor. Implementation of this approach was crucial once we started to work with sensors targeted to cell surface receptors. In fact, in the case of the antibody-based anti-CD14 sensor we used the modular design offered by the biotin-CrA/FAM/avidin conjugates to study cell surface targets unprecedented sensitivity after optimization of incubation conditions and demonstrating two assembling modalities.

Despite the success of this antibody-based sensor in terms of excellent MRI mapping of its presence on macrophages vs. fibroblasts, an alternative sensor design was also investigated in this thesis to address additional challenges. Depending on the desired diagnostic information, it can be beneficial to switch the targeting approach for improving the sensing abilities as follows: i) the clearance of an antibody can be problematic in vivo; therefore, the use of a small peptides can be preferable ii) targeting cell surface receptors with an antibody is always limited by the quantity of the receptor present on cells; this parameter is often in the picomolar range. iii) the binding to a receptor alone does not provide information about the activity of a molecular target which can be an essential information in the context of certain diseases.

To address these challenges, we synthesized a peptidic-based cleavable Cr-A-bearing biosensor which can be recognized by a specific enzyme. A similar design had been previously presented by others but neither the feasibility of monitoring the cleavage itself with NMR after attaching Cr-A as the NMR reporter nor the possibility to perform sensitive Xe MRI detection through saturation transfer had been demonstrated. The big advantage of such an approach is to have both information about enzymatic activity through the number of cleaved sensors and an amplifable signal since each enzyme unit processes multiple substrate molecules. We first choose MMP-11 because of the relevance of this enzyme in cancer progression. We tried different designs in order to obtain the best Xe-NMR response, and we came up with a “Y-shape”-PEGylated Cr-A probe that was characterized by an initially sufficient water solubility and a good Xe-NMR signal. In comparison with a previous simple MMP-7 responsive probe proposed by Wei et al., the spectral dispersion of our sensor was improved. However, measuring a time-course response by using Hyper-CEST spectroscopy to illustrate cleavage of the cage-substrate conjugate turned out to be challenging due to solubility issues of the cleaved compound. Eventually, this prompted us to re-design an activatable sensor and address a new target.

We therefore focused on MMP-2/9, which is a relevant molecular diagnostic target for which an extensive literature and many cellular/animal models are available. Our new design was mainly driven by the interest of circumventing the solubility issue through incorporation of unit that enables translation into cells, a feature provided by charged poly-peptides. Such an approach per se comes with increased hydrophilicity and also retains the activated sensor at the target tissue of enzyme expression. Probes based on activatable cell-penetrating peptides (ACPPs) are particularly suitable for *in cellulo* and *in vivo* studies because, upon cleavage, the unmasked CPP can efficiently accumulate into the cell, giving rise to a high contrast.

Contrary to CPPs, ACPPs are selectively activated by an enzyme, therefore being very specific and efficient in cell uptake. Eventually, this allowed us to use a low, non-toxic concentration for an activatable reporter. Our MMP-2/9-responsive-ACPP probe could produce a strong, specific contrast (up to 80% CEST effect) both in Xe-MRI and in fluorescence upon activation. By using a fairly small amount of probe for only 1 hour incubation (2 μM compared to up to 50 μM even requiring extended incubation periods for the non-activatable cage-dye compounds) we could observe an easily detectable signal, distinguishable from environments with the non-cleaved construct. This also means that not only a positive/negative control

experiment, but also a different degree of MMP-2/9 activaction should theoretically be detectable. Once again, our flow cytometry and fluorescence quantification data agreed with the measurement on Xe-NMR and represented valid methods to pre-determine the optimal conditions for NMR experiments.

Also, the problem of otherwise unspecific binding of Cr-A to the cells was addressed by the structure of uncleaved sensor which masks the lipophilicity of the cage sufficiently. Cellular binding is prevented until cleavage, thus providing considerably better labelling in the positive control sample. However, this change in hydrophobicity upon cleavage (sometimes used as a solubility switch in other MMP studies to enable prolonged retention through association with membrane environment) remains as one of the non-negligible challenges in designing experiments *in cellulo*: in this case, the probe was sufficiently soluble with a cell-compatible DMSO fraction of 0.2% and the ACPP efficiency allowed also a low incubation concentration. Overall this reduced significantly the issue of solubility of our precedent labelling design.

Furthermore, with the aim of the *in vivo* translation of such probes (as also studied elsewherewith PET/SPECT, NIR imaging and MRI), the flexibility of the peptide-based probe is an important point to make our probe more biocompatible and suitable for such studies. To conclude, the ACPP-Cr-A based probe was the result of a rational design that was successful in improving the performance with regard to biocompatibility, sensitivity and specificity of the probe. This sensor, in conjunction with the implementation of the Hyper-CEST Xe-MRI technique, allowed us to obtain for the first time specific MRI signals from cells triggered by an enzymatic activity.

Altogether, the approaches presented in this work advanced the design and synthesis of Xe-based biosensors compared to the initial situation with limitations such as limited design flexibility and unproven NMR/MRI performance in cellular environments. The synthesized probes represent important elements to illustrate the potential and robustness of the Hyper-CEST detection technique. The protocols developed here will contribute to the design and testing of various future sensors. Activatable versions including ACPPs are a promising approach to implement molecular imaging techniques that aim to visualize target activity rather than simple target presence, an aspect which is of particular interest in the context of MMPs where a more complex picture of understanding the role of truly active versus “just expressed” enzyme has emerged in recent years.

Materials and Methods

7.*Synthesis and evaluation of the Cr-A probes*

7.1 Reagents and instrumentation

All solvents were purchased from Carl Roth (Karlsruhe, Germany) at peptide synthesis pure grade. Fmoc-protected amino-acids Fmoc-Gly-OH, Fmoc-Met-OH, Fmoc-Arg(Pbf)-OH, Fmoc-Leu-OH, Fmoc-Asn(Trt)-OH, Fmoc-Ala-OH, Fmoc-Pro-OH, Fmoc-Tyr(Trt)-OH, Fmoc-Lys(Trt)-OH, Fmoc-Glu(OtBu)-OH and Fmoc-Ahx-OH were purchased from Merck Novabiochem (Darmstadt, Germany). Fmoc-Cys(Mob)-OH was obtained from Bachem (Bubendorf, Switzerland). Fmoc-Lys(5/6 FAM)-OH was purchased from Anaspec (Fremont, California), 5,6-Tetramethyl Rhodamine (5,6 TAMRA) and 5,6 Fluoresceine (5,6 FAM) from AAT Bioquest (Sunnyvale, California). PEGylated building blocks Fmoc-PEG_3-COOH, Fmoc-CH_2-PEG_3-COOH (Fmoc-AEAAA), mPEG_{10}-CH_2COOH and biotin-PEG_3-amine were purchased from ChemPep (Miami, Florida) whereas Fmoc-D-Arg(Pbf)-OH and Fmoc-D-Glu(OtBu) were purchased from Iris Biotech GmbH (Marktredwitz, Germany).

Coupling reagents COMU, HATU and PyBOP and bases DIPEA and 2,4,6 trimethylpiridine (collidine) have been purchased from Sigma Aldrich (Munich, Germany), while PyOxim was purchased from Merck Novabiochem (Darmstadt, Germany). 2-Cl Trytil and Gly(NH_2)-2-Cl Trytil resins were purchased from Merck Novabiochem (Darmstadt, Germany), while ChemMatrix® rink amide resin was purchased from PCAS Biomatrix Inc (Saint-Jean-sur-Richelieu, Quebec, Canada). TentaGel® PAP resin was obtained through Rapp Polymere (Tuebigen, Germany). Cr-A monoacid (Cr-A-ma) and Cr-A diacid (Cr-A-da) have been provided by Kangyuan Jiyi Inc. (Shangdong, PRC).

Enzyme's catalytic site of human MMP-11 was purchased from Enzo Life Science (Lörrach, Germany), and human recombinant active human MMP-2 was purchase from Sigma Aldrich (Munich, Germany). Hepes and TRIS buffer and $ZnCl_2$ were purchased from Sigma Aldrich (Munich, Germany), while $CaCl_2$ and NaCl were purchased from Carl Roth (Karlsruhe, Germany).

Mw-assisted synthesis was carried using a Biotage SP wave Initiator+ microwave integrated system for organic synthesis and peptide synthesis (Biotage, Lund, Sweden). All purifications were carried out by RP-HPLC using a CBM10A HPLC equipped with a SPD-M10 PDA detector (Shimadzu, Kyoto, Japan) and a VariTide RPC column, 200 Å, 6 µm, 10 x 250 mm (Agilent, Santa Clara, USA). HPLC-MS/MS analysis were done on UFLC Shimadzu (Toyko, Japan) equipped with a 4000 QTRAP MS/MS (Abi/Sciex, Framinghan, MA, USA). Molecular masses were confirmed using a MALDI-TOF AB SCIEX 5800 mass spectrometer (Applied Biosystems, Forster City, CA, USA), and a MALDI-TOF MicroFlex LT (Bruker Analytics, Berlin, Germany). Cleavage reactions were carried at controlled temperature on a block thermostat (Carl Roth, Karlsruhe, Germany).

7.2 Synthesis of CrA-PEG_3-FAM (2) (§2.2.2)

2 has been synthesized by coupling the fluorogenic peptide PEG_3-FAM to CrA-ma. PEG_3-FAM was synthesized via standard Fmoc-SPPS. [106] Briefly, Fmoc-Lys(5/6 FAM)-OH (2 eq.) was attached on resin previously loaded with glycine (0.63 g/mmol loading) using COMU (2 eq.)/DIPEA (4 eq.) in DMF. The reaction has been carried out overnight. The acylation was confirmed using the Kaiser test. [166] The Fmoc

deprotection was achieved using 25% piperidine in DMF for 15 min, twice, at room temperature. The resin was then coupled with Fmoc-PEG_3OH, using COMU/DIPEA, following the same protocol used for the coupling of Fmoc-Lys(5/6 FAM)-OH. Then, the Fmoc protecting group of the spacer linked to the synthesized peptide was removed prior to cleavage from the resin. The cleavage was carried out with TFA/TIS/H_2O (95:2.5:2.5) for 2 hours and then substrates were precipitated and washed six times with cold diethyl ether. The cleaved peptide was purified with RP-HPLC/UV, and the mass corresponding to PEG-FAM has been confirmed via MALDI/TOF followed by lyophilisation. Cr-A monoacid was coupled in solution with PEG-FAM through its carboxylic unit. Briefly, 1 eq. of Cr-A monoacid dissolved in DMF has been activated with 1 eq. of COMU in presence of DIPEA (2 eq.) at 0°C for 5 min. The coupling reaction has then been carried out for 2 hours at 45°C. After that, the reaction was quenched, the mixture was diluted 1:10 in HPLC mobile phase (30% CH_3CN in water, 0.1% of TFA) and purified. (**2**)

Purification was carried out by RP-HPLC with UV detector scanning the wavelengths scanned 230, 485 and 290 nm. The calculated mass was m/z = 1670 for $C_{92}H_{94}N_4O_{26}$ (**2**). Mass spectra found for **2** was m/z = 1674 (corresponding to m+1 of the quinoid form, 1673).

7.3 Synthesis of Fmoc-Lys(CrA)-OH (§2.3.1)

Probe **3** was used as a model for the coupling of Cr-A-ma to amino-groups. For the first optimization (coupling agents, see Table 1 of Results), 1 eq. of Cr-A-ma was dissolved in DMF and activated for 2 minutes at room temperature with 1 eq. of HATU or PyOxim or COMU or PyBOP, in presence of 2.5 eq. of DIPEA. The activated mixture was then placed in a 1 mL mw vial, and 1 eq. of Fmoc-Lys (OH) dissolved in DMF was added. The final volume was 0.7 mL, and Cr-A-ma was at the concentration of 0.1 M. The vial was irradiated with mw at 50°C for 10 min.

Based on the result, PyOxim was used for the second optimization, concerning the stoichiometry of the reaction (Table 1, §2.3.1) 1 eq. of Cr-A-ma was dissolved in DMF and activated for 2 minutes at room temperature with 2 eq. of PyOxim, or the inverse ratio (2 eq. of Cr-A-ma and 1 eq. of PyOxim) in presence of 2.5 eq. of DIPEA. The activated mixture was then placed in a 1 mL mw vial, and 1 eq. of Fmoc-Lys (OH) dissolved in DMF was added. The final volume was 0.7 mL, and Cr-A-ma was present(?) at the concentration of 0.1 M. The vial was irradiated with mw at 50°C for 10 min.

For the third optimization (time/temperature of reaction, Table 1, §2.3.1), the ratio amine:carboxylic acid 1:1 was chosen. 1 eq. of Cr-A-ma was dissolved in DMF and activated for 2 minutes at room temperature with 1 eq. of PyOxim, in presence of 2.5 eq. of DIPEA. The activated mixture was then placed in a 1 mL mw vial, and 1 eq. of Fmoc-Lys (OH) dissolved in DMF was added. The final volume was 0.7 mL, and Cr-A-ma was at the concentration of 0.1 M. The vial was irradiated with mw at 75°C/30 min or 50°C/20 min or 100°C/5 min. After that, each reaction has been quenched with 4 mL of HPLC mobile phase (30% CH_3CN in water, 0.1% of TFA) and purified via RP-HPLC-UV.

The fractions relative to the calculated mass for **3** ($C_{76}H_{76}N_2O_{17}$, m/z = 1289) m/z = 1311, corresponding to m+23 (mass plus Na^+) were isolated and liophylized. In the best protocol (amine: carboxylic acid:PyOxim, 1:1:1; mw 75°C, 10 minutes) the yield of reaction was 47%.

7.4 Mw-assisted synthesis of CrA-PEG_3-TAMRA (4) (§2.3.2)

4 was synthesized using mw-assisted SPPS. Briefly, 2-Cl-Trityl resin, previously loaded with glycine (resin loading 0.5 mmol/g) has been coupled with 3 eq. of Fmoc-Lys(OH), previously activated with PyOxim (3 eq.)

and DIPEA (6eq.), using microwave irradiation for 10 min at 50ºC.[107] The free ε-amino terminus of the Lys was coupled with 3 eq. of 5,6-TAMRA (10 min at 50º), using PyOxim (3 eq.)/DIPEA (6 eq) to obtain a Lys-(TAMRA) unit. After Fmoc deprotection with 25% Piperidine/DMF (15 min, twice, at room temperature) the resin has been coupled with an Fmoc-protected three PEG units building block (Fmoc-PEG_3OH), using the same protocol of the coupling of Fmoc-Lys-OH. Finally, the α-amino group of the spacer linked to the synthesized peptide was deprotected from Fmoc prior to cleavage from resin. The peptidic backbone has then been cleaved from the resin in mild conditions (acetic acid/trifluoroethanol/dichloromethan 1:1:8 for 30 min at r.t.) [109].The mass analysis showed that the peptide was pure and did not need further purification. 1 eq. of TAMRA-PEG was coupled is solution phase with 1 eq. of Cr-A-ma, dissolved in DMF previous pre-activation for 2 min at r.t. with 1 eq. of PyOxim and 2.5 eq. of DIPEA. The reaction mixture was irradiated with mw for 10 min at 75°C, and subsequently quenched, diluted 1:10 in HPLC mobile phase (30% CH_3CN in water, 0.1% of TFA) and purified.

Purification was carried out by RP-HPLC with a UV detector, and the wavelengths scanned were 230, 560 and 290 nm for **4**. The calculated mass was m/z = 1724 for $C_{96}H_{104}N_6O_{24}$ (**4**), referred to the lactone form, which is present to 70% is aqueous environment. Mass spectra found for **4** was m/z = 1725 (corresponding to m+1 of the lactone form) has been found.

7.4 Mw-assisted synthesis of CrA-PEG_3-biotin (6) (§2.5.2)

CrA-PEG_3-biotin (**6**) has been synthesized using mw-assisted solution synthesis, following the previously mentioned protocol developed for **3**. Briefly, 1 eq. of Cr-A were dissolved in DMF at the concentration of 0.15 M and activated for 2 min at r.t. with 1 eq. of PyOxim (1 eq.) and 2.5 eq. of DIPEA. The mixture was then transfered into a 5 mL mw vial containing biotin-PEG_3-amine (1 eq.) already dissolved in DMF. The acylation was carried using microwave irradiation for 10 min at 75ºC. The reaction was then quenched, diluted 1:10 in HPLC mobile phase (30% CH_3CN in water, 0.1% of TFA) and purified. The calculated mass was m/z = 1338 for $C_{73}H_{86}N_{18}O_{18}S$. For Cr-A-$PEG_3$-biotin m/z = 1339 (corresponding to m+1) and 1361 (corresponding to m+23, mass + sodium) has been found. The final yield was 48%.

7.5. Mw-assisted synthesis of "branched construct" (§2.5.2)

The "branched construct" consist of three parts that are connected together: i) Biotin-PEG_3-amine ii) Cr-A diacid and iii) PEG-FAM-amide. This latter was synthesized via mw-assisted Fmoc-SPPS, as for **2**. Briefly, for iii) Fmoc-Gly-OH (5 eq.), previously activated with PyOxim (5 eq.)/DIPEA (10 eq.) in DMF, was attached on H-Rink amide ChemMatrix® resin (0.45 g/mmol loading)[128-129] using microwave irradiation for 10 min at 50ºC. The degree of acylation calculated with UV-Fmoc determination was 92%. The Fmoc deprotection was achieved using 25% piperidine in DMF for 15 min, twice, at r.t. The peptide on the resin was then coupled with Fmoc-Lys(5/6 FAM)-OH using PyOxim (5 eq.)/DIPEA (10 eq.), deprotected from Fmoc and finally coupled with Fmoc-AEAAA, using the same protocol used for Fmoc-Gly-OH. After the last Fmoc deprotection, the peptide was cleaved from the resin with TFA/TIS/H_2O (95:2.5:2.5) for 2 hours. The substrates were precipitated and washed six times with cold diethyl ether. The cleaved peptide was purified with RP-HPLC/UV, and the mass corresponding to the peptide has been confirmed via MALDI/TOF and lyophilized. The yield was 53%. The synthesis of **7** was performed with the mw using a "one pot" protocol modified for the acylation. [167] Briefly, 1 eq. of Cr-A diacid (ii) has been activated for 5 min at r.t. with 2 eq. of PyOxim and 5 eq. of DIPEA. Then, 1 eq. of biotin-PEG_3-amine (i) and 1 eq. of PEG-FAM-amide (iii) were

added and the mixture has been irradiated with mw for 10 min at 50 ºC. After that, the reaction was quenched, diluted 1:10 in HPLC mobile phase (30% CH_3CN in water, 0.1% of TFA) and purified. The calculated mass was m/z = 2141 for $C_{114}H_{135}N_9O_{30}S$. For **7**, m/z = 2164 (corresponding to m+23) has been found. The fractions corresponding to Biotin-Cr-A-FAM has been lyophilized, and the yield was 10%.

7.7. Synthesis of MMP-11 responsive sensors 8/9 (§4.2)

MMP-11 responsive biosensors **8** and **9** have been synthesized with standard Fmoc-SPPS and in solution acylation with Cr-A ma. The consensus sequence RVL*NAA has been derived from the paper of Pan. [227] As discussed in the results, a paired probe with only the first part of the sequence (RVL) acetylated at the Leu amino terminus has been synthesized.

The reaction is summarized in Scheme 1. Briefly, 2-Cl Trytil resin has been coupled with 3 eq. of Fmoc-Gly (OH), activated with 3 equivalent of Oxyma pure and 6 eq. of DIPEA. The reaction has been carried at r.t. for 2 hours.

The resin loading was calculated as 90%. After Fmoc deprotection, the free amine has been coupled with 3 eq. Fmoc-Lys(Trt)-OH, activated with 3 eq. of COMU and 6 eq. of DIPEA. All the next coupling steps (with Fmoc-Arg(Pbf)OH, Fmoc-Val-OH and Fmoc-Leu-OH) were carried out as described before. At the end of each coupling and decoupling the reaction has been monitored with the Kaiser test [266] and, when the coupling or the decoupling were considered to be incomplete, the reaction was repeated. After the last coupling with Fmoc-Leu-OH, the resin has been carefully washed and split in two parts. One half of the resin has been coupled with Fmoc-Asn(Trt)OH and two Fmoc-Ala-OH as described before. Bulky Fmoc-AA as Fmoc-Asn(Trt)OH has been coupled overnight. At the end of the consensus sequence, two Gly were added as a spacer. The two resins, carrying the sequence GK(Trt)RVL-Fmoc and GK(Trt)RVLNAAGG-Fmoc, respectilvely, were Fmoc-deprotected at the end and each sequence has been capped through acetylation using acetic anhydride (5 eq.) and triethylamine (10 eq.) for 10 min.

The peptides were cleaved from the resin for 2 hours using 95% TFA, 2.5% TIS, 2.5% H_2O. During the treatment with acid, the Trt group of the Lys is removed leaving a free amino terminus. The two peptides have been precipitated with cold ether and then suspended in HPLC mobile phase, separated with RP-HPLC and finally quantified through MALDI-TOF.

For the coupling with Cr-A-ma an in house protocol [46; 74] has been used. 1 eq. of Cr-A-ma at a concentration of 0.1 M in DMF were activated at 0°C with 1 eq. of PyBOP and 1 eq. of HOAt in presence of 2 eq. of collidine. Then, 1 eq. of peptide has been added and the reaction has been carried out for 2 hours at 50°C. At the end, the reaction has been quenched with HPLC mobile phase, separated with RP-HPLC and quantified with MALDI-TOF.

The calculated mass for **8**, $C_{82}H_{103}N_9O_{20}$ is m/z = 1534.74, while for **9** $C_{96}H_{125}N_{15}O_{26}$ it is m/z = 1905.10. The mass found with the MALDI/TOF for **8** was m/z = 1534.66 and for **9** it was m/z = 1904.79, i.e., both corresponding to M. The MALDI-TOF spectra of **8** and **9** are reported in Fig. 1A and 2B, respectively.

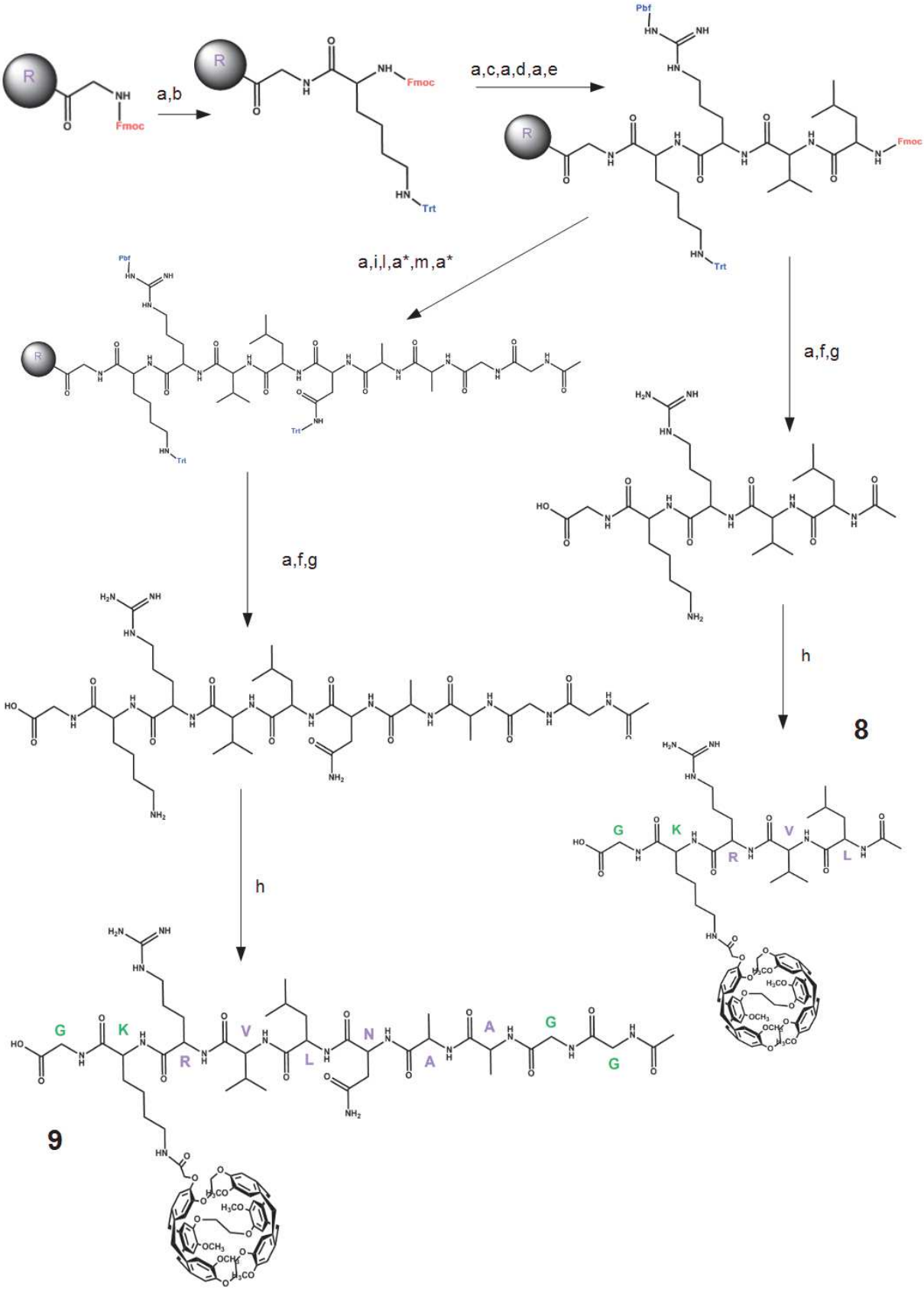

*Scheme 1: synthesis of **8** and **9.** The 2-Cl trytil resin has been coupled with 3 eq. of Fmoc-Gly-OH using 3 eq. of Oxyma/HOAt and 6 eq. of DIPEA. The reaction has been carried out in DMF for 2 hours at r.t. (a) 20% Piperidine/DMF, 15 min, twice (b) 3 eq. Fmoc-Lys(Trt)OH, 3 eq. COMU, 6 eq. DIPEA, in DMF, 2 hrs, r.t. (c) 3 eq. Fmoc-Arg(Pbf)OH, 3 eq. COMU, 6 eq. DIPEA, in DMF, 2 hrs, r.t. (d) 3 eq. Fmoc-Val OH, 3 eq. COMU, 6 eq. DIPEA, in DMF, 2 hrs, r.t. (e) 3 eq. Fmoc-Leu-OH, 3 eq. COMU, 6 eq. DIPEA, in DMF, 2 hrs, r.t. (f) 5 eq. Ac_2O, 10 eq. Et_3N, 10' r.t. (g) 95% TFA, 2.5% TIS, 2.5% H_2O, 2 hours, 2 r.t. Followed by precipitation in cold diethylether, azeotropic evaporation and separation with RP-HPLC. (h) 1 eq. Cr-A-ma, 1 eq. PyBOP, 1 eq. HOAt, 2 eq. collidine, activated for 15 min at 0°C, then carried for 2 hours, 50°C. (i) 3 eq. Fmoc-Asn(Trt)OH, 3 eq. COMU, 6 eq., in DMF, overnight, r.t. (l) 3 eq. Fmoc-Ala-OH, 3 eq. COMU, 6 eq., in DMF, 2 hours, r.t. (m) 3 eq. Fmoc-Gly-OH, 3 eq. COMU, 6 eq., in DMF, 2 hours, r.t.*

(*) This reaction was repeated twice

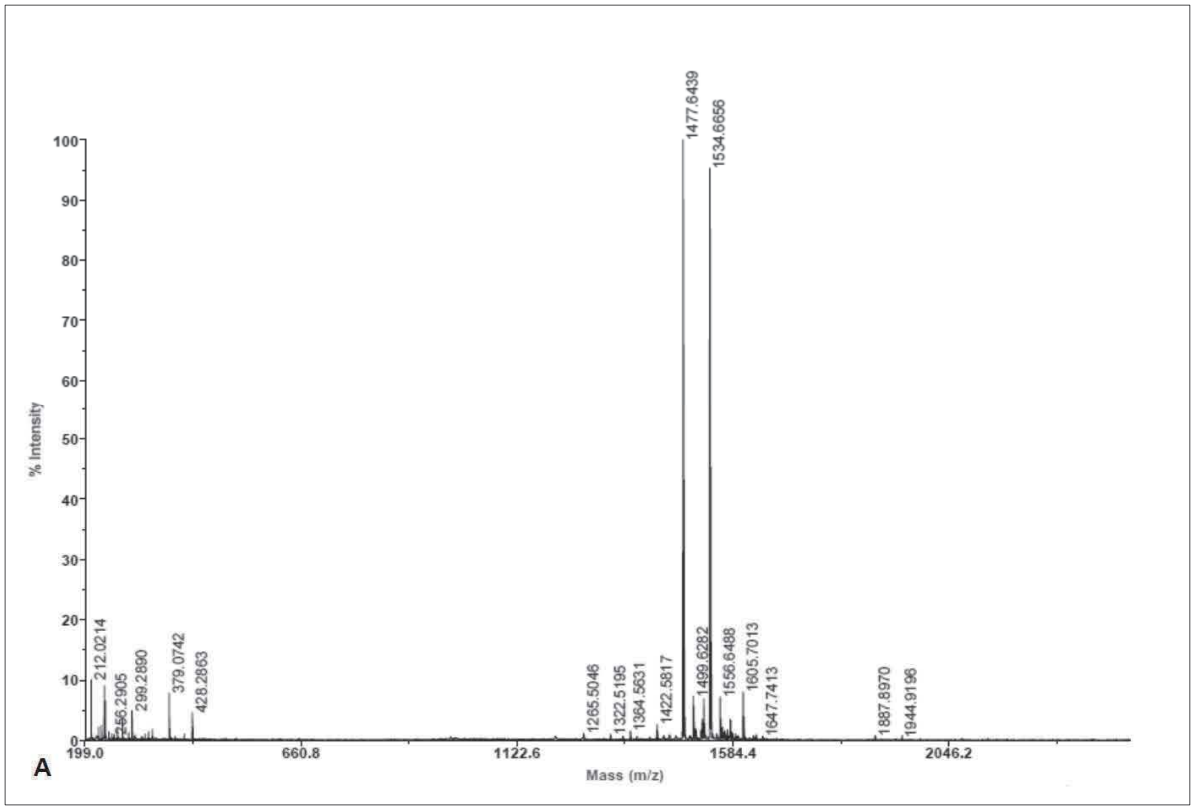

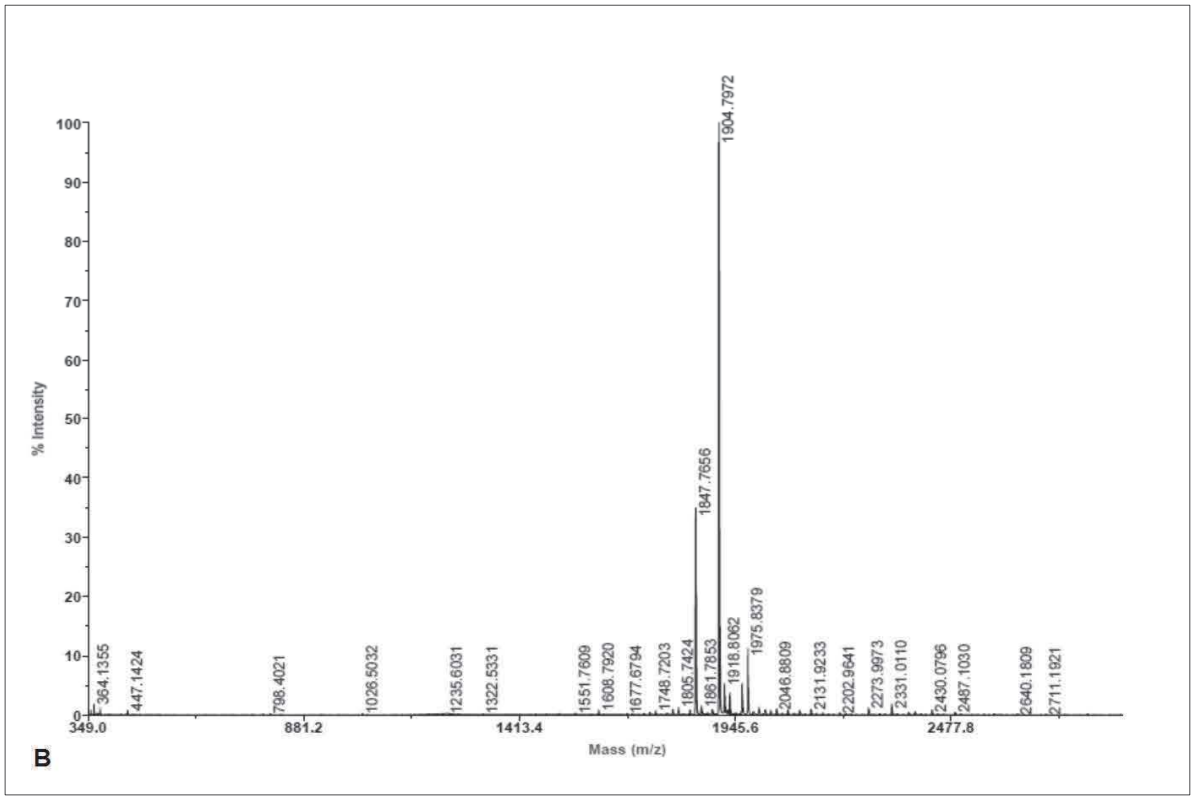

*Fig.1 A and B MALDI/TOF spectra of **8** (calculated m/z = 1534.74) and **9** (calculated m/z = 1905.10)*

7.8 Synthesis of MMP-11 responsive sensors 10 and 11 (§4.2)

MMP-11 responsive biosensors **10** and **11** have been synthesized with standard Fmoc-SPPS and in solution acylation with Cr-A-ma. The consensus sequence MRL*EAY has been derived from the paper of Wei et al, (2003)[227]. As discussed in the results, a paired probe with only the first part of the sequence (MRL) acetylated at the Leu amino terminus has been synthesized.

The reaction is summarized in Scheme 2. Briefly, 2-Cl Trytil resin has been coupled with 3 eq. of Fmoc-Gly(OH), activated with 3 eq. of Oxyma pure and 6 eq. of DIPEA. The reaction has been carried at r.t. for 2 hours with XX eq. Fmoc-Lys(Trt)-OH, activated with 3 eq. of COMU and 6 eq. of DIPEA. All the next coupling steps with Fmoc-Met-OH, Fmoc-Arg(Pbf) OH, Fmoc-Leu-OH were carried out as described before. At the end of each coupling and decoupling, the reaction has been monitored with Kaiser test[266] and, in case the coupling or the decoupling were considered to be incomplete, the reaction has been then repeated. After the last coupling with Fmoc-Leu-OH, the resin has been carefully washed and weighed and then split in two parts.

One half of the resin has been coupled with Fmoc-Glu(tBu)OH, Fmoc-Ala-OH and Fmoc-Tyr(tBu)-OH as described before. Bulky Fmoc-AA as Fmoc-Glu(tBu)OH has been coupled overnight. At the end of the consensus sequence, two Gly were added as a spacer. The two resins, carrying the sequence GK(Trt)MRL-Fmoc and GK(Trt)MRLEAYGG-Fmoc, respectively, were Fmoc-deprotected at the end each sequence was capped through acetylation using acetic anhydride (5 eq.) and trietilamine (10 eq.) for 10 min.

The peptides have been cleaved from the resin for 2 hours using the so called “K reagent”: 82.5% TFA, 5% thioanisol, 2.5% H_2O, 2.5% EDT and 1% phenol. Contrary to **8** and **9**, the use of EDT as scavenger was necessary because of the presence of EDT in the peptide sequence. During the treatment with acid, the Trt group of the Lys is removed leaving a free amino terminus.

The two peptides has been precipitated with cold ether, and then suspended in HPLC mobile phase, separated with RP-HPLC and finally quantified through MALDI-TOF.

For the coupling with Cr-A-ma, an in house protocol has been used.[46; 74] 1 eq. of Cr-A-ma at a concentration of 0.1 M in DMF were activated at 0°C with 1 eq. of PyBOP and 1 eq. of HOAt in presence of 2 eq. of collidine. Then, 1 eq. of peptide has been added and the reaction has been carried out for 2 hours at 50°C. At the end, the reaction has been quenched with HPLC mobile phase, separated with RP-HPLC and quantified with MALDI-TOF

The calculated mass for **10**, $C_{82}H_{103}N_9O_{20}S$, is m/z = 1565.69, while for **11,** $C_{103}H_{130}N_{14}O_{28}S$, it is m/z = 2042.89. The mass found with the MALDI/TOF for **10** is m/z = 1566, corresponding to M+1 and for **11** m/z = 2043 both corresponding to M+1. The MALDI-TOF spectra of 10 and 11 are reported in Fig. 2A and 2B, respectively.

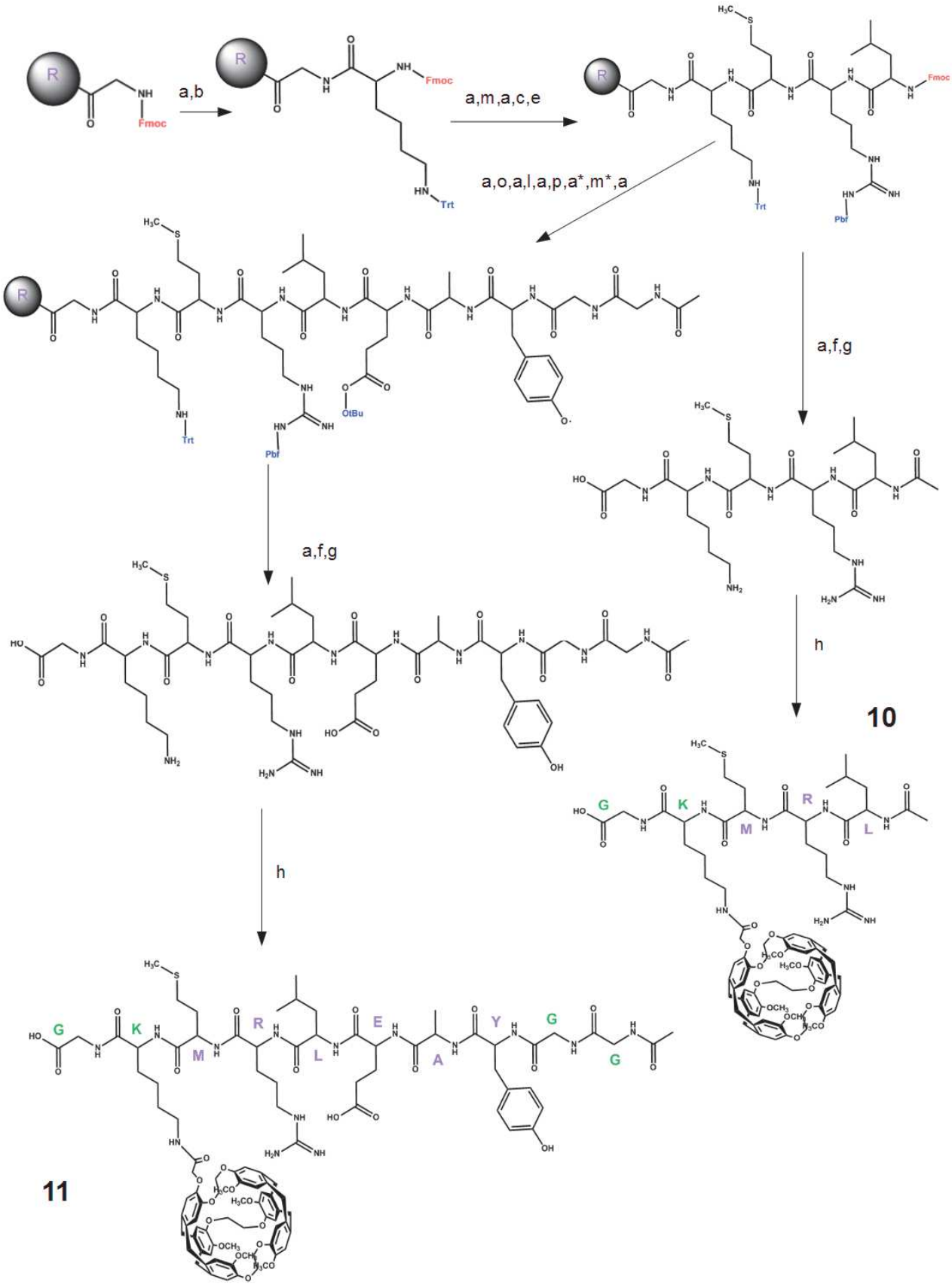

*Scheme 2: synthesis of **10** and **11.** The 2-Cl trytil resin has been coupled with 3 eq. Fmoc-Gly-OH using 3 eq. of Oxyma/HOAt and 6 eq. of DIPEA. The reaction has been carried out in DMF for 2 hours at r.t. (a) 20% Piperidine/DMF, 15 min, twice (b) 3 eq. Fmoc-Lys(Trt)OH, 3 eq. COMU, 6 eq. DIPEA, in DMF, 2 hrs, r.t. (n) 3 eq. Fmoc-Met-OH, 3 eq. COMU, 6 eq. DIPEA, in DMF, 2 hrs, r.t. (c) 3 eq. Fmoc-Arg(Pbf)OH, 3 eq. COMU, 6 eq. DIPEA, in DMF, 2 hrs, r.t. (e) 3 eq. Fmoc-Leu-OH, 3 eq. COMU, 6 eq. DIPEA, in DMF, 2 hrs, r.t. (f) 5 eq. Ac_2O, 10 eq. Et_3N, 10 min. r.t. (g) 95% TFA, 2.5% TIS, 2.5% H_2O, 2 hours, 2 r.t. Followed by precipitation in cold diethylether, azeotropic evaporation and separation with RP-HPLC. (h) 1 eq. Cr-A-ma, 1 eq. PyBOP, 1 eq. HOAt, 2 eq. collidine, activated for 15 min at 0°C, then carried for 2 hours, 50°C. (o) 3 eq. Fmoc-Glu(OtBu)OH, 3 eq. COMU, 6 eq.DIPEA, in DMF, overnight, r.t. (l) 3 eq. Fmoc-Ala-OH, 3 eq. COMU, 6 eq., in DMF, 2 hours, r.t. (p) 3 eq. Fmoc-Tyr(OtBu)OH, 3 eq COMU, 6 eq. DIPEA, in DMF, overnight, r.t. (m) 3 eq. Fmoc-Gly-OH, 3 eq. COMU, 6 eq., in DMF, 2 hours, r.t.*

(*) This reaction repeated twice

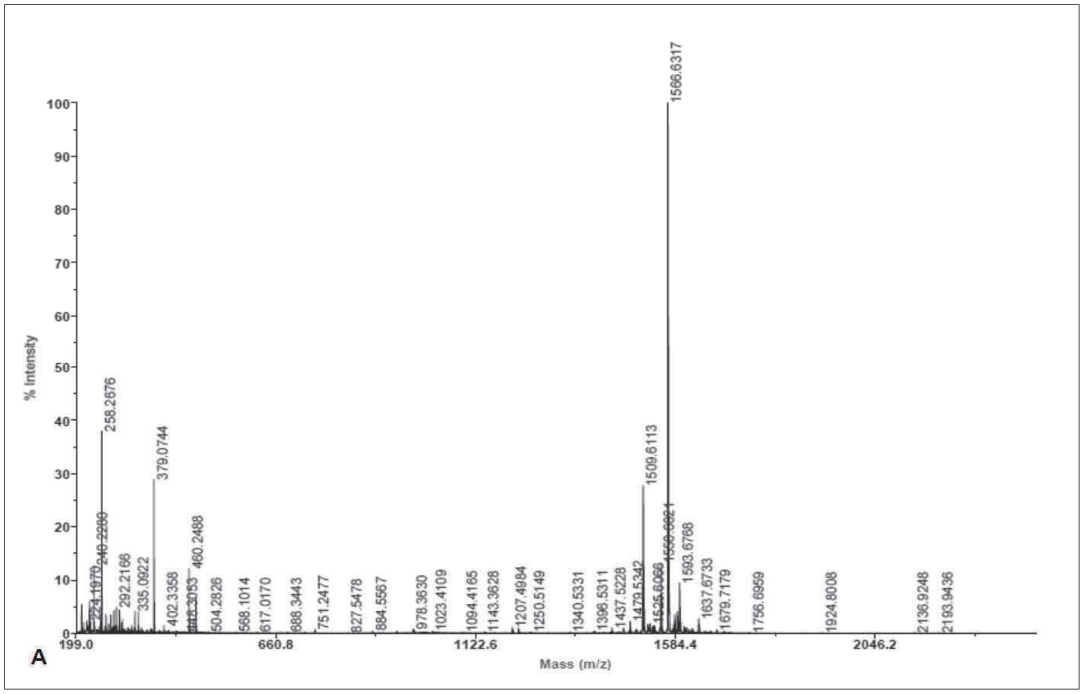

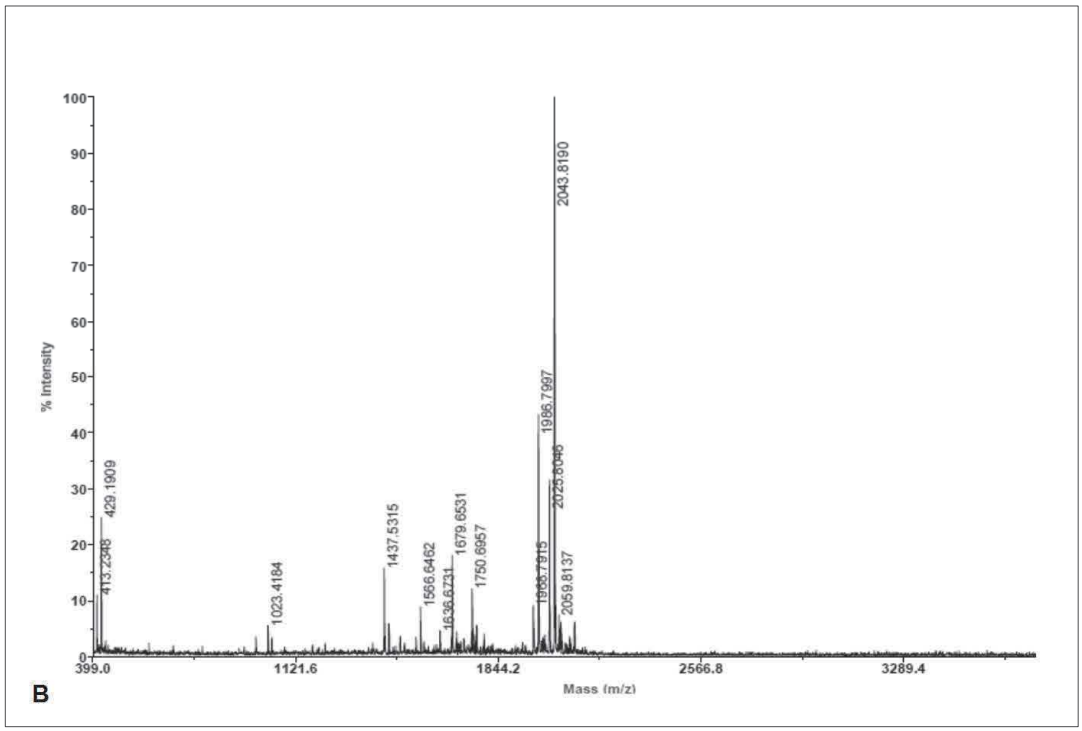

*Fig.2 A and B MALDI/TOF spectra of **10** (calculated m/z = 1565.89) and **11** (calculated m/z = 1846.67)*

7.9 Synthesis of "Y-shape" construct 12/13 (§ 4.2)

MMP-11 responsive biosensors **12** and **13** have been synthesized with standard Fmoc-SPPS and in solution acylation with Cr-A-ma. The consensus sequence MRC(Mob)*NAA has been derived from the paper of Meyeret al. [206]. As discussed in the results, a paired probe with the first part of the sequence (MRC(MOb)) acetylated at the Cys amino terminus has also been synthesized.

Briefly, 2-Cl Trytil resin has been coupled with 3 eq. of Fmoc-Gly(OH), activated with 3 eq. of Oxyma pure and 6 eq. of DIPEA. The reaction has been carried at r.t. for 2 hours. The resin loading was calculated as 70%. After Fmoc deprotection, the free amine has been coupled with 3 eq. Fmoc-AEAAA, activated with 3 eq. of COMU and 6 eq. of DIPEA. The resin, once deprotected, has been coupled with 1.5 eq. of Fmoc-Lys(CrA)OH **4**, 1.5 eq. COMU, 3 eq. of DIPEA, r.t. overnight. **4** is an in-house synthesized building block coupling Fmoc-Lys(OH) and CrA-ma, with the same protocol described before for the Cr-A coupling. All the next coupling steps including Fmoc-Met-OH, Fmoc-Arg(Pbf) OH, Fmoc-Cys(OMeBzl)-OH were carried as described before. At the end of each coupling and decoupling the reaction has been monitored with Kaiser test and, when the coupling or the decoupling was considered to be incomplete, the reaction has been then repeated. After the Fmoc deprotection of Fmoc-Cys(OMeBzl), the resin has been carefully washed and weighed and then split in two parts.

One part has been Fmoc-deprotected and has been capped through acetylation using acetic anhydride (5 eq.) and trietilamine (10 eq.) for 10 min.

The other half of the resin has been coupled with Fmoc-Asn(Trt)OH and Fmoc-Ala-OH twice and Fmoc-Gly-OH, as described before. Bulky Fmoc-AA has been coupled overnight. At the end of the consensus sequence, 1 eq. of the building block **14**, consisting of Fmoc-Lys$(PEG)_{10}$-OH, activated as the other Fmoc-aminoacids, has been added. After Fmoc removal, the free α-amine of the Lys was coupled with m-$PEG_{10}CH_2COOH$, activated as before, in order to obtain a "Y-shape" PEG at the end of the probe. The two peptides, ($GPEG_3K$(CrA)MRC(Mob)-ac and $GPEG_3K$(CrA)MRC(Mob)NAAGK(Y-shapePEG_{10})) have been cleaved from the resin for 2 hours using the so called "K reagent": 82.5% TFA, 5% Thioanisol, 2.5% H_2O, 2.5% EDT and 1% Phenol.

The crude products have been precipitated with cold ether, and suspended in HPLC mobile phase, separated with RP-HPLC and finally quantified through MALDI-TOF.

The calculated mass for $C_{95}H_{120}N_{10}O_{25}S_2$ is m/z = 1866.15 (**12**), while for $C_{159}H_{241}N_{17}O_{54}S_2$ it is m/z = 3318.82 (**13**). The massfound with the MALDI/TOF for **12** is m/z = 1866.12 and for **13** m/z = 3317.57 both corresponding to M. The MALDI-TOF spectra of **12** and **13** are reported in Fig. 3A and 3B, respectively.

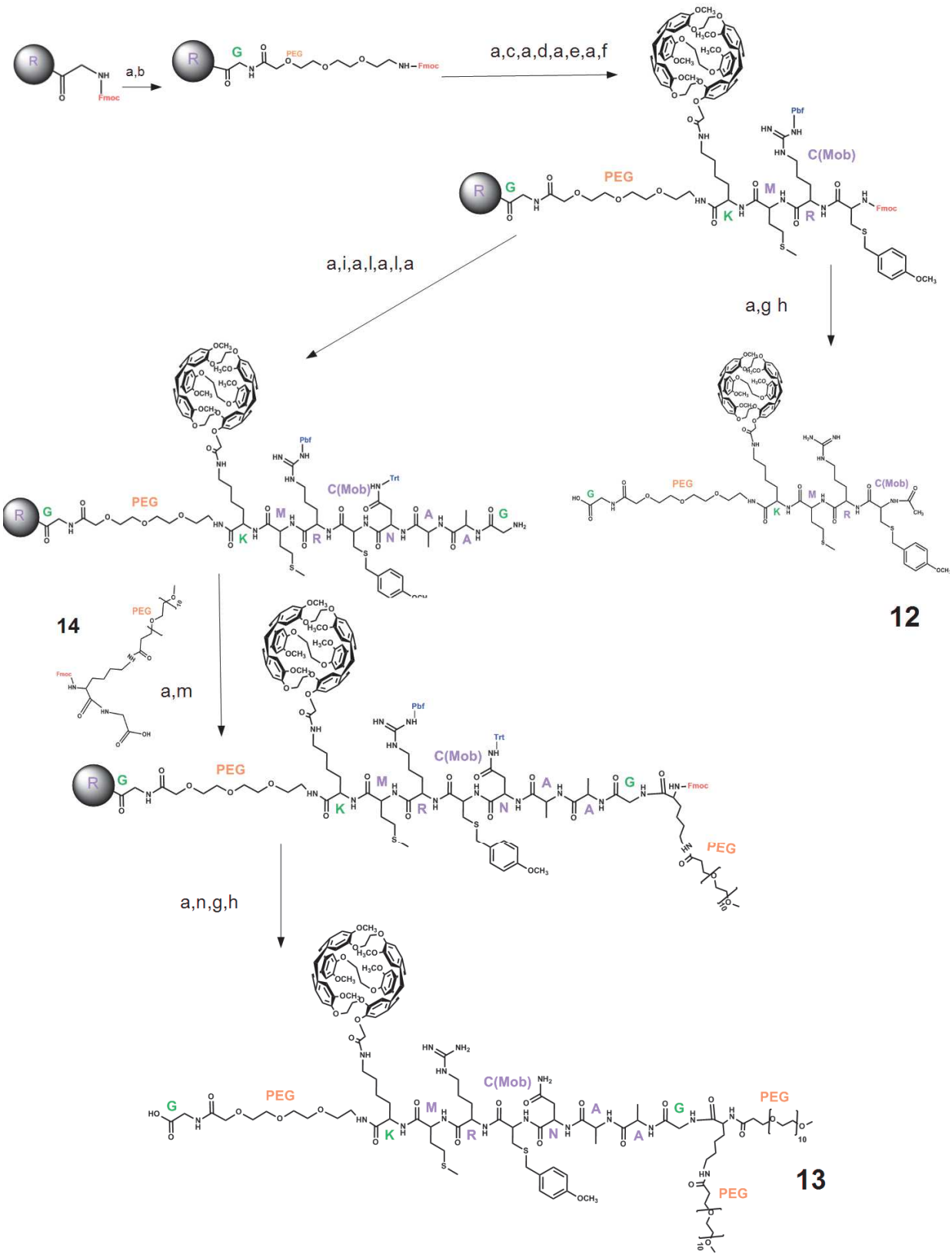

*Scheme 1: synthesis of **12** and **13.** The 2-Cl trytil resin has been coupled with 3 eq. Fmoc-Gly-OH using 3 eq. of Oxyma/HOAt and 6 eq. DIPEA. The reaction has been carried out in DMF for 2 hours at r.t. (a) 20% Piperidine/DMF, 15 min, twice (b) 3 eq. Fmoc-AEAAA, 3 eq. COMU, 6 eq. DIPEA, in DMF, 2 hrs, r.t. (c) 1.5 eq. Fmoc-Lys(Cr-A)-OH, 1.5 eq. COMU, 3 eq. DIPEA, in DMF, overnight, r.t. (d) 3 eq. Fmoc-Met (OH), 3 eq. COMU, 6 eq. DIPEA, 2 hrs, r.t.(e) 3 eq. Fmoc-Arg(Pbf)OH, 3 eq. COMU, 6 eq. DIPEA, in DMF, 2 hrs, r.t. (f) 3 eq. Fmoc-Cys(OMeBzl)-OH, 3 eq. COMU, 6 eq. DIPEA, in DMF, 2 hrs, r.t. (g) 5 eq. Ac_2O, 10 eq. Et_3N, 10' r.t. (h) 95% TFA, 2.5% TIS, 2.5% H_2O, 2 hours, 2 r.t. Followed by precipitation in cold diethylether, azeotropic evaporation and separation with RP-HPLC. (i) 3 eq. Fmoc-Asn(Trt)OH, 3 eq. COMU, 6 eq. DIPEA, in DMF, overnight, r.t. (l) 3 eq. Fmoc-Ala-OH, 3 eq. COMU, 6 eq., in DMF, 2 hours, r.t. (m) 3 eq. **14**, 3 eq. COMU, 6 eq. DIPEA, in DMF, overnight, r.t. (n) 3 eq. $PEG_{10}OCH_3$, 3 eq. COMU, 6 eq., in DMF, 2 hrs, r.t.*

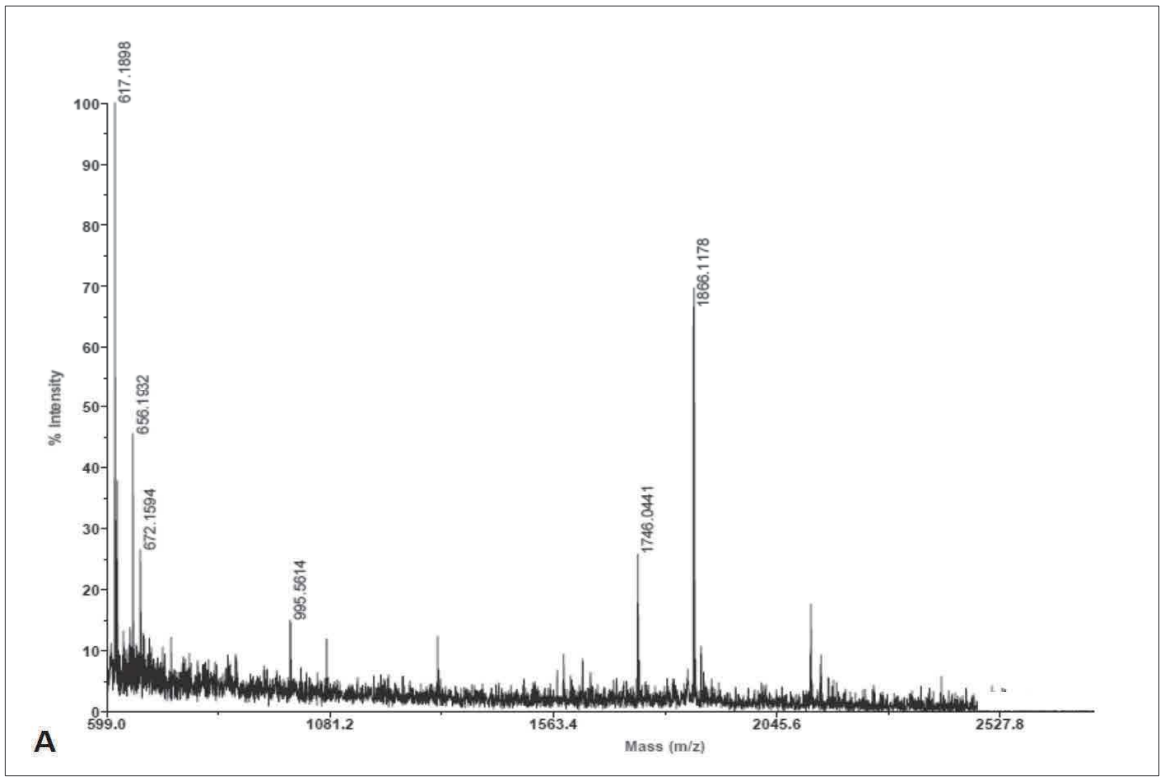

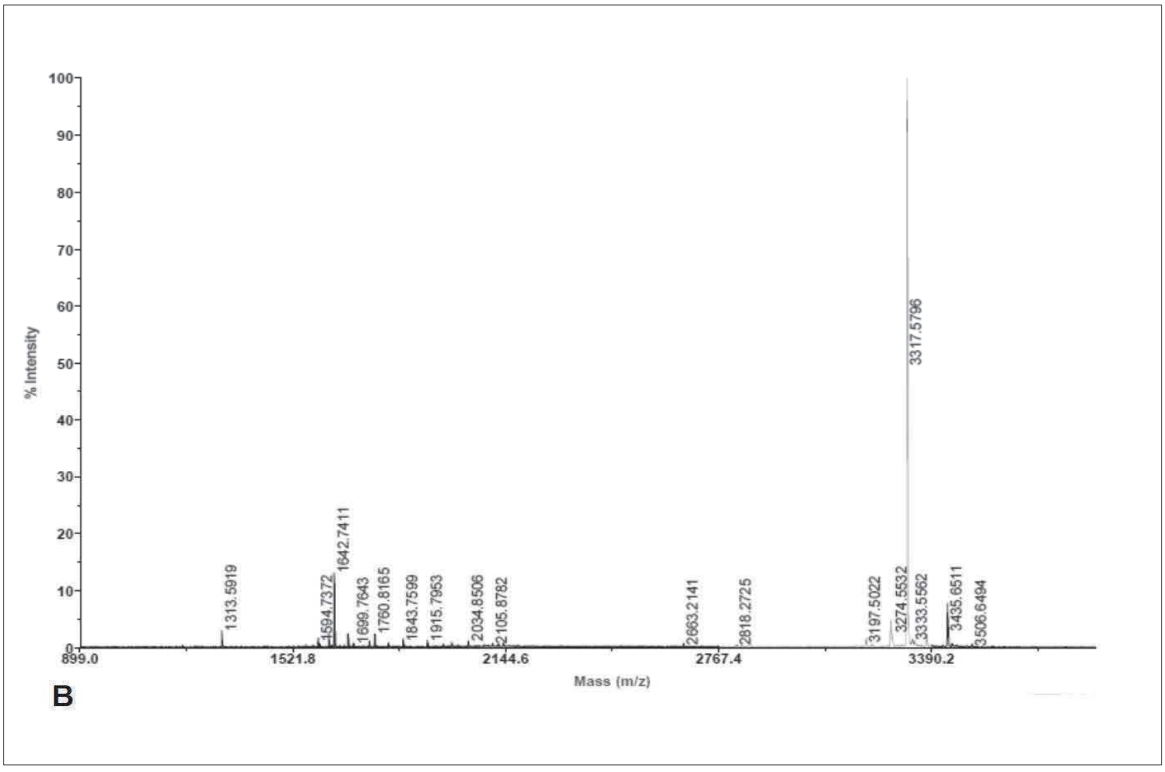

*Fig.3 A and B MALDI/TOF spectra of **12**(calculated m/z = 1866.15) and **13** (calculated m/z=3318.82)*

7.10 Mw-assisted synthesis of 14 (§4.2)

The building block Fmoc-Lys(PEG_{10})-OH (**14**) has been synthesized using mw-assisted solution synthesis, following the previously mentioned protocol for **4**. Briefly, 1 eq. of $mPEG_{10}$-CH_2COOH was dissolved in DMF at the concentration of 0,1 M and activated for 2 min at r.t. with 1 eq. of PyOxim (1 eq.) and 1.5 eq. of DIPEA. The mixture was then transfer in a 5 mL mw vial containing Fmoc-Lys-OH, unprotected (1 eq.) already dissolved in DMF. The amount of DIPEA in the mixture was decreased in order to avoid the unwanted Fmoc cleavage from the α-amino group of the Lys. The acylation was carried using microwave irradiation for 10 min at 75ºC. The reaction was then quenched, diluted 1:10 in HPLC mobile phase (30% CH_3CN in water, 0.1% of TFA) and purified. The calculated mass was m/z = 895.04 for $C_{45}H_{70}N_2O_{16}$. For Fmoc-Lys(PEG_{10})-OH m/z = 895.30 (Fig.4) has been found.

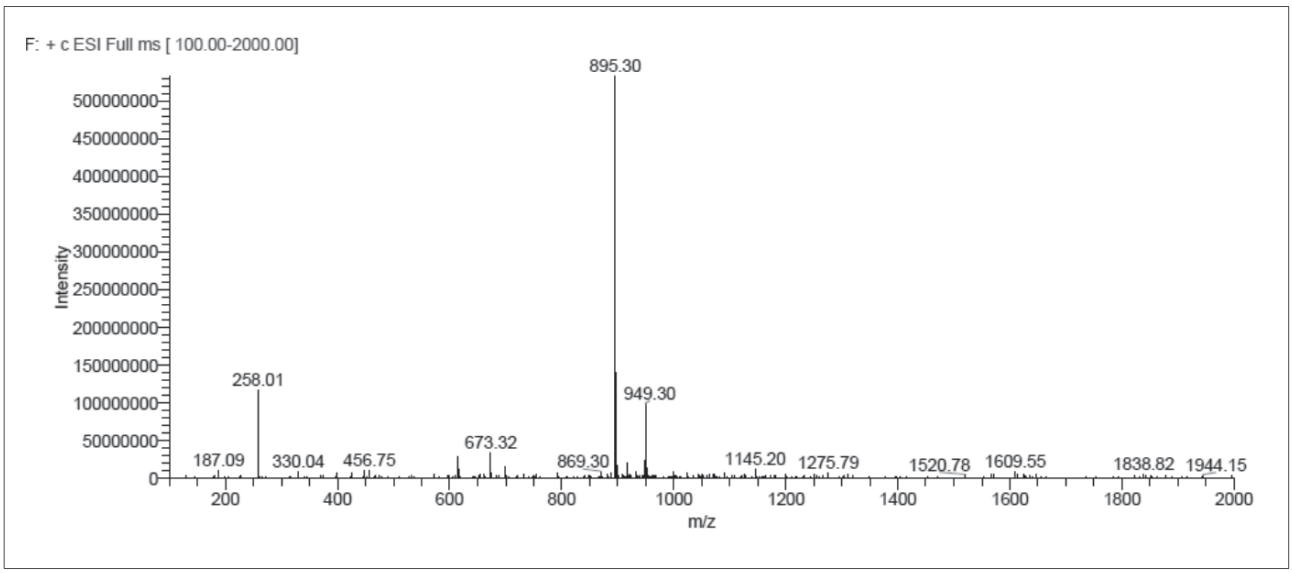

*Fig.4 MS/ESI spectrum of **14** (calculated m/z = 895.04)*

7.11 Synthesis of the ACPP-FAM-CrA dual MMP-2 sensor (15) (§5.2.2)

MMP-2 responsive biosensor **15** has been synthesized with an automated Fmoc-SPPS synthesizer (SYRO MultiSynTech, Witten, Germany) in collaboration with Biosythan GmbH (Berlin, Germany). The probe features a cationic chain of nine D-Arg, separated from an anionic chain of nine D-Glu by a consensus sequence GAL*GLP that has been derived from the paper of Van Duijven et al, (2013). In between the charged chains and the consensus sequence, two 6-hexanoic group (Ahx) as spacer are present. Such probe features Cr-A and FAM as reporters.

Briefly, PAP Tentagel resin (loading 0.28 mmol/g) has been coupled with 6 eq. of Fmoc-Gly-OH previously activated with 6 eq. of O-(Benzotriazol-1-yl)-N,N,N',N'-tetramethyluronium tetrafluoroborate (TBTU) in presence of 12 eq. of N-Methymorpholine. After Fmoc deprotection (20% piperidine in DMF, 15' twice), the resin has been coupled with the aminoacid bearing the first reporter (Fmoc-Lys(FAM)OH) and with Fmoc-Lys(Boc)-OH, which, after cleavage, would be the amino unit to couple CrA-ma. Each step of the reaction was carried with 6 eq. of Fmoc-protected aminoacid, activated with 6 eq. of TBTU and 12 eq. of N-Methymorpholine. Upon negative Kaiser test the coupling were repeated. The protected amino acids used were Fmoc-D-Arg(Pbf)-OH, Fmoc-Gly-OH, Fmoc-Ala-OH, Fmoc-Leu-OH, Fmoc-Pro-OH, Fmoc-D-Glu(OtBu),

Fmoc-Ahx-OH.

The peptide obtained, *GK(FAM)K(Boc)-Ahx-r_9GALGLP-Ahx-e_9* has been cleaved from the resin for 3 hours using TFA/thioanisole/thiocresol (95:2,5:2,5) and finally adding triethylsilane (5%) for 1 hour. The crude products have been precipitated with cold ether, and suspended in HPLC mobile phase, separated with RP-HPLC using an HPLC series LC-9A from Shimadzu equipped with a photodiode array detector SDP-M6A from Shimadzu (Kyoto, Japan). The separation was carried out using a Ultrasep ES (RP-18) column (7 µm, 250x3 mm), Dr.Maisch HPLC GmbH (Ammerbuch, Germany).

The coupling of the peptides with the Cr-A-ma was carried through acylation is solution following a protocol developed by Biosythan GmbH. Briefly, 1 eq. of Cr-A-ma were dissolved in DMF and activated with 1 eq. of TBTU and 2 eq. of DIPEA. After purification, the peptide was analysed with a MALDI-TOF (Axima, Shimadzu, Kyoto, Japan). The calculated mass for $C_{227}H_{327}N_{59}O_{67}$ was m/z = 4954.6, and the detected mass for **15** was m/z = 4955.7, corresponding to m+1.

The chromatogram and mass spectrum of **15** is reported in Fig. 5A and 5B, respectively.

7.12 Calculation of the relative quantum yield

The relative quantum yield Φ has been measured using the single-point method[150] by using as a reference fluorophore 5,6 FAM (Φ=0.95) for **2** and 5,6 TAMRA (Φ=0.68) for **4**.[114] Solutions of 0.1 mM of **2**, **3** and **15** and their reference fluorophores were prepared dissolving the 10 mM dimethylsulphoxyde (DMSO) stock solution in ethanol. The quantum yield has been calculated as follows:

$$\Phi = \Phi_R \frac{I}{I_R} \frac{OD_R}{OD} \frac{n^2}{n^2_R}$$

Where *Φ* is fluorescence quantum yield, *I* integrated fluorescence intensity, *n* refractive index of the solvent, and *OD* is the optical density. The subscript “R” refers to the reference fluorophore of known quantum yield. Fluorescence intensity has been measured with a Jasco FP-6500 spectrofluorometer (Jasco, Gross-Umstadt, Germany), using λ_{ex} = 494 nm and λ_{em} = 516 nm for 5,6-FAM and **2** and λ_{ex} = 541 nm and λ_{em} = 567 nm for 5,6-TAMRA and **3**. Optical density has been measured with an Implen P300 nanophotometer (Implen, Munich, Germany). Solvent refractive index was not taken into account as all the four analytes are dissolved in the same mixture consisting of 1% DMSO in ethanol.

7.13 Cleavage tests

To test sensor **13,** MMP-11 was dissolved in an appropriate buffer (containing 50 mM of Hepes buffer, 10 mM $CaCl_2$, 100 mM NaCl, 20 µM $ZnCl_2$, pH=7.5) at a concentration of 5 nM. The enzyme does not require activation as it is the catalytic site. **13** was dissolved in buffer with 1% DMSO at the concentration of 100 µM. The reaction was carried at 37°C on a block thermostat. Aliquots for measurements with Xe-NMR or with HPLC-MS were collected and immediately frozen with liquid nitrogen and preserved at -20°C for further analysis.

To test sensor **15**, MMP-2 was dissolved in 50 mM of Tris base, 5 mM $CaCl_2$, 300 mM NaCl, 20 µM $ZnCl_2$, pH=7.5 at the final concentration of 5 nM. The enzyme does not require activation as it is the catalytic site.

15 was dissolved in buffer at the concentration of 200 µM (tot DMSO 2%). Aliquots for measurements with Xe-NMR or with HPLC-MS were collected and immediately frozen with liquid nitrogen and preserved at -20°C for further analysis. The mass of **16** was confirmed with MALDI-TOF.

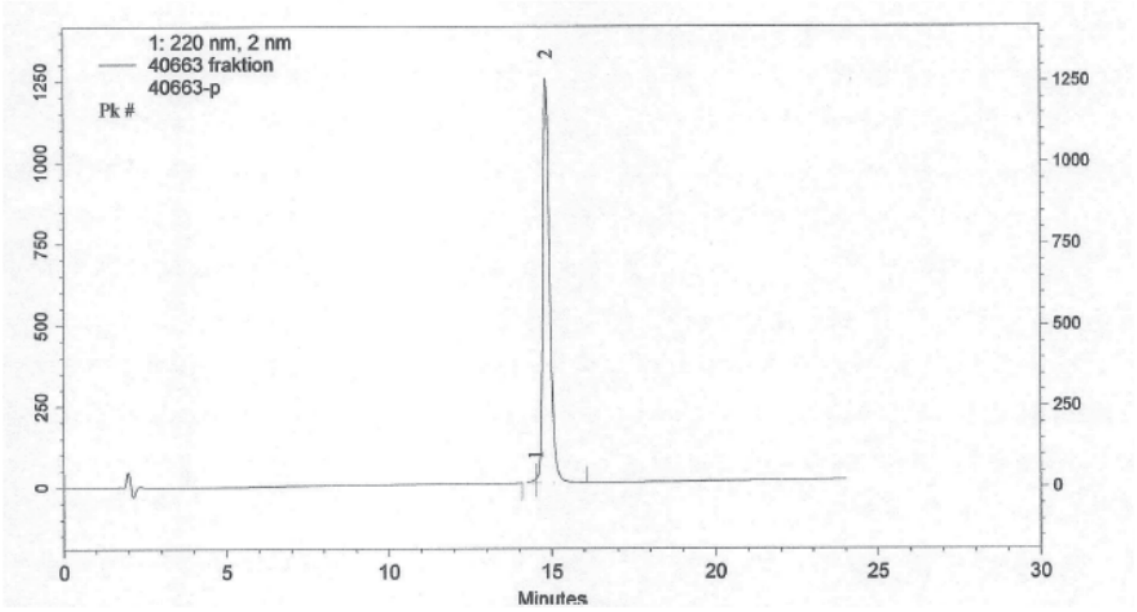

a)

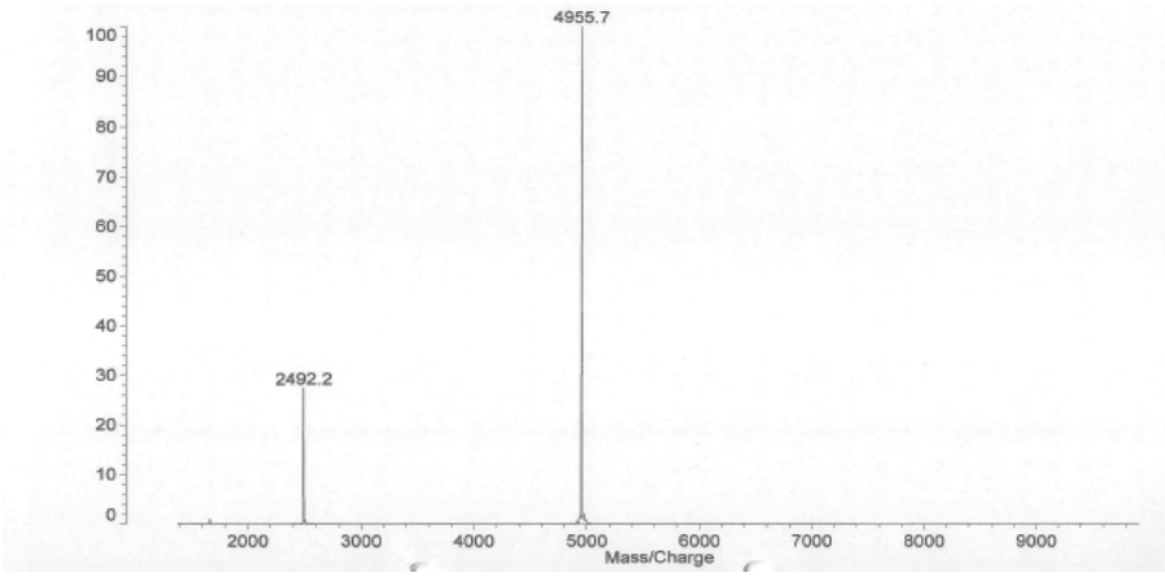

b)

*Fig. 3 a) HPLC trace of the separation of **15**. b) MALDI/TOF spectrum of **15***

8.Cell tests using Cr-A based probes

8.1 Reagents and instrumentation

All reagents were purchased in cell culture purity grade. VLE-Dulbecco's Modified Eagle Medium (VLE-DMEM), stable glutamine, Fetal Bovine Serum (FBS), Phosphate Buffer Saline (PBS), Roswell Park Memorial Institute medium (RPMI) 1640 Medium, Trypsin-ethylenediaminetetraacetate (Trypsin-EDTA), cell culture purity grade DMSO, Trypan Blue, Triton X and SDS were purchased from Biochrom AG (Berlin, Germany). AlamarBlue® Cell Viability Assay and Hoechst 33342 were obtained from Life Technologies (Darmstadt, Germany), while Cell Meter™ Cell viability assay kit (Green Fluorescence) was obtained from Biomol GmbH (Hamburg, Germany).

Monoclonal anti-CD14 specific antibody (ABIN 1176993), and control IgG2b (chain kappa) isotype antibody (ABIN 287151) were purchased from Antibodies Online (Atlanta, GE, USA). The conjugation with avidin was done using a EasyLink Avidin Conjugation Kit (Abcam, Cambridge, UK). Purification of conjugates was done using a Concentrator Amicon Ultra 15,100 kDa (Merck Millipore, Darmstadt, Germany).

Cell lines were grown in a humidified CO_2 incubator Sanyo MCO-20IC (Panansonic Biomedicals, Leichestershire, UK). Cell density and viability were measured with a TC20™ Automated Cell Counter (Biorad, Hercules, CA, USA). Fluorescence intensity of cells was measured using a Safire Micro plate reader (TECAN Deutschland GmbH, Crailskirchen, Germany). FACS analysis was carried out with a BD FACSCalibur flow cytometer using BD CellQuest Pro™ acquisition software. Data was then analyzed with FlowJo analysis software. The absolute fluorescence results from triplicate experiments were plotted in a box plot (range of the plot denotes the first and third quartile, median represented by the white bar).

Microscopy experiments were carried out on a LSM 5100 microscope (Carl Zeiss microimaging GmbH, Oberkochen, Germany) equipped with an X100 oil objective. Images were processed using the ZEN 2009 light Edition (Carl Zeiss Microimaging GmbH).

8.2. Cell lines

Mouse L929 and 3T3 fibroblasts, mouse RAW 264.7 macrophages and human HT1080 fibroblasts were purchased from ATCC (Wesel, Germany). Fibrobasts L929, 3T3 and HT1080 were grown in VLE-DMEM medium with stable glutamine supplemented with 10% FBS, while RAW 264.7 macrophages were grown in RPMI 1640 medium with stable glutamine, supplemented with 10% FBS. Both cell lines were grown at 37 °C in a humidified incubator with 5% CO_2. L929, 3T3 and HT1080 cells were harvested by incubation with 0.05% Trypsin-EDTA, while RAW 264.7 macrophages were harvested by manual detachment of the cells by scraping.

For the cells described in §2.5.3: after reaching ~70% confluency, RAW 264.7 macrophages were stimulated for 18 hrs with 100 ng/ml lipopolysaccharides (LPS) from E.Coli. The harvesting was done with 0.05% Trypsin-EDTA , while for RAW 264.7 macrophages harvesting was achieved by manual detachment of the cells by scraping.

8.3. Incubation with the Cr-A conjugates

Cells were grown in T75 culture flasks. After reaching 60-70% confluency, the cells were washed twice with warm PBS.

For the experiment described in §2.3.4, complete cell culture media containing 50μM of either **2** or 20 μM of **4** in a final concentration of 1% DMSO was added to the flasks and the cells incubated in the dark for 18 hrs at 37 °C in a humidified incubator with 5% CO_2. After 18 hrs, the culture media was removed and the cells washed twice with warm PBS. The cells were observed by light microscopy for any changes in morphology.
For the experiment described in §5.2.4 complete cell culture media containing 20 μL of 200 μM of either **15** (with or without 100 μM of GM6001) or **16** in MMP-2 buffer (consisting of 50 mM TRIS base, 200 mM NaCl, 10 mM $CaCl_2$ and 10 μM of $ZnCl_2$) with in total 0.2% DMSO was added to the flasks and the cells incubated in the dark for 1 hr at 37 °C in a humidified incubator with 5% CO_2. After 1 hr, the culture media was removed and the cells washed five times with warm PBS. The cells were observed by light microscopy for any changes in morphology. In the uptake test described in 5.3, one plate was incubated at 4°C at dark.

8.4 Production and incubation of avidin-antibody biosensor conjugates

1 mg of both monoclonal anti-CD14 specific antibody or control IgG2b were conjugated with avidin using the EasyLink Avidin Conjugation Kit according to manufacturer's instructions. The purification of avidin-antibody conjugates was done adding 10 ml sterile Dulbeco's PBS (DPBS) to the product then concentrating the solution through with three sequential PBS additions, to obtain the final concentration of ~0.5 μg/μL in PBS. For the incubation on cells, 100 μg avidin-antibody conjugate was incubated for 30 min at room temperature with a 40-fold mole excess of biotin-conjugates in a mole ratio of 1:4 of **5:6**, or with 40-fold excess of **7.** After the conjugate was concentrated and separated from any unbound biotin-conjugates.
Harvested cells were pelleted by centrifugation and resuspended in PBS supplied with 3% bovine serum albumin (BSA) and with 2 μg of the avidin-labeled CD14 antibody, the avidin-labeled IgG2b control antibody or the complete CD14 biosensor construct at the final volume of 200 μL/million cells. The cells were incubated for 1 hr in the dark at 4°C. Subsequently, cells were pelleted by centrifugation and washed twice with ice-cold DPBS containing 3% BSA. In the case of the "sequential incubation", 1μM fluorescein-biotin and 4 μM CrA-biotin were used.

8.5. Cell Viability

In experiment §2.2.3 cellular viability was tested using the alamarBlue® Cell Viability Assay for **1** and **2**. Cells were grown in 96 well plates (2000 cells/well) for 48 hrs, followed by 20 h incubation with **1** (0-100 μM) or 2 (0-100 μM) at 37 °C in a humidified incubator with 5% CO_2. **1** and **2** were both dissolved in DMEM in presence of 10 % FBS and 1% DMSO. Then, alamarBlue® (1:10) was added to the cells and incubated for further 3 hrs. Fluorescence intensity was measured with a plate reader.
In the experiment §2.2.4 cell viability was measured for 2 using alamarBlue®as described before, while for **4** Cell Meter ^{TM} was used following the same procedure. Cell viability of **15** was measured by measuring the absorbance of Trypan Blue using a cell counter.

8.6 Intracellular Concentration through cell lysates.

For experiment §2.3.4 the intracellular concentration of both **2** or **4** was estimated by measuring the fluorescence intensity in cell lysates. L929 cells were grown in 96 well plates (2000 cells/well) for 48 h followed by 18 h incubation with **2** (0-100 μM) or **4** (0-100μM) at 37 °C in the dark, in a humidified incubator with 5% CO_2. Both probes were dissolved in DMEM, 10 % FBS, 1 % DMSO. After 18 hrs incubation, media was removed and the cells washed twice with warm PBS. Cell lysates were made *in situ* by adding 50 μL of

cell lysis buffer (PBS containing 2% SDS and 1% Triton X) to each well and incubating for 15 minutes. The cell lysate was diluted by the addition of 150 µL PBS containing DMSO to give a final 200 µL volume of cell lysate in PBS, 0.5% SDS, 0.25% Triton X, 1% DMSO per well. A standard curve was generated by dissolving **2** (0.01-5µM) or **4** (0.01-5µM) in PBS containing 0.5% SDS, 0.25% Triton X, 1% DMSO. The intracellular concentrations were calculated by assuming an average cell volume of ~7200 fL for L929 fibroblasts and ~3300 fL for RAW 264.7 macrophages. The cell volume was estimated by measuring the mean diameter of both cell lines when in suspension, L929 cells (~24µm) and RAW 264.7 cells (~18 µm), using the analysis function of the T cell Counter. The mean value of intracellular concentrations from quadruplicate data is given.

For experiment §2.5.3 RAW 264.7 and 3T3 were lysed as described before. The quantification was based on two standard curves one with CrA-biotin and FAM-biotin at the same ratio of the incubation and the other one with the branched CrA-fluorescein-biotin; all dilutions were done in PBS containing 0.5% SDS, 0.25% Triton X, 1% DMSO final.

8.7. Cellular associated sensor quantification through fluorescence intensity

For experiment §4.3 the sensor concentration in cells was assessed by measuring the fluorescence intensity of FAM (excitation at.495 nm, emission at 512 nm). Briefly, cells were incubated and washed as described before, then, after cell count, cell pellets were dissolved in PBS at the final volume of 100 µL and spotted on 96 well plates. A calibration curve repeated in triplicates of **15** was used for quantification. (range 0-10 µM, R^2=0.98). The fluorescence intensity was given as average of three measurements. The cellular associated concentration was calculated by dividing the µM concentration obtained by the fluorescence intensity by the number of cell in every sample, calculated prior the detection with the cell counter.

8.8 Flow cytometry

Flow cytometry for all experiments was carried on 500,000 cells incubated as described before. All cell samples were resuspended in 500 µL PBS and kept in the dark, on ice before the flow cytometry measurement. The absolute fluorescence intensity of fluorescein was measured on the FL1 channel and compared for each cell line and biosensor under identical acquisition parameters. Data was then analyzed with FlowJo analysis software.

8.9 Laser Scanning Microscopy

400,000 cells were seeded on 30 mm glass coverslips (pretreated with 100 µg/mL poly-L-lysine) in 6-well plates and grown for 24 hrs. The cells were incubated with the CrA-biosensors and then were washed twice with PBS containing additional 1 mM Ca^{2+}, and fresh media added to each well. The cells were incubated with Hoechst 33342 for 15 minutes prior to each imaging. Signals were recorded using the following laser parameters: a 488 nm argon laser/ BP 505-550 nm for the fluorescein coupled biosensor (**2,5,7,15**) , 543 nm UV laser/LP 364nm for Hoechst nuclear stain and 560 argon nm laser/BP 630-660 for the only rhodamine sensor (**4**).

9.Xe-NMR experiments

9.1 Instrumentation

All NMR studies were performed using a 9.4 T Bruker AV 400 wide bore NMR spectrometer (Bruker Biospin, Ettlingen, Germany) equipped with gradient coils for imaging. A 10 mm inner-diameter double-resonant (^{129}Xe and ^{1}H) probe was used for excitation and detection. A custom-designed continuous-flow polarizer was used to produce hp-Xe by spin-exchange optical pumping. A gas mixture of 2% xenon (26.4% ^{129}Xe natural abundance), 10% N_2 and 88% He was used. The achieved ^{129}Xe spin polarization was approximately 25%. hp-Xe was directly bubbled into a 10 mm NMR-tube containing 1.5 mL of the sample by using a spectrometer triggered bubble dispenser (3.5 bar overpressure) via fused silica capillaries (Polymicro Technologies, Molex Incorporated, Caudebec les Elbeuf, France). The bubbling was triggered by using spectrometer-triggered gas flow regulators (mass flow controllers, Omega Newport, Deckenpfronn, Germany). Pluronic L-81 as anti-foam agent was purchased from BASF (Ludwigshafen, Germany), while low-Ca^{2+} PBS was obtained from BioChrom AG (Berlin, Germany).

Image processing was done using MATLAB (R2012a, MathWorks, Natick, MA) or with Python. CEST-spectra were fit to the negative exponential of a sum of Lorentzians in OriginPro 8.6.OG (OriginLab, Northampton, MA).

9.2. Sample preparation for in cells Hyper-CEST experiments

After incubation with the different biosensors, cell pellets were re-suspended at a concentration of 5-10 million cells/mL in low Ca^{2+} PBS. To reduce foam formation when bubbling xenon in the gas mix, 0.2% of Pluronic L-81 was added just prior to MRI measurements. The cell suspension was transferred to an NMR double bubbling chamber, using one compartment for the negative control and one for the positive control.

In the same way solutions containing a Xe-NMR responsive sensor can be prepared as well. This setup was then connected to the hp-Xenon MRI system and placed inside the NMR magnet.

9.3. Hyper-CEST spectroscopy and imaging of §2.2.1 and §2.2.3

Hyper-CEST-adapted single-shot sequence with in plane geometry of 20 x 20 mm^2, matrix size = 32 x 32, in-plane resolution = 625 µm and a 90 degree Gaussian-shaped excitation pulse was used. For experiments with direct Xe delivery through bubbling, echo planar imaging (EPI) readout (slice thickness = 22 mm, Fourier acceleration factor = 1.68, double sampling, bandwidth = 101 kHz, echo time = 5.7 ms, acquisition time = 19.8 ms) was used. A Rapid Acquisition with Relaxation Enhancement (RARE) readout (slice thickness = 20 mm, centric *k*-space encoding, bandwidth = 5 kHz, echo time = 10 ms, acquisition time = 320 ms, rare factor = 32) was used for imaging experiments with the live cell bioreactor based on indirect xenon delivery through perfusion.

9.4.Hyper-CEST spectroscopy and imaging of §2.3.5

For each data point in the CEST-spectrum, the gas mixture was directly bubbled for 15 s into the sample solution (flow rate 0.1 standard liter per minute) followed by a 3 s delay to allow bubbles to collapse. This was followed by a 16 s, 6.5 µT saturation pulse. The saturation pulses were applied in evenly spaced steps of 1 ppm from -110 ppm to -150 ppm (referenced to the xenon in free solution peak at 0 ppm). For each Hyper-CEST image 10 on-resonant (-124 ppm relative to xenon in free solution at 0 ppm) and 10 off

resonant (124 ppm) scans were taken and averaged. For each image the xenon gas mix was bubbled into solution for 15 s followed by a 3 s delay to allow bubbles to collapse. This was followed by a 16 s, 18 µT saturation pulse. The image was read out using a Rapid Acquisition with RARE readout (see 8.3).

9.5. Hyper-CEST spectroscopy and imaging of §2.5.4

For each data point in the CEST-spectrum, the gas mixture was directly bubbled for 12 s into the sample solution (flow rate 0.1 standard liter per minute) followed by a 4 s delay to allow bubbles to collapse. This was followed by a 12 s, 32.4 µT saturation pulse. The saturation pulses were applied in evenly spaced steps of XX ppm from -XXX ppm to -XXX ppm (referenced to the xenon in free solution peak at 0 ppm). For the Hyper-CEST MRI 32 on-resonant (-124 ppm relative to xenon in free solution at 0 ppm) and 32 off-resonant (124 ppm) scans were taken and averaged. The image was read out using a RARE readout (slice thickness = 20 mm, matrix size = 32×32, in-plane resolution = 625 µm, centric k-space encoding, bandwidth = 16 kHz, echo time = 5 ms, acquisition time = 160 ms, rare factor = 32).

9.6. Xe-NMR spectroscopy of 8/9, 10/11 and 12/13 and time course Hyper-CEST spectroscopy of 13.

Xe-NMR of **8-11** was obtained by bubbling the Xe mixture for 10 s and allowing 4 s delay for let the bubbles to collapse. That was followed by a 8 s, 0.32 µT saturation pulse. Xe-NMR of **12/13** was obtained bubbling the Xe mixture for 20 s and allowing 4 s delay for let the bubbles to collapse. That was followed by a 8 s, 0.32 µT saturation pulse. In both cases, the saturation pulses were applied in evenly spaced steps of XX ppm from -XX ppm to -XX ppm (referenced to the xenon in free solution peak at 0 ppm)

For the time course experiment, each sample precentely prepared was thawed and placed in the dedicated Xe-NMR tube. The gas misture already described was bubbled for 20 s into the sample solution at a flow rate 0.1 standard liter per minute followed by a 4 s delay to allow bubbles to collapse, followed by a 20s, 0.32 µT saturation pulse.

9.7 Xe-NMR spectroscopy and imaging of 5.5

For each data point in the CEST-spectrum, the gas mixture (2% Xe, 310 K) was directly bubbled for 15 s into the sample solution (flow rate 0.1 standard liter per minute) followed by a 4 s delay to allow bubbles to collapse. This was followed by a 26 s, 30 µT saturation pulse. For the Hyper-CEST MRI 10 on-resonant (-124 ppm relative to xenon in free solution at 0 ppm) and 10 off-resonant (124 ppm) scans were taken and averaged. 4.7 million cells per mL in each compartment were used. To each compatment was 0.2% Pluronic L-81 was added.

The image was read out using a RARE readout (acquisition parameters see 8.3). Image processing was done using Pytohn. CEST-spectra were fit to the negative exponential of a sum of Lorentzians in OriginPro 8.6.OG (OriginLab, Northampton, MA).

References

1. Dzik-Jurasz ASK (2003). *Molecular imaging in vivo: an introduction*, Brit J Radiol 76 : 98-109.
2. Rudin M, Weissleder R (2003). *Molecular imaging in drug discovery and development*, Nat Rev Drug Discov 4 : 123-129.
3. Weissleder R, Pittet MJ (2008). *Imaging in the era of molecular oncology*, Nature 452 : 580-589.
4. Alford R, Iogawa M, Choyke PL, Kobayashi H (2009). *Molecular probes for the in vivo imaging of cancer*, Mol Biosyst 5: 1279-1291.
5. Weissleder R (2006). *Molecular Imaging in Cancer*, Science 312 : 168-170.
6. Massoud TF, Gambhir SS (2006). *Molecular imaging in living subjects: seeing fundamental biological processes in a new light*, Gene Dev 17 : 545-580.
7. Grenier P and Bader P (2011). *Principles and basic concepts of Molecular Imaging*, Pediatr Radiol 41 : 144-160.
8. Clever HL, 1979. *Krypton, Xenon & Radon: IUPAC solubility series II edition*. Pergamon Press, Oxford, England, .
9. Ruzicka J, Benes J, Bolek L, Markvartova V(2007). *Biological effects of noble gases*, Physiol Res 56 : 39-44.
10. Berthault P, Huber G, Desvaux H. (2009). *Biosensing using laser-polarized xenon NMR/MRI*, Prog Nucl Mag Reson Spectrosc 55 : 35-60.
11. Liu Z, Araki T, Okajima Y, Albert M, Hatabu H(2014). *Pulmonary hyperpolarized noble gas MRI: recent advances and perspectives in clinical application*, Eur J Radiol 83 : 1282-91.
12. Mugler JP 3rd, Driehuys B, Brookeman JR, Cates GD, Berr SS, Bryant RG, Daniel TM, de Lange EE, Downs JH 3rd, Erickson CJ, Happer W, Hinton DP, Kassel NF, Maier T, Phillips CD, Saam BT, Sauer KL, Wagshul ME.(1997). *MR imaging and spectroscopy using hyperpolarized 129Xe gas: preliminary human results.* Magn Res Med 37 : 809-815.
13. Matsuoka S, Patz S, Albert MS, Sun Y, Rizi RR, Gefter WB, Hatabu H (2009). *Hyperpolarized gas MR Imaging of the lung: current status as a research tool.*, J Thor Imaging 24 : 208-2018.
14. Cleveland Z I, Cofer GP, Metz G, Beaver D, Nouls J, Kaushik SS, Kraft M, Wolber J, Kelly KT, McAdams HP, Driehuys B. (2010). *Hyperpolarized 129Xe MR Imaging of Alveolar Gas Uptake in Humans*, PLoS ONE 5 : e12192.
15. Driehuys B, Martinez-Jimenez S, Cleveland ZI, Metz GM, Beaver DM, Nouls JC, Kaushik SS, Firszt R, Willis C, Kelly KT, Wolber J, Kraft M, McAdams HP (2012). *Chronic obstructive pulmonary disease: safety and tolerability of hyperpolarized 129Xe MR imaging in healthy volunteers and patients*, Radiol 262 : 279-89.
16. Couch MJ, Blasiak B, Tomanek B, Ouriadov AV, Fox MS, Dowhos KM, Albert MS (2015). *Hyperpolarized and Inert Gas MRI: The Future*, Mol Imaging Biol 17 : 149-162.
17. Ouriadov A, Farag A, Kirby M, McCormack DG, Parraga G, Santyr GE.(2014) *Pulmonary hyperpolarized 129 Xe morphometry for mapping xenon gas concentrations and alveolar oxygen partial pressure: Proof-of-concept demonstration in healthy and COPD subjects* Magn Res Med doi:10.1002/mrm.25550.
18. Swanson SD, Rosen MS, Coultr KP, Welsh RC, Chupp TE (1999). *Distribution and dynamics of laser-polarized 129Xe magnetization in vivo*, Magnetic Resonance in medicine 42 : 1137-1145.
19. Nakamura K, Kondoh Y, Kinoshita T. (2013). *Hyperpolarized (129)Xe spectra from C6 glioma cells implanted in rat brains*, Conf Proc IEEE Eng Med Biol Soc 2013 : 2972-5.
20. Zhou X. (2011). *Hyperpolarized noble gases as contrast agents*, Methods Mol Biol 771 : 189-204.
21. Mazzanti ML, Walvick RP, Zhou X, Sun Y, Shah N, Mansour J, Gereige J, Albert MS (2011). *Distribution of hyperpolarized xenon in the brain following sensory stimulation: preliminary MRI findings.*, PLoS One 6 : e21607.
22. Imai H, Kimura A, Akiyama K, Ota C, Okimoto K, Fujiwara H.(2012). *Development of a fast method for*

quantitative measurement of hyperpolarized 129Xe dynamics in mouse brain., NMR Biomed 25 : 210-7.

23. Schröder L. (2013). *Xenon for NMR biosensing--inert but alert.*, Phys Med 29 : 3-16.
24. Witte C. and Schröder L. (2013). *NMR of hyperpolarised probes.*, NMR Biomed 26 : 788-802.
25. Gallagher FA Bohndiek SE, Keltunen MI, Lewis DY, Soloviev D Brindle KM(2011). *Hyperpolarized 13C MRI and PET: in vivo tumor biochemistry*, J Nucl Med 52 : 1333-6.
26. Witte C, Kunth M, Döpfert J, Rossella F, Schröder L(2012). *Hyperpolarized xenon for NMR and MRI applications*, J Vis Exp 6 : pii: 4268.
27. Witte C, Kunth M, Rossella F, Schöder L. (2014). *Observing and preventing rubidium runaway in a direct-infusion xenon-spin hyperpolarizer optimized for high-resolution hyper-CEST (chemical exchange saturation transfer using hyperpolarized nuclei) NMR*, J Chem Phys 140 : 084203.
28. Souteyrand E, Nicolas D, Martin J. Chauvet JP, Perez H. (1996). *Behaviour of cryptophane molecules in gas media*, Sensors Actuator 3 : 182-187.
29. Canceill J and Collet A. (1998). *Two-step synthesis of D3 and C3h cryptophanes*, J Chem Soc Chem Commun 9 : 582-584.
30. Zhang C, Shen W, Wen G, Chao J, Qin L, Shuang S, Dong C, Choi MMF. (2008). *Spectral study on the interaction of cryptophane-A and neutral molecules CHnCl4 − n (n = 0, 1, 2)*, Talanta 76 : 235-240.
31. Brotin T and Dutasta J. (2009). *Cryptophanes and their complexes: present and future*, Chem Rev 109 : 88-130.
32. Huber G Beguin L,Desvaux H, Brotin T, Fogarty HA, Dutasta JP, Berthault P. (2008). *Cryptophane-Xenon Complexes in Organic Solvents Observed through NMR Spectroscopy*, J Phys Chem 112 : 11363–11372.
33. Fairchild RM, Joseph AI, Holman KT, Fogarty HA, Brotin T, Dutasta JP, Boutin C, Huber G, Berthault P. (2010). *A water-soluble Xe@cryptophane-111 complex exhibits very high thermodynamic stability and a peculiar (129)Xe NMR chemical shift.*, J Am Chem Soc. 132 : 15505-15507.
34. Tyagi R, Witte C, Haag R, Schröder, L. (2014). *Dendronized cryptophanes as water soluble xenon hosts for 129Xe magnetic resonance imaging*, Org Lett 16 : 4436-4439.
35. Kunth M, Witte C, Schröder L.(2014) *Quantitative chemical exchange saturation transfer with hyperpolarized nuclei (qHyper-CEST): Sensing xenon-host exchange dynamics and binding affinities by NMR* J Chem Phys 141: 194202
36. Canceill J, Collet A, Gottarelli G. (1984). *Optical activity due to isotopic substitution. Synthesis, stereochemistry, and circular dichroism of (+)- and (-)-[2,7,12-2H3]cyclotribenzylene*, J Am Chem Soc 106 : 5997-6003.
37. Schröder L, Lowery TJ, Hilty C, Wemmer DE, Pines A. (2006). *Molecular Imaging using a targeted Magnetic Resonance hyperpolarized biosensor*, Science 314 : 446-449.
38. Bai Y, Hill PA, Dmochowski IJ. (2012). *Utilizing a water-soluble cryptophane with fast xenon exchange rates for picomolar sensitivity NMR measurements*, Anal Chem 84: 9935-41.
39. Fogarty HE, Berthault P, Brotin T, Huber G, Desvaux H, Dutasta JP (2007). *A crypthophane core optimized for xenon incapsulation*, J Am Chem Soc 129 : 10332-10333.
40. Traoré T, Delacour L, Garcia-Argote S, Berthault P, Cintrat JC, Rousseau B. (2010). *Scalable Synthesis of Cryptophane-1.1.1 and its Functionalization*, Org Lett 12 : 960-962.
41. Dubost E, Dognon J-P., Rousseau B, Milanole G, Dugave C, Boulard Y, Léonce E, Boutin C, Berthault P. (2014). *Understanding a Host–Guest Model System through 129Xe NMR Spectroscopic Experiments and Theoretical Studies.*, Angew Chem Int Ed Engl 126 : 9995–9998.
42. Little MA, Donkin J, Fisher J, Halcrow MA; Loder J, Hardie MJ (2011). *Synthesis and Methane-Binding Properties of Disulfide-Linked Cryptophane-0.0.0.*, Angew Chem Int Ed Engl 51: 764-6
43. Delacour L, Kotera N, Traoré T, Garcia-Argote S, Puente C, Leteurtre F, Gravel E, Tassali N, Boutin C, Léonce E, Boulard Y, Berthault P, Rousseau B. (2013). *"Clickable" Hydrosoluble PEGylated Cryptophane as a Universal Platform for 129Xe Magnetic Resonance Imaging Biosensors.* Chem Eur J 16 : 6089–6093..
44. Taratula O, Kim MP, Bai Y, Philbin JP, Riggle BA, Haase DN, Dmochowski IJ (2012). *Synthesis of Enantiopure,*

Trisubstituted Cryptophane-A Derivatives., Org Lett 14 : 3580–3583.

45. Brotin T, Barbe R, Darzac M, Dutasta JP (2003). *Novel Synthetic Approach for Optical Resolution of Cryptophanol-A: A Direct Access to Chiral Cryptophanes and Their Chiroptical Properties*, Chem.Eur.J. 9 : 5784-5792.
46. Traoré T, Clavé G, Delacour L, Kotera N, Renard PY, Romieu A, Berthault P, Boutin C, Tassali N, Rousseau B (2011). *The first metal-free water-soluble cryptophane-111*, Chem Comm 47 : 9702-9704.
47. Hill PA, Wei Q, Troxler T, Dmochowski IJ (2009). *Substituent effects on xenon binding affinity and solution behavior of water-soluble cryptophanes.*, J Am Chem Soc 131 : 3096-3077.
48. Brotin T, Cavagnat D, Jeanneau E, Buffeteau T (2013). *Synthesis of Highly substituted Cryptophane derivatives*, J Org Chem 78 : 6143-6153.
49. Sears DN and Jameson CJ (2003). *Theoretical calculations of the Xe chemical shifts in cryptophane cages*, J Chem Phys119 : 12231-12244.
50. Ruiz EJ Sears DN, Pines A, Jameson CJ (2006). *Diastereomeric Xe chemical shifts in tethered cryptophane cages*, J Am Chem Soc 128 : 16980-16988.
51. Hill PA, Wei Q, Eckenhoff RG, Dmochowski IJ (2007). *Thermodynamics of xenon binding to cryptophane in water and human plasma*, J Am Chem Soc 129 : 9262-9263.
52. Jacobson DR, Khan NS, Collé R, Fitzgerald R, Laureano-Pérez L, Bai Y, Dmochowski IJ (2011). *Measurement of radon and xenon binding to a cryptophane molecular host*, PNAS 108 : 10969-10973.
53. Darzac M, Brotin T, Bouchu D, Dutasta JP (2002). *Cryptophanols, new versatile compounds for the synthesis of functionalized cryptophanes and polycryptophanes*, Chem Commun 1 : 48-49.
54. Darzac M, Brotin T, Rousset-Arzet L, Bouchu D, Dutasta JP. (2004). *Synthesis and application of cryptophanol hosts: 129Xe NMR spectroscopy of a deuterium-labeled (Xe)2@bis-cryptophane complex*, New. J. Chem. 28 : 502-512.
55. Spence MM, Ruiz EJ, Rubin SM, Lowery TJ, Winssinger N, Schultz PG, Wemmer DE, Pines A (2004). *Development of a Functionalized Xenon Biosensor*, J Am Chem Soc 126 : 15287-15294.
56. Spence MM, Rubin SM, Dimitrov IE, Ruiz EJ, Wemmer DE, Pines A, Yao SQ, Tian F, Schultz PG. (2001). *Functionalized Xenon as a biosensor*, PNAS 98 : 10654-10657.
57. Brotin T, Collet A, Lesage A, Emsley L, Collet A. (2001). *Synthesis of Deuterium-Labeled Cryptophane-A and Investigation of Xe@Cryptophane Complexation Dynamics by 1D-EXSY NMR Experiments.*, Chem Eur J 7 : 1561-1573.
58. Brotin T, Roy V, Dutasta J-P (2005). *Improved Synthesis of Functional CTVs and Cryptophanes Using $Sc(OTf)_3$ as Catalyst*, J Org Chem 70 : 6187–6195.
59. Liu G, Song X, Chan KWY, McMahon MT (2012). *Nuts and bolts of chemical exchange saturation transfer MRI*, NMR Biomed 26 : 810–828.
60. Dubes A, Moudrakovski IL, Shahgaldian P, Coleman AW, Ratcliffe CI, Ripmeester JA. (2004). *Distribution and modification of absorption sites in amphiphilic calixarene-based solid lipid nanoparticles from hyperpolarized 129Xe NMR spectroscopy.*, J Am Chem Soc 162 : 6236-7.
61. Kim BS Ko YH, Kim Y, Lee HJ, Selvapalam N, Lee HC, Kim K. (2008). *Water soluble cucurbit[6]uril derivative as a potential Xe carrier for 129Xe NMR-based biosensors.*, Chem Comm (Camb) 28 : 2756-2758.
62. Cheng CY Stamatatos TC, Christou G, Bowers CR. (2010). *Molecular wheels as nanoporous materials: differing modes of gas diffusion through Ga10 and Ga18 wheels probed by hyperpolarized 129Xe NMR spectroscopy.*, J Am Chem Soc 132 : :5387-93.
63. Shapiro MG, Ramirez RM, Sperling LJ, Sun G, Sun J, Pines A, Schaffer DV, Bajaj VS (2014). *Genetically encoded reporters for hyperpolarized xenon magnetic resonance imaging*, Nature Chem 6 : 629-634.
64. Garimella PD, Meldrum T, Witus LS, Smith M, Bajaj VS, Wemmer DE, Frances MB, Pines A (2014). *Hyperpolarized Xenon-Based Molecular Sensors for Label-Free Detection of analytes*, J Am Chem Soc 136 :

164-168.

65. Gherase MR, Wallace JC, Cross AR, Santyr GE. (2006). *Two-compartment radial diffusive exchange analysis of the NMR lineshape of (129)Xe dissolved in a perfluorooctyl bromide emulsion*, J Chem Phys 125 : 44906.
66. Stevens TK, Ramirez RM, Pines A. (2013). *Nanoemulsion contrast agents with sub-picomolar sensitivity for xenon NMR.*, J Am Chem Soc 135 : 9576-9.
67. Klippel S. Freund C., Schoeder L (2014). *Multichannel MRI labeling of mammalian cells by switchable nanocarriers for hyperpolarized xenon*, Nano Letters 14 : 5721-6.
68. Bai Y, Wang Y, Goulian M, Driks A, Dmochowski IJ (2014). *Bacterial spore detection and analysis using hyperpolarized 129Xe chemical exchange saturation transfer (Hyper-CEST) NMR*, Chem Sci 5 : 3197-3203.
69. Meldrum T, Schröder L, Denger P, Wemmer DE, Pines A. (2010). *Xenon-based molecular sensors in lipid suspensions.*, J Magn Reson. 205 : 242-6.
70. Schnurr M, Witte C, Schröder L.(2013). *Functionalized 129Xe as a potential biosensor for membrane fluidity*, Phys Chem Chem Phys 15 : 14178-14181.
71. Boutin C, Desvaux H, Carrière M, Leteutre F, Jamin N, Boulard Y, Berthault P. (2011). *Hyperpolarized 129Xe NMR signature of living biological cells*, NMR Biomed 24 : 1264-1269.
72. Tarantula O and Dmochowski IJ(2010). *Functionalized 129Xe contrast agents for magnetic resonance imaging*, Current Opinion in Chenical Biology 14 : 97-104.
73. Roy V Brotin T, Dutasta JP, Charles MH, Delair T, Mallet F, Huber G, Desvaux H, Boulard Y, Berthault P. (2007). *A cryptophane biosensor for the detection of specific nucleotide targets through xenon NMR spectroscopy*, Chemphyschem 8 : 2082-2085.
74. Schlundt A, Kilian W, Beyermann M, Sticht J, Günther S, Höpner S, Falk K, Roetzschke O, Mitschang L, Freund C. (2009). *A Xenon-129 Biosensor for monitoring MHC-Peptide Interactions.* Angew Chem Int Ed 48 : 1-5.
75. Stevens T ,Palaniappan KK, Ramirez RM, Francis MB, Wemmer DE, Pines A (2012). *HyperCEST detection of a 129Xe-based contrast agent composed of cryptophane-A molecular cages on a bacteriophage scaffold*, Magn Reson Med 69: 1245-52.
76. Palaniappan KK, Ramirez RM, Bajaj VS, Wemmer DE, Pines A, Francis MB. (2013). *Molecular Imaging of Cancer Cells Using a Bacteriophage-Based 129Xe NMR Biosensor*, Angew Chem Int Ed Engl 52 : 4849–4853.
77. Tassali N, Kotera N, Boutin C, Léonce E, Boulard Y, Rousseau B, Dubost E, Taran F, Brotin T, Dutasta JP, Berthault P. (2014). *Smart Detection of Toxic Metal Ions, Pb^{2+} and Cd^{2+}, Using a 129Xe NMR-Based Sensor*, Anal Chem 83 : 1783–1788.
78. Zhang J, Jiang W, Luo Q, Zhang X, Guo Q, Liu M, Zhou X. (2014). *Rational design of hyperpolarized xenon NMR molecular sensor for the selective and sensitive determination of zinc ions*, Talanta 122 : 101-105.
79. Aaron JA Chambers JM, Jude KM, Di Costanzo L, Dmochowski IJ, Christianson DW. (2008). *Structure of a 129Xe-cryptophane biosensor complexed with human carbonic anhydrase II*, J Am Chem Soc 130 : 6942-6943.
80. Chambers JM, Hill PA, Aaron JA, Han Z, Christianson DW, Zuzma NN, Dmochowski IJ. (2009). *Cryptophane Xenon-129 Nuclear Magnetic Resonance Biosensors Targeting Human Carbonic Anhydrase*, J Am Chem Soc 131 : 563-569.
81. Wei Q, Seward GK, Hill PA, Patton B, Dimitrov IE, Kuzma NN, Dmochowski IJ (2006). *Designing 129Xe NMR biosensors for matrix metalloproteinase detection*, J Am Chem Soc. 128 : 13274-83..
82. Lowery TJ, Garcia S, Chavez L, Ruiz EJ, Wu T, Brotin T, Dutasta JP, King DS, Schultz PG, Pines A, Wemmer DE. (2006). *Optimization of Xenon Biosensors for Detection of Protein Interactions*, ChemBioChem 7 : 65-73.
83. Seward GK, Wei Q, Dmochowski IJ. (2008) *Peptide-Mediated Cellular Uptake of Cryptophane*, Bioconjug Chem 19 : 2129-2135.
84. Boutin C, Stopin, Lenda F, Brotin T, Dutasta JP, Jamin N, Sanson A, Boulard Y, Leteurtre F, Huber G, Bogaert-Buchmann A, Tassali N, Desvaux H, Carrière M, Berthault P, (2011) *Cell uptake of a biosensor detected by hyperpolarized (129)Xe NMR: The transferrin case.* Bioorg Med Chem 19:4135-43.

85. Seward GK, Bai Y, Khan NS, Dmochowski IJ (2011). *Cell-compatible, integrin-targeted cryptophane-129Xe NMR biosensors*, Chemical Science 2 : 1103-1110.
86. Sloniec J, Schnurr M, Witte C, Resch-Genger U, Schröder L, Hennig, A. (2013). *Biomembrane Interactions of Functionalized Cryptophane-A: Combined Fluorescence and 129X NMR Studies of a Bimodal Contrast Agent*, Chem Eur J 19 : 3110–3118.
87. Schnurr M, Witte C, Schröder L. (2014). *Depolarization Laplace transform analysis of exchangeable hyperpolarized ^{129}Xe for detecting ordering phases and cholesterol content of biomembrane models.*, Biophys J 106 : 1301-1308.
88. Mynar JL, Lowery TJ, Wemmer DE, Pines A, Fréchet JM.(2006). *Xenon biosensor amplification via dendrimer-cage supramolecular constructs*, J Am Chem Soc 128 : 6334-6335.
89. Meldrum T, Seim KL, Bajaj VS, Palaniappan KK, Wu W, Francis MB, Wemmer DE, Pines A. (2010). *A Xenon-Based Molecular Sensor Assembled on an MS2 Viral Capsid Scaffold*, J. Am. Chem. Soc. 132 : 5936-5937.
90. Schnurr M, Sydow K, Rose HM, Dathe M, Schröder, L. (2015). *Brain Endothelial Cell Targeting Via a Peptide-Functionalized Liposomal Carrier for Xenon Hyper-CEST MRI*, Advance Healthcare Materials 4 : 40-45.
91. Witte C, Martos V, Rose HM, Reinke S, Klippel S, Schröder L, Hackenberger CP. (2015). *Live-cell MRI with Xenon Hyper-CEST Biosensors Targeted to Metabolically Labeled Cell-Surface Glycans*, Angew Chem Int Ed Engl. 54 : 2806-2810.
92. Lebel R and Lepage M. (2014). *A comprehensive review on controls in molecular imaging: lessons from MMP-2 imaging*, Contrast Media Mol I 9 : 187–210.
93. Terreno E, Delli Castelli D, Aime S. (2010). *Encoding the frequency dependence in MRI contrast media: the emerging class of CEST agents*, Contrast Media Mol I 5 : 1-22.
94. Hingorani DV, Bernstein AS, Pagel MD. (2014). *A review of responsive MRI contrast agents:2005-2014*, Constrast Media Mol I. doi:10.1002/cmmi.1629
95. Hindorani DV, Yoo B, Bernstein AS, Pagel MD(2014). *Detecting Enzyme Activities with Exogenous MRI Constrast Agents*, Chem Eur J 20 : 9840-9850.
96. Ward KM Aletras AH, Balaban RS. (2000). *A New Class of Contrast Agents for MRI Based on Proton Chemical Exchange Dependent Saturation Transfer (CEST)*, J Magn Res 143 : 79–87.
97. Sherry AD and Woods M. (2008). *Chemical Exchange Saturation Transfer Contrast Agents for Magnetic Resonance Imaging*, Ann Rev Biomed Eng 10 : 391-411.
98. Vinogradov E Sherry AD, Lenkiski LE. (2012). *CEST: From basic principles to applications, challenges and opportunities*, Journal of Magnetic Resonance 229 : 155-72.
99. Kunth M, Döpfert J, Witte C, Rossella F, Schröder L.(2012). *Optimized Use of Reversible Binding for Fast and Selective NMR Localization of Caged Xenon* Angew. Chem. Int. Ed 51 : 1-5.
100. Döpfert J, Zaiss M, Witte C, Schröder L. (2014). *Ultrafast CEST imaging*, J Magn Reson 243 : 45-53.
101. Schröder L, Lowery TJ, Hilty C, Wemmer DE, Pines A. (2006). *Molecular Imaging Using a Targeted Magnetic Resonance Hyperpolarized Biosensor*, Science 314 : 446-449.
102. Querol M and Bogdanov jr. A. (2006). *Amplification strategies in MR imaging: Activation and accumulation of sensing contrast agents (SCAs)*, J Magn Res Imaging 24 : 971-982.
103. van Zijl PCM and Yadav NN.(2011). *Chemical exchange saturation transfer (CEST): What is in a name and what isn't?*, Magn Reson Med 65 : 927-948.
104. De Leon-Rodriguez LM, Lubag AJ, Malloy CR, Martinez GV, Gillies RJ, Sherry AD. (2009). *Responsive MRI Agents for Sensing Metabolism in Vivo.* Acc Chem Res 7 : 948-957.
105. Zaiss M, Schnurr M, Bachert P. (2012) *Analytical solution for the depolarization of hyperpolarized nuclei by chemical exchange saturation transfer between free and encapsulated xenon (HyperCEST)*, J Chem Phys 136 : 14410
106. Klippel S, Döpfert J, Jayapaul J, Kunth M, Rossella F, Schnurr M, Witte C, Freund C, Schröder L. (2014) *Cell*

Tracking with Caged Xenon: Using Cryptophanes as MRI Reporters upon Cellular Internalization. Angew Chem Int Ed Engl, 53: 493-496

107. Rossella F, Rose HM, Witte C, Jayapaul J, Schröder L. (2014) *Design and Characterization of Two Bifunctional Cryptophane A-Based Host Molecules for Xenon Magnetic Resonance Imaging Applications*. ChemPlusChem 79:1463–1471.
108. Rose HM, Witte C, Rossella F, Klippel S, Freund C, Schröder L. (2014) *Development of an Antibody-based, Modular Biosensor for ^{129}Xe NMR Molecular Imaging of Cells at Nanomolar Concentration.* PNAS, 111: 11697-11702.
109. Santagada V. and Caliendo G. (2003) "*Peptidi e Peptidomimetici*" Piccin Nuova Libraria S.p.A, Padovam 440-441
110. Romieu A, Bruckdorfer T, Clavé G, Grandeclaude V, Massif C, Renard PY (2011). *N-Fmoc-α- sulfo-β-alanine: a Versatile Building Block for the Water Solubilisation of Chromophores and Fluorophores by Solid-phase Strategy*. Org Biomol Chem 9: 5337-5342.
111. Veronese FM (2001) *Peptide and Protein PEGylation: a Review of Problems and Solutions*. Biomaterials 22 (5): 405-417.
112. Veronese FM and Pasut G (2005) *PEGylation, Successful Approach to Drug Delivery.* Drug Discov Today 10 : 1451-1458.
113. Romieu A, Tevernier-Lohr D, Pellet-Rostaing S, Lemaire M, Renard PY (2010) *Water Solubilization of Xanthene Dyes by Post-synthetic Sulfonation in Organic Media*. Tetrahedron Lett 51 :3304-3307
114. Lavis LD and Raines RT (2008) *Bright Idea for Chemical Biology.* ACS Chem Biol 3: 142-155
115. Gonçalves MST (2009) *Fluorescent Labelling of Biomolecules with Organic Probes*. Chem Rev 109: 190-212
116. Jullian M, Hernandez A. Maurras A, Puget K, Anmblard M, Martinez J, Subra G (2009) *N-terminus FITC Labeling of Peptides on Solid Support: the Truth Behind the Spacer.* Tetrahedron Lett 50 : 260-263.
117. Tokmina-Roszyk M, Tokmina-Roszyk D, Fields GB (2013) *The Synthesis and Application of Fmoc-Lys(5-Fam) Building Blocks.* Biopolymers 100:347-355.
118. Fischer R, Mader O, Jung Gand, Brock R (2003) *Extending the Applicability of Carboxyfluorescein in Solid-phase Synthesis*. Bioconj Chem 14: 653:660.
119. Steinman RM, Silver JM, Cohn ZA(1974) *Pinocytosis in Fibroblasts: Quantitative Studies in Vitro.* J Cell Biol 63: 949–969.
120. Lim PJ and Gleeson PA(2011) *Macropinocytosis: an Endocytic Pathway for Internalising Large Gulps.* Immunol Cell Biol, 89 :836– 843.
121. Bacsa B, Desai B, Dibó G, Kappe C.O. (2009) *Rapid Solid-phase Peptide Synthesis Using Thermal and Controlled Microwave Irradiation.* J Pept Sci 12: 633-638.
122. Moltalbetti CAGN and Falque V (2005) *Amide Bond Formation and Peptide Coupling.* Tetrahedron 61:10827-10852.
123. Tierney JP and Lidström P (2005) *Microwave Assisted Organic Synthesis,* Blackwell Publishing Ltd, Oxford, UK Pages 1-21; 178-219.
124. Pedersen SL, Tofteng AP, Malik L, Jensen KJ (2012) *Microwave Heating in Solid-phase Peptide Synthesis* Chem Soc Rev 41: 1826-1844.
125. Fara MA, Diaz-Mocheon JJ, Bradley M (2006) *Microwave-assisted Coupling with DIC/HOBt for the Synthesis of Difficult Peptoids and Fluorescently Labelled Peptides-a Gentle Heat Goes a Long Way* Tetrahedron Lett 47: 1011-1014
126. Palasek SA, Cox ZJ, Collins JM. (2007) *Limiting racemization and aspartimide formation in microwave-enhanced Fmoc solid phase peptide synthesis.* J Pept Sci 13: 143-148
127. Subiros-Funosas R, Acosta GA, El-Faham A, Albericio F. (2009) *Microwave Irradiation and COMU: a Potent Combination for Solid-phase Peptide Synthesis.* Tetrahedron Lett 50:6200-6202.

128. García-Martín F, Quintanar-Audelo M, García-Ramos Y, Cruz LJ, Gravel C, Furic R, Côté S, Tulla-Puche J, Albericio F (2006) *ChemMatrix®, a Poly(ethylene glycol)-based Support for the Solid- phase Synthesis of Complex Peptides* J Comb Chem 8:213-220
129. García-Ramos Y, Paradís-Bas M, Tulla-Puche J, Albericio F (2010). *ChemMatrix® for Complex Peptides and Combinatorial Chemistry*. J Pept Sci 16: 675-678.
130. Yang J, Alemany LB, Driver J, Hartgerink JD, Barron AR.(2007) *Fullerene-Derivatized Amino Acids: Synthesis, Characterization, Antioxidant Properties, and Solid-Phase Peptide Synthesis*. Chem Eur J13:2530-254
131. Valeur E and Bradley M. (2009) *Amide Bond Formation: Beyond the Myth of Coupling Reagents* Chem Soc Rev 38: 606-631.
131. Subiros-Funosas R, Prohens R., Barbas R, El-Faham A, Albericio F (2009) *Oxyma: An Efficient Additive for Peptide Synthesis to Replace the Benzotriazole-Based HOBt and HOAt with a Lower Risk of Explosion*. Chem Eur J 15:9394–9403.
132. El-Faham A and Albericio F. (2011) *Peptide Coupling Reagents, More than a Letter Soup*. Chem Soc Rev 111: 6557-6602.
133. Chantell CA, Onaiyekan MA, Menakuru M. (2012) *Fast Conventional Fmoc Solid-phase Peptide Synthesis: a Comparative Study of Different Activators.* J Pept Sci 18:88-91.
134. El-Faham A, Subiros-Funosas R, Prohens R, Albericio F (2009) *COMU: A Safer and More Effective Replacement for Benzotriazole-Based Uronium Coupling Reagents.* Chem Eur J 15:9404-9416.
135. El-Faham A and Albericio F. (2010) *COMU: a Third Generation of Uronium-type Coupling Reagents*. J Pept Sci 16:6-9.
136. Subiros-Funosas R, Acosta GA, El-Faham A, Albericio F (2009) *Microwave irradiation and COMU: a potent combination for solid-phase peptide synthesis.* Tetraheadron Lett 50: 6200-6202
137. Subiros-Funosas R, El-Faham A, Albericio F. (2010) *PyOxP and PyOxB: the Oxyma-based Novel Family of Phosphonium Salts.* Org Biomol Chem 8: 3665-3673
138. Subiros-Funosas R, Khattab SN, Nieto-Rodríguez L,El-Faham A, Albericio F. (2013) *Advances in Acylation Methodologies Enabled by Oxyma-based Reagents*. Aldrichimica Acta 46:21-41.
139. Subiros-Funosas R, Nieto-Rodríguez L, Jensen KJ, Albericio F. (2013) *COMU: Scope and Limitations of the Latest Innovation in Peptide Acyl Transfer Reagents.* J Pept Sci 19:408-414.
140. Echalier C, Al-Halifa S, Kreiter A, Enjalbal C, Sanchez P, Ronga L, Puget K, Verdié P, Amblard M, Martinez J, Subra G. (2013) *Heating and Microwave Assisted SPPS of C-terminal Acid Peptides on Trityl Resin: the Truth Behind the Yield*. Amino Acids 45:1395-1403.
141. Longmire MR, Ogawa M, Hama Y, Kosaka N, Regino CA, Choyke PL, Kobayashi H. (2008) Determination of Optimal Rhodamine Fluorophore for in Vivo Optical Imaging. *Bioconj Chem* 19 (8):1735-1742
142. Bandichhor R, Petrescu AD ,Vespa A ,Kier AB ,Schröder F ,Burgess K. (2006) *Synthesis of a New Water-Soluble Rhodamine Derivative and Application to Protein Labeling and Intracellular Imaging.* Bioconj Chem 17:1219-1225.
143. Beija M, Afonso CAM, Martinho JMG. (2009) *Synthesis and Applications of Rhodamine Derivatives as Fluorescent Probes.* Chem Soc Rev 38:2410-2433.
144. Cheunga JC, Chiawa PK, Debera CM, Bear CE (2009) *A Novel Method for Monitoring the Cytosolic Delivery of Peptide Cargo.* J Control Rel 137: 2-7.
145. El-Faham A, Khattab SN, Subiros-Funosas R, Albericio F (2014) *BOP-OXy, BOP-OBt, and BOP- OAt: Novel Organophosphinic Coupling Reagents Useful for Solution and Solid-phase Peptide Synthesis*.J Pept Sci 20 :1-6.
146. Unruh JR, Gokulrangan G, Wilson GS, Johnson CK. (2005) *Fluorescence Properties of Fluorescein, Tetramethylrhodamine and Texas Red Linked to a DNA Aptamer.* Photochem Pthotobiol 81: 682-690.
147. Cardenas-Maestre JM and Sanchez-Martin JM. (2011) *Efficient Solid Phase Strategy for Preparation of Modified Xanthene Dyes for Biolabelling.* Org Biomol Chem 9 1720-1722.

148. Lakowitz J.R. *"Principles of Fluorescence Spectroscopy"* (2006) Springer Ed. Heidelberg. Pages 8-59.
149. Resch-Genger U and Rurack K. (2013) *Determination of the Photoluminescence Quantum Yield of Dilute Dye Solutions (IUPAC Technical Report)*. Pure Appl Chem 85: 2005-2013.
150. Jewett JC, and Bertozzi CR. (2011) *Synthesis of a Fluorogenic Cyclooctyne Activated by Cu-Free Click Chemistry.* Org Lett 13 :5937-5939.
151. Choi EJ, Kim E, Lee Y, Jo A, Park SB. (2014) *Rational Perturbation of the Fluorescence Quantum Yield in Emission□Tunable and Predictable Fluorophores (Seoul□Fluors) by a Facile Synthetic Method Involving C-H Activation.* Angew Chem Int Ed Engl 53 :1346-1350.
152. Gai L, Mack J, Lu H, Yamada H, Kuzuhara D, Lai G, Li Z, Shen Z. (2014) *New 2,6-Distyryl-Substituted BODIPY Isomers: Synthesis, Photophysical Properties, and Theoretical Calculations*. Chem Eur J 20:1091-1122.
153. Sjöback R, Nygren J, Kubista M. (1998) *Characterization of Fluorescein–Oligonucleotide Conjugates and Measurement of Local Electrostatic Potential*. Biopolymers 46: 445-453.
154. Bidmanova S, Hlavacek A, Damborsky J, Prokop Z.(2012) *Conjugation of 5(6)-carboxyfluorescein and 5(6)-carboxynaphthofluorescein with Bovine Serum Aalbumin and Their Immobilization for Optical pH Sensing*. Sens Actuators B Chem 161: 93–99
155. Phelps MA, Foraker AB, Gao W, Dalton JT, Swaan PW. (2004) *A novel Rhodamine-riboflavin Conjugate Probe Exhibits Distinct Fluorescence Resonance Energy Transfer that Eenables Riboflavin Trafficking and Subcellular Localization Studies*. Mol Pharm 1: 257-266.
156. Massey M, Algar WR, Krull UJ (2006) *Fluorescence Resonance Energy Transfer (FRET) for DNA Biosensors: FRET Pairs and Förster Distances for Various Dye-DNA Conjugates*. Anal Chim Acta 568:181-189.
157. Miura T,Urano Y, Tanaka K,Nagano T,Ohkubo K, Fukuzumi S. (2003) *Rational Design Principle for Modulating Fluorescence Properties of Fluorescein-Based Probes by Photoinduced Electron Transfer.* J Am Chem Soc 125:8666-8671
158. Sohaebuddin SK, Thevenot PT, Baker D, Eaton JW, Tang L. (2010) *Nanomaterial Cytotoxicity is Composition, Size, and Cell Type Dependent*. Particle and Fibre Toxicology 7 :1-17.
159. Alford R, Simpson HM. Duberman J, Hill GC, Ogawa M, Regino C, Kobayashi H, Choyke PL (2009) *Toxicity of Organic Fluorophores Used in Molecular Imaging: Literature Review.* Mol Imaging 8: 341-354.
160. Wang Z, Zhang L,Wang H,Xiong S,Li Y,Tao Q,Xiao W, Qin H,Wang Y, Zhai Z. (2015) *Tumor-induced CD14(+)HLA-DR (-/low) myeloid-derived suppressor cells correlate with tumor progression and outcome of therapy in multiple myeloma patient.* Cancer Immunol Immunother 64: 389-399.
161. Collin J, Gössl M, Matsuo Y, Cilluffo RR, Flammer AJ, Loeffler D, Lennon RJ, Simari RD, Spoon DB, Erbel R, Lerman LO, Khosla S, Lerman A. (2014) *Osteogenic monocytes within the cor onary circulation and their association with plaque vulnerability in patients with early atherosclerosis*. Int J Cardiol181:57-64.
162. te Boekhost BC, Van Tilborg CA, Strijkers GJ, Nicholay K. (2012) *Molecular MRI of Inflammation in Atherosclerosis.* Curr Cardiovasc Imaging Rep 5: 60-68.
163. Shabo I and Slavink S. (2011) *Expression of macrophage antigens by tumor cells.* Adv Med Exp Biol 714: 141-150
164. Sakahara H and Saga T. (1999) *Avidin-biotin system for delivery of diagnostic agents* Adv Drug Deliv Rev 37: 89-101
165. Coin I, Beyermann M, Bienert M. (2007) *Solid-phase peptide synthesis: from standard procedures to the synthesis of difficult sequences.* Nat Protol 2:3247-3256.
166. Carnaroglio D, Martina K, Palmisano G, Penoni A, Domini C, Cravotto G. (2013) *One-pot sequential synthesis of isocyanates and urea derivatives via a microwave-assisted Staudinger–aza-Wittig reaction*. Bellstein J Org Chem 9: 2378-2386.
168. Bode W, Fernandez-Catalan C, Tschesche H, Grams F, Nagase H, Maskos K. (1999). *Structural properties of matrix metalloproteinases*, Cell Mol Life Sci 55 : 693-652.

169. Löffek S, Schilling O, Franzke CW. (2011). *Biological role of matrix metalloproteinases: a critical balance*, Eur Respir J 38 : 191-208.
170. Nagase H and Woessner Jr. JF (1999). *Matrix Metalloproteinases*, J Biol Chem 274 : 21491-21494.
171. Visse R and Nagase H (2003). *Matrix Metalloproteinases and Tissue Inhibitors of Metalloproteinases: Structure, Function, and Biochemistry*, Circ Res 92 : 827-839.
172. Morrison CJ, Butler GS, Rodríguez C, Overall CM. (2009). *Matrix metalloproteinase proteomics: substrates, targets, and therapy*, Curr Opin Cell Biol 21 : 645-653.
173. Butler GS and Overall CM. (2009). *Updated Biological Roles for Matrix Metalloproteases and New "Intracellular" Substrates Revealed by Degradomics*, Biochemistry 48 : 10830-10845.
174. Nagase H, Visse R, Murphy G (2006). *Structure and function of matrix metalloproteinases and TIMPs*, Cardiovasc Res 69 : 562-573.
175. Hadler-Olsen E, Fadnes B, Sylte I, Uhlin-Hansen L, Winberg JO. (2011). *Regulation of matrix metalloproteinase activity in health and disease*, FEBS J 278 : 28-45.
176. Motrescu ER and Rio MC. (2008). *Cancer cells, adipocytes and matrix metalloproteinase 11: a vicious tumor progression cycle*, Biol Chem 389 : 1037-1041.
177. Overall CM (2002). *Molecular determinants of metalloproteinase substrate specificity: matrix metalloproteinase substrate binding domains, modules, and exosites*, Molec Biotechnol 22 : 51-86.
178. Klein T and Bishoff R. (2011). *Physiology and pathophysiology of matrix metalloproteases*, Amino Acids 41 : 271-290.
179. Maskos K.(2005). *Crystal structures of MMPs in complex with physiological and pharmacological inhibitors*, Biochimie 87 : 249-263.
180. Tallant C, Marrero A, Gomis-Rüth FX. (2010). *Matrix metalloproteinases: Fold and function of their catalytic domains*, Biochim Biophys Acta 1803 : 20-28.
181. Chen EI, Kridel SJ, Howard EW, Li W, Godzik A, Smith JW. (2002). *A unique substrate recognition profile for matrix metalloproteinase-2*, J Biol Chem. 277 : 4485-91.
182. Overall CM and López-Otín C (2002). *Strategies for MMP inhibition in cancer: Innovations for the post-trial era*, Nat Rev Cancer 2 : 657-681.
183. Ra HJ and Parks WC. (2007). *Control of matrix Metalloprotease catalytic Activity*, Matrix Biol 26 : 587-596.
184. McCaw PA, Ewald AJ, Werb Z.(2007). *Matrix metalloprotease and the regulation of tissue remodelling*, Nat Rev Mol Cell Biol 8 : 221-233.
185. Parks WC, Wilson CL, López-Boado YS (2004). *Matrix metalloproteinases as modulators of inflammation and innate immunity*, Nat Rev Immunol 4 : 617-628.
186. Turk BE, Huang LL, Piro ET, Cantley LC (2001). *Determination of protease cleavage site motifs using mixture-based oriented peptide libraries*, Nat Biotechnol 19 : 661-668.
187. Murphy G and Nagase H (2011). *Localizing Matrix Metalloprotease activities in the pericellular environment*, FEBS J 278 : 2-15.

188. Egeblad M and Werb Z. (2002). *New functions for the matrix metalloproteinases in cancer progression*, Nat Rev Cancer 2 : 161-174.
189. Kessenbrock K, Plaks V, Werb Z (2010). *Matrix Metalloproteases: Regulators of the Tumor microenvironment*, Cell 141 : 52-67.
190. Hadler-Olsen E, Winberg JO, Uhlin-Hansen L. (2013). *Matrix metalloproteinases in cancer: their value as diagnostic and prognostic markers and therapeutic targets*, Tumor Biol 34 : 2041-2051.
191. Vizoso FJ,González CM, Corte MD, Rodríguez JC, Vázquez J, Lamelas ML, Junquera S, Merino AM, García-Muñiz JLC. (2007). *Study of matrix metalloproteinases and their inhibitors in breast cancer*, Br J Cancer 96 : 903-911.

192. Chen Q, Jin M, Yang F, Zhu J, Xiao Q, Zhang L. (2013). *Matrix Metalloproteinases: Inflammatory Regulators of Cell Behaviors in Vascular Formation and Remodeling*, Mediators Inflamm 928315 : 14.
193. Su H, Spinale FG, Dobrucki LW, Song J, Hua J, Sweterlitsch S, Dione DP, Cavaliere P, Chow C, Bourke BN, Hu XY, Azure M, Yalamanchili P, Liu R, Cheesman EH, Robinson S, Edwards DS, Sinusas AJ . (2005). *Noninvasive Targeted Imaging of Matrix Metalloproteinase Activation in a Murine Model of Postinfarction Remodeling,* Circulation 112 : 3156-3167.
194. Schäfers M Schober O, Hermann S. (2010). *Matrix-Metalloproteinases as Imaging Targets for Inflammatory Activity in Atherosclerotic Plaques*, J Nuclear Med 51 : 663-666.
195. Felsen CN Savariar EN, Whitney M, Tsien RY. (2014). *Detection and monitoring of localized matrix metalloproteinase upregulation in a murine model of asthma.*, Am J Physiol Lung Cell Mol Physiol 308 : L764-74.
196. Li WP and Anderson CJ (2003). *Imaging matrix metalloproteinase expression in tumors*, Q J Nucl Med. 47 : 201-08.
197. Van de Wiele C and Oltenfreiter R (2006). *Imaging probes targeting matrix metalloproteinases.*, Cancer Biother Radiopharm 21 : 409-417.
198. Scherer RL, McIntyre JO, Matrisian LM (2008). *Imaging matrix metalloproteinases in cancer.*, Cancer Metastasis Rev. 27 : 679-690.
199. Giambernardi TA Grant GM, Grant GM, Taylor GP, Hay RJ, Maher VM, McCormick JJ, Klebe RJ. (1998) *Overview of matrix metalloproteinase expression in cultured human cells*, Matrix Biol 16 : 483-96.
200. Roomi MW Monterrey JC,Kalinovsky T, Rath M, Niedzwiecki A (2009). *Patterns of MMP-2 and MMP-9 expression in human cancer cell lines*, Oncol Rep 21 : 1323-1333.
201. Roomi MW Monterrey JC, Kalinovsky T, Rath M, Niedzwiecki A. (2010). *In vitro modulation of MMP-2 and MMP-9 in human cervical and ovarian cancer cell lines by cytokines, inducers and inhibitors*, Oncol Rep 23 : 605-614.
202. Hattori S, Fujisaki H, Kiriyama T, Yokoyama T, Irie S. (2002). *Real-Time Zymography and Reverse Zymography: A Method for Detecting Activities of Matrix Metalloproteinases and Their Inhibitors Using FITC-Labeled Collagen and Casein as Substrates*, Anal Biochem 301 : 27-34.
203. Krizkova S, Zitka O, Masarik M, Adam V, Stiborova M, Eckschlager T, Chavis GJ, KIzek R (2011). *Assays for determination of matrix metalloproteinases and their activity*, Trends Analyt Chem 30 : 1819-1832.
204. Zhang Y, So MY, Rao J (2006). *Protease-Modulated Cellular Uptake of Quantum Dots*, Nano Lett 6 : 1988-1992.
205. Lebel R Bonin MA, Zriba R, Radulska A, Neugebauer W, Lepage M. (2012). *Impact of H-aggregation on activatable MMP-2-specific probes for optical imaging*, Contrast Media Mol Imaging 7 : 328-337.
206. Meyer BS and Rademann J. (2012). *Extra- and Intracellular Imaging of human Matrix Metalloprotease 11 (hMMP-11) with a Cell-Penetrating FRET-Substrate*, J Biol Chem 45:37857-67
207. Bremer C, Tung CH, Weissleder R. (2001). *In vivo molecular target assessment of matrix metalloproteinase inhibition.*, Nat Med 7 : 743-8..
208. Lebel R Jastrzebska B, Therriault H, Cournoyer MM, McIntyre JO, Escher E, Neugebauer W, Paquette B, Lepage M. (2008). *Novel solubility-switchable MRI agent allows the noninvasive detection of matrix metalloproteinase-2 activity in vivo in a mouse model.*, Magn Reson Med 60 : 1056-1065.
209. Jastrzebska B Lebel R, Therriault H, McIntyre JO, Escher E, Guérin B, Paquette B, Neugebauer WA, Lepage M (2009). *New enzyme-activated solubility-switchable contrast agent for magnetic resonance imaging: from synthesis to in vivo imaging.*, J Med Chem. 26 : 1576-81..
210. Harris TJ, van Maltzahn G, Derfus AM, Ruoslahti E, Bhatia SN. (2006). *Proteolytic actuation of nanoparticle self-assembly*, Angew Chem Int Ed Engl. 45 : 3161-3165.
211. Akers WJ, Xu B, Xu B, Lee H, Sudlow GP, Fields GB, Achilefu S, Edwards WB. (2012). *Detection of MMP-2 and MMP-9 Activity in Vivo with a Triple-Helical Peptide Optical Probe*, Bioconj Chem 23 : 656-663.
212. Aguilera TA, Olson ES, Timmers MM, Jiang T, Tsien RY (2009). *Systemic in vivo distribution of activatable cell*

penetrating peptides is superior to that of cell penetrating peptides, Integr Biol (Camb). 1 : 371-381.

213. Olson ES, Jiang T, Aguilera TA, Nguyen QT, Ellies LG, Scadeng M, Tsien RY.(2010). *Activatable cell penetrating peptides linked to nanoparticles as dual probes for in vivo fluorescence and MR imaging of proteases.*, Proc Natl Acad Sci 107 : 4311-4316.
214. van Duijnhoven SM, Robillard MS, Nicolay K, Grüll H. (2011). *Tumor targeting of MMP-2/9 activatable cell-penetrating imaging probes is caused by tumor-independent activation.*, J Nucl Med 52 : 279-286.
215. Savariar EN Felsen CN, Felsen CN, Nashi N, Jiang T, Ellies LG, Steinbach P, Tsien RY, Nguyen QT. (2013). *Real-time in vivo molecular detection of primary tumors and metastases with ratiometric activatable cell-penetrating peptides.*, Cancer Res 73 : 855-64.
216. van Duijnhoven SM Robillard MS, Hermann S, Kuhlmann MT, Schäfers M, Nicolay K, Grüll H.(2014). *Imaging of MMP activity in postischemic cardiac remodeling using radiolabeled MMP-2/9 activatable peptide probes.*, Mol Pharm 11 : 1415-1423.
217. van Duijnhoven SM Robillard MS, Nicolay K, Grüll H. (2015). *In vivo biodistribution of radiolabeled MMP-2/9 activatable cell-penetrating peptide probes in tumor-bearing mice.*, Contrast Media Mol Imaging 10: 59-66.
218. Crisp JL Savariar EN, Glasgow HL, Ellies LG, Whitney MA, Tsien R (2014). *Dual Targeting of Integrin αvβ3 and Matrix Metalloproteinase-2 for Optical Imaging of Tumors and Chemotherapeutic Delivery.*, Mol Cancer Ther 13 : 1514-25.
219. Olson ES, Whitney MA, Friedman B, Aguilera TA, Crisp JL, Baik FM, Jiang T, Baird SM, Tsimikas S, Tsien RY, Nguyen QT. (2012) *In vivo fluorescence imaging of atherosclerotic plaques with activatable cell-penetrating peptides targeting thrombin activity*. Integ Biol (Chemb) 4: 595-605.
220. Watkins GA Jones EF, Jones EF, Scott Shell M, VanBrocklin HF, Pan MH, Hanrahan SM, Feng JJ, He J, Sounni NE, Dill KA, Contag CH, Coussens LM, Franc BL. (2009). *Development of an optimized activatable MMP-14 targeted SPECT imaging probe*, Bioorg Med Chem 17 : 653-659.
221. Jiang T Olson ES, Nguyen QT, Roy M, Jennings PA, Tsien RY. (2004). *Tumor imaging by means of proteolytic activation of cell-penetrating peptides.*, Proc Natl Acad Sci 101 : 17867-17872.
222. Olson ES Aguilera TA, Whitney MA, Friedman B, Aguilera TA, Crisp JL, Baik FM, Jiang T, Baird SM, Tsimikas S, Tsien RY, Nguyen QT (2009). *In vivo characterization of activatable cell penetrating peptides for targeting protease activity in cancer.*, Integr Biol (Camb) 1 : 382-393.
223. von Marschall Z, Riecken EO, Rosewicz S.(1998) *Stromelysin 3 is overexpressed in human pancreatic carcinoma and regulated by retinoic acid in pancreatic carcinoma cell lines*, Gut 43 : 692-698.
224. Jones LE Humphreys MJ, Campbell F, Neoptolemos JP, Boyd MT.(2004) *Comprehensive Analysis of Matrix Metalloproteinase and Tissue Inhibitor Expression in Pancreatic Cancer: Increased Expression of Matrix Metalloproteinase-7 Predicts Poor Survival*, Clin Cancer Res10 : 2832–2845.
225. Yang YH, Deng H, Li WM, Zhang QY, Hu XT, Xiao B, Zhu HH, Geng PL, Lu YY.(2008). *Identification of matrix metalloproteinase 11 as a predictive tumor marker in serum based on gene expression profiling*, Clin Cancer Res 14 : 74-81.
226. Zhao ZS, Chu YQ, Ye ZY, Wang YY, Tao HQ.(2010) *Overexpression of matrix metalloproteinase 11 in human gastric carcinoma and its clinicopathologic significance*, Hum Path 41 : 686-696.
227. Pan W, Arnone M, Kendall M, Grafstrom RH, Seitz SP, Wasserman ZR, Albright CF. (2003). *Identification of peptide substrates for human MMP-11 (stromelysin-3) using phage display*, J Biol Chem 278 : 27820-27827.
228. Holtz B Cuniasse P, Boulay A, Kannan R, Mucha A, Beau F, Basset P, Dive V (1999). *Role of the S1‘ Subsite Glutamine 215 in Activity and Specificity of Stromelysin-3 by Site-Directed Mutagenesis*, Biochem 38 : 1274-12179.
229. Peruzzi D, Mori F, Conforti A, Lazzaro D, De Rinaldis E, Ciliberto G, La Monica N, Aurisicchio L. (2009). *MMP11: A Novel Target Antigen for Cancer Immunotherapy*, Clin Cancer Res 15 : 4104-4112.
230. Klein G, Vellenga E, Fraaije MW, Kamps WA, de Bont ES(2004). *The possible role of matrix metalloproteinase*

(MMP)-2 and MMP-9 in cancer, e.g. acute leukemia, Crit Rev Oncol Hematol 50 : 87-100.

231. Bauvois, B. (2012). *New facets of matrix metalloproteases MMP-2 and MMP-9 as cell surface transducers: Outside-in signaling and relationship to tumor progression*, Biochem Biophys Acta 1825 : 29-36.
232. Seltzer JL, Akers KT, Weingarten H, Grant GA, McCourt DW, Eisen AZ. (1990). *Cleavage specificity of human skin type IV collagenase (gelatinase). Identification of cleavage sites in type I gelatin, with confirmation using synthetic peptides.*, J Biol Chem 265 : 20409-20413.
233. Xiao J Addabbo RM, Addabbo RM, Lauer JL, Fields GB, Baum J. (2010). *Local Conformation and Dynamics of Isoleucine in the Collagenase Cleavage Site Provide a Recognition Signal for Matrix Metalloproteinases*, J Biol Chem 285 : 34181-34190.
234. Kridel SJ, Chen E, Kotra LP, Howard EW, Mobashery S, Smith JW. (2001). *Substrate Hydrolysis by Matrix Metalloproteinase-9*, The Journal of Biological Chemistry 276 : 20572-20578.
235. Berman J, Green M, Green M, Sugg E, Anderegg R, Millington DS, Norwood DL, McGeehan J, Wiseman J (1992). *Rapid optimization of enzyme substrates using defined substrate mixtures.*, J Biol Chem 267 : 1434-1437.
236. McGeehan GM, Bickett DM, Green M, Kassel D, Wiseman JS, Berman J. (1994). *Characterization of the peptide substrate specificities of interstitial collagenase and 92-kDa gelatinase. Implications for substrate optimization.*, J Biol Chem 269 : 32814-32820.
237. Whitney M, Crisp JL, Olson ES, Aguilera TA, Gross LA, Ellies LG, Tsien RY. (2010). *Parallel in Vivo and in Vitro Selection Using Phage Display Identifies Protease-dependent Tumor-targeting Peptides*, J Biol Chem 285 : 22535-22541.
238. Bremer C, Bredow S, Mahmood U, Weissleder R, Tung CH. (2001). *Optical imaging of matrix metalloproteinase-2 activity in tumors: feasibility study in a mouse model.*, Radiol 221 : 523-9.
239. Veiseh O, Sun C, Gunn J, Kohler N, Gabikian P, Lee D, Bhattarai N, Ellenbogen R, Sze R, Hallahan A, Olson J, Zhang MG. (2005). *Optical and MRI Multifunctional Nanoprobe for Targeting Gliomas*, Nano Lett 5 : 1003-1008.
240. Faust A, Waschkau B, Waldeck J, Höltke C, Breyholz HJ, Wagner S, Kopka K, Schober O, Heindel W, Schäfers M, Bremer C. (2009). *Synthesis and Evaluation of a Novel Hydroxamate Based Fluorescent Photoprobe for Imaging of Matrix Metalloproteinases*, Biocoj Chem 20 : 904-912.
241. auf dem Keller U, Bellac CL, Li Y, Lou Y, Lange PF, Ting R, Harwig C, Kappelhoff R, Dedhar S, Adam MJ, Ruth TJ, Bénard F, Perrin DM, Overall CM.(2010). *Novel matrix metalloproteinase inhibitor [18F]marimastat-aryltrifluoroborate as a probe for in vivo positron emission tomography imaging in cancer*, Can Res 70 : 7562-9.
242. Zhai X-H, Liu M, Guo X-J, Wang S-C, Zhang H-X, Guo Y-M(2011). *SKOV-3 cell imaging by Paramagnetic particles labeled with hairpin Cell-Penetrating peptides.*, Chin Med J 124 : 111-117.
243. Matsumura S, Aoki I, Saga T, Shiba K (2011). *A Tumor-Environment-Responsive Nanocarrier That Evolves Its Surface Properties upon Sensing Matrix Metalloproteinase-2 and Initiates Agglomeration to Enhance T2 Relaxivity for Magnetic Resonance Imaging*, Mol Pharma 8 : 1970-1974.
244. Waschkau B, Faust A, Schäfers M,Bremer C. (2013). *Performance of a new fluorescence-labeled MMP inhibitor to image tumor MMP activity in vivo in comparison to an MMP-activatable probe*, Contrast Media Mol Imaging 8 : 1–11.
245. Shi NQ Gao W, Xiang B, Qi XR. (2012). *Enhancing cellular uptake of activable cell-penetrating peptide-doxorubicin conjugate by enzymatic cleavage.*, Int J Nanomed 7 : 1613-21.
246. Mebrathu E, Zheleznyak A, Hur MA, Laforest R, Lapi SE. (2012). *Initial characterization of a dually radiolabeled peptide for simultaneous monitoring of protein targets and enzymatic activity*, Nuc Med Biol 40 : 190-196.
247. Casalini F, Fugazza L, Esposito G, Cabella C, Brioschi C, Cordaro A, D'Angeli L, Bartoli A, Filannino AM, Gringeri CV, Longo DL, Muzio V, Nuti E, Orlandini E, Figlia G, Quattrini A, Tei L, Digilio G, Rossello A, Maiocchi A.(2013). *Synthesis and preliminary evaluation in tumor bearing mice of new (18)F-labeled arylsulfone matrix metalloproteinase inhibitors as tracers for positron emission tomography.*, J Med Chem. 56 : 2676-89.

248. Temma T, Hanaoka H, Yonezawa A, Kondo N, Sano K, Sakamoto T, Seiki M, Ono M, Saji H (2014). *Investigation of a MMP-2 activity-dependent anchoring probe for nuclear imaging of cancer*, PLOS one 9 : e102180.
249. Gao H, Zhang S, Cao S, YAng Z, Pang Z, Jiang X (2014). *Angiopep-2 and Activatable Cell-Penetrating Peptide Dual-Functionalized Nanoparticles for Systemic Glioma-Targeting Delivery*, Mol Pharma 11 : 2755-2763.
250. Yue X, Wang Z, Zhu L, Wang Y, Qian C, Ma Y, Kiesewetter DO, Niu G, Chen X. (2014) *Novel 19F activatable probe for the detection of matrix metalloprotease-2 activity by MRI/MRS,* Mol Pharm 11: 4208-4217.
251. Jang ES, Lee SY, Cha EJ, Sun IC, Kwon IC, Kim D, Kim YI, Kim K, Ahn CH.(2014) *Fluorescent dye labeled iron oxide/silica core/shell nanoparticle as a multimodal imaging probe,* Pharm Res 31: 3371-8
252. Tansi F, Kallweit E, Kaether C, Kappe K, Schumann C, Hilger I, Reissmann S.(2014) I*nternalization of near-infrared fluorescently labeled activatable cell-penetrating peptide and of proteins into human fibrosarcoma cell line HT-1080,* J Cell Biochem, Dec 25. doi: 10.1002/jcb.25075
253. Kasper G Reule M, Tschirsmann M, Dankert N, Stout-Weider K, Lauster R, Schrock E, Mennerich D, Duda GN, Lehmann KE (2007). *Stromelysin-3 over-expression enhances tumourigenesis in MCF-7 and MDA-MB-231 breast cancer cell lines: involvement of the IGF-1 signalling pathway*, BMC Cancer 7 : 1-12.
254. Voland P Besig S, Besig S, Rad R, Braun T, Baur DM, Perren A, Langer R, Höfler H, Prinz C.(2009). *Correlation of Matrix Metalloproteinases and Tissue Inhibitors of Matrix Metalloproteinase Expression in Ileal Carcinoids, Lymph Nodes and Liver Metastasis with Prognosis and Survival*, Neuroendocrinology 89 : 66-78.
255. Yang YH Deng H, Deng H, Li WM, Zhang QY, Hu XT, Xiao B, Zhu HH, Geng PL, Lu YY (2008). *Identification of matrix metalloproteinase 11 as a predictive tumor marker in serum based on gene expression profiling*, Clin Cancer Res 14 : 74-81.
256. Zhao ZS, Chu YQ, Ye ZY, Wang YY, Tao HQ(2010). *Overexpression of matrix metalloproteinase 11 in human gastric carcinoma and its clinicopathologic significance*, Hum Path 41 : 686-696.
257. Kwon YJ, Hurst DR, Steg AD, Yuan K, Vaidya KS, Welch DR, Frost AR (2011). *Gli1 enhances migration and invasion via up-regulation of MMP-11 and promotes metastasis in ERα negative breast cancer cell lines*, Clin Exp Metastasis 28 : 437-449.
258. Mucha A Cuniasse P, Kannan R, Beau F, Yiotakis A, Basset P, Dive V. (1998). *Membrane type-1 matrix metalloprotease and stromelysin-3 cleave more efficiently synthetic substrates containing unusual amino acids in their P1' positions*, J Biol Chem 273 : 2763-2768.
259. Mañes S Mira E, Mira E, Barbacid MM, Ciprés A, Fernández-Resa P, Buesa JM, Mérida I, Aracil M, Márquez G, Martínez-A C. (1997). *Identification of insulin-like growth factor-binding protein-1 as a potential physiological substrate for human stromelysin-3.*, J Biol Chem 272 : 25706-12..
260. Uryga-Polowy V, Kosslick D, Freund C, Rademann J. (2008). *Aminofluorescein for C-Terminal Labeling of Peptides: High-Affinity Polarization Probes Binding to Polyproline-Specific GYF Domains.*, ChemBioChem 9 : 2452-2462.
261. Ramso-Tomillero I, Mendive-Tapia L, Gongora-Benitez M, Nicolas E, Tulla-Puche J, Albericio F. (2013). *Understanding Acid Lability of Cysteine Protecting Groups*, Molecules 18 : 5155-5163.
262. Berthault P, Desvaux H, Wendlinger T, Gyejacquot M, Stopin A, Brotin T, Dutasta JP, Boulard Y.(2010). *Effect of pH and Counterions on the Encapsulation Properties of Xenon in Water-Soluble Cryptophanes*, Chem Eur J 16 : 12941-12946.
263. Hazra S Guha R, Jongkey G, Palui H, Mishra A, Vemuganti GK, Basak SK, Mandal TK, Konar A.(2012). *Modulation of matrix metalloproteinase activity by EDTA prevents posterior capsular opacification*, Mol Vis 18 : 1701-11.
264. Elias DR, Thorek DL, Chen AK, Czupryna J, Tsourkas A. (2008). *In vivo imaging of cancer biomarkers using activatable molecular probes.*, Cancer Biomarkers 4 : 287-305.
265. Lee S, Xie J, Chen X.(2010). *Activatable molecular probes for cancer imaging*, Curr Top Med Chem 20 : 1134-

1144.
266. Law B and Tung CH. (2009). *Proteolysis: A Biological Process Adapted in Drug Delivery, Therapy, and Imaging*, Bioconj Chem 20 : 1683-1696.
267. Metildi CA, Felsen CN, Savariar EN, Nguyen QT, Kaushal S, Hoffman RM, Tsien RY, Bouvet M (2014). *Ratiometric Activatable Cell-Penetrating Peptides Label Pancreatic Cancer, Enabling Fluorescence-Guided Surgery, Which Reduces Metastases and Recurrence in Orthotopic Mouse Model*, Ann Surg Oncol. doi: 10.1245/s10434-014-4144-1
268. Wang Y, Shen P, Li C, Wang Y, Liu Z. (2012). *Upconversion Fluorescence Resonance Energy Transfer Based Biosensor for Ultrasensitive Detection of Matrix Metalloproteinase-2 in Blood*, Anal Chem 84 : 1466-1473.
269. Kim YP, Daniel WL, Xia Z, Xie H, Mirkin CA, Rao J. (2010). *Bioluminescent nanosensors for protease detection based upon gold nanoparticle-luciferase conjugates*, Chem Commun (Camb) 46 : 76-78.
270. Krishnamurthy VM, Semetey V, Semetey V, Bracher PJ, Shen N, Whitesides GM. (2007). *Dependence of effective molarity on linker length for an intramolecular protein-ligand system*, J 129 : 1312-20.
271. Scmidt N,Mishra A, Lai GH, Wong GCL. (2010). *Arginine-rich cell-penetrating peptides*, FEBS Lett 584 : 1806-1813
272. Futaki S Nakase I, Tadokoro A, Takeuchi T, Jones A. (2007). *Arginine-rich peptides and their internalization mechanisms*, Biochem Soc Trans 35 : 784-787.
273. Madani F, Lindberg S, Langel U, Futaki S, Gräslund A.(2011). *Mechanisms of cellular uptake of cell-penetrating peptides*, J Biophys 2011 : 414729.
274. Regberg J, Srimanee A, Langel U. (2012). *Applications of cell-penetrating peptides for tumor targeting and future cancer therapies*, Pharmaceuticals (Basel) 5 : 991-1007.
275. Futaki S, Suzuki T, Ohashi W, Yagami T, Tanaka S, Ueda K, Sugiura Y (2001). *Arginine-rich peptides. An abundant source of membrane-permeable peptides having potential as carriers for intracellular protein delivery*, J Biol Chem 276 : 5836-5840.
276. Futaki S. (2005). *Membrane-permeable arginine-rich peptides and the translocation mechanisms*, Adv. Drug Delivery Rev. 57 : 547-558.
277. Lättig-Tünnemann G, Prinz M, Hoffmann D, Behlke J, Palm-Apergi C, Morano I, Herce HD, Cardoso MC (2011). *Backbone rigidity and static presentation of guanidinium groups increase cellular uptake of arginine rich cell-penetrating peptides*, Nat Commun 2 : 435.
278. Farkhani SM, Valizadeh A, Karami H, Mohammadi S, Sohrabi N, Badrzadeh F. (2014). *Cell penetrating peptides: efficient vectors for delivery of nanoparticles, nanocarriers, therapeutic and diagnostic molecules*, Peptides 57 : 78-94.
279. Tünnemann G, Ter-Avetisyan G, Martin MM, Stöckl M, Herrmann A, Cardoso MC. (2008) *Live-cell analysis of cell penetration ability and toxicity of oligo-arginines.* J Pept Sci 14: 469-476.
280. Bechara C and Sagan S. (2013). *Cell-penetrating peptides: 20 years later, where do we stand?*, FEBS Letters 587 : 1693-702.
281. Szeto HH, Schiller PW, Zhao K, Luo G. (2004). *Fluorescent dyes alter Intracellular targeting an function of Cell-Penetrating peptides*, FEBS J 19:118-120.
282. Schnorrenberg G and Gerhardt H (1989). *Fully automatic simultaneous multiple peptide synthesis in micromolar scale - rapid synthesis of series of peptides for screening in biological assays.*, tetrahedon 45 : 7759-7764.
283. Pearson DA, Blanchette M, Baker ML, Guindon CA. (1989). *Trialkylsilanes as scavengers for the trifluoroacetic acid deblocking of protecting groups in peptide synthesis*, tetrahedon lett 30 : 2739–2742.
284. Deres K, Schild H, Wiesmüller KH, Jung G, Rammensee HG. (1989). *In vivo priming of virus-specific cytotoxic T lymphocytes with synthetic lipopeptide vaccine*, Nat 342 : 561-564.
285. Bremer C, Tung CH, Weissleder R (2001). *In vivo molecular target assessment of matrix metalloproteinase inhibition.*, Nat Med 7 : 743-8..

286. Walrant A, Correia I, Jiao CY, Lequin O, Bent EH, Goasdoué N, Lacombe C, Chassaing G, Sagan S, Alves ID. (2011). *Different membrane behaviour and cellular uptake of three basic arginine-rich peptides*, Biochem 1808 : 382-93.

Acknowledgements

I would like to thanks, first of all, my supervisor Dr. Leif Schröder for giving me the opportunity to work on this very stimulating project. Then, I would like to thanks my colleagues for their help, support and good brainstorming through all those years, especially Honor and Chris for helping me with my final experiments.
I would like to thanks infinitely my family, my sweet half, my friends, my bandmates (Will over all) and my comrades for all moral and material support and understanding.
And finally, a special thanks go to Alice, and to Silvia, that in their own way made me understand how great it is to be a scientist.